Modeling of Dynamic Behavior in Closed Crack and Nonlinear Ultrasonic Array Imaging

A DISSERTATION

SUBMITTED TO THE DEPARTMENT OF CIVIL ENGINEERING

AND THE COMMITTEE ON GRADUATE STUDIES

OF EHIME UNIVERSITY

IN PARTIAL FULFILLMENT OF THE REQUIREMENTS

FOR THE DEGREE OF

DOCTOR OF ENGINEERING

ASRIANA IBRAHIM

MARCH 2017

Prof. Dr. Kazuyuki Nakahata
(Principal Advisor)

Prof. Dr. Mitao Ohga

Prof. Dr. Manabu Takahashi

ABSTRACT

MODELING OF DYNAMIC BEHAVIOR IN CLOSED CRACK AND NONLINEAR ULTRASONIC ARRAY IMAGING

Ultrasonic testing (UT) utilizes the traveling time and amplitude of a scattered wave from cracks in a material. A distinct scattered wave can be obtained from a crack with opening faces. It is difficult, by contrast, to detect signals from closed cracks such as stress corrosion and fatigue cracks using the conventional UT. Since the crack faces are in contact due to a residual stress, most of the incident wave penetrates the crack faces and a little scattered wave will be generated. A nonlinear ultrasonic method based on contact acoustic nonlinearity (CAN) which utilizes the dynamic behaviors of the contact and separation states of the crack faces is a promising method. The clapping motion of the crack faces generates harmonics in the frequency spectrum. However, the generation of the harmonics from the crack faces is so sensitive that the voltage, angle, cycle, and frequency of the incident wave should be set in a well-chosen method.

In this thesis, a modeling of the generation of the harmonics wave from the closed crack was performed to enhance the reliability of the nonlinear ultrasonic method. Here, an elastodynamic finite integration technique (EFIT) was introduced to simulate a transient motion of the scattered wave from the closed crack. The EFIT adopted a set of split computational nodes at the interface of the closed crack to show the contact and separation depending on the stress and opening displacement of the interface. The numerical results for one-dimensional wave field showed good agreement with the analytical solutions. The simulation results revealed that a closing velocity of the interface was determined by the compressive pressure of the material and was validated by the experimental measurement with polymethylmethacrylate (PMMA) specimens. The appropriate conditions to obtain the nonlinear ultrasonic wave

in the case of ultrasonic array testing were determined by performing two-dimensional simulations.

An imaging method of the closed crack using an array transducer was investigated using the EFIT simulation. The full waveforms sampling and processing (FSAP) was applied as the imaging technique. For the generation of the nonlinear ultrasonic wave from the closed crack, the FSAP was modified to an algorithm which can transmit a strong beam from the array transducer by setting the delay for all elements electronically. The second harmonic component which extracted from the scattered wave using a band-pass filter was used as the input to the FSAP imaging technique. From the results, it was found that the shape and the location of the closed crack can be reconstructed when the amplitude, frequency, cycle, and angle of the incident wave are set at appropriate values.

ACKNOWLEDGMENT

Praise to Allah. First of all, I would like to express my sincere gratitude and special appreciation to my advisor Dr. Kazuyuki Nakahata, Professor of Ehime University, for his continuous support, excellent guidance, constant motivation, and immense knowledge. His guidance helped me in all the time of research, writing of this thesis and also life in Japan.

I would like to thank Dr. Yamawaki Hisashi, Researcher of NIMS for shared knowledge, theoretical and technical guidance on measurement activities, also for Dr. Ikumu Watanabe, Researcher of NIMS for all supports throughout three months internship period in National Institute for Materials Science (NIMS).

Besides, I would like to thank the rest of my thesis committee: Prof. Dr. Mitao Ohga, Prof. Dr. Manabu Takahashi, and Assist. Prof. Dr. Pang Jo Chun for their insightful comments and encouragement. All these great guidance mainly directed to contribute an original research to the field. Also, great thanks to all fellow team in Structural Engineering Laboratory for the stimulating discussions and for all the fun we have had in the last three years. In particular, I thank to the secretary, Mrs. Yuko Katsura for assisting me throughout my academic session in Ehime University.

My appreciation also extend to Universiti Teknikal Malaysia Melaka (UTeM) and Malaysia Ministry of Higher Education for the financial support I received during the study. I would also like to thank all of my friends especially Malaysian community in Japan for their encouragement and companionship throughout the life in Japan and incented me to strive towards my goal.

Lastly and most importantly, I wish to thank my late father Ibrahim bin Abd Aziz (1949-2005), beloved mother Asiah binti Bikom, beloved husband Mohd Zaki bin Salehan and beloved daughter Asdaqul Afrah binti Mohd Zaki. They supported me, taught me, and loved me. Words cannot express how grateful I am for all of the sacrifices that you've made on my behalf. To them I dedicated this thesis.

CONTENTS

LIST OF TABLES

LIST OF FIGURES

1 INTRODUCTION

(1) Purpose of Study

Non-Destructive Testing (NDT) has been widely used to evaluate a damaged state in a structural material without destroying or damaging it. The term 'Non-Destructive Evaluation' (NDE) has been used when the quantitative estimation is required to increase the reliability of the inspection[1, 2]. The main purpose of NDE is to determine the properties of materials such as fracture toughness, formability and microstructure characteristics[3]. NDT has been carried out using several techniques. Out of which ultrasonic testing (UT) is one of practical and popular methods. UT can be applied to detect the shape[4], size[5], orientation, and location[6] of the defect and the inclusion[7, 8].

When dealing with an interfacial problem, the evaluation of an imperfect interface is one of the challenging problems. At such the interface is partially bonding and temporary closing, the ultrasonic wave penetrates the interface and a little scattered wave will be generated. In order to overcome this problem, researchers have focused their efforts on exploiting nonlinear phenomena arising from the interaction of ultrasonic waves with imperfect interfaces. It has been experimentally proved that the frequency spectrum of a wave scattered by the imperfect interface had higher harmonics components. The ultrasonic method using the harmonics had been applied to the evaluation of closed cracks[9, 10] as well as the interface[11, 12] of materials.

A number of studies were carried out to understand the nonlinear wave generated in elastic solid material. There are several sources of generation when it comes to nonlinearity in solid material[13-15]. In the nonlinearity of elastic wave, the contact acoustic nonlinearity (CAN)[16] was exposed to exhibit a substantial departure for the higher harmonics generation and acoustic wave interaction. Hence, this has been a predominant subject for a majority

of studies in classical nonlinear acoustics. These results were then supplemented by direct observation of efficient higher harmonics generation in bulk acoustic wave reflection from an interface between two nonlinear solids[17]. The experiments revealed an increase in acoustic nonlinearity, by several orders of magnitude for both surface and bulk waves[18] in a weakly bonded contact.

In spite of a great wealth of experimental results, the understanding of the mechanism responsible for the generation of nonlinear effects has lagged behind. This leads to the aim of this study which is to develop a numerical model based on the CAN concept and to apply it to a realistic simulation for the nonlinear ultrasonic testing of closed cracks. A numerical simulation using an elastodynamic finite integration technique (EFIT) is introduced to model the CAN and predict the ultrasonic signals from the closed crack. The research for appropriate conditions to generate the harmonics through the simulation would enhance the reliability of the UT for the closed crack.

(2) Background of Ultrasonic Testing

The UT utilizes the traveling time and amplitude of a scattered wave from the cracks in a material[5]. A distinct scattered wave can be obtained from a crack with opening faces. However, it is difficult to detect signals from a crack with a closed face such as stress corrosion and fatigue cracks using a linear UT. Since most of the incident waves can penetrate the crack faces, a little scattered wave will be generated. Recently, nonlinear ultrasonic methods that use the CAN have been reported. The CAN is based on the dynamic behavior of contact and separation of the crack face when the incident wave with a large amplitude has been transmitted. The analytical model of the CAN was developed by Richardson[19], followed by which several experimental studies were conducted to evaluate the closed crack[20-23]. There have also been several numerical modeling studies to investigate the CAN. Notable techniques used were boundary element method (BEM), finite difference time domain (FDTD), and finite element method (FEM). Mendelsohn & Doong[24] and Hirose[25, 26] proposed the

nonlinear interfacial model using the BEM and carried out the dynamic contact analyses in two-dimensional (2-D) out-of-plane and in-plane wave fields, respectively. Besides, the BEM was also utilized to model the generation of nonlinearity between solid-solid interfaces[27-29]. The FDTD technique was used to solve one-dimensional (1-D)[30] as well as 2-D[31-34] in-plane problems. The nonlinear behavior of the interacting interface[35-39] was studied in detail using the FEM analysis.

In this study, a numerical modeling using the EFIT[40, 41] is applied to model the dynamics of a nonlinear interface. The EFIT performs integration over volumes in the process of the discretization. This method results in staggered grids and provides very stable code, allowing easy and flexible treatment of various boundary conditions. This is also useful to model the elastic wave propagation in inhomogeneous material[42-46]. In the EFIT framework, digital 2-D and three-dimensional (3-D) images with a unified cell size are used as the input data for the simulation[47-49]. Using the image-based EFIT, the inhomogeneous cracks distributed in a material can be modeled with a small preprocessing cost. Since the CAN is based on a finite amplitude theory, the measurements are use the tone burst and continuous waves. A tone burst[50-52] creates an enveloped single frequency signal in the material.

To treat the interfacial problem strictly, a model with pressure-dependent nonlinear stiffness[53-55] was introduced. Besides, Solodov[56] proposed an interface friction model caused by sliding in the tangential direction. In this study, a measurement of harmonics is demonstrated to verify the simple CAN theory assuming the 1-D wave field. In the measurement, polymethylmethacrylate (PMMA) specimens with a smooth interface were used. By using the nonlinear ultrasonic wave, imaging methods were reported to show the location and height of the closed crack. A simulation model[33] using the FDTD method and its experimental[57-59] validation were carried out to obtain the image of the closed crack using subharmonics. Furthermore, the nonlinear effects by higher harmonics[60-62] were also used for the nonlinear ultrasonic imaging.

(3) Outline of the Dissertation

This thesis is arranged as follows:

- Chapter **1** describes the introductory concepts in the field of NDT, UT, and states the outline of the thesis by briefly describing the contents of each chapter.
- Chapter **2** explains the fundamental concept of the CAN. The generation of nonlinear ultrasonic wave at an interface in a linear elastic material is formulated. The analytical solution of interfacial displacement is formulated based on Richardson's theory.
- Chapter **3** proposes a 1-D numerical model of the CAN where the 1-D EFIT formulations are described. In the modeling, a set of split computational nodes is introduced to express the separation state of the interface. The numerical solutions are compared with the analytical solutions to check the accuracy of the proposed model.
- Chapter **4** reports the results of the experiment to measure the harmonics from an interface between two PMMA specimens. These experiments validate the 1-D interfacial model by the EFIT. According to the CAN, it is said a sawtooth wave is generated. The sawtooth wave that was generated by the clapping at the interface was experimentally observed using a laser doppler vibrometer for PMMA specimens. The characteristics of the sawtooth wave, in particular, the relationship between the compressive pressure at the interface and the closing velocity of the interface are discussed.
- Chapter **5** explains how the numerical model of the CAN is applied to 2-D wave field using EFIT. The 2-D simulation is performed to investigate the generation of harmonics from the closed crack. A phased array UT modeling is employed for the evaluation of the closed crack where the crack is located at the lower surface of the material. The characteristics of the harmonics generation are investigated by varying the incident angle and by studying the correlation between the compressive pressure and the incident stress amplitude.

- Chapter **6** describes the phased array imaging of the closed crack by using full-waveforms sampling and processing (FSAP) method. Here, the second harmonic extracted from the scattered wave from the closed crack is fed into the FSAP method. The simultaneous firing of array elements is employed to transmit ultrasonic waves with high amplitude and synthesize the scattered waves using the post processing of the FSAP. The simulation of the FSAP imaging is demonstrated using the scattered wave calculated with the EFIT.

- Chapter **7** concludes with the results obtained and also explains the conclusions of this research while highlighting the future works that are possible to be undertaken.

2 CONTACT ACOUSTIC NONLINEARITY (CAN) AND ITS APPLICATION TO NONDESTRUCTIVE TESTING

(1) Introduction

Reliable, accurate, and quantitative techniques for nondestructively evaluating the damage state are required for materials that are used in severe environments. Although the ultrasonic method is widely used in the NDT, considerable effort has also been focused on the development of the nonlinear ultrasonic method. The nonlinear response from the crack in the material is provided by the contact and separation behavior of the crack faces. This phenomenon can be examined with the CAN theory. In this chapter, a 1-D unbonded planar crack interface is considered and the analytical model for the clapping of the interface is described according to Richardson's[19] theory. The correlation of the compressive pressure applied at the interface and the incident stress amplitude is described and a nonlinear parameter is defined.

(2) Generation of Nonlinearity at Crack Interface

The first step is to present the stress wave propagation in a linear elastic material. The theory will be described in the most basic case as acoustic harmonics generation at an unbonded planar crack interface. These harmonics, in the simplest sense, are generated by the cyclical increase and decrease of the contact area of cracks under the stresses of an acoustic wave. This is necessarily dependent on the relative smoothness, the deformability, and the normal stress induced by the stress wave on the crack interface.

It is perfectly valid to use the elasticity theory[63)] to solve equations of small motion. In terms of Lamé's constants (λ and G), volumetric expansion (e), and assuming no body forces except inertia:

$$\begin{aligned}(\lambda+G)\frac{\partial e}{\partial x}+G\nabla^2 u-\rho\frac{\partial^2 u}{\partial t^2}&=0\\(\lambda+G)\frac{\partial e}{\partial x}+G\nabla^2 v-\rho\frac{\partial^2 v}{\partial t^2}&=0\\(\lambda+G)\frac{\partial e}{\partial x}+G\nabla^2 w-\rho\frac{\partial^2 w}{\partial t^2}&=0\end{aligned} \tag{2.1}$$

where

$$\nabla^2=\frac{\partial^2}{\partial x^2}+\frac{\partial^2}{\partial y^2}+\frac{\partial^2}{\partial z^2}. \tag{2.2}$$

The displacements u, v, and w are derived from a single function ϕ such that:

$$u=\frac{\partial\phi}{\partial x}\ ;\ v=\frac{\partial\phi}{\partial y}\ ;\ w=\frac{\partial\phi}{\partial z}. \tag{2.3}$$

Then, writing the volumetric expansion ($e=\varepsilon_x+\varepsilon_y+\varepsilon_z$) in terms of ϕ from Eq. (2.3) and subtituting back into Eq. (2.1), we get:

$$\begin{aligned}(\lambda+2G)\nabla^2 u-\rho\frac{\partial^2 u}{\partial t^2}&=0\\(\lambda+2G)\nabla^2 v-\rho\frac{\partial^2 v}{\partial t^2}&=0\\(\lambda+2G)\nabla^2 w-\rho\frac{\partial^2 w}{\partial t^2}&=0.\end{aligned} \tag{2.4}$$

The longitudinal plane waves have the following form if we assume the propagation occurs

along in the x-direction ($v = w = 0$ in Eq. (2.4)).

$$\frac{\partial^2 u}{\partial t^2} = c_L^2 \frac{\partial^2 u}{\partial x^2} \tag{2.5}$$

The displacement u from the above equation can be solved by substituting any function of the form in Eq. (2.6) into the differential equation in Eq. (2.5).

$$u = f(x - c_L t) + f_1(x + c_L t) \tag{2.6}$$

First of all, notice that these results pertain to the longitudinal waves in an infinite bulk medium. As a further simplication, consider only the steady state solution:

$$(u)_{t=0} = f(x) + f_1(x) \tag{2.7}$$

$$\left(\frac{\partial u}{\partial t}\right)_{t=0} = c_L\left[f_1'(x) - f'(x)\right]. \tag{2.8}$$

Then, assuming $(v)_{t=0} = 0$ and $(u)_{t=0} = F(x)$,

$$f(x) = f_1(x) = \frac{1}{2}F(x) \tag{2.9}$$

a wave of half the amplitude will travel in each direction away from the source. At a free surface, we apply a forcing function and find that the forward moving half of the displacement function $f(x - c_L t)$ is the only part of significance, because the backward moving part $f_1(x + c_L t)$ is generally reflected in phase with $f(x - c_L t)$ by design in a transducer assembly.

The particle velocity due to the stress wave is defined as:

$$\dot{u} = \frac{\partial u}{\partial t} = -c_L f'(x - c_L t) \tag{2.10}$$

where $f'(x - c_L t)$ is derivative of $f(x - c_L t)$ with respect to $(x - c_L t)$. The strain (ε_x) can be calculated directly from u (Eq. (2.6)):

$$\varepsilon_x = \frac{\partial u}{\partial x} = f'(x - c_L t) \tag{2.11}$$

and stress (σ_x) can be derived as:

$$\sigma_x = -\rho c_L \dot{u} \tag{2.12}$$

with consideration of only the longitudinal, forward moving wave, propagating in the positive *x*-direction from its origination. Accordingly, a sine function solution is used as in the following form:

$$u = u_0 \sin \frac{2\pi}{l}(x - c_L t) \tag{2.13}$$

where l is the wavelength of the input function and u_0 is the displacement amplitude. By substitute u into Eq. (2.10), the particle velocity becomes:

$$\frac{\partial u}{\partial t} = \dot{u} = -\frac{2\pi c_L}{l} u_0 \cos \frac{2\pi}{l}(x - c_L t). \tag{2.14}$$

The stress wave can be calculated from Eqs. (2.11) and (2.12) by substituting $\dot{u}$ as in the following:

$$\sigma_x = \rho \frac{2\pi c_L^2}{l} u_0 \cos \frac{2\pi}{l}(x - c_L t). \tag{2.15}$$

Since the aim is to analyze the complex case of the multiple wave interaction, we considered a bi-tone stress wave. At a point not far from the transducer, the waves overlap each other as follows with the subscripts LF (low frequency) and HF (high frequency):

$$\sigma_x = \rho \frac{2\pi c_L^2}{l_{LF} l_{HF}} \left[l_{HF} u_{LF} \sin \frac{2\pi}{l_{LF}}(x - c_L(t - \tau_{LF})) + l_{LF} u_{HF} \sin \frac{2\pi}{l_{HF}}(x - c_L(t - \tau_{HF})) \right]. \tag{2.16}$$

The Fourier transform of Eq. (2.16) is shown in the following form:

$$F[\sigma_x(t)] = \rho \frac{\sqrt{2\pi^3} c_L^2}{l_{LF} l_{HF}} \left[l_{HF} u_{LF} A \delta\left(\frac{2\pi c_L}{l_{LF}} + \omega \right) + l_{LF} u_{HF} B \delta\left(\frac{2\pi c_L}{l_{HF}} + \omega \right) \right] \tag{2.17}$$

where A and B in Eq. (2.17) are defined as:

$$\begin{aligned} A &= \cos \frac{2\pi}{l_{LF}}(x + c_L \tau_{LF}) \\ B &= \cos \frac{2\pi}{l_{HF}}(x + c_L \tau_{HF}). \end{aligned} \tag{2.18}$$

Here, $\delta(\omega)$ is the Dirac delta function where:

$$\delta(\omega) = \begin{cases} \infty : \dfrac{2\pi c_L}{l_{LF}} + \omega = 0 \\ \infty : \dfrac{2\pi c_L}{l_{HF}} + \omega = 0 \\ 0 : elsewhere. \end{cases} \tag{2.19}$$

In the above description, the propagation of the plane longitudinal waves in the infinite linear elastic medium, by defining a planar crack at the origin and orthogonal to the axis of the stress wave propagation, we can investigate the most simplified form of acoustic interaction with a crack. Though the bulk body behaves in a linear elastic manner in response to acoustive wave propagation, yet under some conditions the interface will produce a nonlinear response. In other word, despite expectation of zero-phase lag sinusoidal strain response (linear response) from a sinusoidal stress input, depending on the pressure holding the interface together, the response may be non-sinusoidal across the interface.

From a physical point of view, this may be seen as the two faces bounching apart resulting in intermittent transmission and reflection of a sine wave propagating on one-side of the interface. From here on, we will consider this particular geometric nonlinearity source as the interface chattering effect.

(3) Analytical Model of Unbonded Planar Crack Interface

Richardson[19] has developed a solid foundation for the nonlinearity generation at an unbonded planar crack interface. The following is the summary of his approach to the problem.

By considering the small displacement, elastic wave equations discussed in previous section showed a stress-strain relationship as in Eq. (2.12), and add an initial compressive stress (σ_c) in the medium closing the interface as follows:

$$\sigma_x = \lambda_E \frac{\partial u}{\partial x} + \sigma_c \tag{2.20}$$

where, λ_E is a generalized elastic constant.

Consider an unbonded planar crack interface embedded in an infinite elastic medium, we can simplify the system to the plane wave propagation along in the x-direction. The modulus elasticity of the material (E) then replaces λ_E in Eq. (2.20). The origin is located at the interface as shown in Fig. 2.1 (a). In Fig. 2.1 (b), the crack faces at left-hand side (LHS) and right-hand side (RHS) of the origin are indicated by 0_- and 0_+, respectively. The boundary conditions across the crack faces must include both states of the contact and

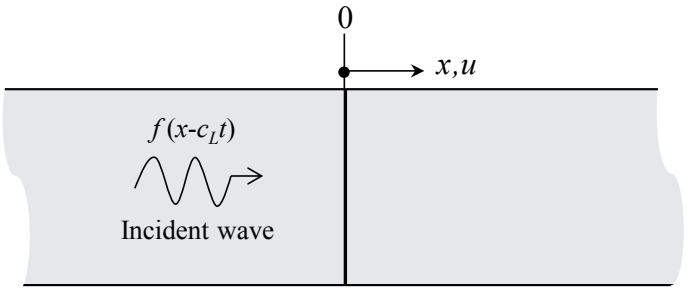

(a) Contact state.

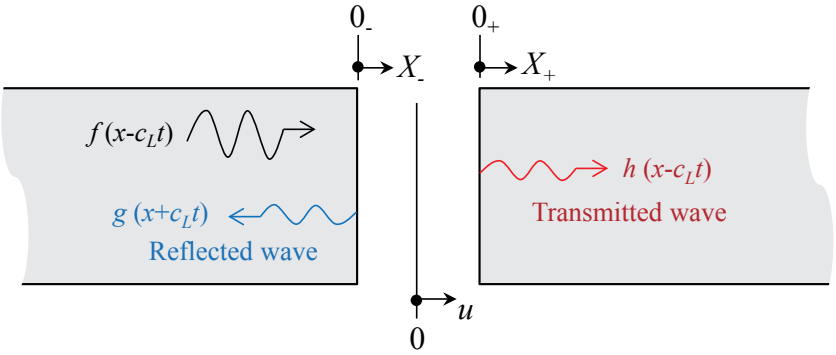

(b) Separation state.

Fig. 2.1 Conceptual model of an unbonded planar crack interface.

separation conditions. When the crack faces are in the contact state, the displacement of both LHS and RHS must be equal and both crack faces must be in the compression condition:

$$\begin{aligned} u(0_+, t) &= u(0_-, t) \\ \sigma(0_+, t) &= \sigma(0_-, t) < 0. \end{aligned} \tag{2.21}$$

While, when the crack faces are in the separation state, the displacement of the crack face at the RHS must be greater than the LHS and the stress at the interface must be zero:

$$\begin{aligned} u(0_+, t) &> u(0_-, t) \\ \sigma(0_+, t) &= \sigma(0_-, t) = 0. \end{aligned} \tag{2.22}$$

The initial conditions also included in the time domain. As the crack faces are assummed to be contacted in the initial state, by considering the incident wave propagate from the LHS,

$$u(x, 0) = \begin{cases} 0 : 0 \le x < \infty \\ f(x) : -\infty < x < 0 \end{cases} \tag{2.23}$$

$$\frac{\partial u}{\partial t}(x,0) = \begin{cases} 0 : 0 \le x < \infty \\ -c_L f'(x) : -\infty < x < 0. \end{cases} \tag{2.24}$$

Now, the wave propagation in this system will be described. The right propagation stress wave, which called as “incident wave”, as it approaches the crack interface as shown in Fig. 2.1 (a). Interaction with the interface results in two possibilities: a right propagating wave transmitted into the right-half of the system when the crack faces are in the contact state, which called as “transmitted wave”, and a left propagating wave reflected by the free surface when the crack faces are in the separation state, which called as “reflected wave” (Fig. 2.1 (b)). The displacements for the left and right-halves of the system can be written as in Eqs. (2.25) and (2.26), respectively:

$$u = f(x - c_L t) + g(x + c_L t) \quad : \quad (x < 0, t > 0) \tag{2.25}$$

$$u = h(x - c_L t) \quad : \quad (x > 0, t > 0). \tag{2.26}$$

The interest of this section is the determination of the transmitted wave $h(x - c_L t)$ if the given incident wave is $f(x - c_L t)$. By substituting the interface boundary conditions as well as the initial conditions in Eq. (2.20), the stress at the interface becomes:

$$\sigma = \begin{cases} E[f'(x - c_L t) + g'(x + c_L t)] + \sigma_c \quad : \quad x < 0 \\ E[h'(x - c_L t)] + \sigma_c \quad : \quad x > 0 \end{cases} \tag{2.27}$$

where supercscript $()'$ means the derivative of the function. The stresses at both LHS and RHS of the interface can be expressed as:

$$\begin{aligned} \sigma(0_-, t) &= 2E f'(-c_L t) + \rho c_L \frac{\partial u(0_-, t)}{\partial t} + \sigma_c \\ \sigma(0_+, t) &= -\rho c_L \frac{\partial u(0_+, t)}{\partial t} + \sigma_c \end{aligned} \tag{2.28}$$

respectively. Then, the boundary conditions can be rewritten for the crack faces in the separation state:

$$\begin{aligned} \rho c_L \frac{\partial u(0_+, t)}{\partial t} &= +\sigma_c \\ \rho c_L \frac{\partial u(0_-, t)}{\partial t} &= -2E f'(-c_L t) - \sigma_c \end{aligned} \tag{2.29}$$

and for the crack faces in the contact state:

$$-\rho c_L \frac{\partial u(0_+,t)}{\partial t} + \sigma_c = \rho c_L \frac{\partial u(0_-,t)}{\partial t} + 2E f'(-c_L t) + \sigma_c < 0. \tag{2.30}$$

Next, to simplify the solution, a new coordinate system is created at the interface. X is defined as the center gravity of the interface and Y is the interfacial displacement as shown in Fig. 2.2. These new coordinates are expressed as:

$$X = \frac{1}{2}\left(u(0_+,t) + u(0_-,t)\right) \tag{2.31}$$

$$Y = u(0_+,t) - u(0_-,t). \tag{2.32}$$

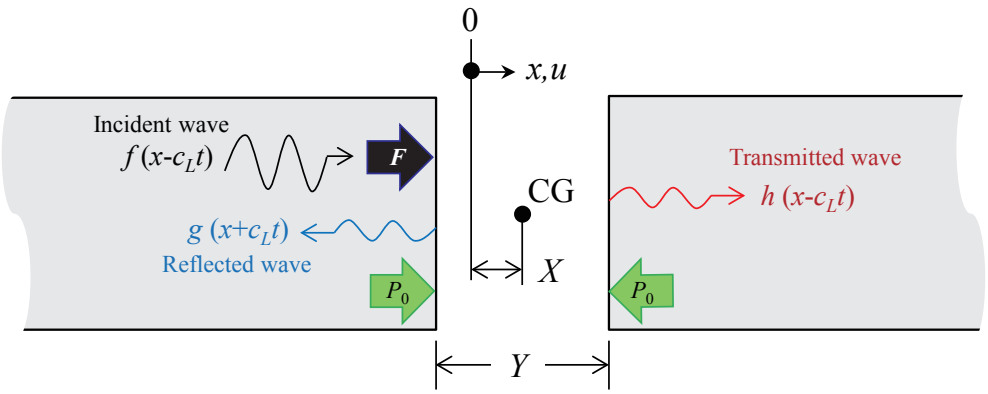

Fig. 2.2 New coordinate system for the conceptual model.

By substituting the new coordinate system in the boundary conditions, we can solve functions of $g(x)$ and $h(x)$ as a response to the surface pressure on the interface as:

$$g(x + c_L t) = -\frac{1}{2} Y\left(t + \frac{x}{c_L}\right) \tag{2.33}$$

$$h(x - c_L t) = f(x - c_L t) + \frac{1}{2} Y\left(t - \frac{x}{c_L}\right). \tag{2.34}$$

A sinusoidal input wave is used and assumed the interface initially in the contact state:

$$f(x) = -A\cos\frac{2\pi}{l}x \tag{2.35}$$

$$f(-c_L t) = -A\cos\frac{2\pi}{l}c_L t. \tag{2.36}$$

Now, by substituting the equation $f(x - c_L t)$ into Eqs. (2.31) and (2.32), we can solve the functions $X(t)$ and $Y(t)$ which governing the crack interface. As result, $X(t)$ remain the same for all time as follows:

$$X(t) = f(-c_L t) = -u_0\cos\frac{2\pi}{l}c_L t. \tag{2.37}$$

$Y(t)$ is more complex and must be determined in a stepwise manner following the boundary conditions for the system. Since the boundary conditions depend on the contact and separation states, $Y(t)$ must also depend on those conditions.

Here, assuming a constant compressive stress is appplied to the interface by replacing σ_c with an equivalent surface pressure (P_0) acting on the crack faces. Since the crack faces are in the contact state in the initial condition, $Y(t)$ must be zero until the force from the incident wave exceeds the compressive pressure:

$$Y(t) = 0 \quad : \quad 0 \le t \le t_1. \tag{2.38}$$

Let the force of the incident wave, $F = -2Ef'(-c_L t)$ (Fig. 2.2), by comparing Eqs. (2.30) and (2.32), the stress at the interface (in a compressive condition) is expressed as:

$$\sigma_- = \sigma_+ = F + 2P_0 \tag{2.39}$$

and

$$\rho c_L \dot{X}(t) = \frac{1}{2}F \tag{2.40}$$

for all time. Thus, it is necessary to solve for time (t_1) at which the crack faces are in the separation state, or $F + 2P_0 \to 0$ moving from positive to negative as follows:

$$t_1 = \frac{\pi + \sin^1\left(\dfrac{P_0}{\rho c_L u_0 \omega}\right)}{\omega} \quad : \quad \omega = \frac{2\pi}{l}c_L. \tag{2.41}$$

From t_1 to some time (t_2), the interface will change to the separation state and $Y(t)$ can be determined from the separation stress condition (Eq. (2.29)) and the interfacial coordinates

(Eq. (2.32)). By rearranging, the interfacial displacement rate $\dot{Y}(t)$ can be written as:

$$\begin{aligned} \rho c_L \dot{Y} &= -F + 2\sigma_0 = -F - 2P_0 \\ \rho c_L \dot{Y} &= -2\rho c_L u_0 \omega \sin(\omega t) - 2P_0. \end{aligned} \tag{2.42}$$

Then, solve the $Y(t)$ where $Y(t_1) = 0$;

$$Y(t) = 2\left[u_0\Big(\cos(\omega t) - \cos(\omega t_1)\Big) - \frac{P_0}{\rho c_L}(t - t_1)\right] \quad : \quad t_1 \le t \le t_2. \tag{2.43}$$

During this interval, the resultant stress on the interface is zero and the static pressure acts as a closing pressure on the crack faces. It is then necessary to find the time (t_2) at which the interface will change to the contact state again. It can be determine as simply find the first positive root of Eq. (2.43) in the interval $t_1 \le t \le t_2$.

After the crack faces are contacted, it will effectively return to the initial conditions, and so we can shift the time axis by the period of the oscillations and repeat the above process (Eqs. (2.38) to (2.43)) for each new cycle.

Now, by using a discrete time series, the effect of transmitting an incident wave through the simple plane crack interface can be represented. This is done by writing the equations in a finite difference format, we can set $Y(t)$=0 which provided $F + 2P_0 < 0$ (contacted) and then set $Y(t)$ as in Eq. (2.43) until it reaches zero again.

Let t_i be the time at any time increment i, then $\Delta t = t_i - t_{i-1}$. The value t_1 can be set-up as a digital switch to become:

$$t_1 = t_{i-1} + \Delta t\left(\frac{(F + 2P_0)_{t_{i-1}}}{(F + 2P_0)_{t_{i-1}} - (F + 2P_0)_{t_i}}\right) \tag{2.44}$$

when $(F + 2P_0)_{t_i} < 0$ (contacted) for the first time and t_1 only exists for $Y(t) > 0$ (separated). During this interval (separated), the stress at the interface is zero ($\sigma = 0$). When $Y(t)$ passes through zero again, its value is once more set to the constant value of zero (contacted) until t_1 comes into existance again (separated) according to Eq. (2.44). The displacement on the RHS of the interface is calculated from Eqs. (2.31) and (2.32) as follows:

$$u_+ = X(t) + \frac{1}{2}Y(t). \tag{2.45}$$

The stress can be calculated from Eq. (2.28) by using a finite difference approach as follows:

$$\dot{u} = \frac{du}{dt} = \frac{\left(\frac{\Delta u_{i-1/2}}{\Delta t_{i-1/2}} + \frac{\Delta u_{i+1/2}}{\Delta t_{i+1/2}}\right)}{2}. \tag{2.46}$$

Now, consider the second harmonic generated by a nonlinear motion of the interface. According to Eqs. (2.33) and (2.34), the reflected $g(x + c_L t)$ and transmitted $h(x - c_L t)$ waves will contain second harmonic of equal magnitude but difference phases contributed by second harmonic of $\frac{1}{2}Y(t)$. While, the incident wave $f(x - c_L t)$ assumed does not contain a second harmonic. The second harmonic of $Y(t)$ can be defined by:

$$\bar{Y} \cong T^{-1} \int_{t_1}^{t_2} dt \exp(-2i\omega t) Y(t) \tag{2.47}$$

where T is the opening time interval $[0, T]$ in the time interval $t_1 \leq t \leq t_2$.

The interfacial displacement $Y(t)$ and the stress at the interface are both affected greatly by the compressive pressure (P_0) acting on the interface. When the compressive pressure is not applied ($P_0 = 0$), the crack faces will never contacted due to a large force from the incident wave acting on the crack faces. As result, there is no transmitting stress wave across the interface and the displacement of the RHS shows a stair-wave pattern as shown in Fig. 2.3 (a). When a large compressive pressure is applied ($2P_0 \geq F$), there is unsufficient force to make the separation state of the interface due to large compressive pressure acting on the crack faces. As results, the model acted as continuous media (Fig. 2.3 (b)). Hence, a nonlinear paramater introduced by Richardson[19] to indicate the relative level of the initial pressure acting on the interface is defined as following:

$$\eta = \frac{2P_0}{F} = \frac{P_0}{\rho c_L u_0 \omega}. \tag{2.48}$$

Theoretically, the interface will generates harmonics in the range of $0 < \eta < 1$ which the contact and separation are occured. The schematic diagram of the contact and separation crack interface due to the compressive pressure and the force from the incident wave with $0 < \eta < 1$ is shown in Fig. 2.3 (c).

(4) Summary

This chapter starts with the description of the stress wave propagation in a linear elastic material. Based on a pioneer work by Richardson[19], for the most simplified planar crack system in the linear elastic medium, the only source of the nonlinearity is an unbonded interface. The unbonded planar interface in an infinite elastic medium is considered to describe the formulation of the contact and separation behaviors. The solution is reduced to the consideration of new coordinates which corresponds to the center of gravity of the interface and the interfacial displacement. The center of gravity motion is the same as though the interface was perpetually contacted. The relative motion of the interface boundary as measured by the interfacial displacement has two schemes: one for the contact state and another one for the separation state. Furthermore, both interfacial displacement and the stress at the interface were affected greatly by the compressive pressure and the force from the incident wave acting on the interface. These parameters were an important criteria as the nonlinearity of the interface depended on them.

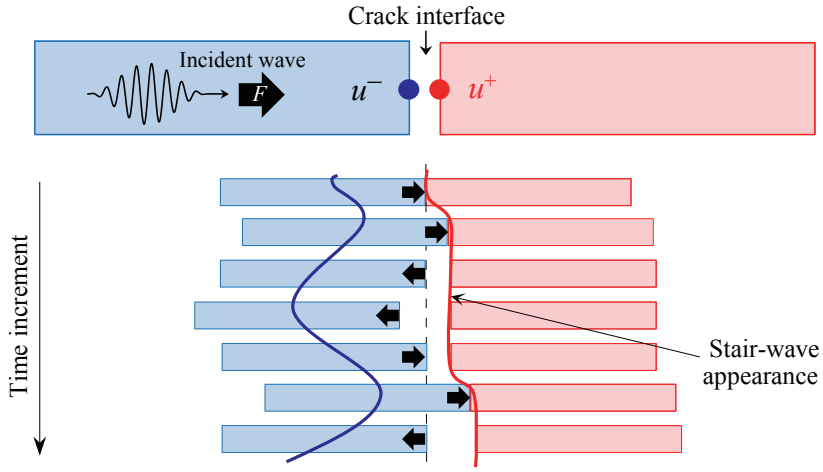

(a) Compressive pressure is not applied ($\eta = 0$).

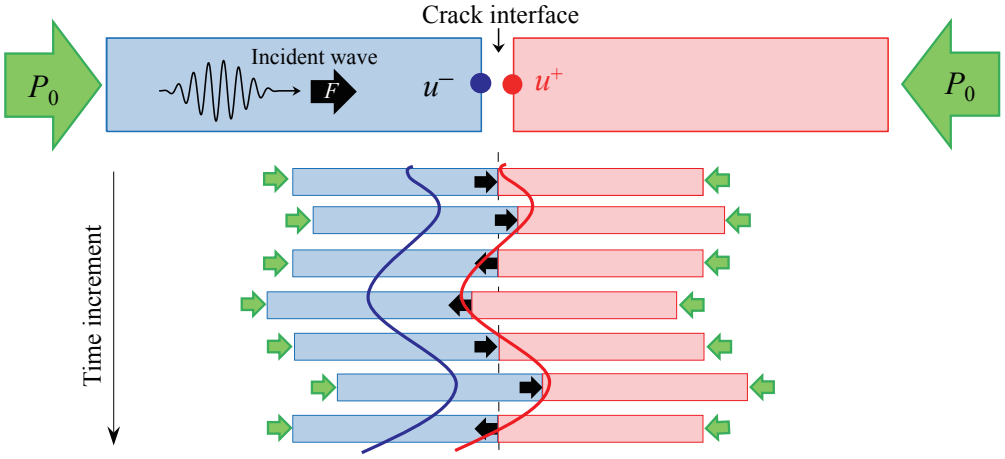

(b) Compressive pressure is applied ($\eta \geq 1$).

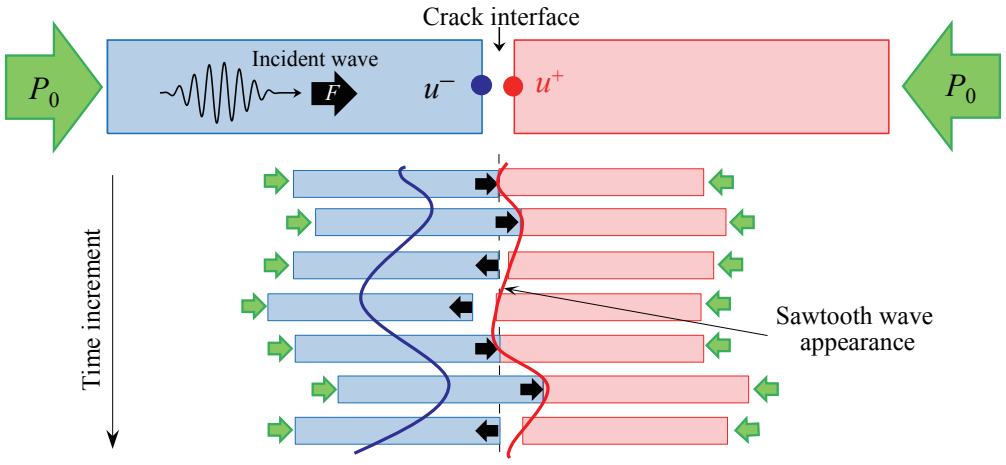

(c) Compressive pressure is applied ($0 < \eta < 1$).

Fig. 2.3 Schematic diagram for the behaviors of the crack interface.

3 ONE-DIMENSIONAL NUMERICAL MODELING OF CAN

(1) Introduction

The EFIT[40] is a method to simulate the elastic wave propagation in the time domain. In the EFIT, a shape of integration cell is represented as a structural grid of square (2-D) or cube (3-D). The EFIT updates the solutions of the particle velocity and stress alternately (leap-frog scheme). In the discretization process, the parameters of the elastic stiffness and density are uniquely defined within the integral cell. Therefore, the EFIT can easily set the dissimilar materials at the interface. In addition, the EFIT provides a theoretical treatment of a traction-free boundary which is vital in the boundary value problem of the elastic waves. The EFIT can be used to model the ultrasonic wave propagation in isotropic and anisotropic, homogeneous and heterogeneous as well as dissipative and non-dissipative elastic media [64-66]. In this study, the EFIT is introduced in a modeling of the clapping behavior at the crack faces. The states of the contact and separation of the crack interface are modeled by utilizing a set of split computational nodes at the crack faces. The 1-D EFIT is formulated with the description of the initial and boundary conditions under a compressive pressure at the crack faces. Numerical studies are carried out to investigate the nonlinear behavior of the crack interface. To investigate the accuracy of the EFIT application, the results of 1-D EFIT were compared with the analytical results[19].

(2) Formulation of 1-D EFIT

The governing equations in 3-D elastic wave field were used as a starting point for the formulation of 1-D EFIT. The summation convention is used for the index (i, j=1,2,3). The particle velocity vector v_i, the stress tensor τ_{ij}, and the body force vector f_i were satisfied in the equation of motion and the constitutive law:

$$\rho(\boldsymbol{x})\frac{\partial v_i(\boldsymbol{x})}{\partial t} = \frac{\partial \tau_{ij}(\boldsymbol{x})}{\partial x_j} + f_i(\boldsymbol{x}) \;\; (i, j = 1, 2, 3) \tag{3.1}$$

$$\frac{\partial \tau_{ij}(\boldsymbol{x})}{\partial t} = \lambda(\boldsymbol{x})\frac{\partial v_k(\boldsymbol{x})}{\partial x_k}\delta_{ij} + \mu(\boldsymbol{x})\left(\frac{\partial v_i(\boldsymbol{x})}{\partial x_j} + \frac{\partial v_j(\boldsymbol{x})}{\partial x_i}\right) \;\; (i, j = 1, 2, 3) \tag{3.2}$$

where ρ denotes the mass density, and λ and μ are the Lamé constants. Since the material is assumed as isotropic, the longitudinal wave velocity c_L and shear wave velocity c_T were expressed by the following equation:

$$c_L = \sqrt{\frac{\lambda + 2\mu}{\rho}} \;\; , \;\; c_T = \sqrt{\frac{\mu}{\rho}}. \tag{3.3}$$

Consider a vertical interface with an infinite height ($h \to \infty$) embedded in a linear elastic material. When a plane and longitudinal wave incidents normal to the interface, it can be considered as the scattering problem in the 1-D wave field. The velocity $v_1 (= \frac{\partial u_1}{\partial t})$ and stress σ_{11} were satisfied with the following integral forms:

$$\int \rho \frac{\partial v_1(x_1, t)}{\partial t} dA = \int \frac{\sigma_{11}(x_1, t)}{\partial x_1} dA = \int \sigma_{11}(x_1, t) n_1(x_1) dL \tag{3.4}$$

$$\int \frac{\partial \sigma_{11}(x_1, t)}{\partial t} dA = \int (\lambda + 2\mu)\frac{\partial v_1(x_1, t)}{\partial x_1} dA = \int (\lambda + 2\mu) v_1(x_1, t) n_1(x_1) dL \tag{3.5}$$

where n_1 is the outward normal vector component in the x_1-direction. The integration is performed over a cell A whose the size is uniformly $\Delta x \times h$ as shown in Fig. 3.1. Δx is the cell length. Assuming that v_1 and σ_{11} were constant within A, it retains the following forms:

$$\bar{\rho}\dot{v}_1 h \Delta x = h\left[(\sigma_{11})^R - (\sigma_{11})^L\right] \tag{3.6}$$

$$\dot{\sigma}_{11} h \Delta x = h\left[(\lambda + 2\mu)\left((v_1)^R - (v_1)^L\right)\right] \tag{3.7}$$

where $\dot{\sigma}_{11} = \partial\sigma_{11}/\partial t$, and the LHS and RHS of the cell are abbreviated as (L) and (R), respectively. The average value $\bar{\rho} = (\rho^{(L)} + \rho^{(R)})/2$ is used in the integration of v_1 in Eq. (3.6).

In the time domain, the velocities v_1 are allocated at full-time steps, while the stress components σ_{11} are allocated at half-time steps. The central difference approximation yields an explicit leap-frog scheme:

$$(v_1)_i^{k+1} = (v_1)_i^k + \left[\frac{\Delta t}{\Delta x}\frac{1}{\bar{\rho}}\left((\sigma_{11})_{i+\frac{1}{2}}^{k+\frac{1}{2}} - (\sigma_{11})_{i-\frac{1}{2}}^{k+\frac{1}{2}}\right)\right] \tag{3.8}$$

$$(\sigma_{11})_{i+\frac{1}{2}}^{k+\frac{1}{2}} = (\sigma_{11})_{i+\frac{1}{2}}^{k-\frac{1}{2}} + \left[\frac{\Delta t}{\Delta x}(\lambda + 2\mu)\left((v_1)_{i+1}^k - (v_1)_i^k\right)\right] \tag{3.9}$$

where Δt is the time interval. The v_1-grid and σ_{11}-grid are located as shown in Fig. 3.2. Equations (3.8) and (3.9) are then solved explicitly using the spatial staggered grid expressed as i and time increment expressed as k.

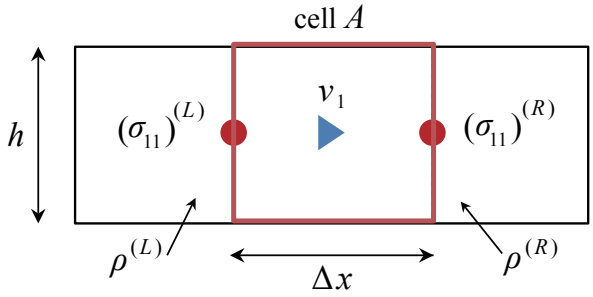

Fig. 3.1 Integration cell of v_1 in EFIT.

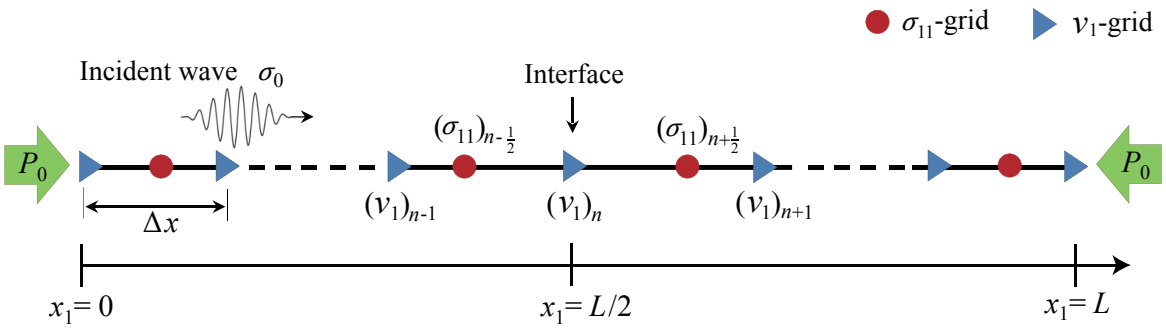

Fig. 3.2 Grid allocation of 1-D EFIT model.

(3) Modeling of Nonlinear Behavior at Closed Crack

This section shows a 1-D model of the EFIT which a set of split computational nodes is used at the crack interface. As shown in Fig. 3.2, the crack interface is located in the center of the model at the velocity grid $i = n$. When the interface is separated, the node at the interface is split into two nodes. The LHS and RHS of the nodes at the interface are indicated as $n-$ and $n+$, respectively (Fig. 3.3). The crack opening displacement is defined as $[u_1]$ as in Eq. (3.11). When $[u_1]$ is positive, i.e., the interface is separated, the traction-free condition is satisfied as:

$$(\sigma_{11})_n = 0 \tag{3.10}$$

$$[u_1] = (u_1)_{n+} - (u_1)_{n-} \ , \ \ [u_1] > 0. \tag{3.11}$$

The velocities at both sides on the interface are then expressed as:

$$(v_1)_{n+}^{k+1} = (v_1)_{n+}^{k} + \left[\frac{\Delta t}{\Delta x}\frac{1}{\rho}\left(2(\sigma_{11})_{n+\frac{1}{2}}^{k+\frac{1}{2}}\right)\right] \tag{3.12}$$

$$(v_1)_{n-}^{k+1} = (v_1)_{n-}^{k} - \left[\frac{\Delta t}{\Delta x}\frac{1}{\rho}\left(2(\sigma_{11})_{n-\frac{1}{2}}^{k+\frac{1}{2}}\right)\right]. \tag{3.13}$$

On the other hand, the continuity conditions:

$$(v_1)_{n-} = (v_1)_{n+} = (v_1)_n \tag{3.14}$$

$$(\sigma_{11})_n < 0 \tag{3.15}$$

are applied when the interface was in the contact state. Here, the split nodes are bound together as shown in Fig. 3.2. In this model, the velocity and displacement after the crack closure can be related as:

$$(v_1)_n = \frac{\rho_{n+\frac{1}{2}}(v_1)_{n+} + \rho_{n-\frac{1}{2}}(v_1)_{n-}}{\rho_{n+\frac{1}{2}} + \rho_{n-\frac{1}{2}}} \tag{3.16}$$

$$(u_1)_n = \frac{(u_1)_{n+} + (u_1)_{n-}}{2}. \tag{3.17}$$

In modeling the interacting faces, the contact and separation states of the crack interface vary according to the explicit scheme as shown in Fig. 3.4. The transitions of the contact and separation states are described as in the following:

1.If the interface in the contact state:

At $t = k + \frac{1}{2}$, calculate $(\sigma_{11})_n^{k+\frac{1}{2}}$.

If $(\sigma_{11})_n^{k+\frac{1}{2}} > 0$, in the next time $t = k+1$, the interface is separated and $(v_1)_n$ grid is split into $(v_1)_{n-}$ and $(v_1)_{n+}$.

2.If the interface in the separation state:

At $t = k$, calculate $[u_1]^k$.

If $[u_1]^k \le 0$, in the next time $t = k + \frac{1}{2}$, the interface is contacted. The split grids $(v_1)_{n-}$ and $(v_1)_{n+}$ are bound together to $(v_1)_n$.

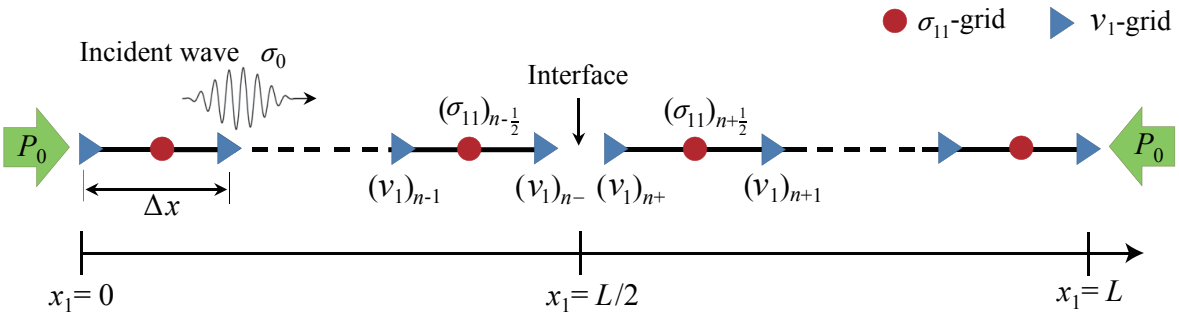

Fig. 3.3 Grid allocation of 1-D EFIT model with the split nodes.

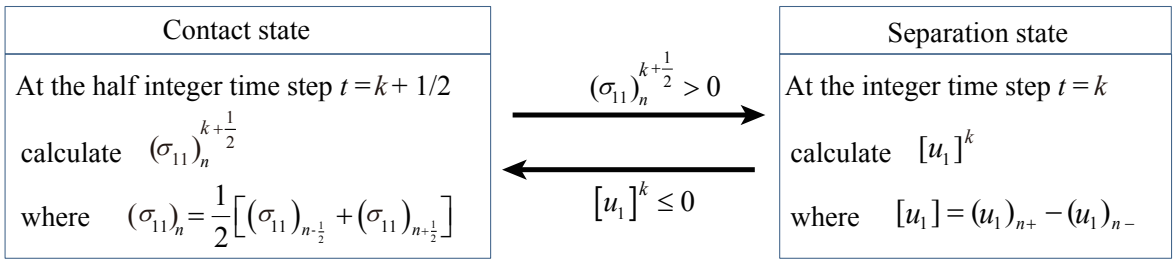

Fig. 3.4 The contact and separation states of the crack interface in the EFIT simulation.

(4) Initial and Boundary Conditions

In the initial condition, it is assumed that the interface is in the contact state. The material was subjected to the constant compressive pressure from the left and right edges as illustrated in Fig. 3.2.

$$\sigma_{11}^{st}(0,t) = \sigma_{11}^{st}(L,t) = -P_0 \tag{3.18}$$

The velocity and the stress in the initial state were given by:

$$v_1(x_1,0) = v_1^{in}(x_1,0) \tag{3.19}$$

$$\sigma_{11}(x_1,0) = \sigma_{11}^{in}(x_1,0) + \sigma_{11}^{st}(x_1,0) \tag{3.20}$$

where v_1^{in} and σ_{11}^{in} are the velocity and stress excited by the input wave, respectively.

(5) Courant Friedrich Lewy Condition

In order to perform the calculation at stable conditions, the time interval Δt must satisfy the Courant Friedrichs Lewy (CFL)[67] condition:

$$\Delta t \leq \frac{\Delta x}{c_{max}} \tag{3.21}$$

where c_{max} refers to the fastest longitudinal wave velocity c_L in the material.

(6) Verification with Analytical Solution

In order to check the accuracy of the EFIT, the numerical results were compared with the analytical solutions[19]. The input wave in terms of the stress field is given by:

$$\sigma_{11}^{in}(x_1,t) = \sigma_0 f\left(t - \frac{x_1}{c_L}\right) \tag{3.22}$$

where σ_0 is the incident stress amplitude. The incident wave in this simulation is a tone burst signal with period T. The incident velocity field corresponding to the stress field in Eq. (3.22) is given by:

$$v_1^{in}(x_1,t) = -v_0 f\left(t - \frac{x_1}{c_L}\right) \tag{3.23}$$

where v_0 is defined as:

$$v_0 = \frac{\sigma_0}{\rho c_L}. \tag{3.24}$$

If the incident wave has the angular frequency $\omega(= 2\pi/T)$, the displacement is described as:

$$u_1^{in}(x_1, t) = \frac{\sigma_0}{\rho\omega c_L} f\left(t - \frac{x_1}{c_L}\right) \tag{3.25}$$

where the displacement amplitude is defined as:

$$A = \frac{\sigma_0}{\rho\omega c_L}. \tag{3.26}$$

The nonlinear parameter was derived by Richardson[19] as discussed in Chapter **2** in Eq. (2.48) can be rewritten as:

$$\eta = \frac{P_0}{\rho\omega c_L A}. \tag{3.27}$$

Using Eq. (3.26), the parameter η in Eq. (3.27) can be defined as:

$$\eta = \frac{P_0}{\sigma_0}. \tag{3.28}$$

Here, the parameter η can be concluded as a ratio of the compressive pressure to the incident stress amplitude.

(7) Behavior of the Closed Crack

In the current analysis, the material was assumed as stainless steel (c_L=5,800 m/s, ρ=7,800 kg/m^3). Here, Δx is 0.725 mm, Δt is 0.1 μs, and the period T is 10.0 μs. The CFL number in the present numerical analysis is γ = 0.8 and the numerical parameter is $c_L T/\Delta x$ = 80. Figure 3.5 indicates the numerical results of the crack opening displacement for η = 0.1, 0.5, and 0.9. The numerical solutions were overlaid onto a carbon copy of the analytical solutions by Richardson[19]. The proposed EFIT modeling results were in close agreement with the analytical solutions. From these results, it was found that a large incident wave opens the interface widely. On the other hand, when the incident wave is small, the interface is subjected to the compressive force which keeps the interface in the contact state.

Subsequently, the calculation accuracy was examined by the differences of the CFL numbers. It is known that the numerical dispersion occurs when the CFL number is small. The CFL number should be made as large as possible but without exceeding the value of 1. The results for crack opening displacement for η = 0.1 is indicated with different CFL numbers which were set to be γ = 0.29, 0.58, and 0.8 as shown in Fig. 3.6. From these results, the CFL number of γ = 0.8 showed a good stability. Therefore, this simulation showed that using a small CFL number is not required.

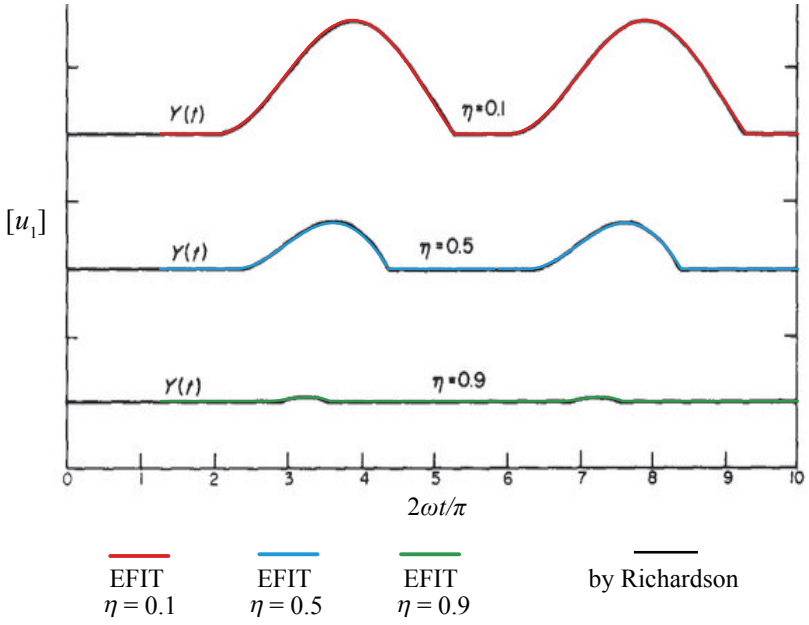

Fig. 3.5 The crack opening displacement for η = 0.1, 0.5, and 0.9.

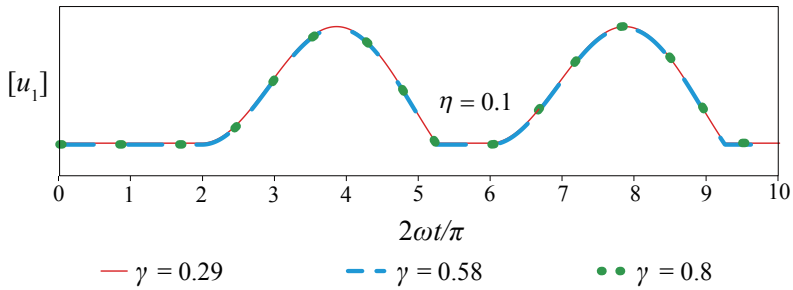

Fig. 3.6 The crack opening displacement for η = 0.1 with different CFL numbers of γ = 0.29, 0.58, and 0.8.

(8) Summary

The 1-D EFIT simulation was introduced to modeling the dynamic behavior of the contact and separation states of the crack interface. The EFIT utilized the split nodes at the interface at which the contact and separation states vary depending on the stress and the crack opening displacement. In order to check the accuracy of the developed model, the simulation results were compared with the analytical solutions for the several cases of η (ratio of the compressive pressure to the incident stress amplitude). The simulation results showed positive similarity with the analytical solutions and showed high accuracy as well as good stability to update the calculated data explicitly. A large amplitude of the incident wave is required to cause the opening of the crack interface. Temporal opening and closing of the crack causes the opening displacement which leads to the generation of the nonlinear ultrasonic wave.

4 EXPERIMENTAL OBSERVATION OF CAN

(1) Introduction

When a large amplitude of the incident wave reaches the crack interface, a nonlinear ultrasonic wave was generated by the opening and the closing of the interface. In this case, some of the incident wave components reflect to the incident side and the other components transmit to the penetrated side. At this instance, a sawtooth pattern appeared in the displacement on the penetrated side.

The characteristics of the sawtooth wave were investigated by experimental measurements. In the beginning, the 1-D EFIT was performed to simulate a sawtooth wave by changing the parameter η (ratio of the compressive pressure to the incident stress amplitude). Then, the sawtooth wave was validated through experimental measurements using a laser doppler vibrometer (LDV) with PMMA specimens.

Although the previous studies employed interfacial model with pressure-dependent nonlinear stiffness[53-55] or interface friction model caused by sliding in the tangential direction (slip-stick condition)[56], this study assumes the PMMA interface to be smooth. Hence, a simple CAN concept is applicable for the experiment.

(2) Generation of the Sawtooth Wave

When an incident wave with a negative phase arrives at the interface, it causes the interface to separate. However, the positive phase of the incident wave causes the contact state of the interface. At this instance, the displacement on the penetrated side shows a sawtooth waveform. The characteristics of the sawtooth wave were investigated, and it demonstrated that the closing velocity of the interface corresponds to the angle of the sawtooth wave that is been generated.

For the purpose of the sawtooth waveform generation, the material was assumed to be PMMA (c_L = 2,730 m/s, ρ = 1,180 kg/m^3), Δx is 0.04 mm and Δt is 0.01 μs. The CFL number was set at γ = 0.6825. An adequate size of the numerical mesh was required to avoid any numerical oscillation. Since the period of the incident wave was T=1.0 μs, the simulation used a mesh of $c_L T/\Delta x$ = 68.25. An 8-cycle, 1 MHz modulated tone burst wave was transmitted from the LHS of the material. The time history data of the incident wave and its Fourier spectrum are shown in Fig. 4.1 (a) and (b) respectively.

The following conditions were set to perform the simulations. The compressive pressure P_0 was changing while the incident stress amplitude σ_0 was maintained at a constant level. The incident stress amplitude σ_0 was changing while the compressive pressure P_0 was kept constant.

Once the conditions were set, the simulations were carried out with a constant value of the incident stress amplitude σ_0 = 1.0 kPa. The compressive pressures were varied as P_0 = 0.1, 0.2, 0.4, 0.8, and 1.6 kPa which resulted in the parameter η = 0.1, 0.2, 0.4, 0.8, and 1.6 respectively. The displacements of the penetrated wave through the interface are as plotted in Fig. 4.2 (a).

Then, the compressive pressure was set at a constant value of P_0 = 0.4 kPa and the incident stress amplitudes were varied as σ_0 = 0.25, 0.5, 1.0, 2.0, and 4.0 kPa which resulted in the parameter η = 1.6, 0.8, 0.4, 0.2, and 0.1 respectively. The displacements of the penetrated wave through the interface at these conditions are as plotted in Fig. 4.3 (a).

It was found that the displacement of the sawtooth wave increases when the parameter η decreases for both the cases demonstrated above. However, it was also found that the sawtooth wave did not appear in the case when the parameter η exceeded the value of 1 or became inferior than 0. Hence, it is proved that a large amplitude of the incident wave is required to generate the sawtooth wave as well as to make the opening of the crack interface.

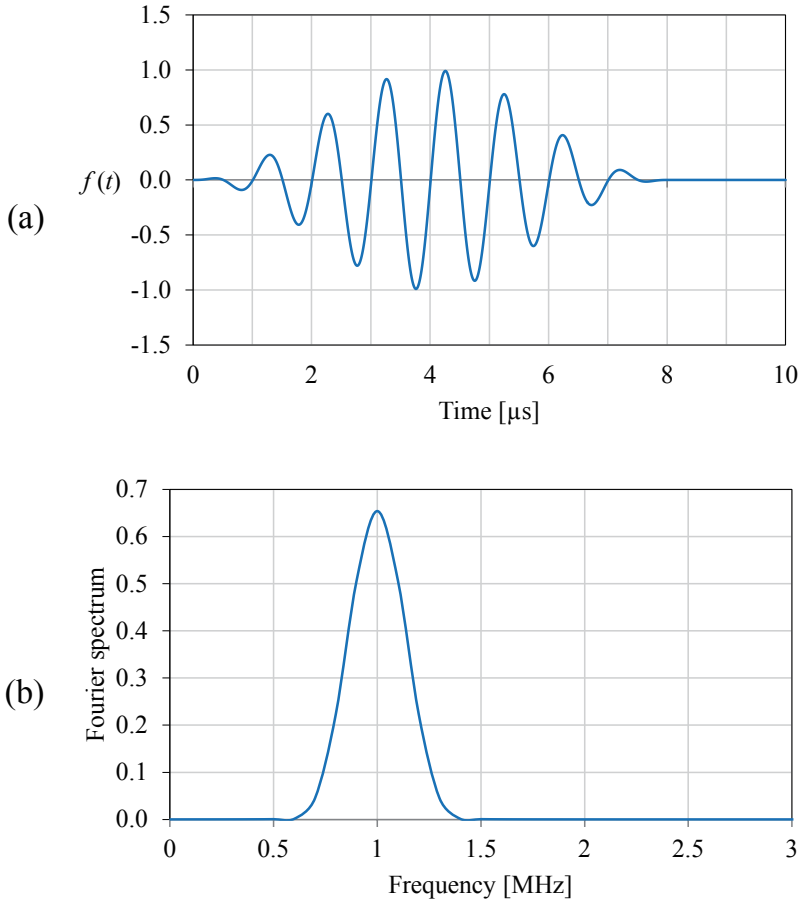

Fig. 4.1 (a) Incident wave in time domain. (b) Fourier spectrum of the incident wave.

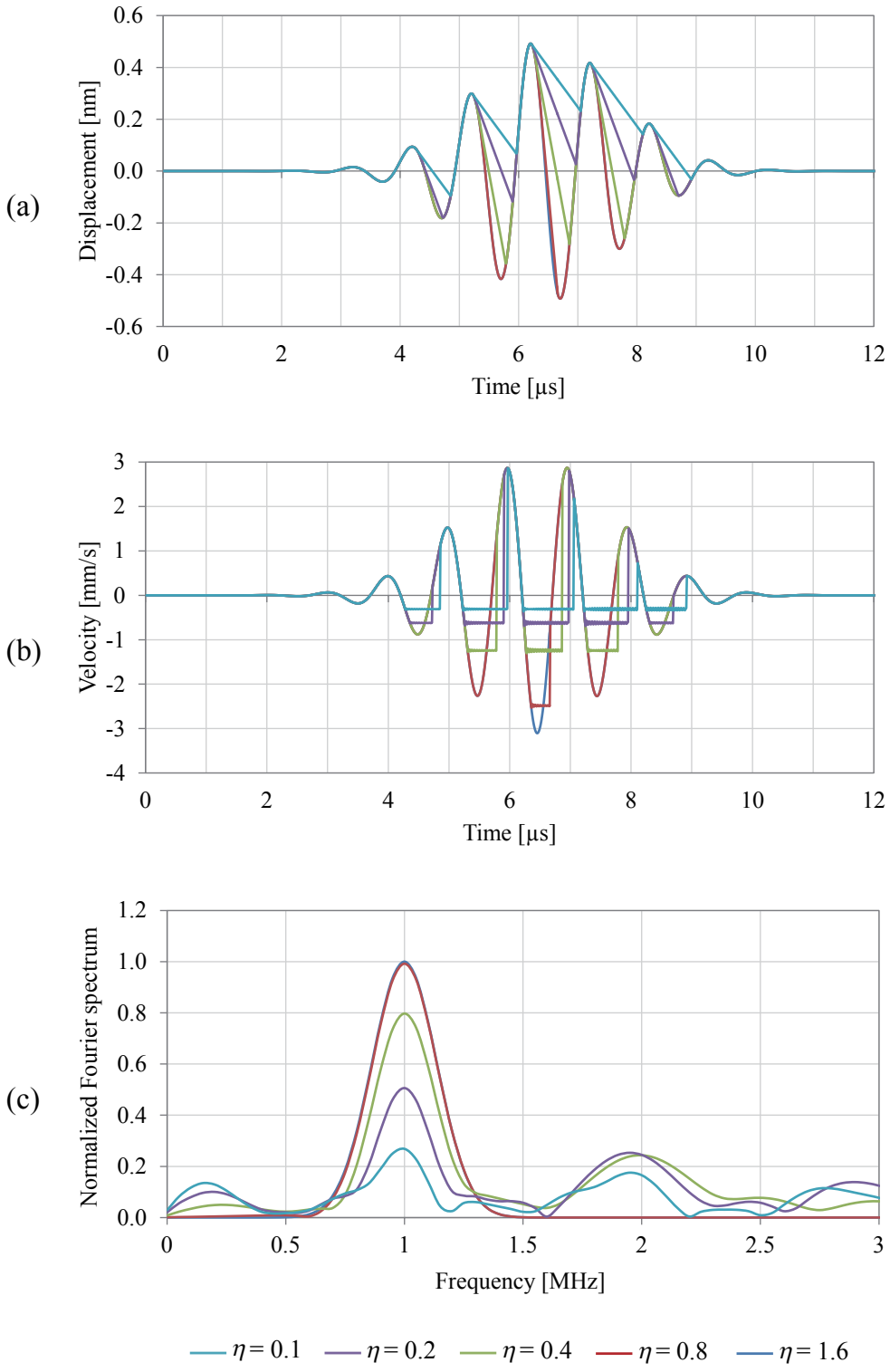

Fig. 4.2 (a) Displacement and (b) velocity measured at the penetrated side when a constant σ_0 is transmitted while P_0 were increased. (c) Fourier spectrum of the velocity.

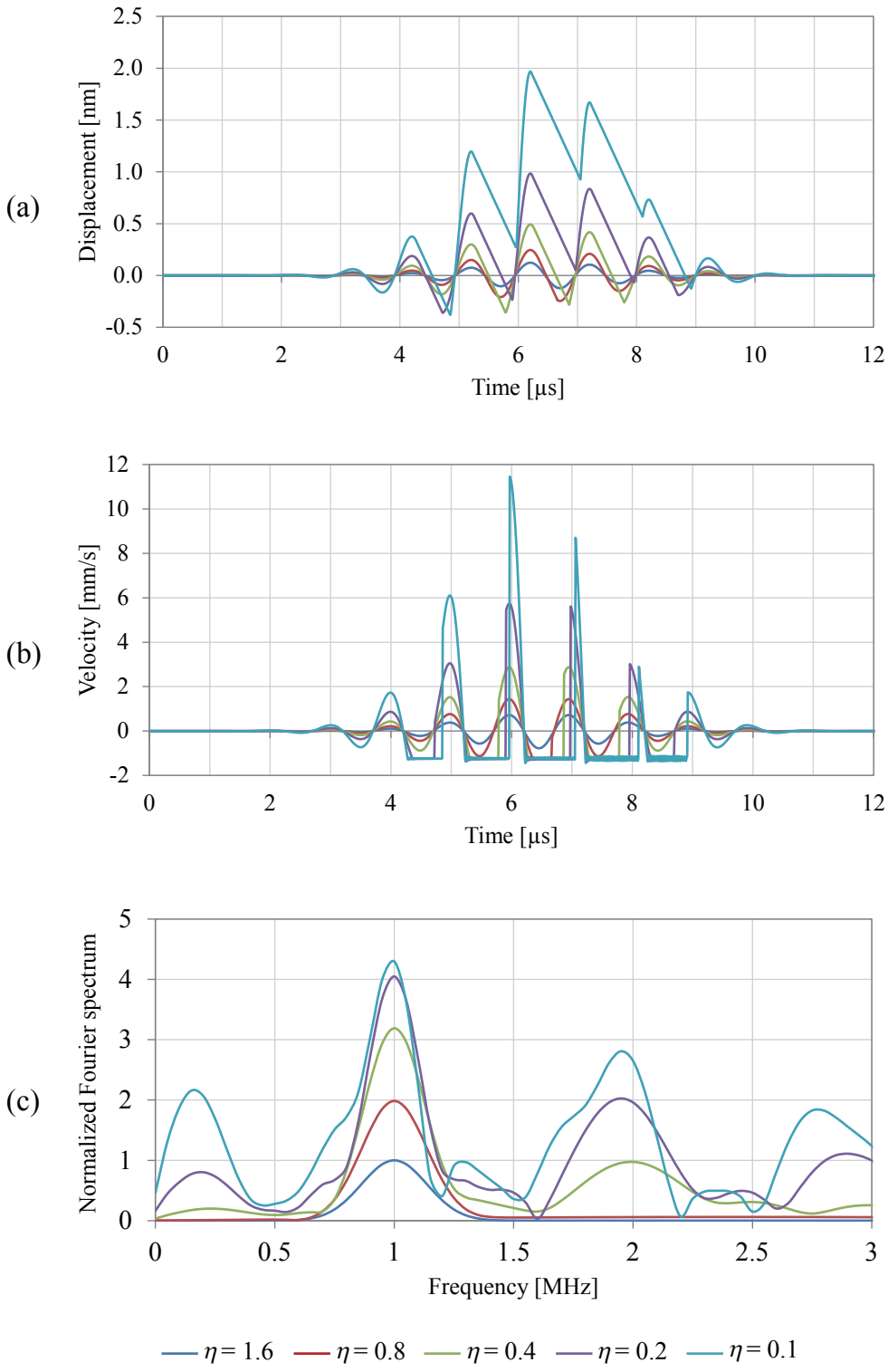

Fig. 4.3 (a) Displacement and (b) velocity measured at the penetrated side when σ_0 were increased while P_0 kept constant. (c) Fourier spectrum of the velocity.

Surprisingly, it was found that the sawtooth waves showed a constant tilt angle even if the amplitude of the incident wave was increased as in Fig. 4.3 (a). The reason for the tilt angle of the displacement field is because of the constant negative velocity (Fig. 4.3 (b)). The closing velocity of the interface was determined by the compressive pressure and it can be expressed as:

$$v = -\frac{P_0}{\rho c_L}. \tag{4.1}$$

The Fourier spectrum of the velocity waveforms for both cases are shown in Fig. 4.2 (c) and 4.3 (c). The values were normalized by the maximum amplitude in the result of $\eta = 1.6$. In these figures, the second harmonic in the case of large values of $\eta = 0.8$ and 1.6 were not recognized. This means that the crack is always closed due to the larger compressive pressure than the incident stress amplitude. These figures also showed that the second harmonic is generated when the value of η is small.

It can also be noted that from Fig. 4.3 (c), the amplitude of the fundamental frequency when $\eta = 0.8$ is about twice as higher as compared to when $\eta = 1.6$ which increase in proposition to the incident amplitude, indicating no occurrence of the nonlinearity. Instead, when η is less than 0.4, the amplitude of the fundamental frequency does not increase in proposition to the incident amplitude, but the amplitude of the second harmonic increases, indicating the occurrence of the nonlinearity. It is seen that the appearance of the sawtooth wave is related to the significant generation of harmonics.

In reality, it is difficult to know the compressive pressure at the crack interface. However, the intensity of the incident wave from the transducer can be easily managed. Hence, a 2-D simulation of the ultrasonic testing of the closed crack by using a constant compressive pressure P_0 with changing the incident stress amplitude σ_0 is dissussed in the next chapter.

(3) Measurement Setup

The numerical results are compared with the experiment results obtained by observing the dynamic state of the interface. In order to perform this measurement, two plates com-

posed of PMMA (c_L = 2,778 m/s, ρ = 1,180 kg/m^3) were used. The thicknesses of these PMMA plates were 5 mm. The surfaces of these plates were polished while keeping dry and the interface of the PMMA was stuck by the intermolecular attraction due to mirror polishing. These plates were set up in parallel on the table and there was no strong tension applied but only a rubber band was used to keep them stable. A contact transducer (RITEC) was attached to one side of the plate, and the velocity or displacement on the opposite side was measured using a LDV device (OPTOMET Vector Series). A 5-cycle, 1 MHz tone burst signal was generated using a high power ultrasonic generator (RITEC Advanced Measurement System RAM-5000). The measurement setup is shown in Fig. 4.4. Figure 4.5 shows the experimental devices used in the measurement. During the measurements, the input voltage of the generator was increased as 350, 750, 1,190, and 1,530 peak-to-peak voltage (Vpp).

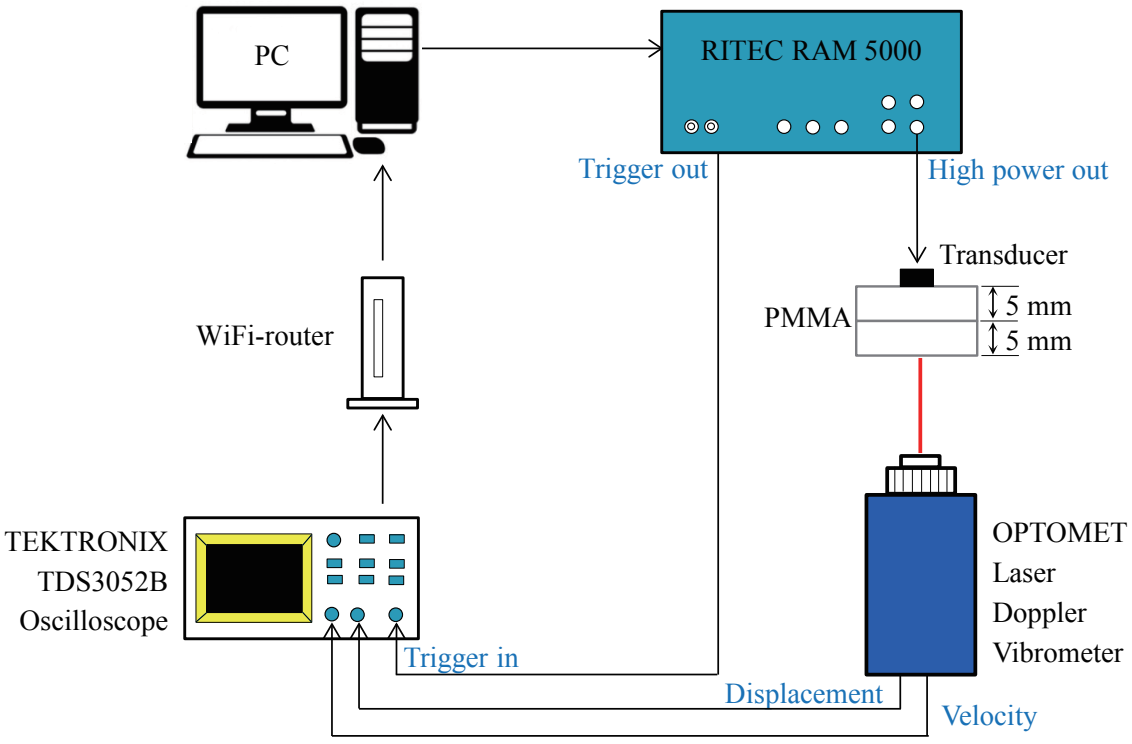

Fig. 4.4 Measurement setup for the generation of sawtooth wave.

High Power Tone Burst Signal Generator
(RITEC Advanced Measurement System RAM-5000)

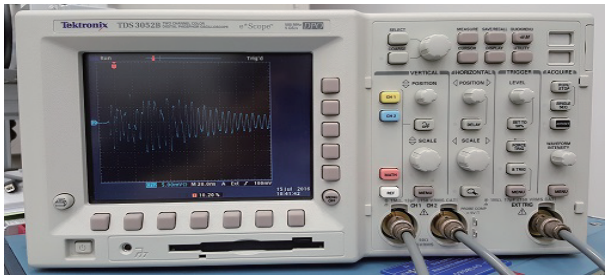

Digital Oscilloscope
(TEKTRONIX TDS 3052B 500MHz 5GS/s)

Laser Doppler Vibrometer
(OPTOMET Vector Series)

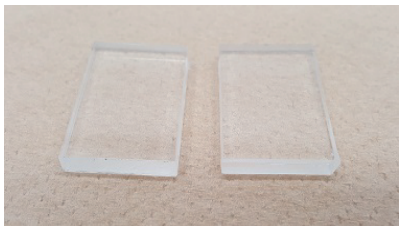

Polymethylacrylate (PMMA)
Thickness of 5 mm

Transducer
(RITEC RC-513-LQ S/N H1135)
Center frequency of 5.0 MHz
Diameter of 13 mm

Fig. 4.5 Experimental devices.

(4) Experimental Results

Figures 4.6 (a) and (b) show the waveforms of velocity and displacement at the surface of a single PMMA specimen with 10 mm thick (no interface), respectively. The Fourier spectrums of the velocity waveforms were shown in Fig. 4.7. These spectrums were normalized by the maximum value in the spectrum at 350 Vpp. Since the components of the fundamental frequency increased as the input voltage became high, it was understood that influence of nonlinearity by the voltage increase was small.

Figure 4.8 shows the velocity of the penetrated wave as measured by the LDV. Although the velocity was not constant in the first and second cycles of the tone burst wave. The third and fourth cycles showed a constant velocity (approximately v = - 0.1 mm/s). This indicates that the interfacial separation occurs during this time. The compressive pressure P_0 can be calculated using Eq. (4.1), and the incident stress amplitude can be calculated using Eq. (3.24) as:

$$\sigma_0 = v_0 \rho c_L \tag{4.2}$$

where v_0 is the velocity amplitude which was measured with the reference PMMA of 5 mm thickness by LDV at 1,190 and 1,530 Vpp as shown in Fig. 4.9. The results obtained from these measurements are summarized in Table 4.1.

The Fourier spectrums of the measured velocity waveforms are shown in Fig. 4.10. All the spectrums were normalized by the maximum value in the spectrum at 350 Vpp. The amplitude of the fundamental frequency at 750 Vpp is about twice as high as at 350 Vpp, and harmonics do not appear at the latter voltage. As the excitation voltage exceeds 1,190 Vpp, the amplitude of the fundamental frequency ceases to increase in proportion to the voltage. However, the amplitude of the second harmonic becomes large. In these measurements, the ratio of the amplitude of the fundamental frequency to that of the second harmonic varies between simulation and measurement. This is attributable to nonlinear interfacial stiffness caused by surface roughness[53] and an interface friction caused by the sliding in the tangential direction[56] which were not incorporated into the CAN framework.

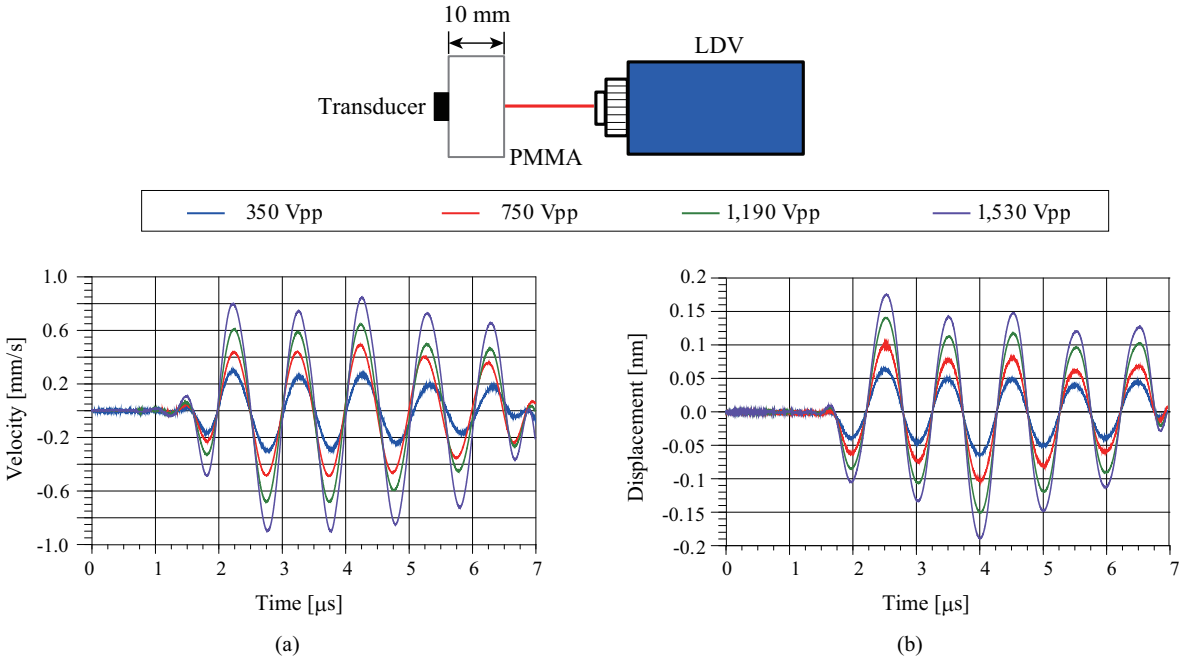

Fig. 4.6 Waveforms of (a) velocity and (b) displacement at the surface of a single PMMA.

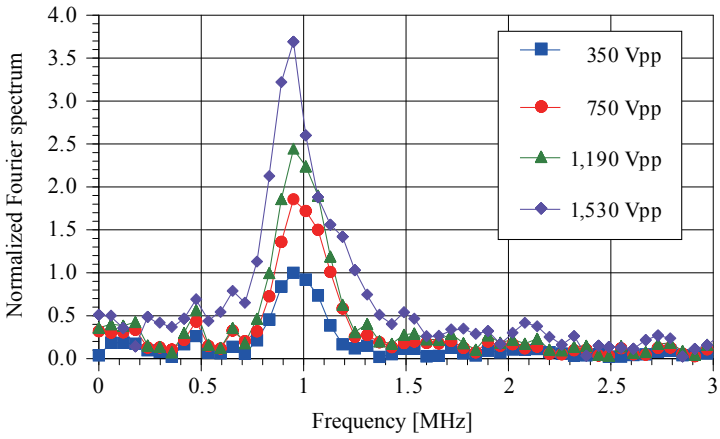

Fig. 4.7 Fourier spectrum of the velocity waveform at the surface of a single PMMA.

Table 4.1 Ratio of the compression and incident stress measured by LDV.

Input voltage (Vpp)	v_0 (mm/s)	P_0 (kPa)	σ_0 (kPa)	η
1,190	0.55	0.328	1.8	0.18
1,530	0.7	0.328	2.3	0.14

(5) Summary

In this chapter, the 1-D EFIT simulation was proposed as a means for modeling the interfacial dynamic behavior of the contact and separation state. The investigation in this chapter was done with the view toward application in the ultrasonic testing of the closed cracks. The study focused on the investigation of the sawtooth waves which were produced in the 1-D CAN framework as the velocity of the interfacial closure can be found from the tilt angle of the sawtooth wave. It was found that the velocity corresponds to the compressive pressure applied on the interface. The sawtooth waves were then observed in the measurements using PMMA specimens where increasing the voltage produced the sawtooth patterns and increased the Fourier spectrum of the second harmonic generated.

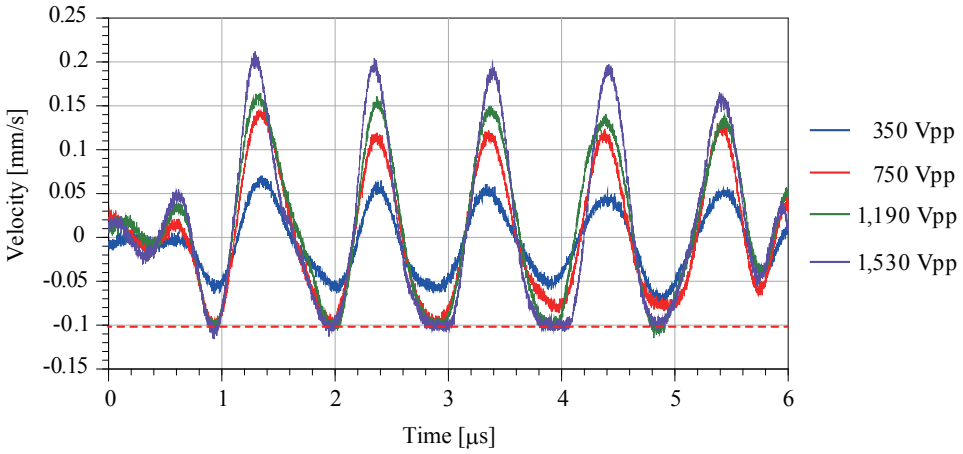

Fig. 4.8 Velocity of penetrated wave.

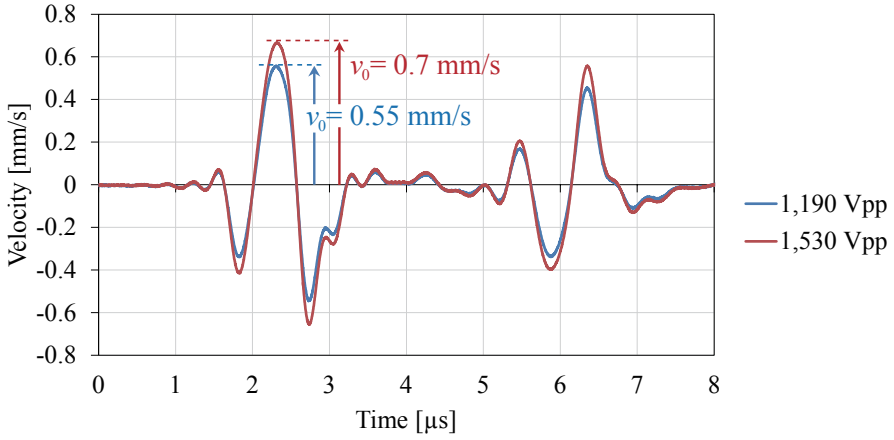

Fig. 4.9 Surface velocity at a reference PMMA with 5 mm thickness.

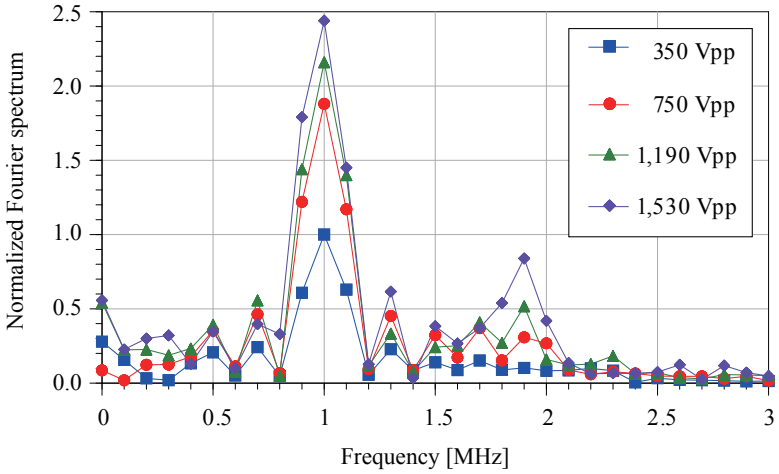

Fig. 4.10 Fourier spectrum of the measured velocity.

5 TWO-DIMENSIONAL MODELING OF CAN

(1) Introduction

In this chapter, the 1-D EFIT was extended to the 2-D wave field to model a realistic UT for the closed crack. This chapter treats the description of the 2-D EFIT plane strain problem. At first, an interfacial crack model was checked for the verification of the coding. The displacement results at the crack faces were compared with the analytical solutions[34]. Following that, the model of the closed crack located at the lower surface was simulated in the case of an oblique incident angle from the phased array transducer. Since the closed crack was subjected to the compression in the actual situation, the initial stress analysis was performed using FEM to calculate the stress distribution around the crack. The scattered waves from the 2-D numerical simulations were demonstrated for the three models; intact (without crack), slit (linear case), and closed crack (nonlinear case). At this juncture, the visualization of the scattered wave was shown to promote the understanding of the scattering around the crack. Furthermore, the visualization results by the 2-D EFIT model were validated with the experimental results[68].

(2) 2-D EFIT

The EFIT method is based on the integral scheme results in staggered grids and provides a stable code, allowing easy and flexible treatment of various boundary conditions. This is essential to model the elastic wave propagation in inhomogeneous material[42, 43].

a) Spatial Discretization

The equation of motion in the 2-D wave field is considered and assuming that the body force is zero, the integral forms in Eq. (3.1) were expressed as:

$$\frac{\partial}{\partial t}\int_V \rho(\boldsymbol{x})\, v_1\, dV = \int_S (\sigma_{11}n_1 + \sigma_{12}n_2)\, dS \tag{5.1}$$

$$\frac{\partial}{\partial t}\int_V \rho(\boldsymbol{x})\, v_2\, dV = \int_S (\sigma_{12}n_1 + \sigma_{22}n_2)\, dS \tag{5.2}$$

where $\boldsymbol{n} = (n_1, n_2)$ is the outward normal vector on S. The integral forms of the constitutive law in Eq. (3.2) are expressed as:

$$\frac{\partial}{\partial t}\int_V \sigma_{11}\, dV = \int_S \left\{(\lambda(\boldsymbol{x}) + 2\mu(\boldsymbol{x}))v_1 n_1 + \lambda(\boldsymbol{x})v_2 n_2\right\} dS \tag{5.3}$$

$$\frac{\partial}{\partial t}\int_V \frac{\sigma_{12}}{\mu(\boldsymbol{x})}\, dV = \int_S (v_1 n_2 + v_2 n_1)\, dS \tag{5.4}$$

$$\frac{\partial}{\partial t}\int_V \sigma_{22}\, dV = \int_S \left\{\lambda(\boldsymbol{x})v_1 n_1 + [\lambda(\boldsymbol{x}) + 2\mu(\boldsymbol{x})]v_2 n_2\right\} dS. \tag{5.5}$$

Here, a square integration cell was adopted. The size of the integral area is $\Delta x \times \Delta x$. The integration was performed over volume V whose surface is S, assuming that the velocity and stress were constant within V and on S. In the integration cell, the physical quantities on the upper and lower sides were represented by superscript (U) and (D), respectively. Similarly, the physical quantities on the left and right sides were represented by superscript (L) and (R), respectively. Material constants ρ, λ, and μ were constant in the integration cell of σ_{ii} (no sum for i).

The discretization of v_1, v_2, σ_{11}, σ_{22}, and σ_{12} were described as follows. To start with, the discretization of v_1 is performed. As shown in Fig. 5.1, the integral cell of v_1 is indicated

by a red square. Since v_1 is constant within the red cell, Eq. (5.1) becomes:

$$\bar{\rho}_1 \dot{v}_1 (\Delta x)^2 = \left[\sigma_{11}^{(R)} - \sigma_{11}^{(L)}\right]\Delta x + \left[\sigma_{12}^{(U)} - \sigma_{12}^{(D)}\right]\Delta x \tag{5.6}$$

where the superscript ($\dot{}$) represent $\frac{d(\_)}{dt}$. When both sides of Eq. (5.6) is divided by $\bar{\rho}(\Delta x)^2$, the equation becomes:

$$\dot{v}_1 = \frac{1}{\bar{\rho}_1}\left\{\frac{1}{\Delta x}\left[\sigma_{11}^{(R)} - \sigma_{11}^{(L)} + \sigma_{12}^{(U)} - \sigma_{12}^{(D)}\right]\right\}. \tag{5.7}$$

The value of ρ_1 in Eq. (5.7) is constant within the integration cell of σ_{ii}. When dealing with the interface of a different material, the average of the kinetic momentum was considered as:

$$\bar{\rho}_1 \dot{v}_1 = \frac{1}{2}\left[\rho^{(R)}\dot{v}_1 + \rho^{(L)}\dot{v}_1\right] \tag{5.8}$$

where $\bar{\rho}_1$ can be defined as:

$$\bar{\rho}_1 = \frac{1}{2}\left(\rho^{(R)} + \rho^{(L)}\right). \tag{5.9}$$

Then, the discretization of v_2 is performed. The discretization of Eq. (5.2) can be expressed as:

$$\dot{v}_2 = \frac{1}{\bar{\rho}_2}\left\{\frac{1}{\Delta x}\left[\sigma_{12}^{(R)} - \sigma_{12}^{(L)} + \sigma_{22}^{(U)} - \sigma_{22}^{(D)}\right]\right\} \tag{5.10}$$

where $\bar{\rho}_2$ can be defined as:

$$\bar{\rho}_2 = \frac{1}{2}\left(\rho^{(U)} + \rho^{(D)}\right). \tag{5.11}$$

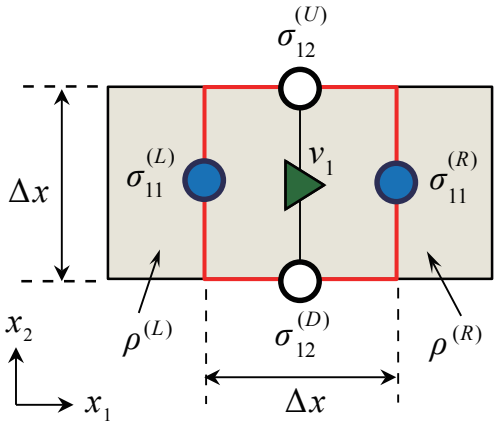

Fig. 5.1 Integral cell of v_1.

The discretization of σ_{12} is described as below. Assuming that the integral cell is the same side as σ_{ii}, the Eq. (5.4) becomes:

$$\frac{\dot{\sigma}_{12}}{\bar{\mu}}(\Delta x)^2 = \left[v_2^{(R)} - v_2^{(L)}\right]\Delta x + \left[v_1^{(U)} - v_1^{(D)}\right]\Delta x \tag{5.12}$$

When both sides of Eq. (5.12) is divided by $\bar{\mu}(\Delta x)^2$, the equation becomes:

$$\frac{\dot{\sigma}_{12}}{\bar{\mu}} = \frac{1}{\Delta x}\left[v_2^{(R)} - v_2^{(L)} + v_1^{(U)} - v_1^{(D)}\right]. \tag{5.13}$$

At this instance, the kinetic momentum of μ was considered. Since σ_{12} is constant within the integral cell, the LHS of the Eq. (5.12) is considered as:

$$\frac{\dot{\sigma}_{12}}{\bar{\mu}} = \frac{1}{4}\left[\frac{\dot{\sigma}_{12}}{\mu^{(U,R)}} + \frac{\dot{\sigma}_{12}}{\mu^{(D,R)}} + \frac{\dot{\sigma}_{12}}{\mu^{(U,L)}} + \frac{\dot{\sigma}_{12}}{\mu^{(D,L)}}\right] \tag{5.14}$$

where the superscripts (U,R), (D,R), (U,L), and (D,L) were represented by the cell positions of upper right, lower right, upper left, and lower left, respectively as shown in Fig. 5.2.

From Eq. (5.14), the average $\bar{\mu}$ is represented by:

$$\bar{\mu} = \frac{4}{\left[\frac{1}{\mu^{(U,R)}} + \frac{1}{\mu^{(D,R)}} + \frac{1}{\mu^{(U,L)}} + \frac{1}{\mu^{(D,L)}}\right]}. \tag{5.15}$$

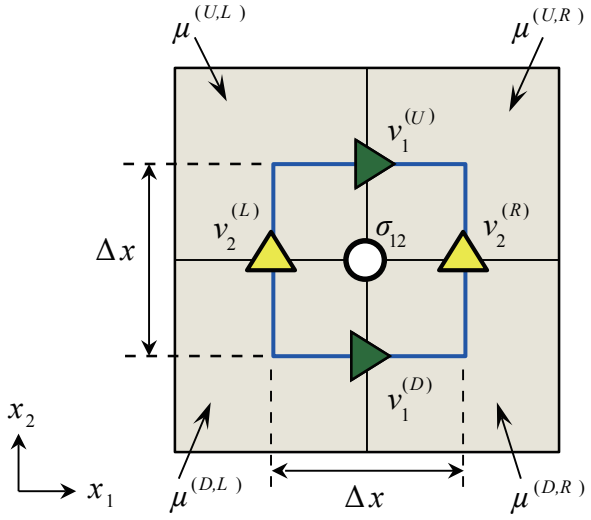

Fig. 5.2 Integral cell of σ_{12}.

The discretization forms of σ_{11} and σ_{22} were expressed as in the following:

$$\dot{\sigma}_{11} = \frac{1}{\Delta x}\left\{(\lambda + 2\mu)\left[v_1^{(R)} - v_1^{(L)}\right] + \lambda\left[v_2^{(U)} - v_2^{(D)}\right]\right\} \tag{5.16}$$

$$\dot{\sigma}_{22} = \frac{1}{\Delta x}\left\{\lambda\left[v_1^{(R)} - v_1^{(L)}\right] + (\lambda + 2\mu)\left[v_2^{(U)} - v_2^{(D)}\right]\right\}. \tag{5.17}$$

The stress components $\boldsymbol{\sigma} = (\sigma_{11}, \sigma_{22}, \sigma_{12})$ and the velocity components $\boldsymbol{v} = (v_1, v_2)$ were discretized into spatial i, j grids based on the layout in Fig. 5.3.

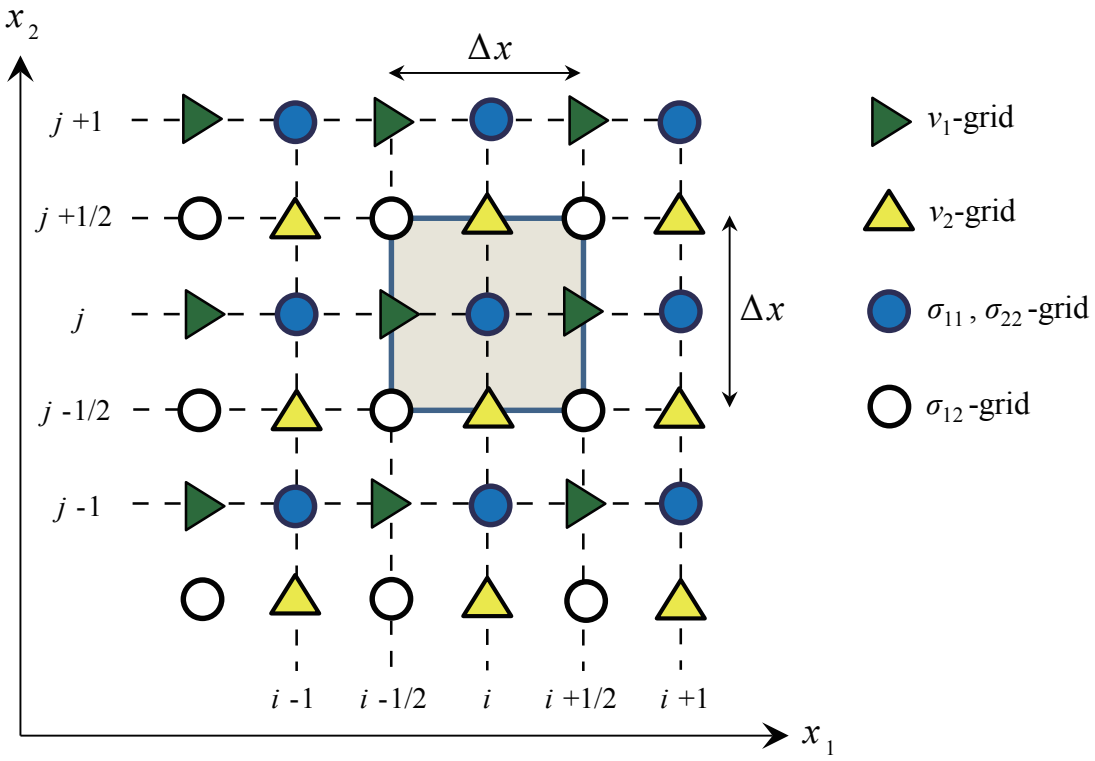

Fig. 5.3 Grid allocation in 2-D EFIT.

b) Time Discretization

In the time domain, the stress components $\boldsymbol{\sigma}$ were allocated at half-time steps, while the velocity components $\boldsymbol{v}$ were allocated at full-time steps. The following time discretization yields an explicit leap-frog scheme:

$$\{\boldsymbol{\sigma}\}^{z+\frac{1}{2}} = \{\boldsymbol{\sigma}\}^{z-\frac{1}{2}} + \Delta t\{\dot{\boldsymbol{\sigma}}\}^{z}, \quad \{\boldsymbol{v}\}^{z} = \{\boldsymbol{v}\}^{z-1} + \Delta t\{\dot{\boldsymbol{v}}\}^{z-\frac{1}{2}}, \tag{5.18}$$

where Δt is the time interval and the superscript z denotes the integer number of the time step. The EFIT repeats the operations in Eq. (5.18) from $z = 1$ to N under suitable initial and boundary conditions.

c) Stability Condition

Since the EFIT used a square grid in the numerical calculation, the shape of the scatterer and outer boundary are modeled as stair-step patterns. In order to avoid this problem, it is necessary to make the cell length as small as possible. Nakahata et. al[45] proposed the following equation to keep the accuracy in the EFIT as:

$$\Delta x \leq \frac{1}{12}\lambda_{min} = \frac{1}{12}\frac{c_{min}}{f_{max}} \tag{5.19}$$

where c_{min} is referred to as the slowest transverse wave velocity c_T in the material, f_{max} is the maximum frequency component of the incident wave. Eq. (5.19) is an expression proposed for a 3-D wave field, but it also applicable to the 2-D wave field.

$$\Delta t \leq \frac{1}{c_{max}}\sqrt{\frac{1}{(1/\Delta x_1)^2 + (1/\Delta x_2)^2}} \tag{5.20}$$

(3) Modeling for Clapping of the Crack Faces

A closed crack model in the 2-D wave field can be developed based on the 1-D model. Here, the closed crack interface is placed in parallel with the x_2-direction. Therefore, the opening displacement in the x_1-direction is modeled in this simultion. As shown in Fig. 5.4, the interface is located on the velocity grid $(v_1)_{n,j}$ and shear stress grid $(\sigma_{12})_{n,j}$. When the crack faces were separated, the node of v_1 and σ_{12} at the interface were split into two nodes. The LHS and RHS of the nodes at the interface were indicated as $n(-)$ and $n(+)$, respectively. The opening displacement $[u_1]$ between the crack faces is defined as:

$$[u_1] = (u_1)_{n(+),j} - (u_1)_{n(-),j} \tag{5.21}$$

When $[u_1]$ is positive then the crack faces were separated and the traction-free condition was applied as:

$$(\sigma_{11})_{n,j} = 0 \tag{5.22}$$

The velocities at both sides of the interface were expressed as:

$$(v_1)^{k+1}_{n(+),j+1/2} = (v_1)^{k}_{n(+),j+1/2} + \left[\frac{\Delta t}{\Delta x}\frac{1}{\overline{\rho}_1}\left(2(\sigma_{11})^{k+\frac{1}{2}}_{n+1/2,j}\right)\right] \tag{5.23}$$

$$(v_1)^{k+1}_{n(-),j+1/2} = (v_1)^{k}_{n(-),j+1/2} - \left[\frac{\Delta t}{\Delta x}\frac{1}{\overline{\rho}_1}\left(2(\sigma_{11})^{k+\frac{1}{2}}_{n-1/2,j+1/2}\right)\right]. \tag{5.24}$$

The stresses at the separation state were expressed as:

$$(\sigma_{11})^{k+\frac{1}{2}}_{n+1/2,j+1/2} = (\sigma_{11})^{k-\frac{1}{2}}_{n+1/2,j+1/2} + \frac{\Delta t}{\Delta x}\Big[(\lambda+2\mu)\Big[(v_1)^{k}_{n+1,j+1/2} - (v_1)^{k}_{n(+),j+1/2}\Big] + \lambda\Big[(v_2)^{k}_{n+1/2,j+1} - (v_2)^{k}_{n+1/2,j}\Big]\Big] \tag{5.25}$$

$$(\sigma_{11})^{k+\frac{1}{2}}_{n-1/2,j+1/2} = (\sigma_{11})^{k-\frac{1}{2}}_{n-1/2,j+1/2} + \frac{\Delta t}{\Delta x}\Big[(\lambda+2\mu)\Big[(v_1)^{k}_{n(-),j+1/2} - (v_1)^{k}_{n-1,j+1/2}\Big] + \lambda\Big[(v_2)^{k}_{n-1/2,j+1} - (v_2)^{k}_{n-1/2,j}\Big]\Big]. \tag{5.26}$$

$$(\sigma_{22})^{k+\frac{1}{2}}_{n+1/2,j+1/2} = (\sigma_{22})^{k-\frac{1}{2}}_{n+1/2,j+1/2} + \frac{\Delta t}{\Delta x}\Big[\lambda\Big[(v_1)^{k}_{n+1,j+1/2} - (v_1)^{k}_{n(+),j+1/2}\Big] + (\lambda+2\mu)\Big[(v_2)^{k}_{n+1/2,j+1} - (v_2)^{k}_{n+1/2,j}\Big]\Big] \tag{5.27}$$

$$(\sigma_{22})^{k+\frac{1}{2}}_{n-1/2,j+1/2} = (\sigma_{22})^{k-\frac{1}{2}}_{n-1/2,j+1/2} + \frac{\Delta t}{\Delta x}\Big[\lambda\Big[(v_1)^{k}_{n(-),j+1/2} - (v_1)^{k}_{n-1,j+1/2}\Big] + (\lambda+2\mu)\Big[(v_2)^{k}_{n-1/2,j+1} - (v_2)^{k}_{n-1/2,j}\Big]\Big] \tag{5.28}$$

$$(\sigma_{12})^{k+\frac{1}{2}}_{n(+),j} = 0, \quad (\sigma_{12})^{k+\frac{1}{2}}_{n(-),j} = 0 \tag{5.29}$$

On the other hand, the continuity condition in the contact state ($(\sigma_{11})_{n,j} < 0$) is given by:

$$(v_1)_{n(-),j+1/2} = (v_1)_{n(+),j+1/2} = (v_1)_{n,j+1/2}. \tag{5.30}$$

Here, the split-nodes are bound together as shown in Fig. 5.5. After the crack faces were contacted, the velocity and displacement at ($i = n$) were represented as:

$$(v_1)_{n,j+1/2} = \frac{\rho_{(n+1/2,j)}(v_1)_{n(+),j+1/2} + \rho_{(n-1/2,j+1/2)}(v_1)_{n(-),j+1/2}}{\rho_{(n+1/2,j+1/2)} + \rho_{(n-1/2,j+1/2)}} \tag{5.31}$$

$$(u_1)_{n,j+1/2} = \frac{(u_1)_{n(+),j+1/2} + (u_1)_{n(-),j+1/2}}{2} \tag{5.32}$$

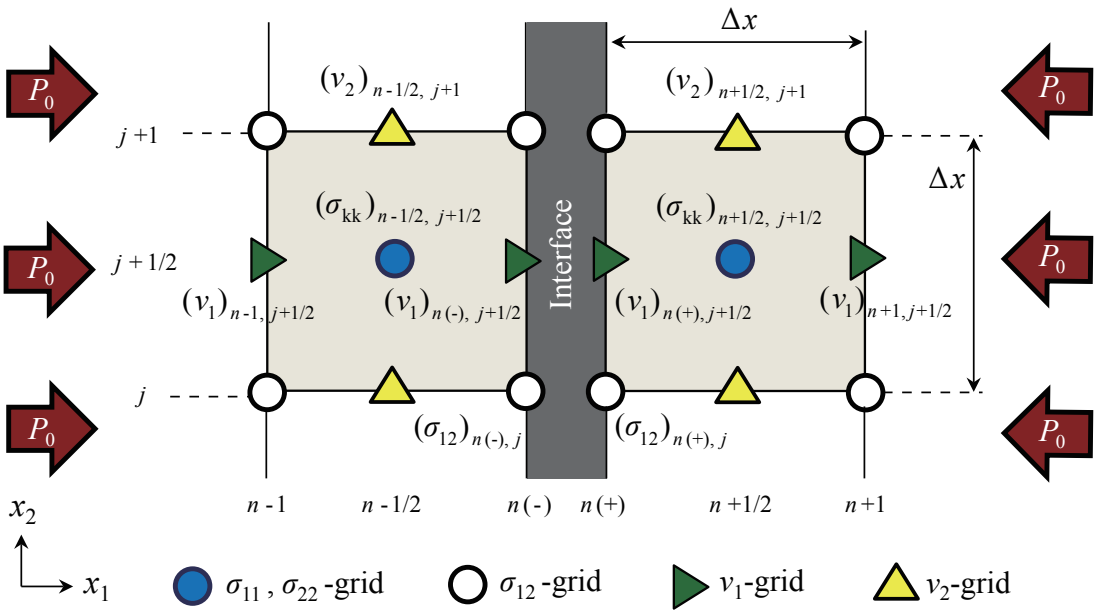

Fig. 5.4 Grid allocation of the 2-D EFIT model with the split nodes.

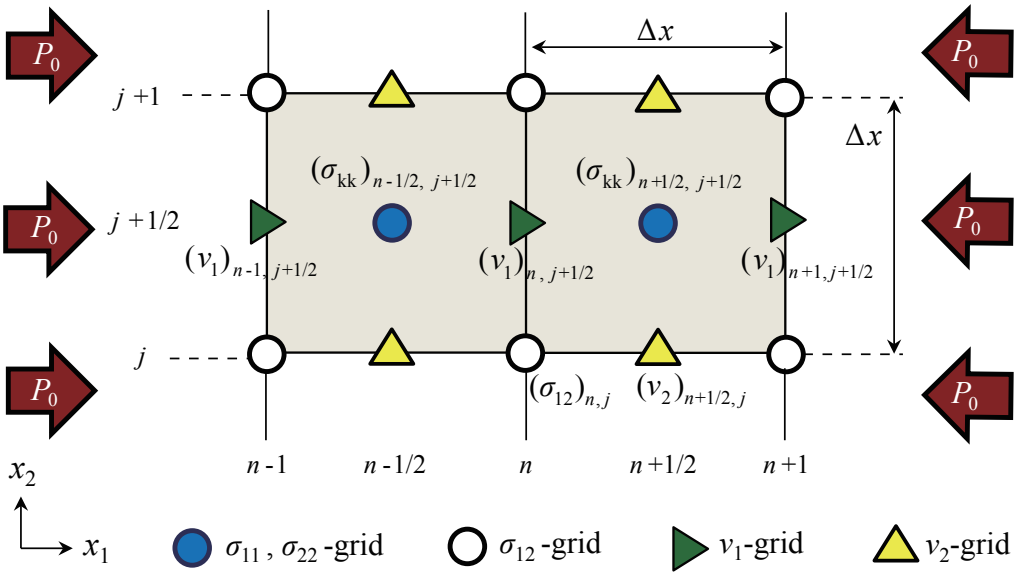

Fig. 5.5 Grid allocation of the 2-D EFIT model when the crack faces in the contact state.

In the initial state, it is assumed that the crack faces were contacted by the compressive pressure. The velocities and the stresses in the initial state were given by:

$$\begin{aligned} v_1(x_1, x_2, 0) &= v_1^{in}(x_1, x_2, 0) \\ v_2(x_1, x_2, 0) &= v_2^{in}(x_1, x_2, 0) \end{aligned} \tag{5.33}$$

$$\begin{aligned} \sigma_{11}(x_1, x_2, 0) &= \sigma_{11}^{in}(x_1, x_2, 0) + \sigma_{11}^{st}(x_1, x_2, 0) \\ \sigma_{22}(x_1, x_2, 0) &= \sigma_{22}^{in}(x_1, x_2, 0) + \sigma_{22}^{st}(x_1, x_2, 0) \\ \sigma_{12}(x_1, x_2, 0) &= \sigma_{12}^{in}(x_1, x_2, 0) + \sigma_{12}^{st}(x_1, x_2, 0) \end{aligned} \tag{5.34}$$

where v_i^{in} and σ_{ij}^{in} are the particle velocities and stresses excited by the input wave. σ_{ij}^{st} is the initial stress distributed around the interface. The initial stress distribution was calculated by the FEM analysis.

(4) Initial Stress Analysis with FEM

In order to model the closed crack, a compressive pressure must be applied at the edge of the material. Therefore, the initial stress state was made with the static stress analysis with the FEM. In the FEM modeling, the left side of the model was completely restrained and the compressive pressure (P_0 = 0.2 kPa) was applied from the right side as shown in Fig. 5.6 (a). The FEM analysis was performed to get the values of normal stresses (σ_{11} and σ_{22}) and shear stress (σ_{12}) of all mesh elements. These values were used as the initial stresses (σ_{11}^{st}, σ_{22}^{st}, and σ_{12}^{st}) in the 2-D EFIT simulation. The FEM result for σ_{11} is shown in Fig. 5.6 (b) where the red color indicates that the compressive stress is large.

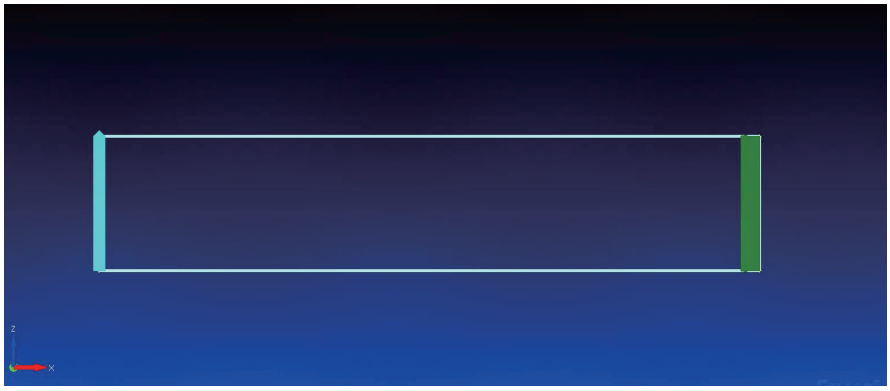

(a) Model for the initial compression analysis.

(b) Result of the static stress analysis for P_0 = 0.2 kPa.

Fig. 5.6 Initial stress analysis performed by the FEM.

(5) Verification of the 2-D EFIT Simulation

In order to verify the 2-D EFIT simulation, the numerical results were compared with the analytical results by Kimoto & Ichikawa[34].

Figure 5.7 (a) shows the model of the closed crack with no compressive pressure $P_0 = 0$ ($\eta = 0$). The displacement at the interface is shown in Fig. 5.7 (b). The displacement at the incident side was labeled as $u_1^{(-)}$, while the displacement at the penetrated side was labeled as $u_1^{(+)}$. The opening displacement was defined by $[u] = u_1^{(+)} - u_1^{(-)}$. When there was no compressive pressure, the displacement at the penetrated side showed a stair-step pattern. Figure 5.7 (c) shows the visualization of the wave propagation from the LHS toward the interface. The color represents the intensity of the von Mises stress. The result shows that most of the incident wave is reflected back to the incident side. Since there is no compressive pressure, the crack faces were contacted by the positive phase of the incident wave, but the crack face at the incident side (-) was pulled by the negative phase of the incident wave in the next time. At this moment, the deformation at the penetrated side (+) can not return to the initial state, then the separation state remains.

Figure 5.8 (a) shows the model of the closed crack with compressive pressure $P_0 = \sigma_0/5$ ($\eta = 0.2$). The displacement at the interface in the case of $\eta = 0.2$ is shown in Fig. 5.8 (b). From the result, the displacement $u_1^{(+)}$ at the penetrated side showed a sawtooth pattern. At this time, $[u]$ showed positive (opening) and zero (closing) values. Figure 5.8 (c) indicates that a part of the incident wave was reflected to the incident side and the other part was transmitted to the penetrated side.

Figures 5.9 (a) and (b) show the numerical model of the closed crack and the displacement at the interface in the case of $P_0 = \sigma_0$ ($\eta = 1.0$), respectively. In this case, $[u]$ only showed a zero value where the interface retained the contact state. Figure 5.9 (c) indicates that the incident wave was transmitted to the penetrated side and there was no reflection wave from the interface.

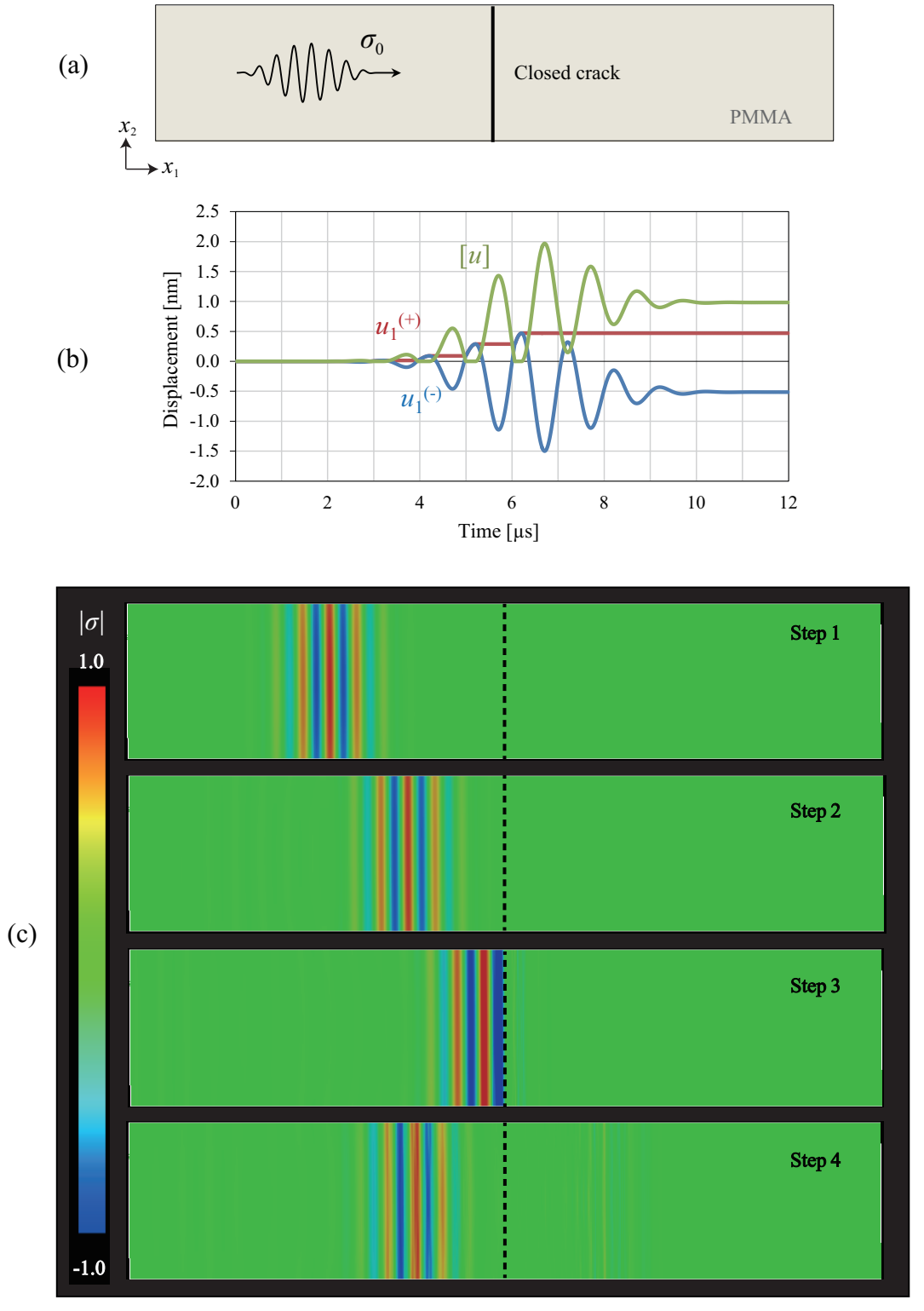

Fig. 5.7 (a) 2-D model of the interface without compression $P_0 = 0$ ($\eta = 0$). (b) Displacement at the interface. (c) Visualization of the wave propagation.

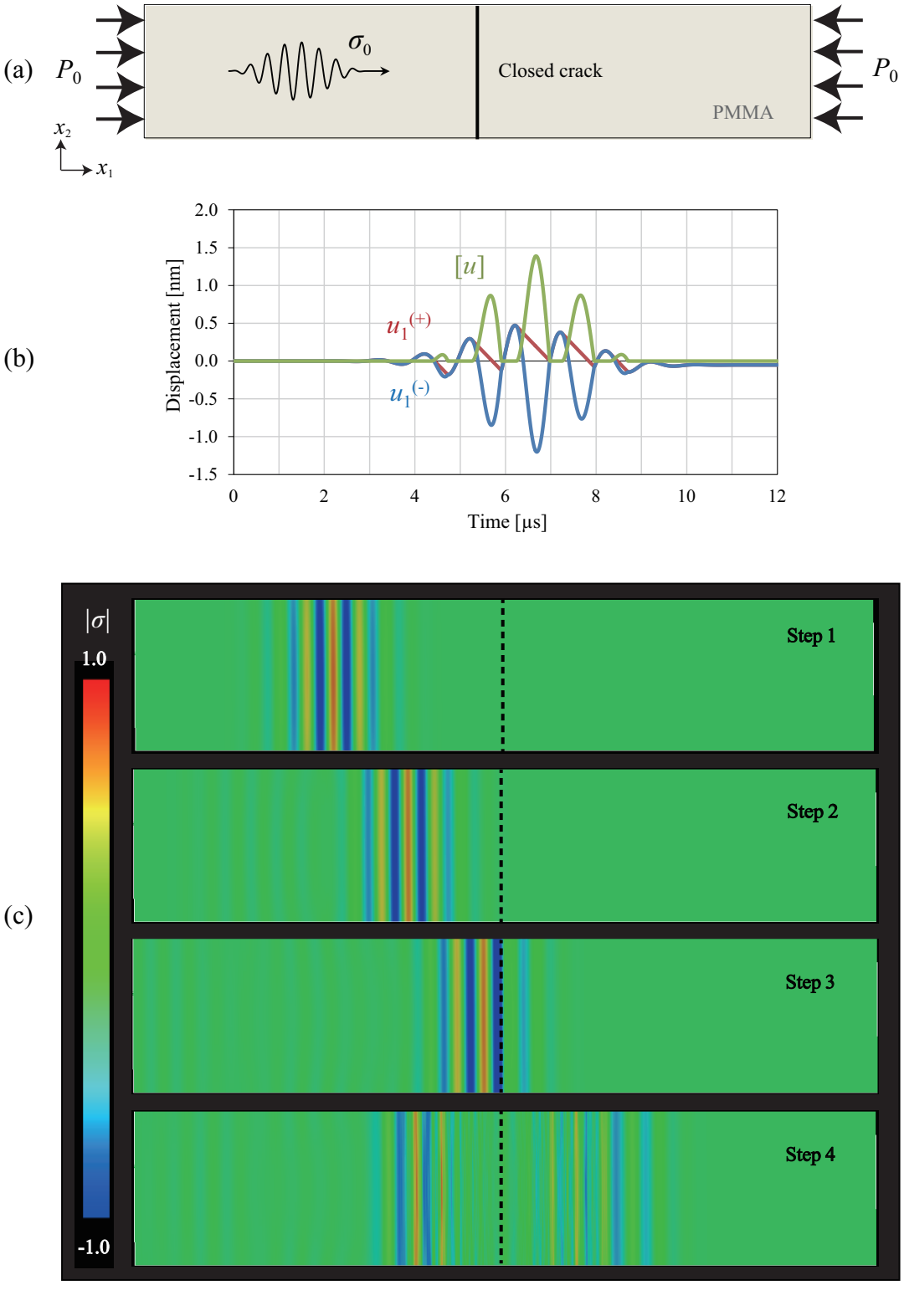

Fig. 5.8 (a) 2-D model of the interface with compression $P_0 = \sigma_0/5$ ($\eta = 0.2$). (b) Displacement at the interface. (c) Visualization of the wave propagation.

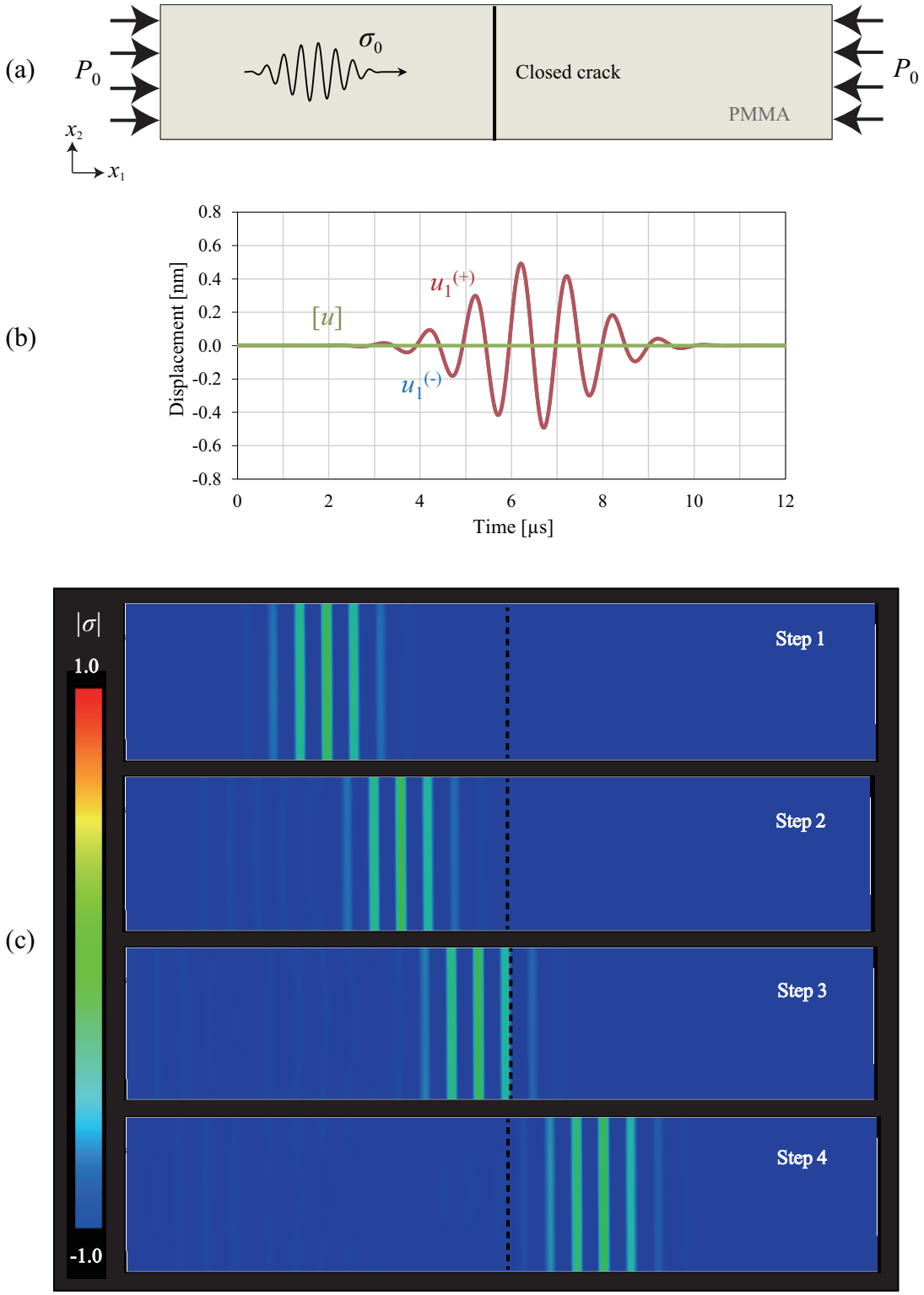

Fig. 5.9 (a) 2-D model of the interface with compression $P_0 = \sigma_0$ (η = 1.0). (b) Displacement at the interface. (c) Visualization of the wave propagation.

(6) Validation of the 2-D EFIT Simulation

For the validation of the 2-D EFIT, the simulation results were compared with the experimental results conducted by Takatsubo & Imade[68]. Numerical models which are slit (0.3 mm width and 10 mm height) and closed crack were used as shown in Fig. 5.10 (a) and (b), respectively. The material was assumed to be steel nickel chromium molybdenum alloy steel (c_L = 5,850 m/s, c_T = 3,250 m/s, ρ = 7,850 kg/m^3). A phased array transducer transmitted a Ricker wave with center frequency of 5 MHz at 90° incident angle. The visualization results for the slit and the closed crack by the EFIT simulations are displayed in Fig. 5.11. The experimental results of the visualization for the slit and fatigue crack are shown in Fig. 5.12.

It can be noted that there is a big difference in the wave propagation between the slit and the closed crack cases. In the case of slit, the wave was reflected from the slit surface. In the case of closed or fatigue crack, part of the transmitted wave penetrated the crack faces and the other part reflected at the crack face. Hereby, the 2-D EFIT simulation results showed good agreement with the experimental results.

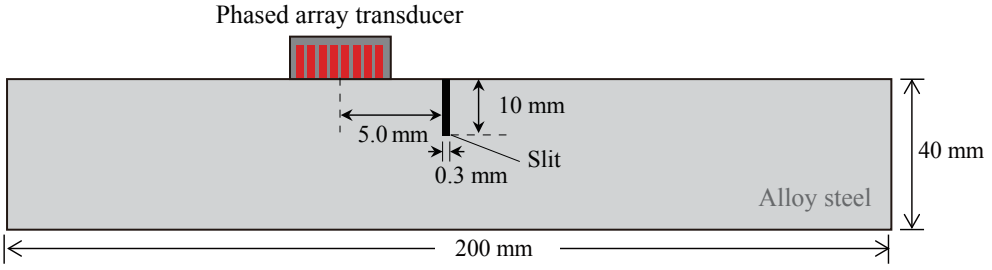

(a) Slit model.

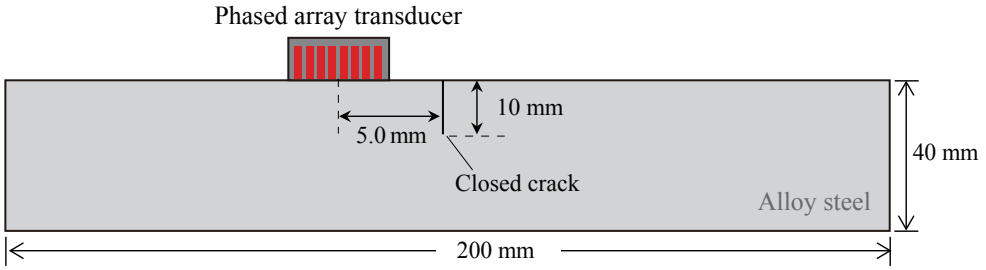

(b) Closed crack model.

Fig. 5.10 Simulation models for the validation of the 2-D EFIT.

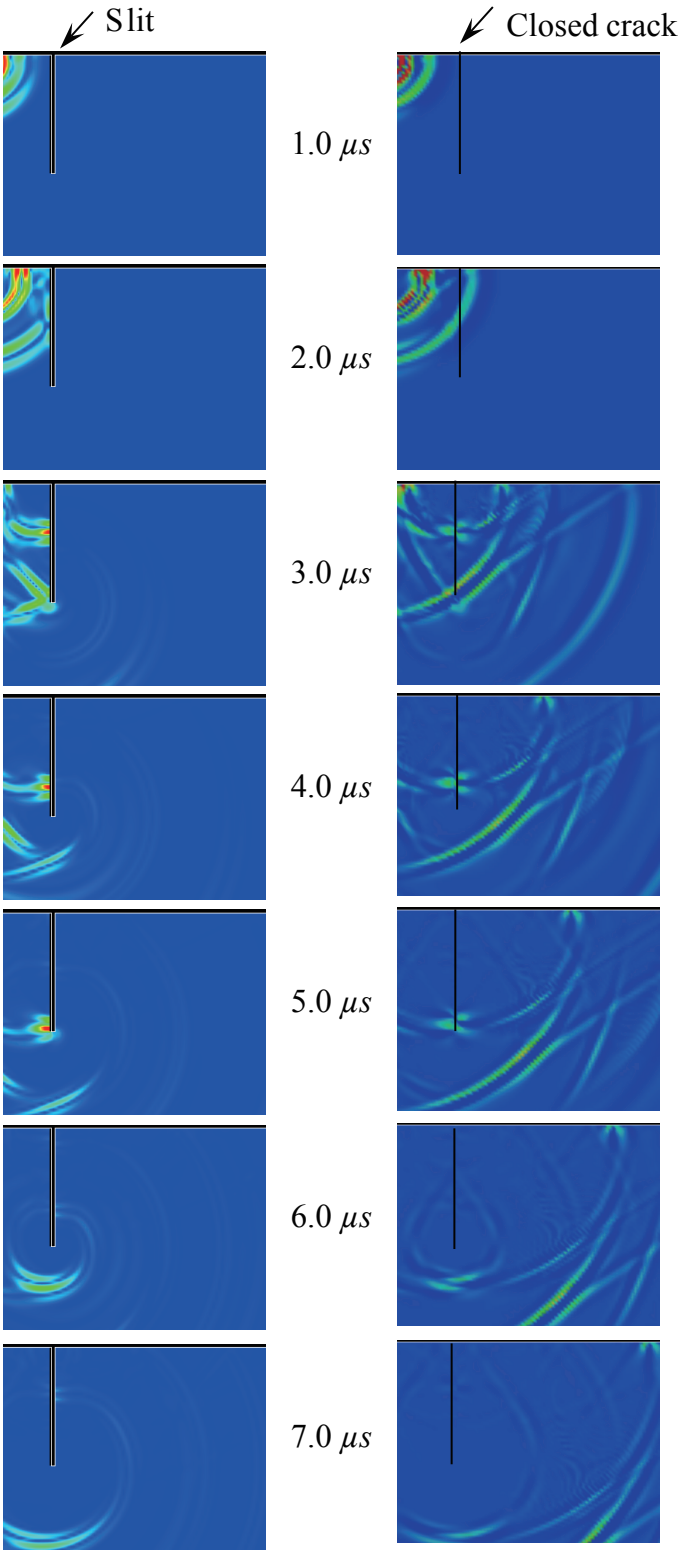

Fig. 5.11 Visualization of propagation wave at slit and closed crack by EFIT simulation.

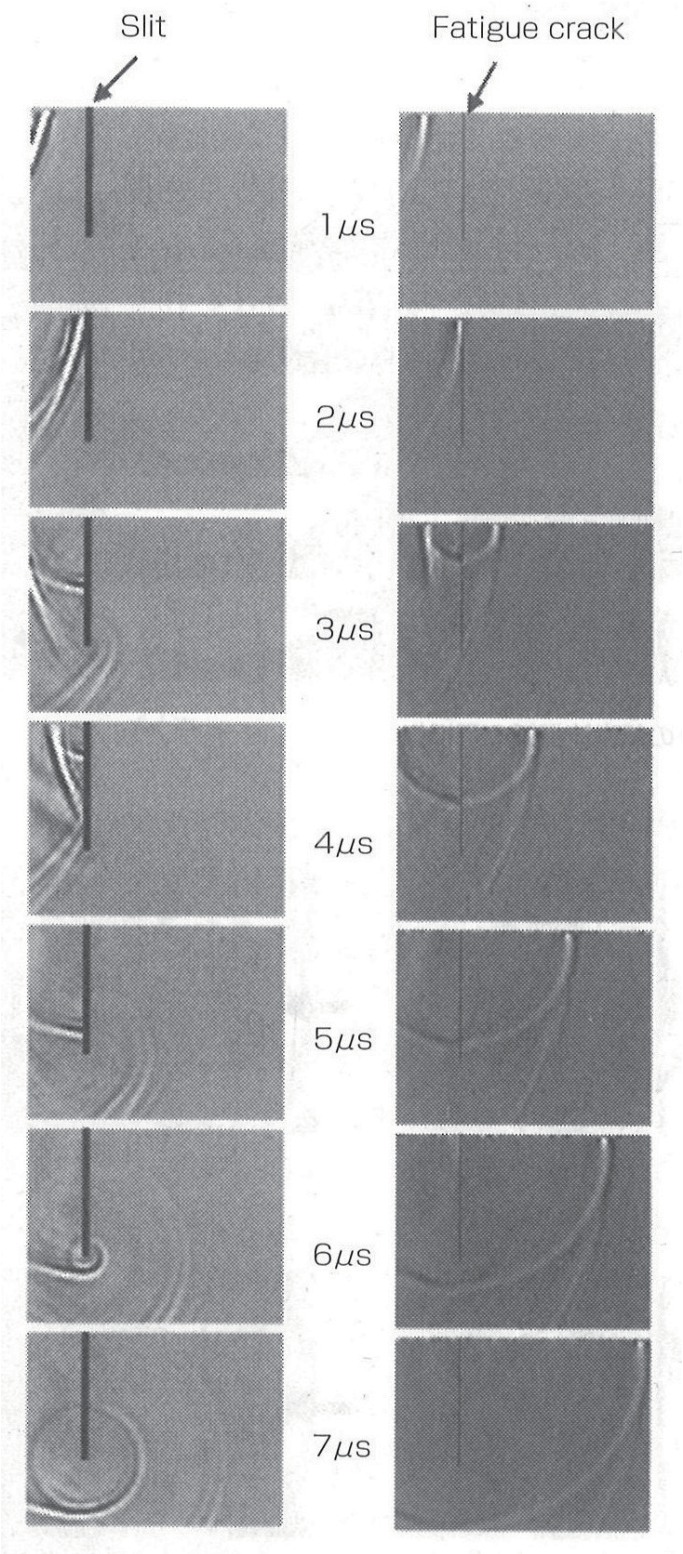

Fig. 5.12 Visualization of propagation wave at slit and closed crack by experimental measurement.

(7) 2-D EFIT Simulation

A 2-D model for the nonlinear UT is indicated in Fig. 5.13. A closed crack was located at the bottom of the model. A phased array transducer was located at the top of the surface which can transmit the ultrasonic wave with oblique incident angle θ towards the middle of the closed crack height. In this case, the edge of the material was subjected to uniform compressive pressure P_0. The number of elements in the phased array transducer was 32, pitch was 1.0 mm, and the element width was 0.9 mm. The material was assumed to be aluminium (c_L = 6,400 m/s, c_T = 3,040 m/s, ρ = 2,700 kg/m^3). Since the cell size of the numerical EFIT was 0.05 mm, the number of cells in the calculation was 400 × 800 = 320,000. A phased array transducer transmits an 8-cycle of the ultrasonic wave with center frequency of 2 MHz. The time history data of the incident wave and its Fourier spectrum are shown in Fig. 5.14 (a) and (b) respectively. The normal stress in the x_2-direction was set to σ_0 on the transducer surface. An incremental time step is Δt = 5 ns in consideration of the CFL condition.

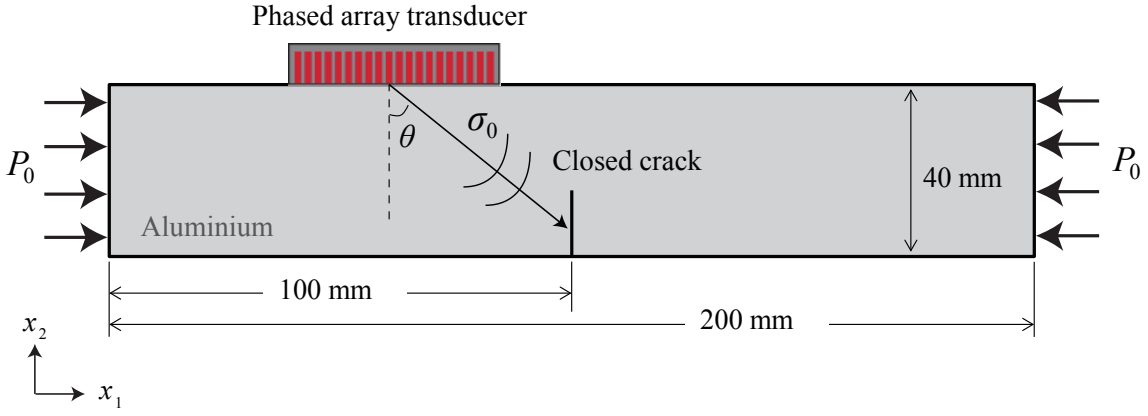

Fig. 5.13 Simulation model of the nonlinear UT with an oblique incident angle.

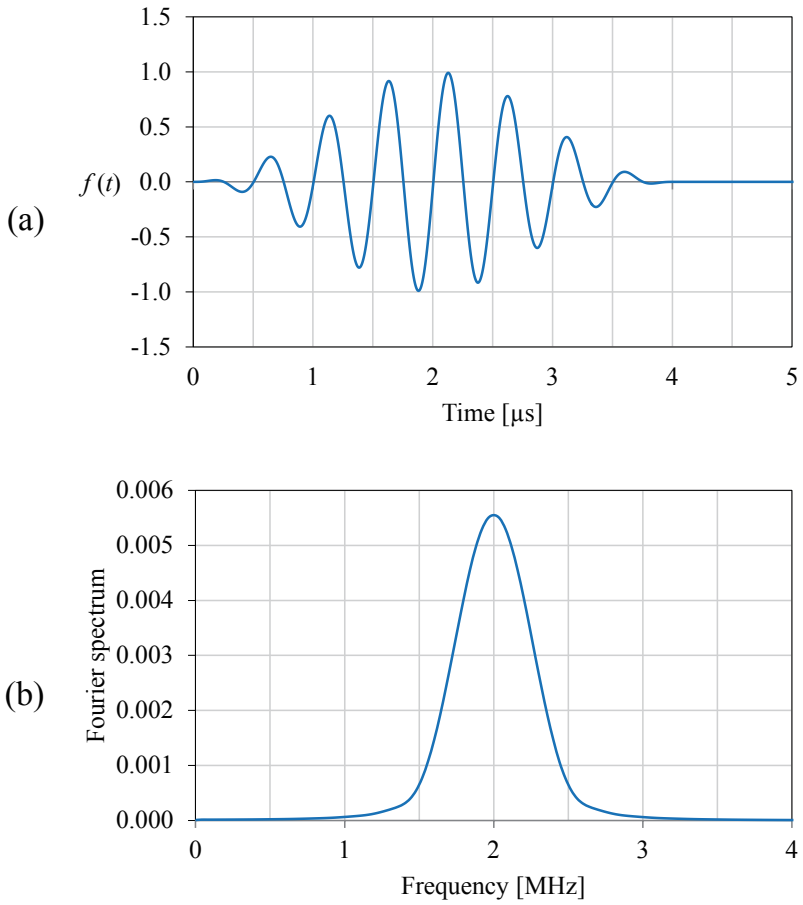

Fig. 5.14 (a) An 8-cycle incident wave. (b) Fourier spectrum of the incident wave.

a) Scattered Wave from the Crack

In this section, the scattered waves from the 2-D numerical simulations were demonstrated for the three models; intact, slit, and closed crack models as shown in Fig. 5.15. Four patterns of the crack with a height of 5, 10, 15, and 20 mm were considered. The ultrasonic wave transmits at incident angle of 30° towards the middle of the closed crack height is considered for the investigation. The positions of the phased array for each pattern are shown in Fig. 5.16. These positions of the phased array transducer were fixed in each model (intact, slit, and closed crack) with the incident angle of 30°. The scattered waveform was observed at a point A. The displacements in the x_1 and x_2-directions at the observation point A are plotted in Figs. 5.17 and 5.18, respectively.

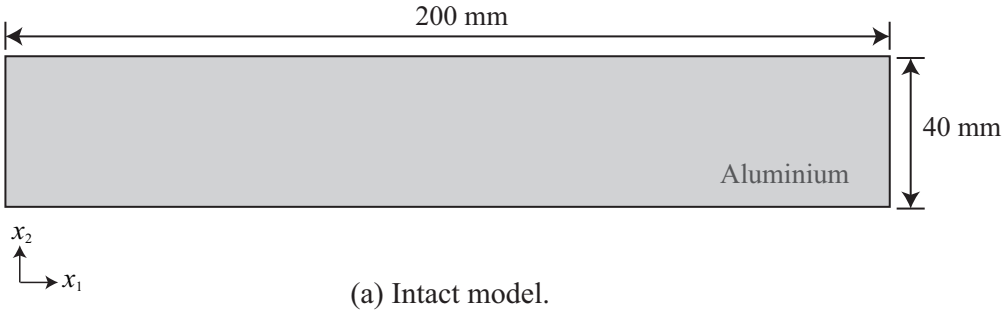

(a) Intact model.

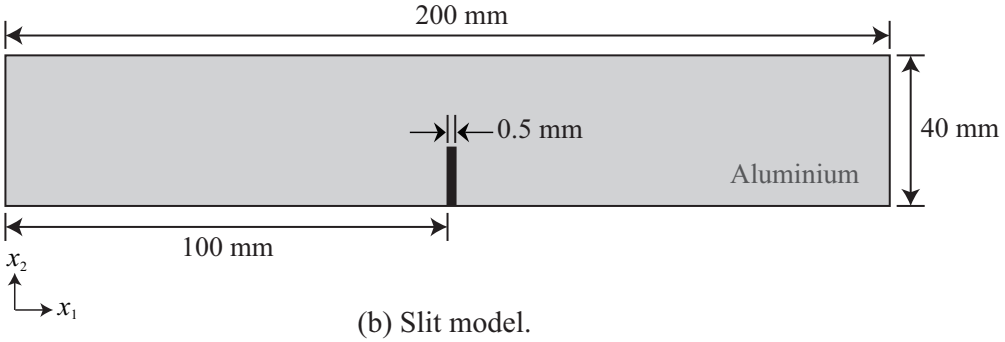

(b) Slit model.

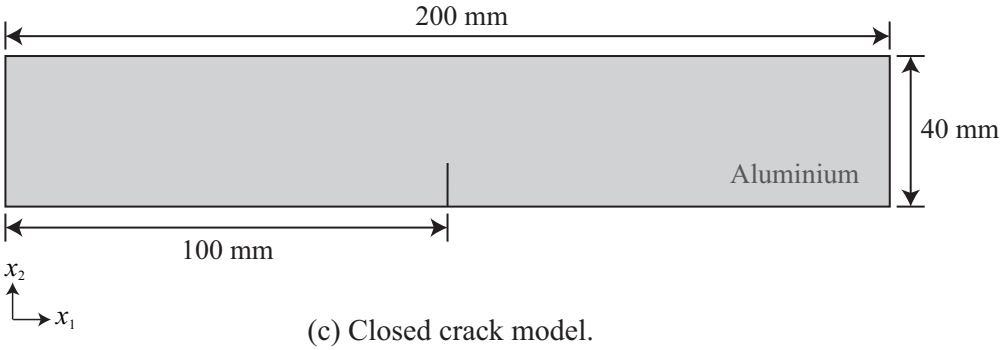

(c) Closed crack model.

Fig. 5.15 Intact, slit and closed crack models.

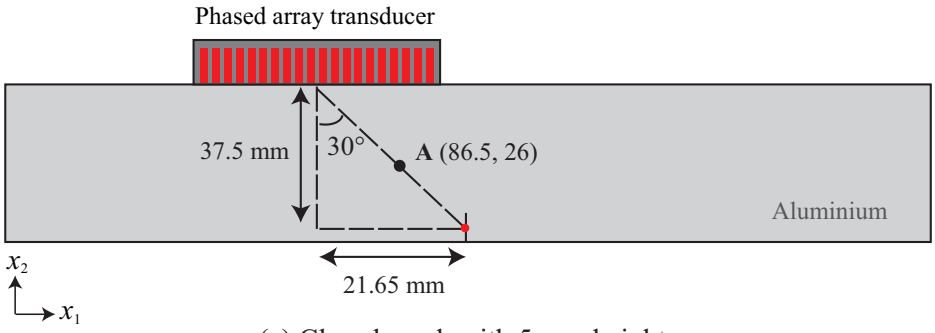

(a) Closed crack with 5 mm height.

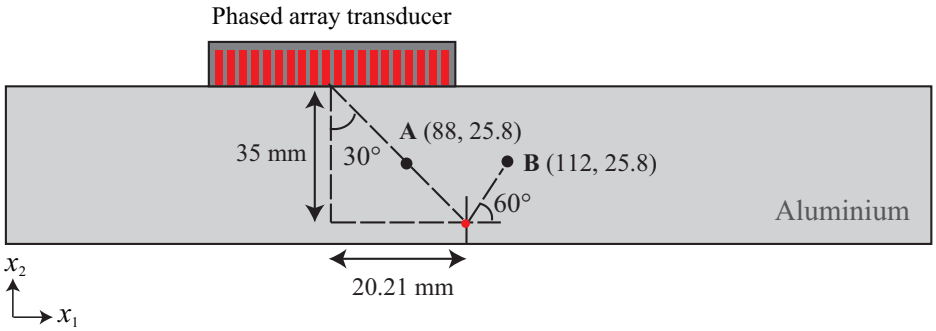

(b) Closed crack with 10 mm height.

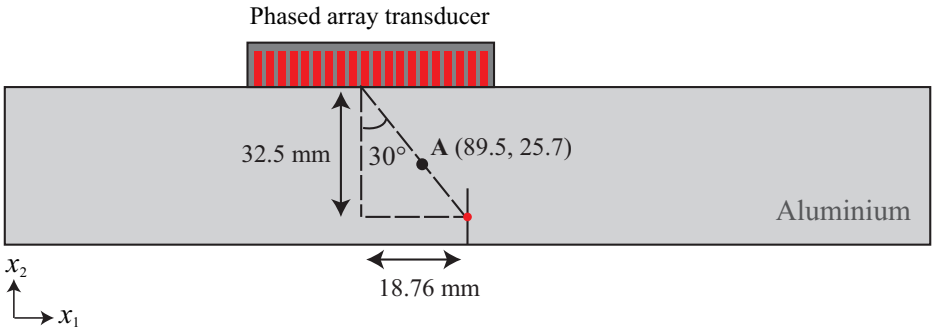

(c) Closed crack with 15 mm height.

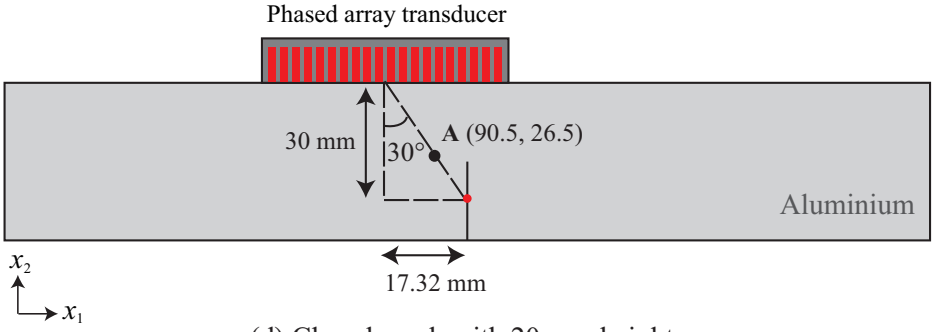

(d) Closed crack with 20 mm height.

Fig. 5.16 Location of the phased array transducer at 30° incident angle.

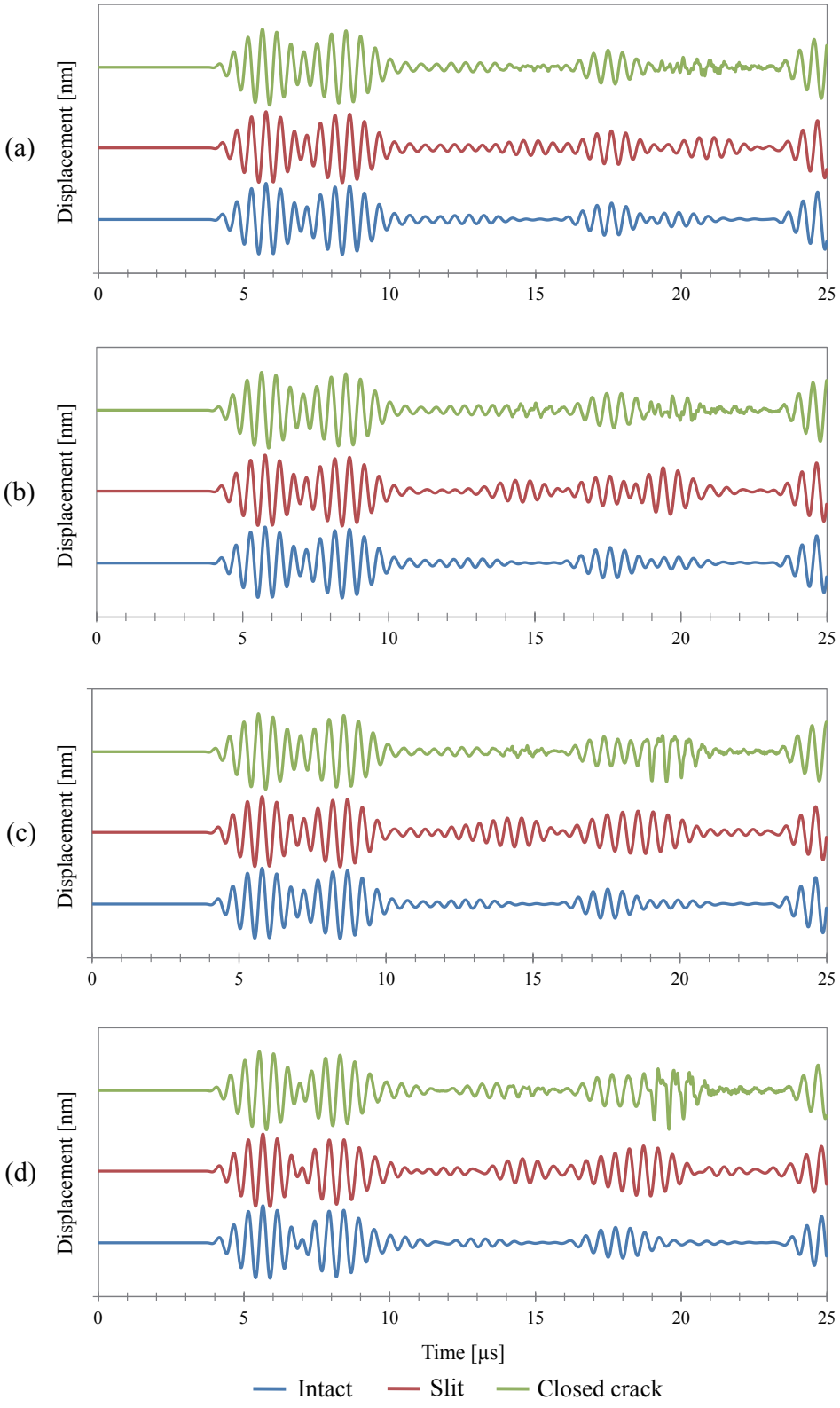

Fig. 5.17 Scattered waveforms in the x_1-direction at point A for the crack with a height of (a) 5 mm, (b) 10 mm, (c) 15 mm, and (d) 20 mm.

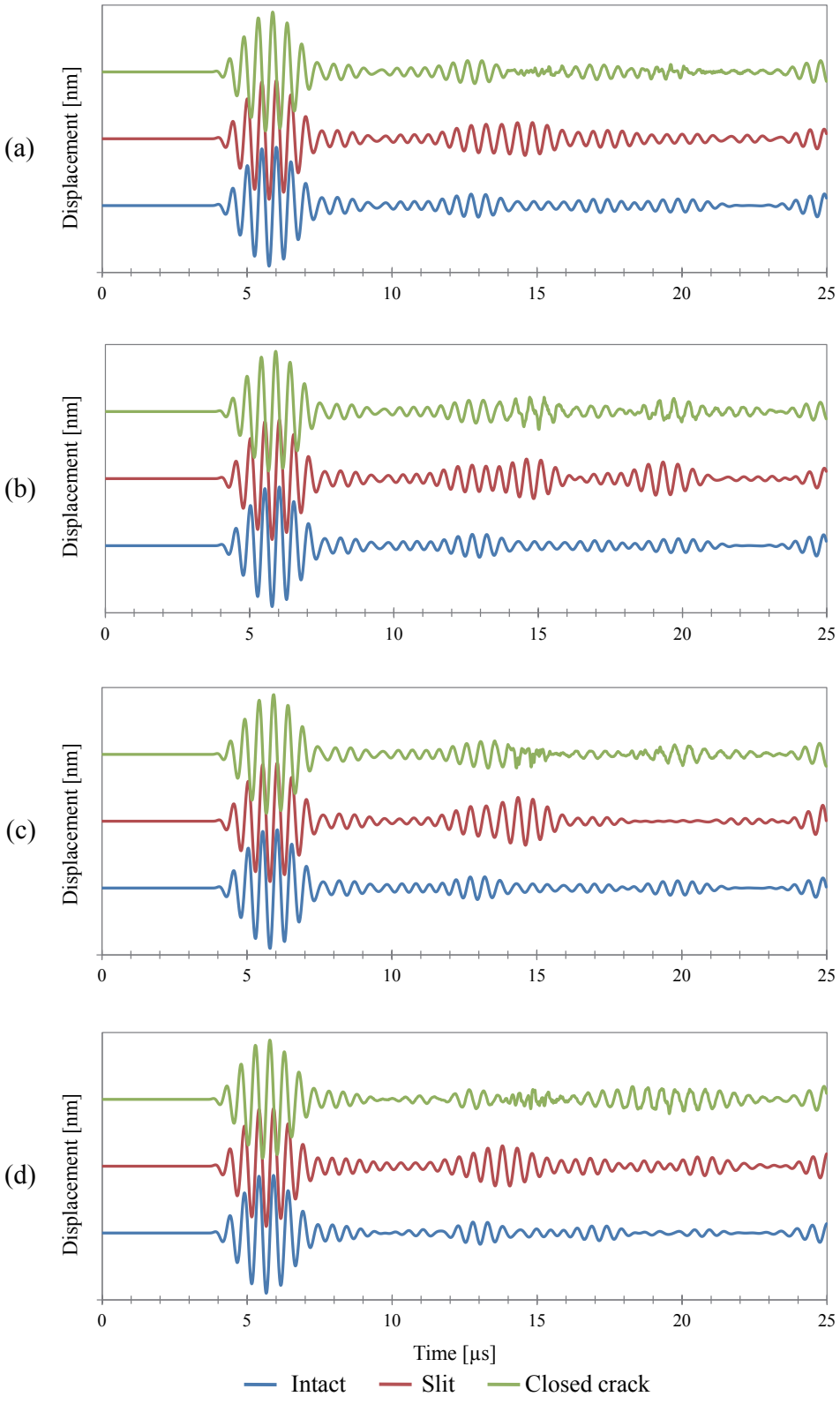

Fig. 5.18 Scattered waveforms in the x_2-direction at point A for the crack with a height of (a) 5 mm, (b) 10 mm, (c) 15 mm, and (d) 20 mm.

It should be noted that, for the slit case, the crack faces are not in contact. Therefore, the initial stress is zero. Whereas in the case of the closed crack, the analysis of η=0.4 was performed in this section. The scattered waveform for the intact case was used as a reference for the both slit and closed crack cases.

In the case of slit, as the height of the slit increased, the displacement amplitude also increased for the results in both the x_1 and x_2-directions. This is because most of the incident wave components were reflected from the slit surface to the incident direction.

However, in the case of closed crack, some of the incident waves were reflected and the others were transmitted through the crack faces due to the contact and separation states of the crack. At this instance, a minimal scattered wave was generated where the displacement amplitude increases as the height of the closed crack increases in both the x_1 and x_2-directions. This is because of the fact that the transducer became closer to the crack when the crack height was increased as shown in Fig. 5.16. As the transducer became closer, the intensity of the reflected wave became larger due to the short propagation distance.

The influence of the difference values of the parameter η was also investigated where η is the ratio of the compressive pressure to the incident stress amplitude. It is difficult to know the compressive pressure in the actual nonlinear UT. Hence, the compressive pressure was set to a constant (P_0 = 0.2 kPa) and the incident stress amplitude σ_0 was varied as 0.125, 0.25, 0.5, 1.0, and 2.0 kPa. These correspond to η = 1.6, 0.8, 0.4, 0.2, and 0.1 respectively. The scattered waveforms for the closed crack with a height of 10 mm at the incident angle of 30° observed in the point A (reflected wave from the closed crack) and the point B (transmitted wave from the closed crack) in the x_1 and x_2-directions are plotted in Figs. 5.19 and 5.20, respectively.

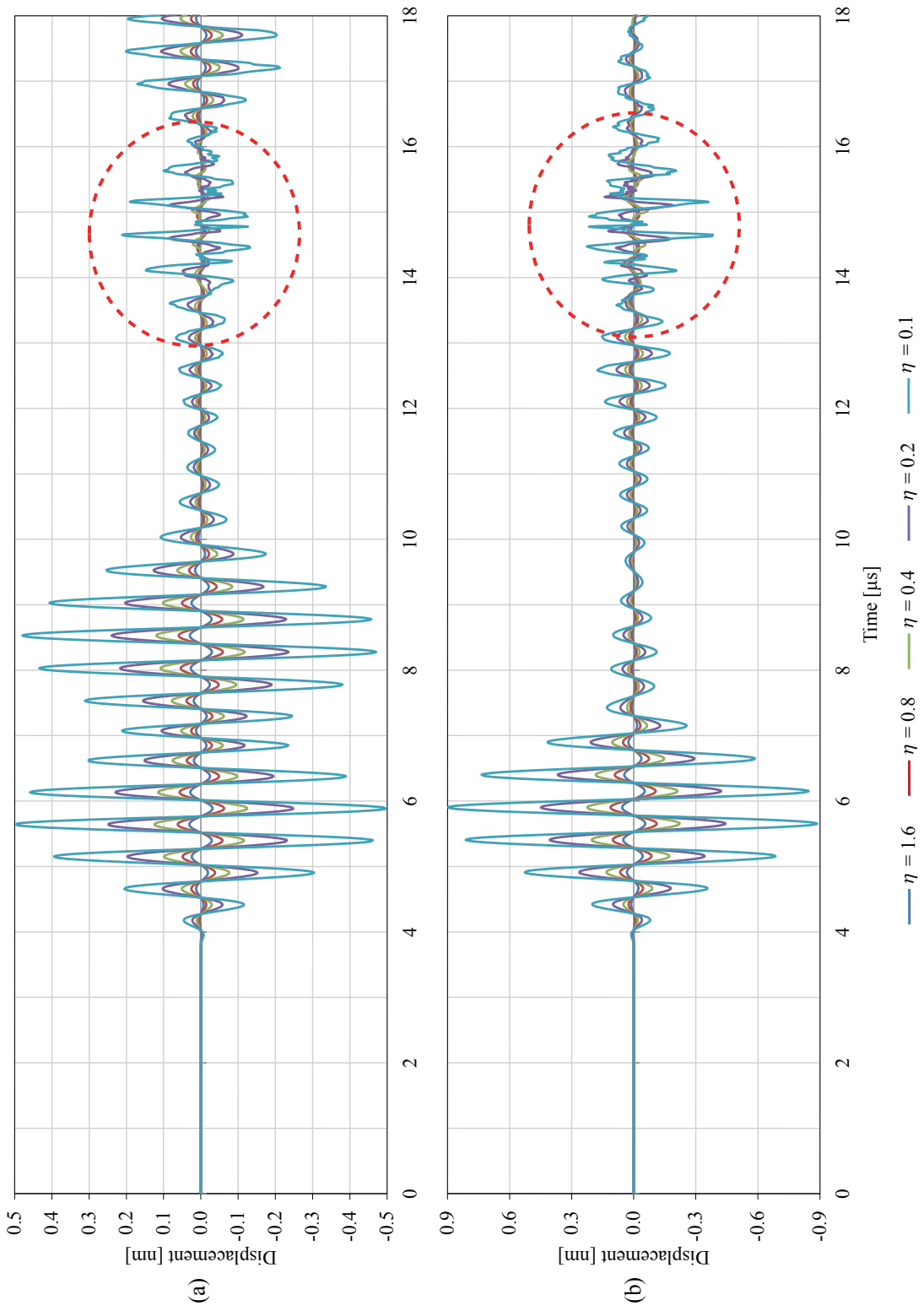

Fig. 5.19 Reflected waveforms observed at point A for the closed crack with a heigh of 10 mm at 30° incident angle and η=1.6, 0.8, 0.4, 0.2, and 0.1 in the (a) x_1-direction and (b) x_2-direction.

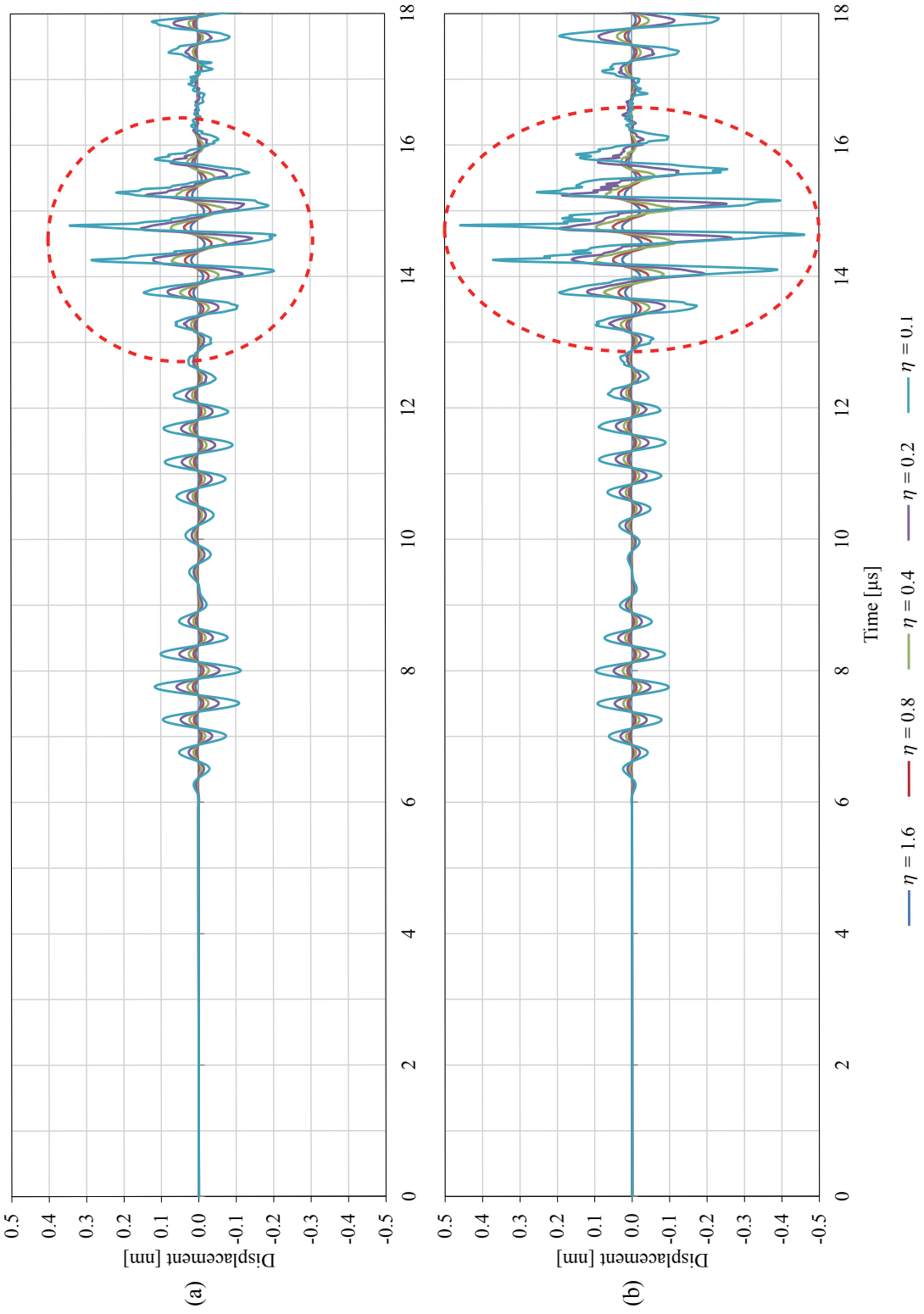

Fig. 5.20 Transmitted waveforms observed at point B for the closed crack with a heigh of 10 mm at 30° incident angle and η=1.6, 0.8, 0.4, 0.2, and 0.1 in the (a) x_1-direction and (b) x_2-direction.

b) Second Harmonic Generation

The Fourier spectrums of the scattered wave from the closed crack in both the x_1 and x_2-directions (indicated by a dotted red line in Figs. 5.19 and 5.20) are displayed in Figs. 5.21 and 5.22, respectively. These Fourier spectrums of the scattered waves indicate the occurrence of the second harmonic component (4 MHz).

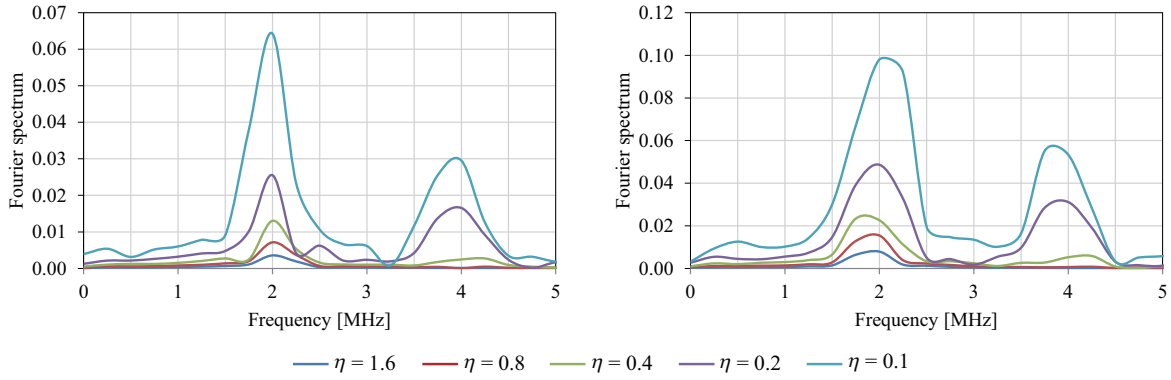

(a) x_1-direction. (b) x_2-direction.

Fig. 5.21 Fourier spectrums of the reflected waveforms observed at point A for the closed crack with a height of 10 mm at 30° incident angle and η=1.6, 0.8, 0.4, 0.2, and 0.1.

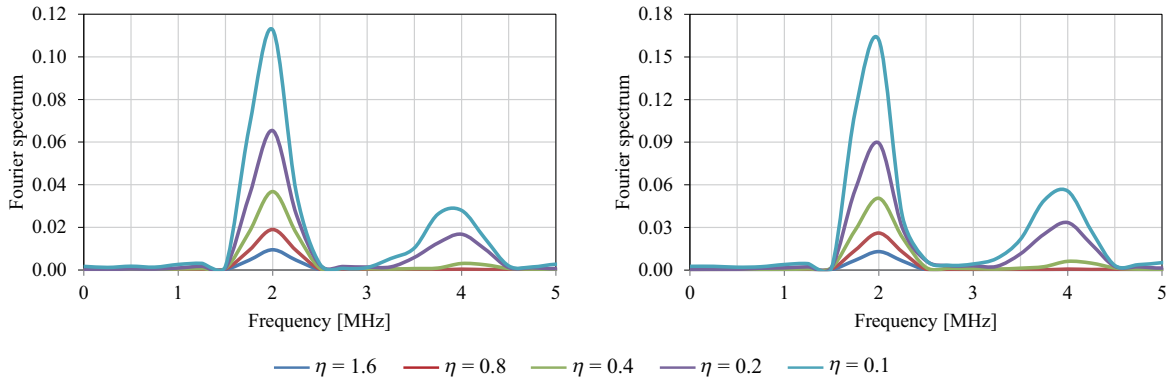

(a) x_1-direction. (b) x_2-direction.

Fig. 5.22 Fourier spectrums of the transmitted waveforms observed at point B for the closed crack with a height of 10 mm at 30° incident angle and η=1.6, 0.8, 0.4, 0.2, and 0.1.

Now, the influence of changing the incident angle was investigated for the second harmonic generation. The incident angle of the radiated wave from the transducer was set to 15°, 30°, 45°, and 60°. All the positions of the phased array transducer for all patterns of the crack height at each incident angle are shown in Figs. A.1, A.2, A.3, and A.4.

The ratio of the second harmonic amplitude A_2 to the fundamental frequency amplitude A_1 of the displacement in the x_1 and x_2-directions is shown in Figs. 5.23 and 5.24, respectively. Here, the ratio A_2/A_1 was represented by the vertical axis and it is used to evaluate the magnitude of the generated second harmonic. The horizontal axis represents the value of η. When the initial stress was zero (the crack faces always in the separation state), the second harmonic component was not observed. When η was larger than 1, i.e., when is compressive pressure P_0 was larger than incident stress amplitude σ_0, the second harmonic component was not generated.

The second harmonic component was generated when the value was in the range of $0 < \eta < 1$. At $\eta = 0.2$, the second harmonic component was significantly generated. At this condition, the closed crack was widely open because the tensile component from the incident wave was larger than the compression at the interface. But, the compressive stress must be sufficient enough to cause the closing of the interface. Otherwise, the interface will maintain in the separation state and the second harmonic component will not generated ($\eta = 0$). Both results in the x_1 and x_2-directions showed a similar trend.

Also, the second harmonic component increases as the crack lengthened. Besides, it can be seen that the second harmonic component was mostly observed at the 30° incident angle at the observation point A (reflected wave from the closed crack). Even if the crack was lengthened, still the second harmonic component appeared mostly at 30° incident angle. This is because the incident wave travels for a short propagation distance between the transducer and the crack (refer in Fig.A.1 to A.4). However, the intensity of the generated second harmonic at the interface is small when the incident angle was just 15°. At this angle, it is difficult to generate the clapping at the interface. Therefore the ratio A_2/A_1 becomes small for the small incident angle.

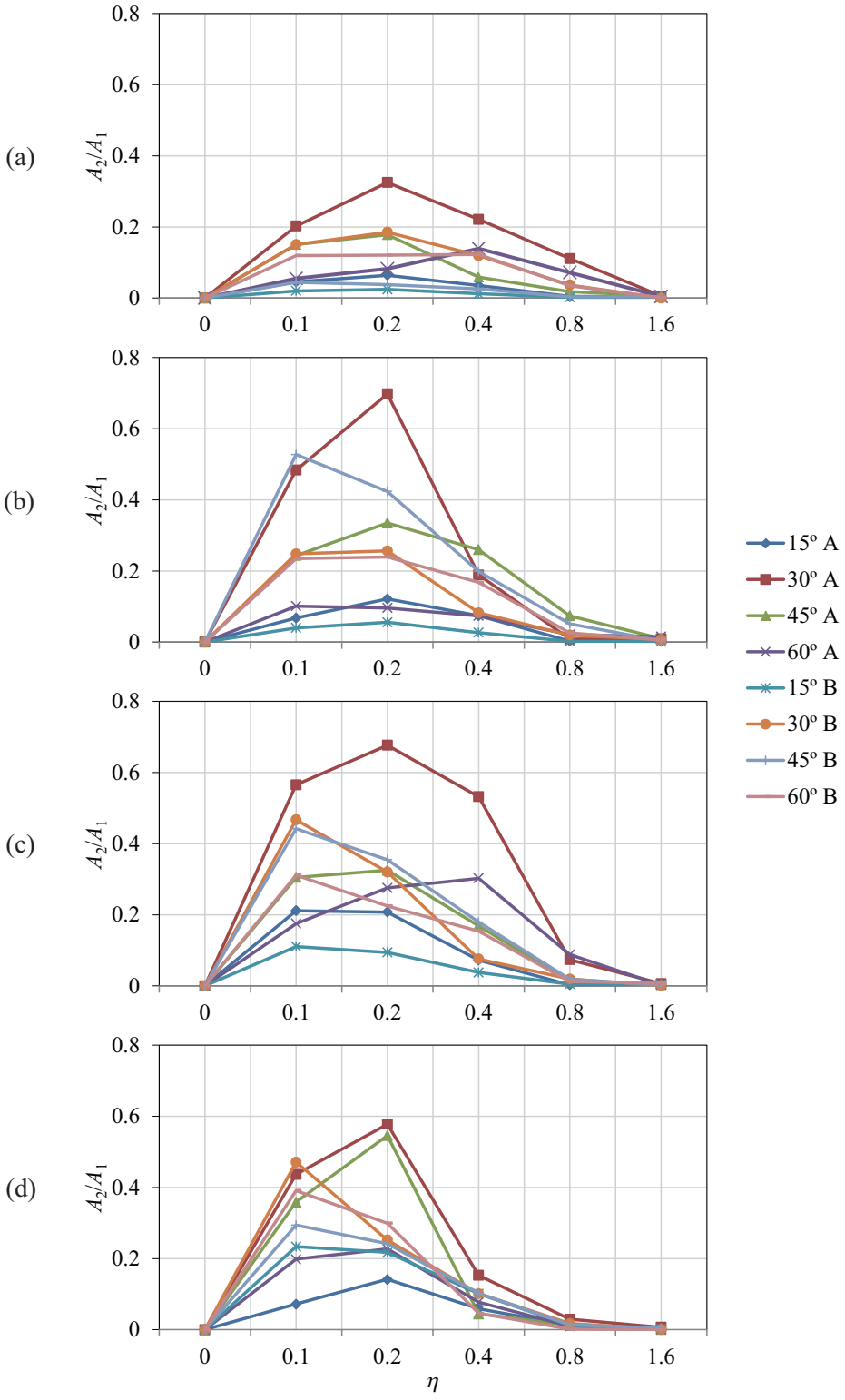

Fig. 5.23 Ratio of the second harmonic amplitude A_2 to the fundamental frequency amplitude A_1 for the closed crack with a height of (a) 5 mm, (b) 10 mm, (c) 15 mm, and (d) 20 mm in the x_1-direction.

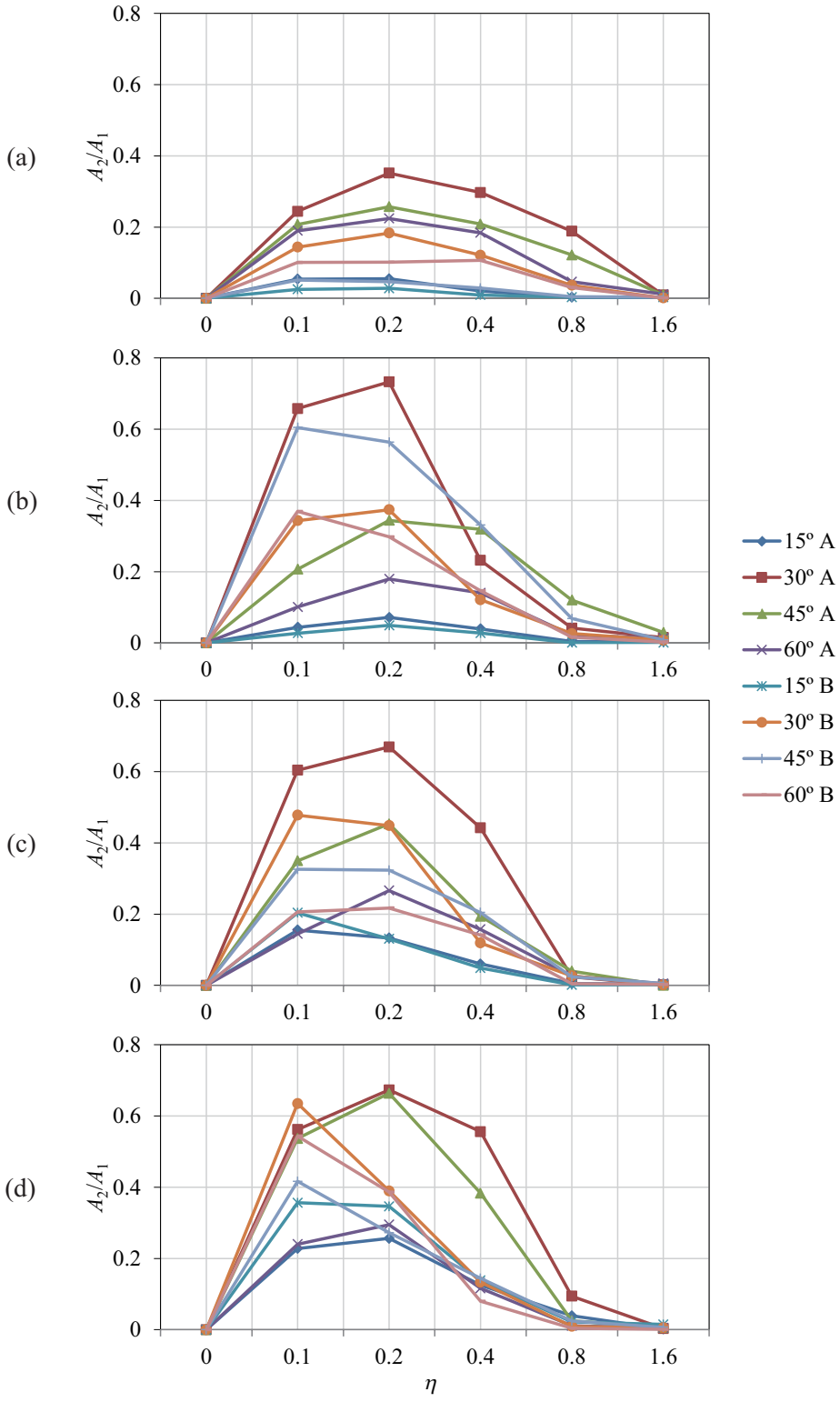

Fig. 5.24 Ratio of the second harmonic amplitude A_2 to the fundamental frequency amplitude A_1 for the closed crack with a height of (a) 5 mm, (b) 10 mm, (c) 15 mm, and (d) 20 mm in the x_2-direction.

c) Visualization of the Scattered Wave

The propagation of the scattered wave at the incident angles of 15°, 30°, 45°, and 60° in the case of η = 1.6, 0.8, 0.4, 0.2, and 0.1 for a crack height of 5, 10, 15, and 20 mm are visualized in Figs.B.1 to B.20, Figs. B.21 to B.40, Figs. B.41 to B.60, and Figs. B.61 to B.80, respectively. The visualization results show the snapshot of the ultrasonic wave at a certain interval time where the color represents the intensity of the von Mises stress. The first snapshot in each figure shows the radiated wave from the transducer. Each of the second snapshot shows that the radiated wave was traveling to the middle of the crack. When the incident wave reaches the crack, the scattered wave was generated from the crack. Each of the last snapshot shows that the scattered wave was propagating to the upper part of the model. From the visualization, it was shown that, at the observation points A and B, the first arrival is the incident wave, the second arrival is the longitudinal wave component scattered from the crack and the third arrival at the observation points is the shear wave component. In the case of η = 1.6, the crack remains in the contact state and the incident wave was mostly transmitted to the penetrated side. In the case of η = 0.1, the crack interface was wide open and the scattered wave was generated from the crack face and it propagated back to the incident direction. These conditions are similar to the results in Figs. 5.8 and 5.9.

(8) Summary

The 1-D EFIT model was extended to the 2-D wave field and the simulation of the phased array UT was performed for the investigation of the second harmonic generation from the closed crack at the bottom surface. The compressive pressure was maintained at a constant and only the incident stress amplitude was changed. It was found that the generation of the second harmonic depended on the incident angle and the intensity of the incident stress. Furthermore, the harmonics were generated from the crack face since the harmonics increased as the crack lengthened. The 2-D EFIT was verified with the visualization of the wave propagation.

6 IMAGING OF CLOSED CRACK USING PHASED ARRAY TRANSDUCER

(1) Introduction

The ultrasonic array imaging systems set a number of time delays to stagger the firing of elements in an array during the emission process. A high-pressure wave generated from the transducer propagates in a specific direction. The signal received at each element was properly delayed and summed and an image line was obtained. In the recent years, a post-processing beam-forming technique has been adopted and this technique utilizes a combination of signals of the transmission and reception elements which is referred to as full-waveforms sampling and processing (FSAP)[69, 70] method.

In this chapter, the simulation of the array imaging of the closed crack was performed with the scattered wave calculated by the 2-D EFIT. In the simulation, the incident angle was set at around 30° towards the face of the closed crack with 10 mm height. The image of the closed crack was reconstructed from the waveform received at all elements of the phased array transducer. The waveform with a second harmonic was extracted from the received signal and fed into the FSAP method.

(2) Ultrasonic Phased Array Transducer

The coordinate system for the linear phased array transducer is defined as shown in Fig. 6.1. The delay laws imposed on the n-th element positioned at $\boldsymbol{x} = (x_n, y_n)$ for an angled beam with focal point $\boldsymbol{F}$ in a material characterized by velocity c is expressed by the difference of the propagation time:

$$\Delta\tau_n(\boldsymbol{x}; \boldsymbol{F}) = (|\boldsymbol{F} - \boldsymbol{x}_0| - |\boldsymbol{F} - \boldsymbol{x}|)/c \tag{6.1}$$

where $\boldsymbol{x}_0$ is the center position of the array transducer. The center position was set to the origin. The focal point $\boldsymbol{F}$ is expressed by the incident angle θ, that is $\boldsymbol{F} = (R\cos\theta, R\sin\theta)$. Therefore, the delay law $\Delta\tau_n$ is obtained as:

$$\Delta\tau_n(\boldsymbol{x}; \boldsymbol{F}) = R\left[1 - \sqrt{(\sin\theta - x_n/R)^2 + \cos^2\theta}\right]/c \tag{6.2}$$

In the finite limitation of the focal length R, Eq. (6.2) was simplified to the following expression:

$$\Delta\tau_n(\boldsymbol{x}; \theta) = x_n \sin\theta/c \tag{6.3}$$

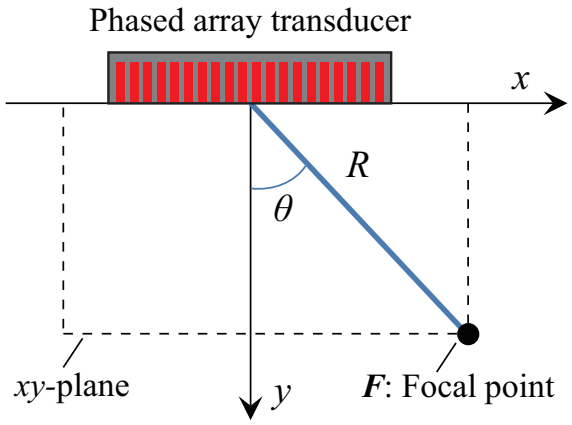

Fig. 6.1 Coordinate system and focal point of phased array tranducer.

(3) Imaging Principle of Steering Type FSAP Method

In the pointwise element firing FSAP method, each element of the phased array transducer transmitted an ultrasonic wave in a sequential order. After obtaining all the patterns of the transmission and reception of the ultrasonic wave, the focal beam to a target pixel can be made in the post-processing. Because of a dozen times of the transmission, it is possible to reconstruct a defect image with high resolution. However, it takes more time to acquire the waveforms for N times of the transmission in the case of array transducer with total N elements. When each element is fired in a sequential order, there is concern that the noise of the image might increase because of the law of signal to noise ratio (S/N) for the pointwise shot. Especially, a large amplitude should be sent to the crack to generate the clapping of the crack faces. By simultaneous excitation with all the elements, the large amplitude can be transmitted to the target. However, the transmission for the target direction might lead to the lack of information for the shape reconstruction.

Therefore, multiple transmission of the ultrasonic wave was considered by changing the steering direction of the beam and increasing the information of the scattered waves. Figure 6.2 shows the transmission direction and the data acquisition by the array transducer with N elements where n and s indicate the number of the transmission elements used for simultaneous excitation and the total number of the ultrasonic beam incident angles, respectively. The ultrasonic waves were excited at the incident angles (θ_1 to θ_s), and each element received the scattered wave. As a result, the signal storage matrix M_{ij} was filled with the scattered waves (Fig. 6.2).

Contemplating the imaging of the pixel $\boldsymbol{x}[k, l]$ as shown in Fig. 6.3, the coordinate of the center of the array transducer is defined as (x_0, H) and the traveling time from the center of the array transducer to the pixel $\boldsymbol{x} = (x_k, y_l)$ is T_{kl}^0. Next, the path of the scattered waves was considered from the pixel $\boldsymbol{x}$ to the element i of the array transducer. The propagation time is expressed as:

$$T_{kl}^i = \frac{\sqrt{(x_k - x_i)^2 + (H - y_l)^2}}{c_L}. \tag{6.4}$$

In the case of all the elements firing FSAP, the time delay in the scattering process should be considered for the post-processing.

$$\Delta T_{kl}^{i} = T_{kl}^{0} - T_{kl}^{i}. \tag{6.5}$$

Then, the scattered waves $M_{ij}(t)$ from the signal storage matrix was synthesized in consideration with the delay Δ_{kl}^{i} where ΔT_{kl}^{i} was shifted from $M_{ij}(t)$. However, in an actual electronic scanning apparatus, the time origin was set to the firing element first. Therefore, there was a time deviation ΔD^{p} as shown in Fig. 6.3. Correcting the time ($\Delta D^{p} = \frac{\frac{D}{2}\sin\theta_{p}}{c_{L}}$), the components in the signal storage matrix were combined.

$$F(\boldsymbol{x}[k,l],t) = \sum_{p=1}^{s}\sum_{i=1}^{n} M_{pi}(t - \Delta T_{kl}^{i} + \Delta D^{p}) \tag{6.6}$$

For the imaging in the target area, the amplitude Y corresponding to the round trip time $t = 2T_{kl}^{0}$ was extracted:

$$Y(\boldsymbol{x}) = F(\boldsymbol{x}[k,l], 2T_{kl}^{0}) \tag{6.7}$$

Finally, the value of Y in Eq. (6.7) was plotted with color distribution.

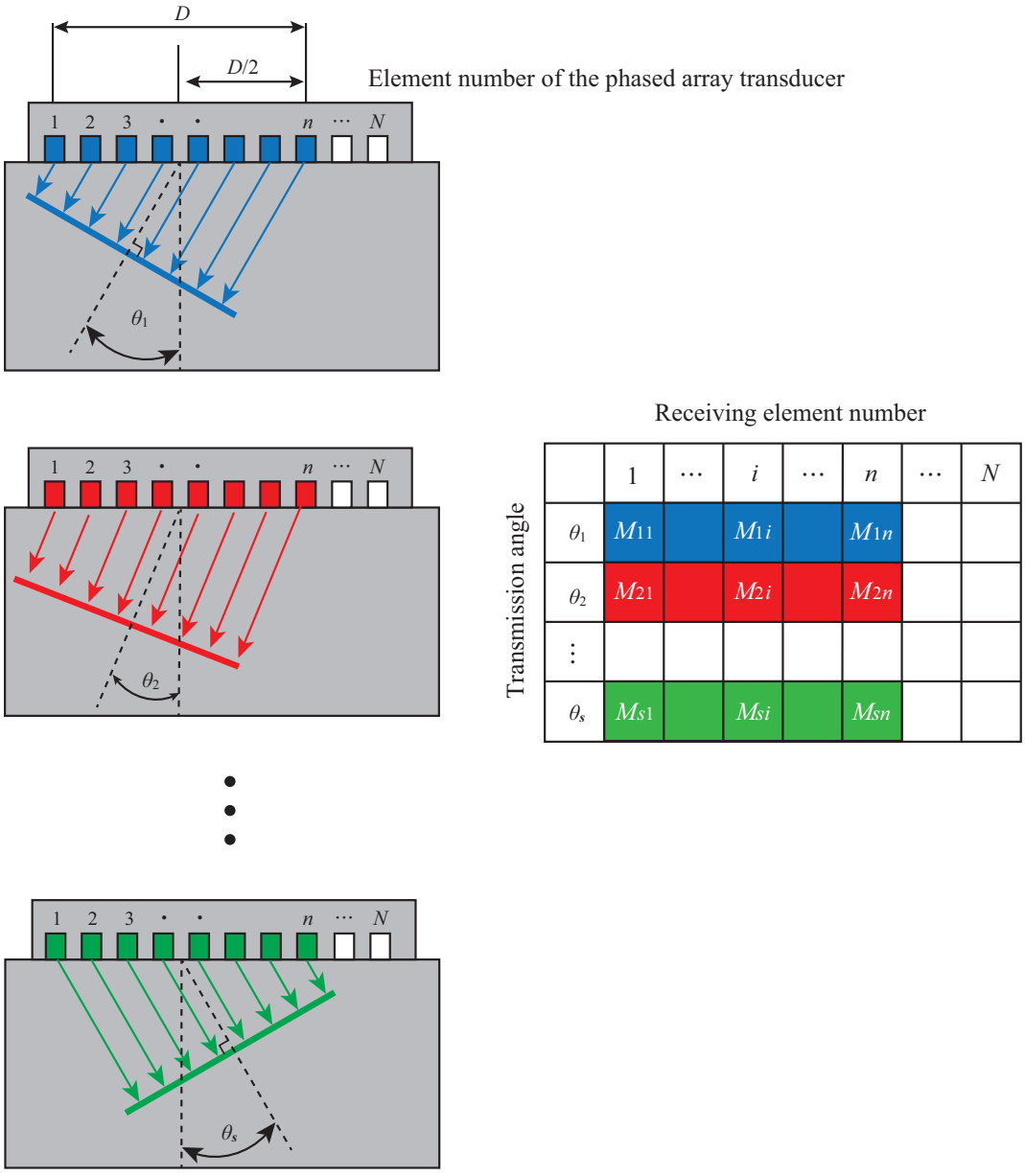

Fig. 6.2 Signal storage matrix (steering type FSAP method).

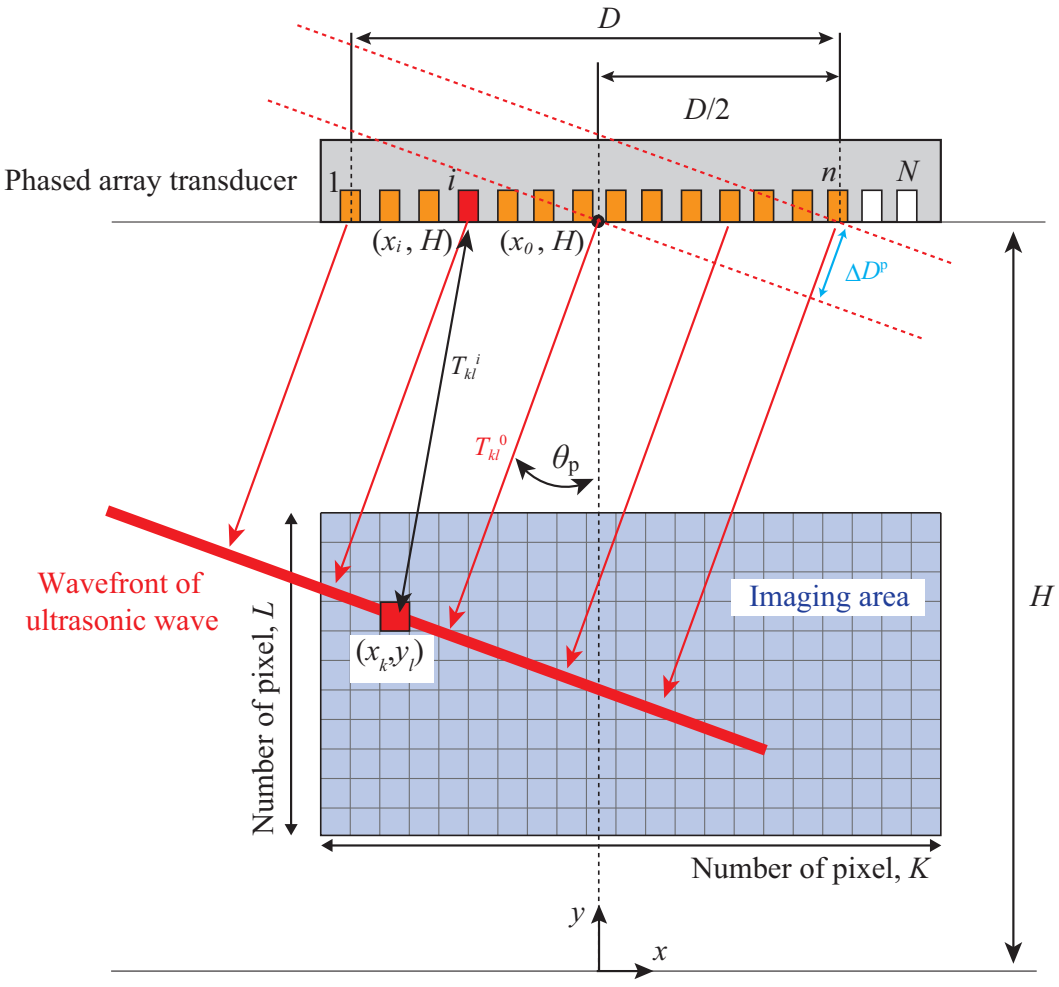

Fig. 6.3 The position of the phased array transducer and the imaging area.

(4) Imaging of the Closed Crack

To model the scattered wave from the crack, the 2-D EFIT simulations were demonstrated using two models; slit and closed crack as shown in Figs. 6.4. The height of the slit and the closed crack were set as 10 mm. The width of the slit was 0.5 mm. The material in the simulation was assumed to be aluminium (c_L = 6,400 m/s, c_T = 3,040 m/s, ρ = 2,700 kg/m^3). A phased array transducer (total elements number N = 32, pitch = 0.6 mm, and element width = 0.5 mm) was placed on the top of the models and the ultrasonic wave which was radiated at the incident angle $\theta = 30°$ propagated to the middle of the crack height. In the 2-D EFIT, the cell size Δx was 0.05 mm, the time step was chosen as Δt = 4 ns by considering the CFL condition.

For the imaging with the FSAP, the second harmonic component has to be extracted from the raw ultrasonic signal. The displacement waveforms in the x and y-directions received by each element were used as the input data for the FSAP. However, the imaging results in the y-direction were the most important in the actual ultrasonic testing, because the contact transducer can detect the motion in the y-direction.

Figures. 6.6 and 6.7 show the imaging result in the case of η = 0.1 for the x and y-directions, respectively. In this simulation, the ultrasonic beam at the incident angle $\theta = 26°$ and $\theta = 34°$ reach the bottom and the top of the crack (Fig. 6.4 (a)), respectively. Here, the incident waveform with a 4-cycle and center frequency of 5 MHz was used. The time history data of the incident wave and its Fourier spectrum are shown in Fig. 6.5 (a) and (b) respectively.

The second harmonic was extracted using a signal processing with band-pass filter between 8 MHz and 12 MHz. Here, the ultrasonic array imaging of both the slit and the closed crack were performed with five patterns of the incident angles at 26°, 28°, 30°, 32°, and 34°. The value Y was normalized by the maximum value in each image and plotted with color.

For the imaging with the fundamental frequency (linear ultrasonic imaging), it is difficult to discriminate between the slit and the closed crack. However, the difference between the

slit and the closed crack can be observed clearly by using the second harmonic (nonlinear ultrasonic imaging). The face of the closed crack can be observed only by the nonlinear imaging as there is no signal from the crack interface in the linear imaging.

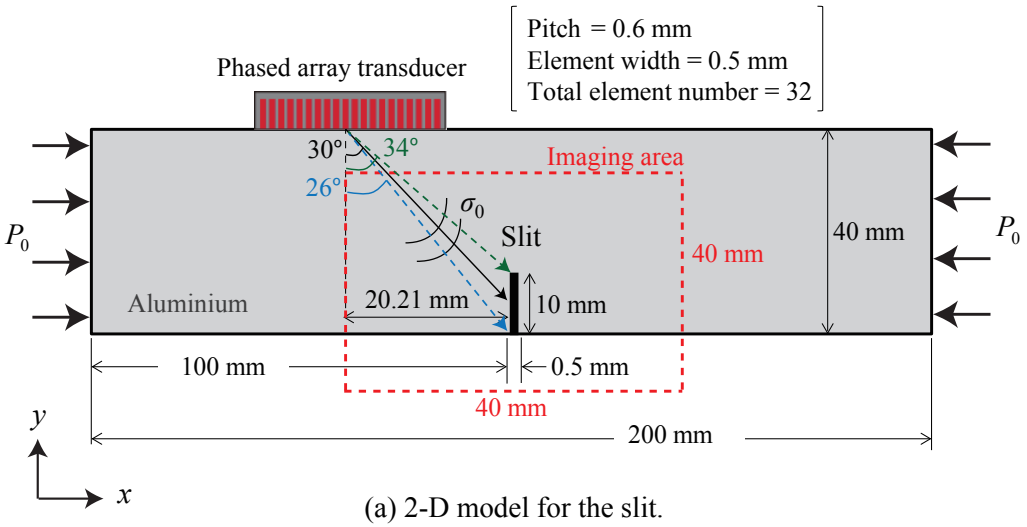

(a) 2-D model for the slit.

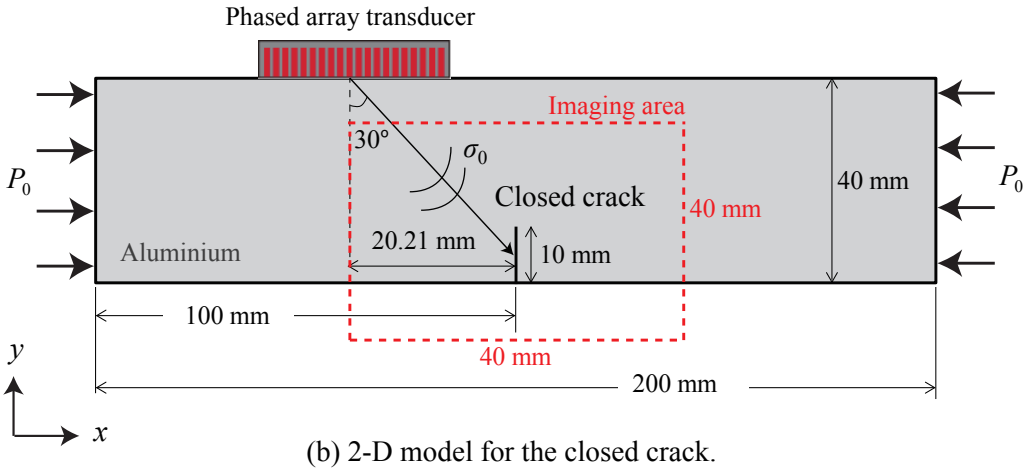

(b) 2-D model for the closed crack.

Fig. 6.4 FSAP simulation models for the ultrasonic array imaging.

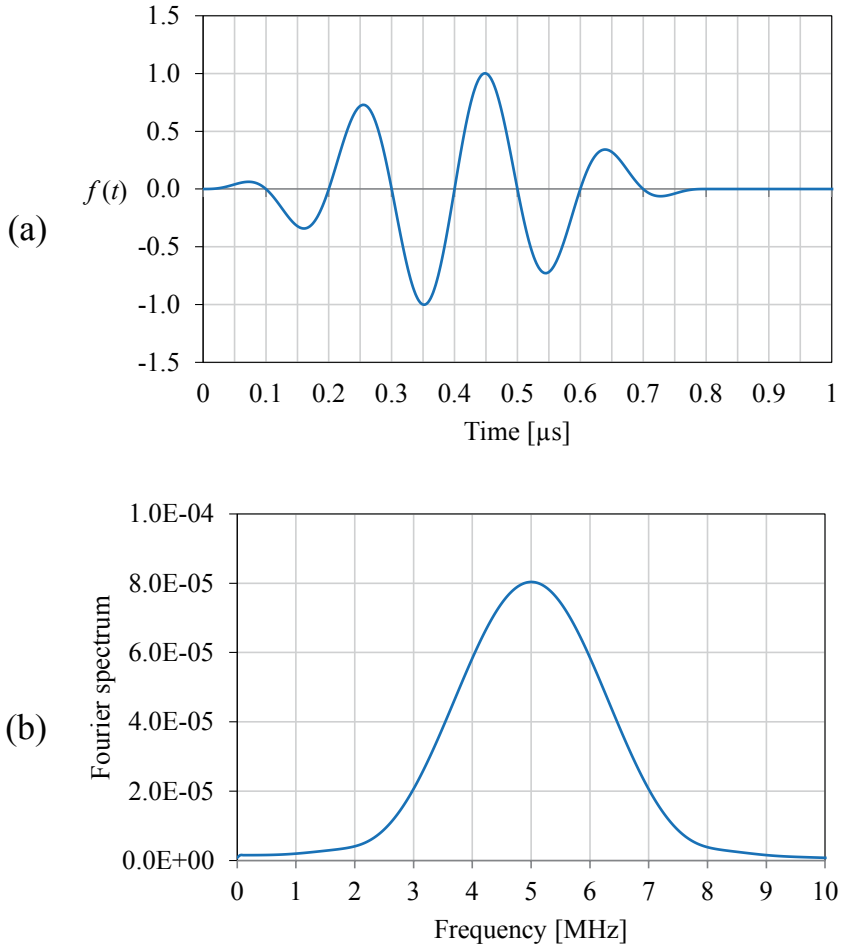

Fig. 6.5 (a) A 4-cycle incident wave in time domain. (b) Fourier spectrum of the incident wave.

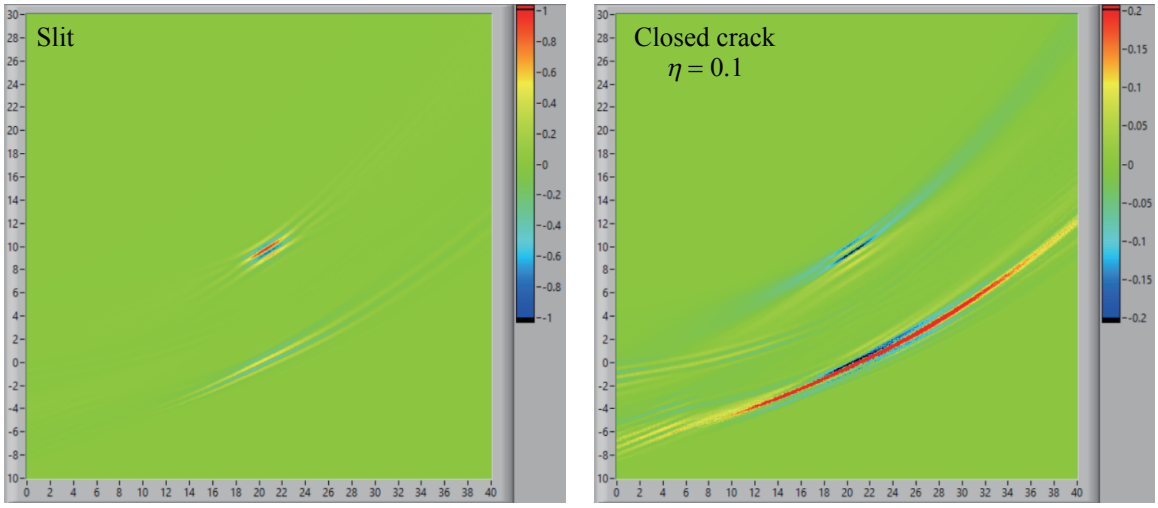

(a) Linear ultrasonic imaging.

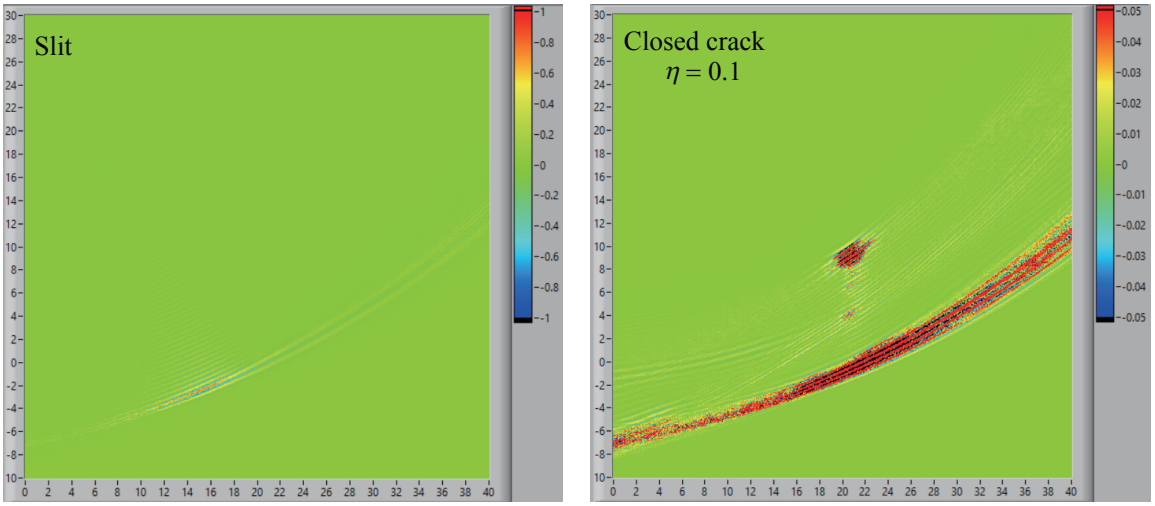

(b) Nonlinear ultrasonic imaging.

Fig. 6.6 Imaging results using the displacement data in the *x*-direction for the slit and the closed crack by five incident angles of 26°, 28°, 30°, 32°, and 34°.

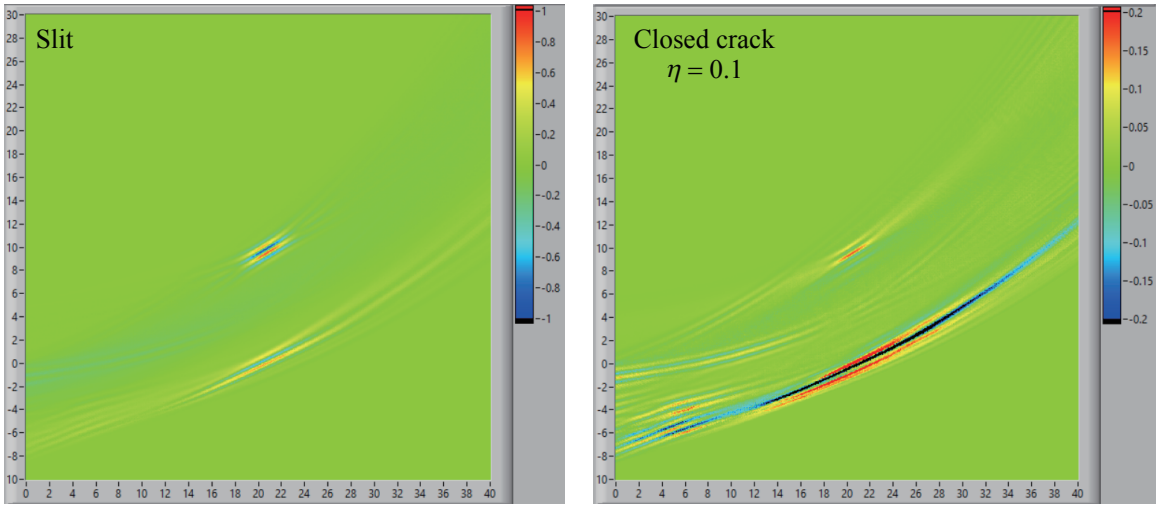

(a) Linear ultrasonic imaging.

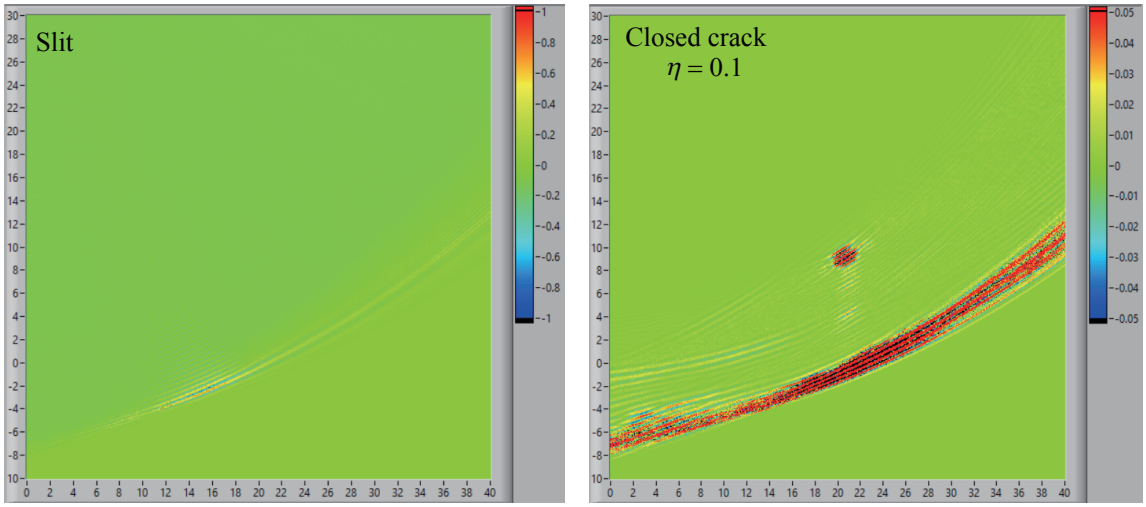

(b) Nonlinear ultrasonic imaging.

Fig. 6.7 Imaging results using the displacement data in the *y*-direction for the slit and the closed crack by five incident angles of 26°, 28°, 30°, 32°, and 34°.

The second harmonic component was extracted from the received scattered waveform by using a band-pass filter with the pass band range of 8 MHz to 12 MHz. The raw data was labeled as non-process waveform and the extracted data was labeled as second harmonic waveform. The Fourier spectrums of the non-process and second harmonic waveform for both the slit and the closed crack in the *x* and *y*-directions as shown in Fig. 6.8. It can be observed that the slit does not generate the second harmonic component. On the other hand, the closed crack generated a significant second harmonic component.

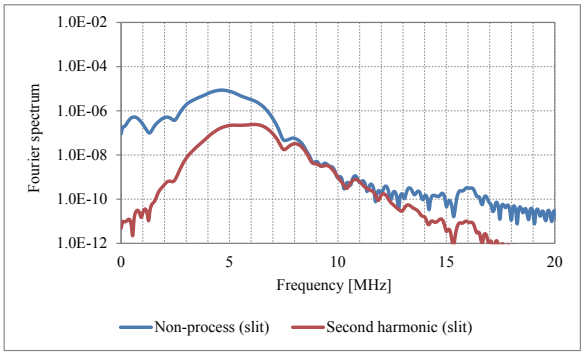

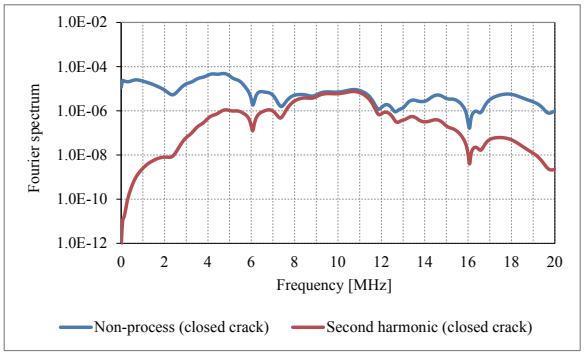

(a) ***x***-direction.

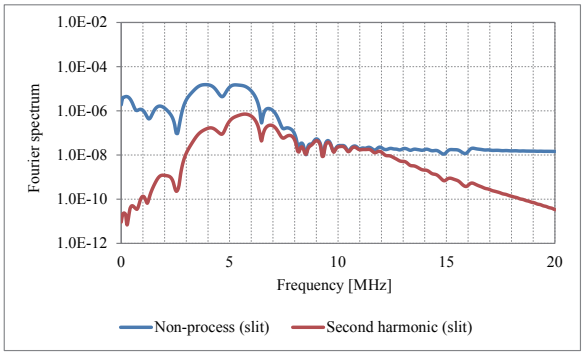

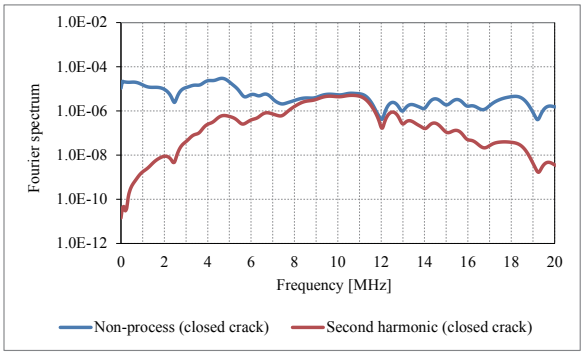

(b) ***y***-direction.

Fig. 6.8 Fourier spectrums of non-process and second harmonic waveforms of the slit and the closed crack in the *x* and *y*-directions.

The nonlinear imaging results for the closed crack at the incident angles of 26°, 28°, 30°, 32°, and 34° in the *x* and *y*-directions are shown in Figs. 6.10 and 6.11, respectively. Here, the face of the closed crack can be observed due to the contact and separation behaviors as the incident angle is increased. If the incident wave reached at the interface in a perpendicular direction to the crack face, a large force acts on the crack faces then the faces became separate. Therefore, an acute angle of the ultrasonic beam needs a large incident stress to cause the opening of the crack faces. Conversely, an obtuse incident angle can add a large stress in the perpendicular direction to the crack faces.

The linear and nonlinear imagings for the closed crack were also investigated in the case of the different compression conditions of η as = 0.1, 0.4, and 1.6. The imaging results reconstructed by five incident angles of 26°, 28°, 30°, 32°, and 34° in the *x* and *y*-directions are shown in Figs. 6.12 and 6.13, respectively. The shape of the closed crack cannot be observed when the crack faces are in the contact state (η = 1.6).

The imaging results are investigated when the number of cycles of the incident wave was changed. The incident wave of a 6-cycle with the center frequency of 6 MHz was chosen. The time history data of the incident wave and its Fourier spectrum are shown in Fig. 6.9 (a) and (b) respectively. The nonlinear imaging results of the closed crack for the different values of η = 0.1, 0.4, and 1.6 are shown in Figs. 6.14 and 6.15 for the *x* and *y*-directions, respectively. The second harmonic component was gained as the frequency and the number of cycle of the incident wave increased. The reason was that the incident wave became a narrow frequency band due to the multiple cycle numbers and then the second harmonic component was generated intensively in the pass band. Also the beam directivity was enhanced by the high frequency transmission.

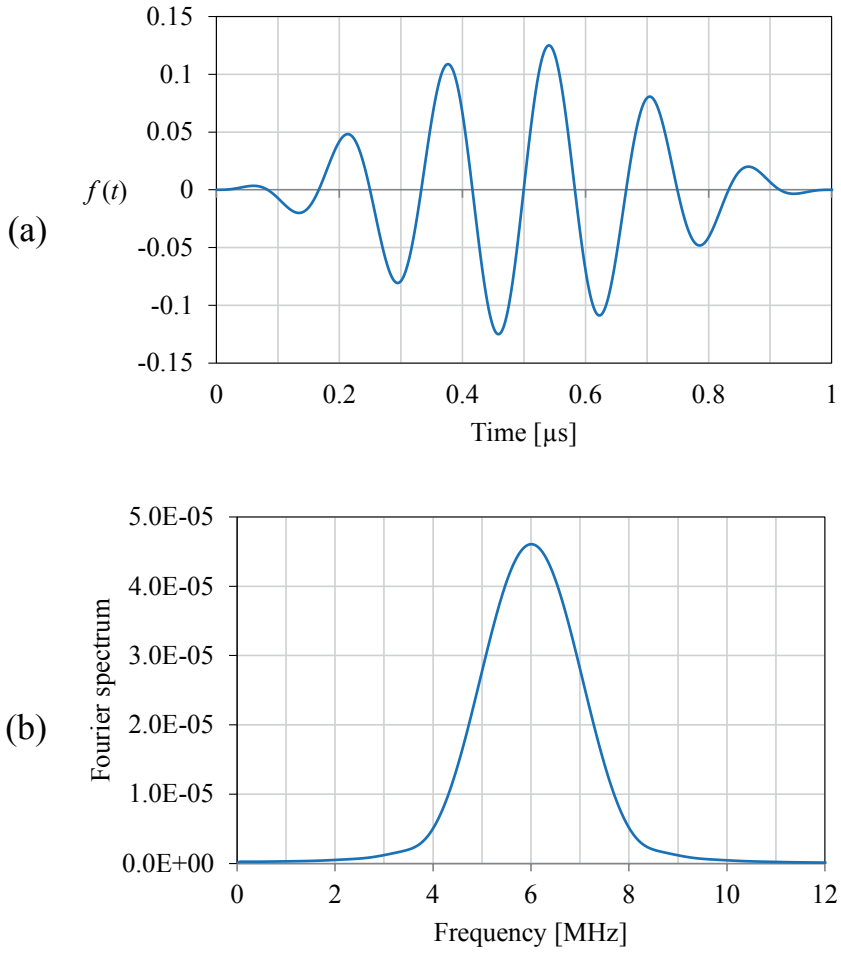

Fig. 6.9 (a) A 6-cycle incident wave in time domain. (b) Fourier spectrum of the incident wave.

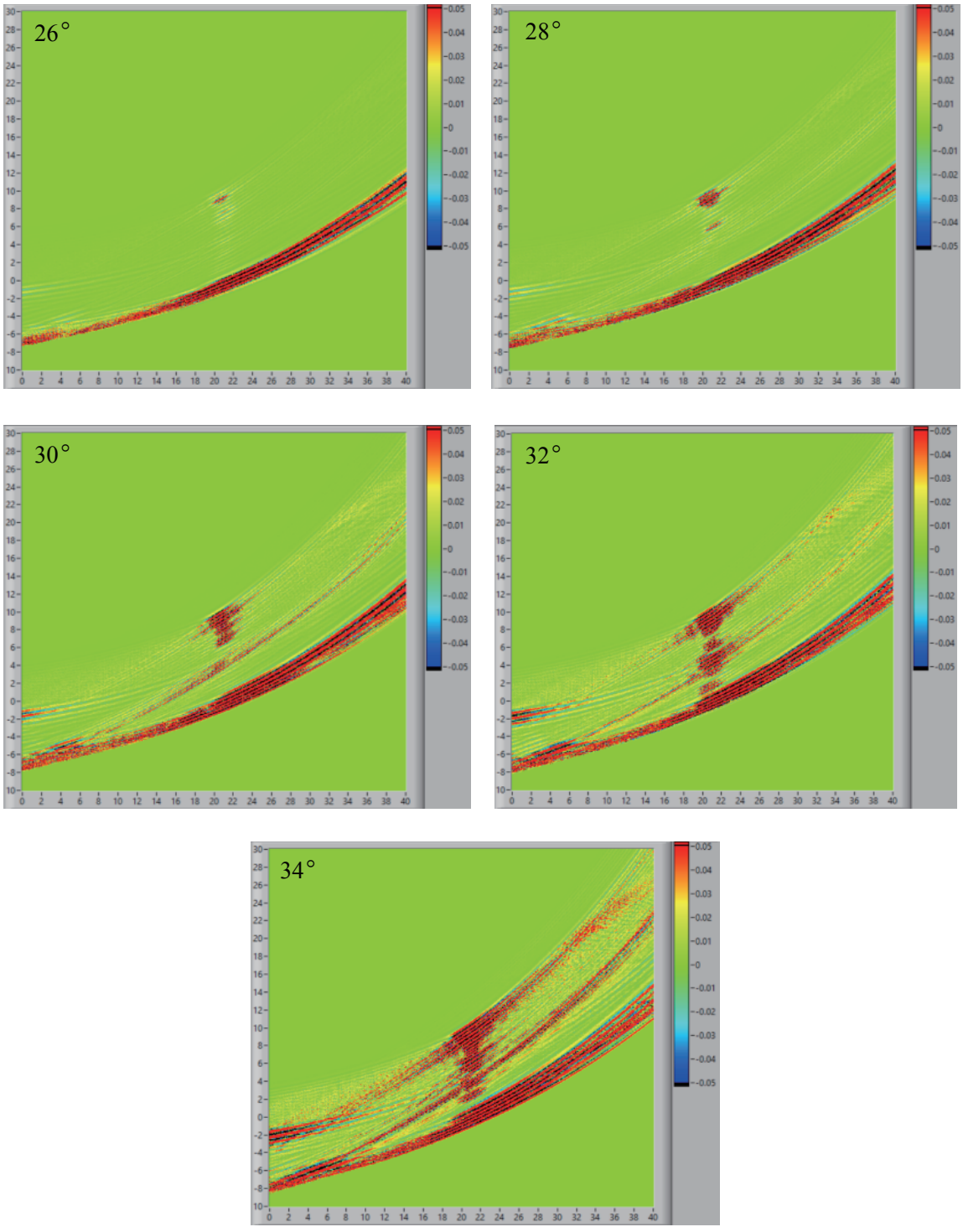

Fig. 6.10 Nonlinear imaging results using the displacement data in the *x*-direction for the closed crack at the incident angles of 26°, 28°, 30°, 32°, and 34°.

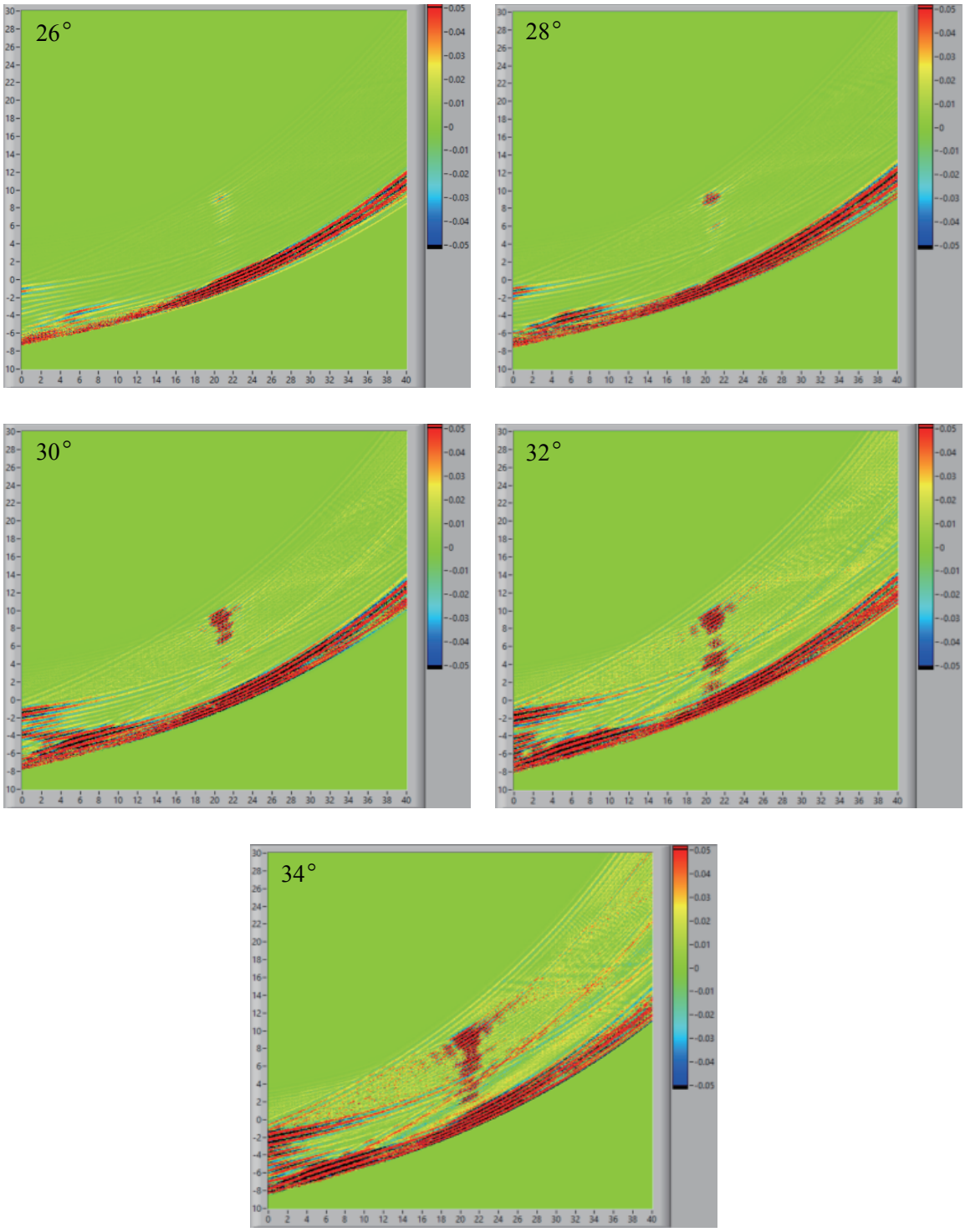

Fig. 6.11 Nonlinear imaging results using the displacement data in the *y*-direction for the closed crack at the incident angles of 26°, 28°, 30°, 32°, and 34°.

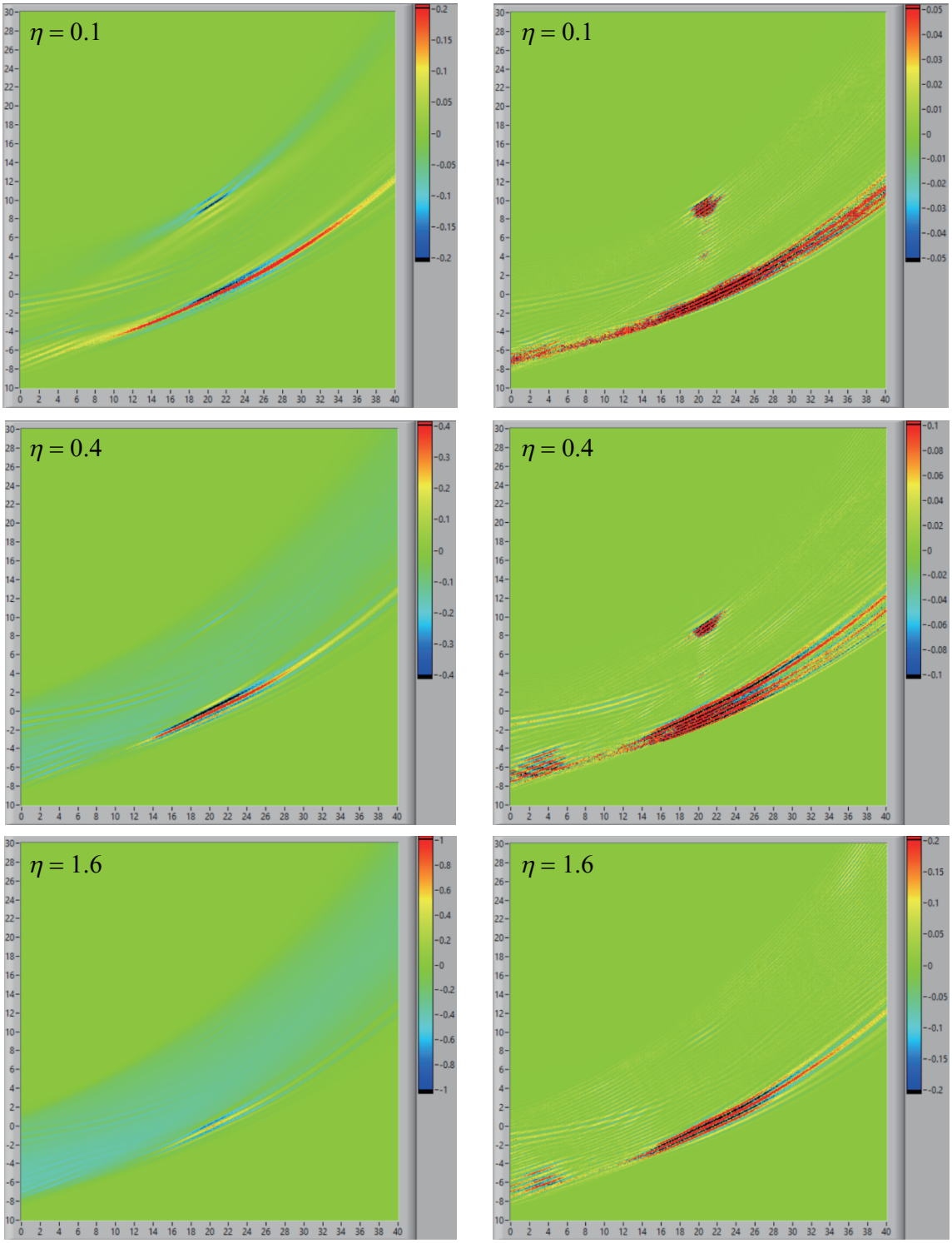

(a) Linear ultrasonic imaging.

(b) Nonlinear ultrasonic imaging.

Fig. 6.12 Linear and nonlinear imaging results for the closed crack in the case of $\eta = 0.1$, 0.4, and 1.6. These shapes were reconstructed by the displacement in the x-direction when five incident angles 26°, 28°, 30°, 32°, and 34° were used.

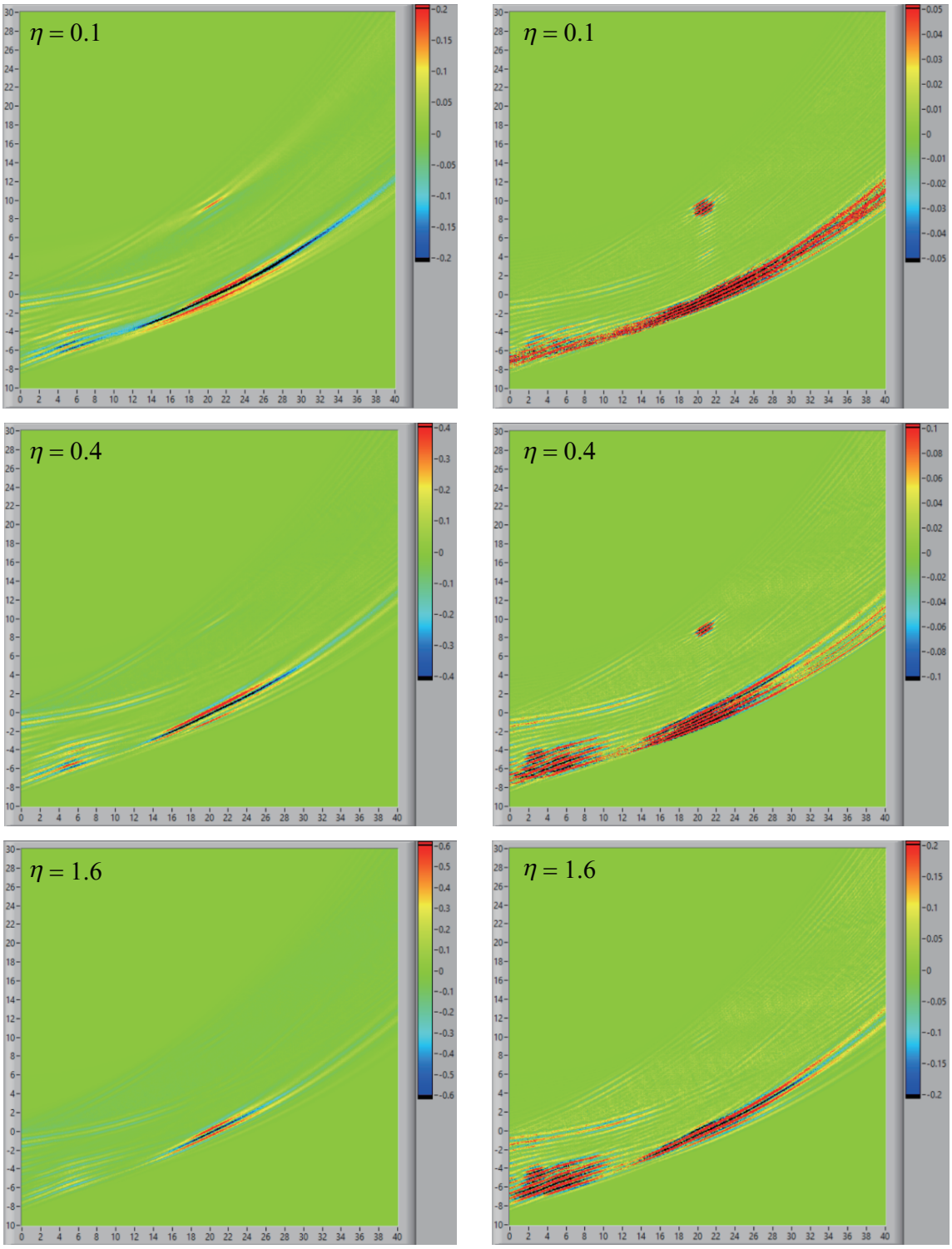

(a) Linear ultrasonic imaging. (b) Nonlinear ultrasonic imaging.

Fig. 6.13 Linear and nonlinear imaging results for the closed crack in the case of $\eta = 0.1$, 0.4, and 1.6. These shapes were reconstructed by the displacement in the y-direction when five incident angles 26°, 28°, 30°, 32°, and 34° were used.

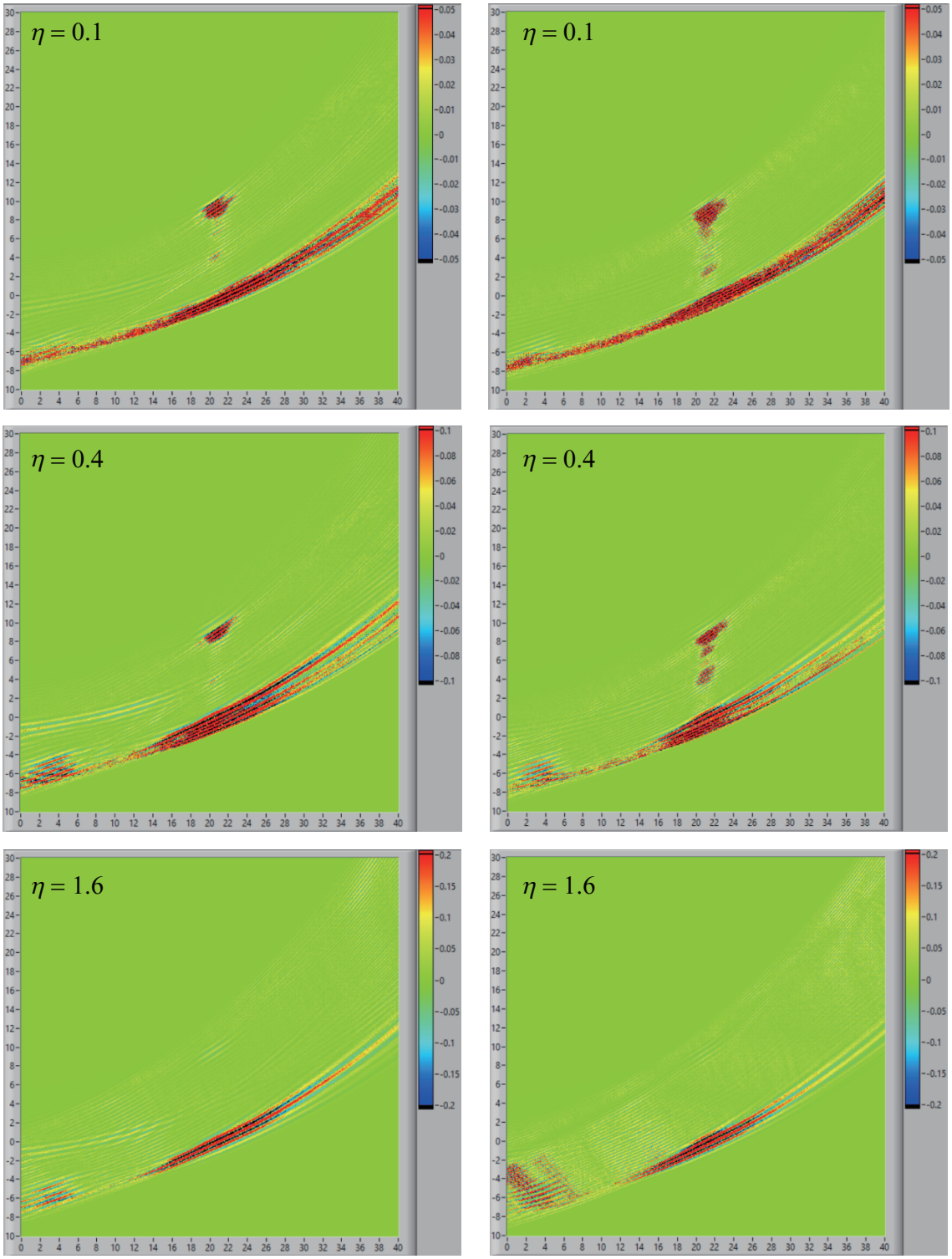

(a) 5MHz 4-cycle (b) 6MHz 6-cycle

Fig. 6.14 Nonlinear imaging results for the closed crack with incident wave of 5 MHz 4-cycle and 6 MHz 6-cycle in the case of η = 0.1, 0.4, and 1.6. The displacement data in the *x*-direction and five incident angles 26°, 28°, 30°, 32°, and 34° were used.

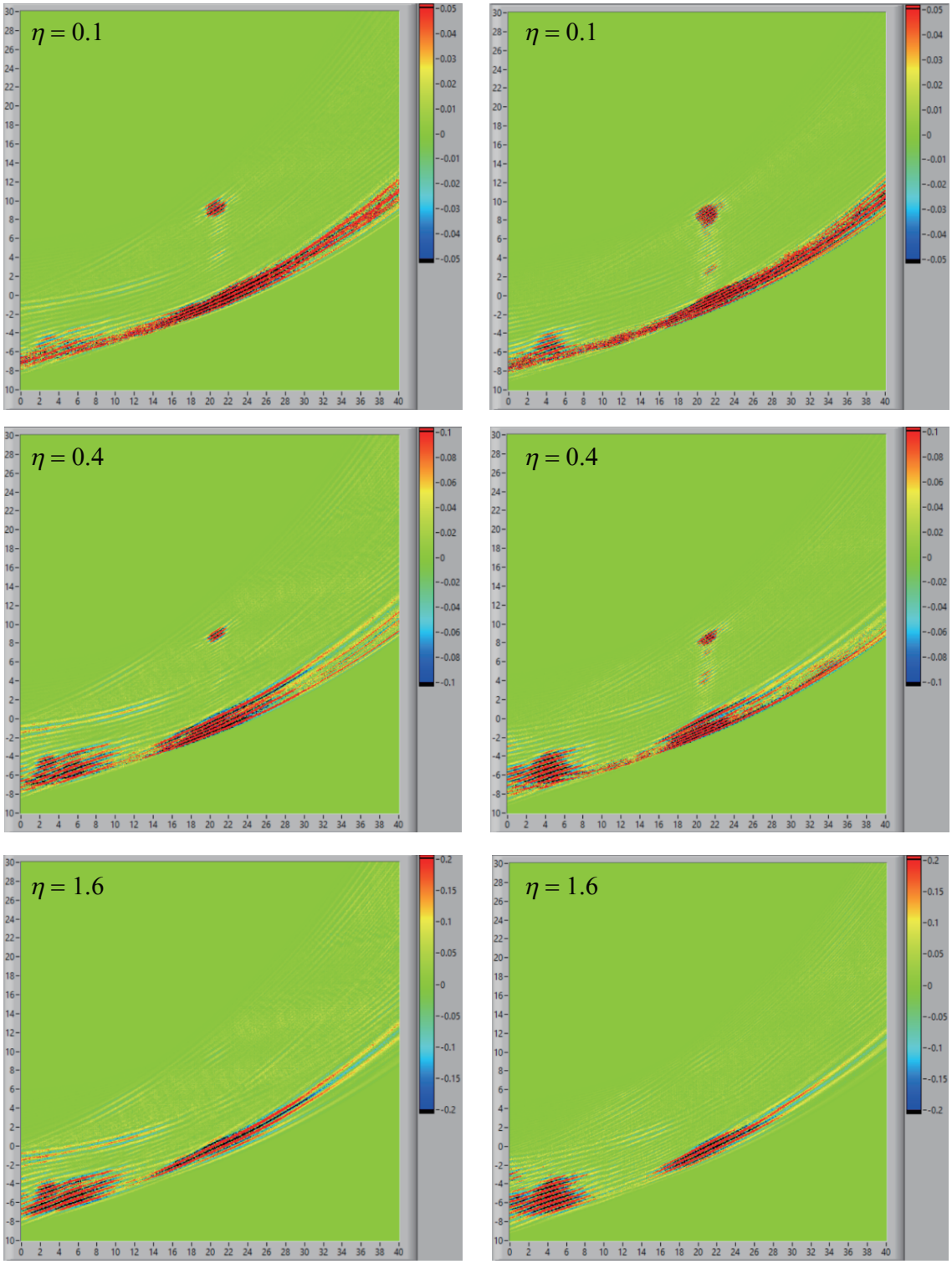

(a) 5MHz 4-cycle (b) 6MHz 6-cycle

Fig. 6.15 Nonlinear imaging results for the closed crack with incident wave of 5 MHz 4-cycle and 6 MHz 6-cycle in the case of η = 0.1, 0.4, and 1.6. The displacement data in the *y*-direction and five incident angles 26°, 28°, 30°, 32°, and 34° were used.

(5) Summary

The linear and nonlinear ultrasonic imaging by the all element firing FSAP using a phased array transducer were described with illustrations in this chapter. The FSAP is based on the post-processing beam-forming technique and checked with the scattered wave calculated by the 2-D EFIT. The beams with various steering directions were generated by the phased array transducer. The beam direction was controlled through a delay which served as the excitation timing of an element.

A linear ultrasonic imaging was successfully demonstrated and the tip of the slit was reconstructed. However, the linear ultrasonic imaging can show the closed crack when the compressive pressure applied to the crack face was small than the incident stress amplitude ($P_0 = \sigma_0/10$). In the nonlinear ultrasonic imaging, the second harmonic component was extracted from the raw ultrasonic signals using bandpass filter. From the nonlinear ultrasonic imaging, the face of the closed crack can be clearly observed for both case $\eta = 0.1$ and 0.4. However, there is no shape of the closed crack in the imaging result for $\eta = 1.6$ because the crack faces were always in the contact state.

It was found that the incident wave with high frequency and multiple cycle numbers was effective for the nonlinear ultrasonic imaging. The reason for this occurrence was that the incident wave became a narrow frequency band due to the multiple cycle numbers, and then the second harmonic component was generated intensively in the pass band. Also the beam directivity was enhanced by the high frequency transmission. Furthermore, the angle of the transmission should also be taken into account in the phased array UT.

7 CONCLUSIONS

The modeling of the nonlinear ultrasonic method based on the contact acoustic nonlinearity (CAN) and its verification by the numerical simulation and validation by the experimental measurement were described in this dissertation. The nonlinear ultrasonic method can be applied to the evaluation of the closed crack subjected to compressive pressure. Here, the harmonic generated from the clapping between the crack faces by the incident wave with large stress amplitude was investigated. The result obtained in each chapter was summarized as below.

In Chapter **2**, the conceptual model of the dynamic behavior of the contact and non-contact at the crack interface was described which is termed as CAN. The interaction of the compressive pressure on the interface and the tensile stress by the incident wave causes the intermittent separation state of the interface. After that, the interface contacts due to the compressive pressure acting on the interface. Here, the mechanical model of the CAN and the analytical solution of the interfacial displacement were described according to the Richardson's work.

In Chapter **3**, the dynamic behavior at the crack interface was modeled with one-dimensional (1-D) elastodynamic finite integration technique (EFIT). In the modeling, a set of split nodes was used to express the separation state at the interface. To investigate the accuracy of the numerical model, the numerical solution was compared with the analytical solution by Richardson. The numerical results were in good agreement with the analytical solutions while maintaining computational stability.

In Chapter **4**, the experimental work to measure the harmonics from an interface between polymethylmethacrylate (PMMA) was performed to validate the 1-D interfacial model by the EFIT. The wave penetrating through the interface showed a sawtooth waveform in the displacement. In the 1-D simulation, it was found that the tilt angle of the sawtooth wave was

in close association with the compressive pressure acting on the interface. The generation of the sawtooth wave was validated through an experimental measurement using a laser doppler vibrometer (LDV). The generation of the sawtooth wave was observed by using a large input voltage. The generation of the sawtooth wave leaded to the increase of the second harmonic component.

In Chapter **5**, the two-dimensional simulations with the EFIT were performed to investigate the generation of harmonics from the closed crack in the case of a phased array ultrasonic testing. The subsurface crack was located at the bottom of the model, and then the ultrasonic wave was generated from the array transducer. The characteristics of the second harmonic generation wereinvestigated by varying the incident angle. Here, the closed crack with a height of 5, 10, 15, and 20 mm were prepared and the scattered waves were calculated. From the simulation results, the second harmonic component was generated the most at 30° incident angle. It was found that the second harmonic component increased as the closed crack lengthened and incident stress amplitude was gained.

In Chapter **6**, the full waveforms sampling and processing (FSAP) method was applied to the imaging of the closed crack using a phased array transducer. Since the closed crack is difficult to detect by a linear ultrasonic testing, the second harmonic component extracted from the raw ultrasonic signal was used to reconstruct the shape of the closed crack. From the simulation result, the image of the closed crack can be clearly reconstructed by using second harmonic component. The incident angle should be chosen adequately to enhance the tensile stress in the direction perpendicular to the crack face. The incident wave with high frequency and multiple cycle numbers was effective for the nonlinear ultrasonic imaging.

As for future works, the numerical model will be improved by considering the effect of the interfacial roughness and friction. Also, we will apply this model to the three-dimensional simulation. Furthermore, we will develop the imaging system of the closed crack with the FSAP.

REFERENCES

[1] Achenbach, J.D.: Quantitative nondestructive evaluation, *International Journal of Solids and Structures*, Vol.37, No.1-2, pp.13–27, 2000.

[2] Datta, S.K., Achenbach, J.D. and Rajapakse, Y.S.: Elastic waves and ultrasonic nondestructive evaluation, North-Holland, ISBN-978-0444874856, 1990.

[3] Willems, H. and Goebbels, K.: Characterization of microstructure by backscattered ultrasonic waves, *Metal Science*, Vol.15, pp.549–553, 1981.

[4] Achenbach, J.D., Adler, L., Lewis, D.K. and McMaken, H.: Diffraction of ultrasonic waves by penny-shaped cracks in metals: theory and experiment, *The Journal of the Acoustical Society of America*, Vol.66, No.6, pp.1848–1856, 1979.

[5] Silk, M.G.: Defect detection and sizing in metals using ultrasound, *International Materials Reviews*, No.1, pp.28–50, 1982.

[6] Chirnenti, D.E.: Guided waves in plates and their use in materials characterization. *Applied Mechanics Reviews*, Vol.50, No.5, 247, 1997.

[7] Bifulco, F. and Sachse, W.: Ultrasonic pulse spectroscopy of a solid inclusion in an elastic solid, *Ultrasonics*, Vol.13, No.3, pp.113–116, 1975.

[8] Ibrahim, A., Zabri, A. and Nakahata, K.: Identification of elastic parameters of an inclusion by a particle filter using ultrasonic waves, *International Journal of Mechanical and Materials Engineering*, Vol.10, No.1, pp.1–7, 2015.

[9] Solodov, I.Y.: Ultrasonics of non-linear contacts: propagation, reflection and NDE-applications, *Ultrasonics*, Vol.36, No.1, pp.383–390, 1998.

[10] Solodov, I.Y. and Korshak, B.A.: Instability, chaos, and memory in acoustic-wave crack interaction, *Physical Review Letters*, Vol.88, No.1, p.014303, 2001.

[11] Solodov, I.Y., Krohn, N. and Busse, G.: CAN: an example of nonclassical acoustic nonlinearity in solids, *Ultrasonics*, Vol.40, No.1, pp.621–625, 2002.

[12] Donskoy, D., Sutin, A. and Ekimov, A.: Nonlinear acoustic interaction on contact interfaces and its use for nondestructive testing, *NDT & E International*, Vol.34, No.4, pp.231–238, 2001.

[13] Shui, Y. and Solodov, I.Y.: Nonlinear properties of Rayleigh and stoneley waves in solids, *Journal of Applied Physics*, Vol.64, No.11, pp.6155–6165, 1988.

[14] Shull, D.J., Hamilton, M.F., Il'insky, Y.A. and Zabolotskaya, E.A.: Harmonic generation in plane and cylindrical nonlinear Rayleigh waves, *The Journal of the Acoustical Society of America*, Vol.94, No.1, pp.418–427, 1993.

[15] Jeremiah J. Rushchitsky, Nonlinear Elastic Waves in Materials, Springer, ISBN 978-3319004631, 2014.

[16] Solodov, I.Y.: Nonlinear NDE using contact acoustic nonlinearity (CAN), *In Ultrasonics Symposium, IEEE Proceedings*, Vol.2, pp.1279–1283, 1994.

[17] Severin, F.M., Solodov, I.Y. and Shkulanov, Y.N.: Experimental observation of sound nonlinearity in the reflection from an interface between solids, *Moscow University Physics Bulletin*, Springer, Vol.43, pp.105–107, 1988.

[18] Len, K.S., Severin, F.M., Solodov, I. and Wood, J.: Experimental observation of the influence of contact nonlinearity on the reflection of bulk acoustic waves and the propagation of surface acoustic waves, *Soviet Physics Acoustics*, Vol.37, No.6, pp.610–612, 1991.

[19] Richardson, J.M.: Harmonic generation at an unbonded interface-I. planar interface between semi-infinite elastic media, *International Journal of Engineering Science*, Vol.17, No.1, pp.73–85, 1979.

[20] Buck, O., Morris, W. L. and Richardson, J. M.: Acoustic harmonic generation at unbonded interfaces and fatigue cracks, *Applied Physics Letters*, Vol.33, No.5, pp.371–373, 1978.

[21] Nagy, P. B.: Fatigue damage assessment by nonlinear ultrasonic materials characterization, *Ultrasonics*, Vol.36, No.1, pp.375–381, 1998.

[22] Cantrell, J. H. and Yost, W. T.: Nonlinear ultrasonic characterization of fatigue microstructures, *International Journal of Fatigue*, Vol.23, pp.487–490, 2001.

[23] Ohara, Y. and Kawashima, K.: Detection of internal micro defects by nonlinear resonant ultrasonic method using water immersion, *Japanese Journal of Applied Physics*, Vol.43, No.5B, pp.3119–3120, 2004.

[24] Mendelsohn, D.A. and Doong, J.M.: Transient dynamic elastic frictional contact: a general 2D boundary element formulation with examples of SH motion, *Wave Motion*, Vol.11, No.1, pp.1–21, 1989.

[25] Hirose, S.: 2-D scattering by a crack with contact-boundary conditions, *Wave Motion*, Vol.19, No.1, pp.37–49, 1994.

[26] Hirose, S. and Achenbach, J.D.: Higher harmonics in the far field due to dynamic crack- face contacting, *The Journal of the Acoustical Society of America*, Vol.93, No.1, pp.142–147, 1993.

[27] Nakahata, K. and Hirose, S.: Simulation of non-linear ultrasonic wave through an interface including imperfections, *Review of Progress in Quantitative Nondestructive Evaluation*, Vol.25A, No.25, pp.270–276, 2005.

[28] Saitoh, T., Nakahata, K. and Hirose, S.: Improved time-domain BEM analysis for a solid-solid interface with contact boundary conditions, *Theoretical and Applied Mechanics Japan*, Vol.58, pp.9–17, 2010.

[29] Hirose, S. and Saitoh, T.: Numerical simulation of nonlinear ultrasonic waves due to bi-material interface contact. *In Journal of Physics: Conference Series, IOP Publishing*, Vol.520, No.1, 012007, 2014.

[30] Yamawaki, H.: 1-dimensional analysis of ultrasound at closed interface of solid,*In Journal of Physics: Conference Series, IOP Publishing*, Vol.520, No.1, 012020, 2014.

[31] Kim, K.C., Jhang, K.Y., Yamawaki, H. and Saito, T.: Finite difference method analysis of ultrasonic nonlinearity in partially degraded material, *JSME International Journal Series A*, Vol.44, No.3, pp.390–395, 2001.

[32] Sugawara, A., Jinno, K., Ohara, Y. and Yamanaka, K.: Closed-crack imaging and scattering behavior analysis using confocal subharmonic phased array, *Japanese Journal of Applied Physics*, Vol.54, 07HC08, 2015.

[33] Jinno, K., Sugawara, A., Ohara, Y. and Yamanaka, K.: Analysis on nonlinear ultrasonic images of vertical closed cracks by damped double node model, *Materials Transactions*, Vol.55, No.7, pp.1017–1023, 2014.

[34] Kimoto, K. and Ichikawa, Y.: A finite difference method for elastic wave scattering by a planar crack with contacting faces, *Wave Motion*, Vol.52, pp.120–137, 2015.

[35] Kawashima, K., Omote, R., Ito, T., Fujita, H. and Shima, T.: Nonlinear acoustic response through minute surface cracks: FEM simulation and experimentation, *Ultrasonics*, Vol.40, No.1, pp.611–615, 2002.

[36] Hirata, S. and Sugiura, T.: Detection of a closed crack by nonlinear acoustics using ultrasonic transducers, *In Quantitative Nondestructive Evaluation, AIP Publishing*, Vol.820, No.1, pp.277–282, 2006.

[37] Shen, Y. and Giurgiutiu, V.: Predictive simulation of nonlinear ultrasonics, *In SPIE Smart Structures and Materials Nondestructive Evaluation and Health Monitoring, International Society for Optics and Photonics*, 83482E, 2012.

[38] Blanloeuil, P., Meziane, A. and Bacon, C.: Numerical study of nonlinear interaction between a crack and elastic waves under an oblique incidence, *Wave Motion*, Vol.51, No.3, pp.425–437, 2014.

[39] Hong, M., Su, Z., Wang, Q., Cheng, L. and Qing, X.: Modeling nonlinearities of ultrasonic waves for fatigue damage characterization: Theory, simulation, and experimental validation, *Ultrasonics*, Vol.54, No.3, pp.770–778, 2014.

[40] Fellinger, P., Marklein, R., Langenberg, K. J. and Klaholz, S.: Numerical modeling of elastic wave propagation and scattering with EFIT-elastodynamic finite integration technique, *Wave Motion*, Vol.21, No.1, pp.47–66, 1995.

[41] Schubert, F.: Numerical time-domain modeling of linear and nonlinear ultrasonic wave propagation using finite integration techniques-theory and applications, *Ultrasonics*, Vol.42, No.1, pp.221–229, 2004.

[42] Marklein, R., Langenberg, K.J., Bärmann, R. and Brandfass, M.: Ultrasonic and electromagnetic wave propagation and inverse scattering applied to concrete, *Review of Progress in Quantitative Nondestructive Evaluation*, Vol.15B, pp.1839–1846, 1996.

[43] Schubert, F. and Köhler, B.: Three-dimensional time domain modeling of ultrasonic wave propagation in concrete in explicit consideration of aggregates and porosity, *Journal of Computational Acoustics*, Vol.9, No.4, pp.1543–1560, 2001.

[44] Schubert, F. and Marklein, R.: Numerical computation of ultrasonic wave propagation in concrete using the elastodynamic finite integration technique (EFIT), *In Ultrasonics Symposium, IEEE Proceedings*, Vol.1, pp.799–804, 2002.

[45] Nakahata, K., Tokunaga, J., Kimoto, K. and Hirose, S.: A large scale simulation of ultrasonic wave propagation in concrete using parallelized EFIT, *Journal of Solid Mechanics and Materials Engineering*, Vol.2, No.11, pp.1462–1469, 2008.

[46] Nakahata, K., Kawamura, G., Yano, T. and Hirose, S.: Three-dimensional numerical modeling of ultrasonic wave propagation in concrete and its experimental validation, *Construction and Building Materials*, Vol.78, pp.217–223, 2015.

[47] Nakahata, K., Hirose, S., Schubert, F. and Köehler, B.: Image based EFIT simulation for nondestructive ultrasonic testing of austenitic steel, *Journal of Solid Mechanics and Materials Engineering*, Vol.3, No.12, pp.1256-1262, 2009

[48] Nakahata, K., Schubert, F., Köhler, B.: 3-D image-based simulation for ultrasonicwave propagation in heterogeneous and anisotropic materials, *In Quantitative Nondestructive Evaluation, AIP Publishing*, Vol.1335, No.1, pp.51–58, 2011.

[49] Nakahata, K., Terada, K., Kyoya, T., Tsukino, M. and Ishii, K.: Simulation of ultrasonic and electromagnetic wave propagation for nondestructive testing of concrete using image-based FIT, *Journal of Computational Science and Technology*, Vol.6, No.1, pp.28-37, 2012.

[50] Gauster, W.B. and Breazeale, M.A.: Ultrasonic measurement of the nonlinearity parameters of copper single crystals, *Physical Review*, Vol.168, No.3, pp.655–661, 1968.

[51] Cantrell, J.H. and Salama, K.: Acoustoelastic characterisation of materials, *International Materials Reviews*, Vol.36, No.1, pp.125–145,1991.

[52] Yost, W.T. and Cantrell, J.H.: Absolute ultrasonic displacement amplitude measurements with a submersible electrostatic acoustic transducer, *Review of Scientific Instruments*, Vol.63, No.9, pp.4182–4188, 1992.

[53] Biwa, S., Nakajima, S. and Ohno, N.: On the acoustic nonlinearity of solid-solid contact with pressure-dependent interface stiffness, *Journal of Applied Mechanics*, Vol.71, No.4, pp.508–515, 2004.

[54] Suzuki, A., Biwa, S. and Ohno, N.: Numerical and experimental evaluation of ultrasonic wave propagation characteristics at contact interface, *JSME International Journal Series A Solid Mechanics and Material Engineering*, Vol.48, No.1, pp.20–26, 2005.

[55] Yan, D., Drinkwater, B.W. and Neild, S.A.: Measurement of the ultrasonic nonlinearity of kissing bonds in adhesive joints, *NDT & E International*, Vol.42, No.5, pp.459–466, 2009.

[56] Solodov, I., Döring, D. and Busse, G.: New opportunities for NDT using non-linear interaction of elastic waves with defects, *Strojniški Vestnik-Journal of Mechanical Engineering*, Vol.57, No.3, pp.169–182, 2011.

[57] Ohara, Y., Mihara, T., Sasaki, R., Ogata, T., Yamamoto, S., Kishimoto, Y. and Yamanaka, K.: Imaging of closed cracks using nonlinear response of elastic waves at subharmonic frequency, *Applied Physics Letters*, Vo.90, No.1, 011902, 2007.

[58] Ohara, Y., Yamamoto, S., Mihara, T. and Yamanaka, K.: Ultrasonic evaluation of closed cracks using subharmonic phased array, *Japanese Journal of Applied Physics*, Vol.47, No.5S, 3908, 2008.

[59] Ohara, Y., Endo, H., Mihara, T. and Yamanaka, K.: Ultrasonic measurement of closed stress corrosion crack depth using subharmonic phased array, *Japanese Journal of Applied Physics*, Vol.48, No.7S, 07GD01, 2009.

[60] Christopher, T.: Experimental investigation of finite amplitude distortion-based, second harmonic pulse echo ultrasonic imaging, *IEEE Transactions on Ultrasonics, Ferroelectrics, and Frequency Control*, Vol.45, No.1, pp.158–162, 1998.

[61] Christopher, T.: Finite amplitude distortion-based inhomogeneous pulse echo ultrasonic imaging, *IEEE Transactions on Ultrasonics, Ferroelectrics, and Frequency Control*, Vol.44, No.1, pp.125–139, 1997.

[62] Humphrey, V.F.: Nonlinear propagation in ultrasonic fields: measurements, modelling and harmonic imaging, *Ultrasonics*, Vol.38, No.1, pp.267–272, 2000.

[63] Timoshenko, S.P. and Goodier, J.N.: Theory of elasticity, *MacGraw Hill International Book*, 1982.

[64] Marklein, R., Bärmann, R. and Langenberg, K.J.: The ultrasonic modeling code EFIT as applied to inhomogeneous dissipative isotropic and anisotropic media, *In Review of Progress in Quantitative Nondestructive Evaluation*, Vol.14, pp.251–258, 1995.

[65] Schubert, F. and Koehler, B.: Numerical modeling of elastic wave propagation in random particulate composites, *In Nondestructive Characterization of Materials VIII, Springer US*, pp.567–574,1998.

[66] Langenberg, K.J. and Marklein, R.: Transient elastic waves applied to nondestructive testing of transversely isotropic lossless materials: a coordinate-free approach, *Wave Motion*, Vol.41, No.3, pp.247–261, 2005.

[67] Courant, R., Friedrichs, K. and Lewy, H.: On the partial difference equations of mathematical physics, *IBM Journal*, Vol.11, No.2, pp.215–234, 1967.

[68] Takatsubo, J. and Imade, M.: Visualization of ultrasonic waves with laser application, *Transactions of Ultrasonic Technology (TECHNO)*, Vol.16, No.2, pp.15–19, 2004. (in Japanese)

[69] Nakahata, K., Hirata, M. and Hirose, S.: Flaw reconstruction from scattering amplitude using full-waveform sampling and processing (FSAP), *Journal of JSNDI*, Vol.59, No.6, pp.277–283, 2010. (in Japanese)

[70] Nakahata, K. and Horiguchi, T.: GPU accelerated 3-D ultrasonic flaw imaging using full waveforms sampling and processing technique, *Transactions of the JSME*, Vol.81, No.832, pp.1–14, 2015. (in Japanese)

Appendix A MODEL OF THE CLOSED CRACK

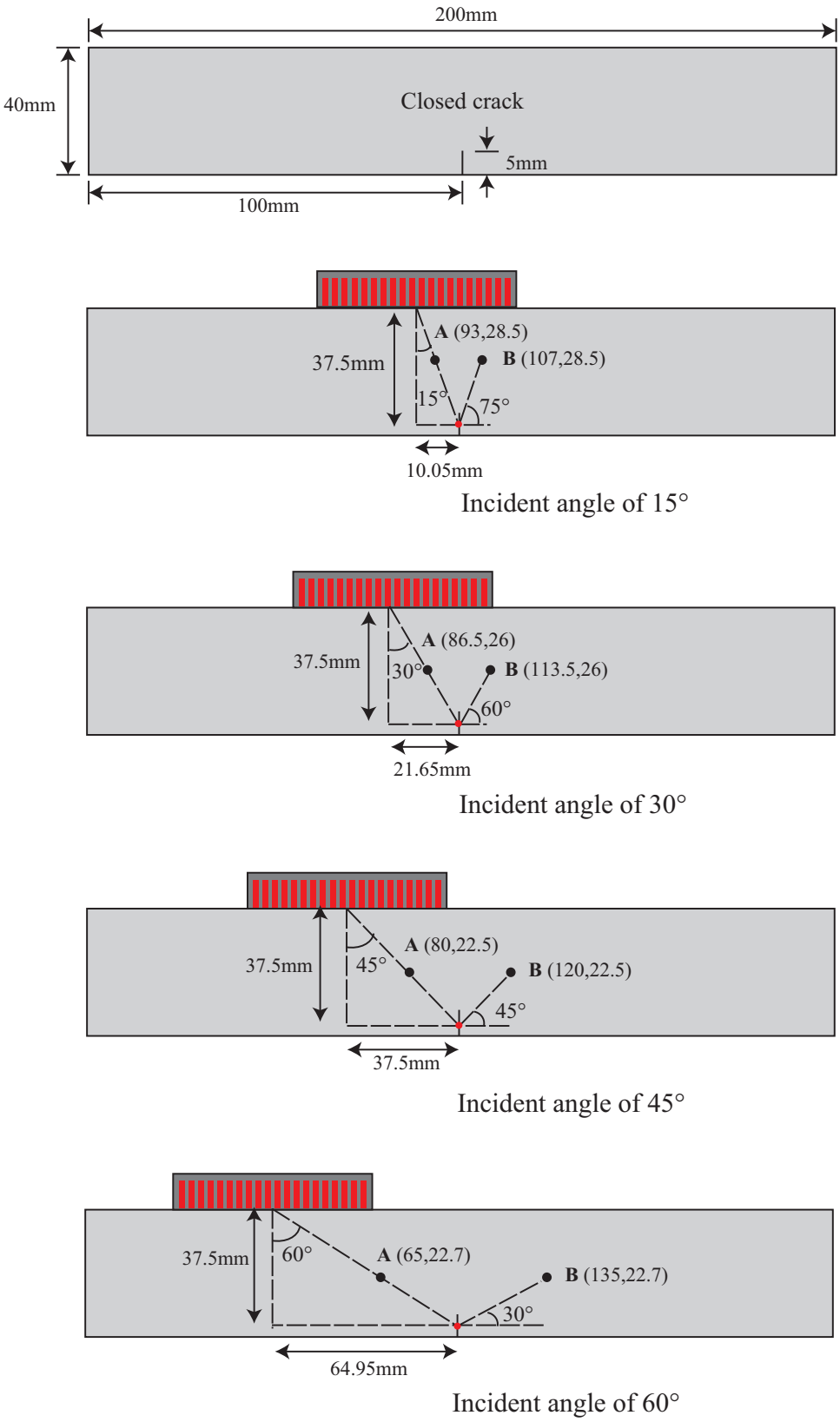

Fig. A.1 Model of the closed crack with a height of 5 mm.

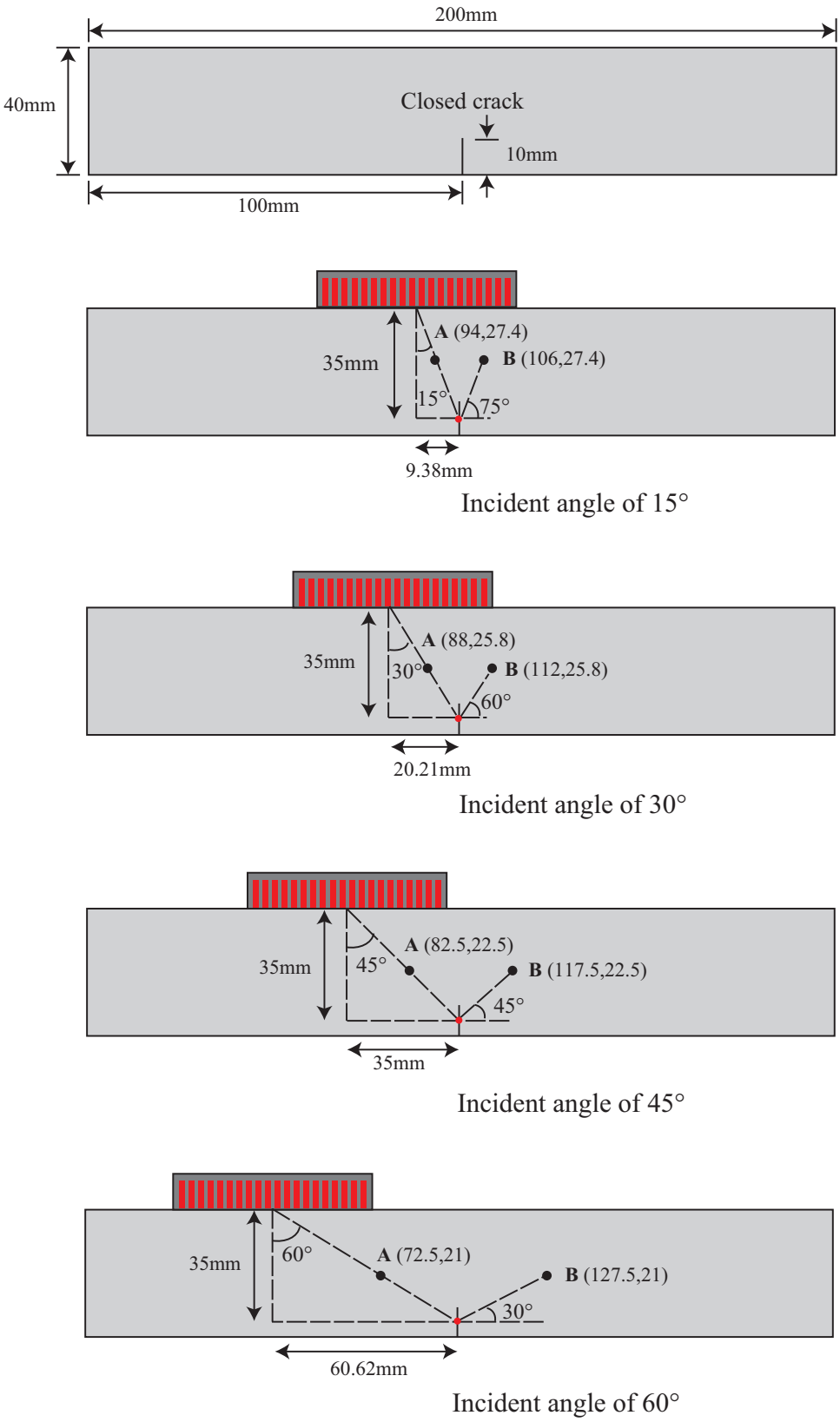

Fig. A.2 Model of the closed crack with a height of 10 mm.

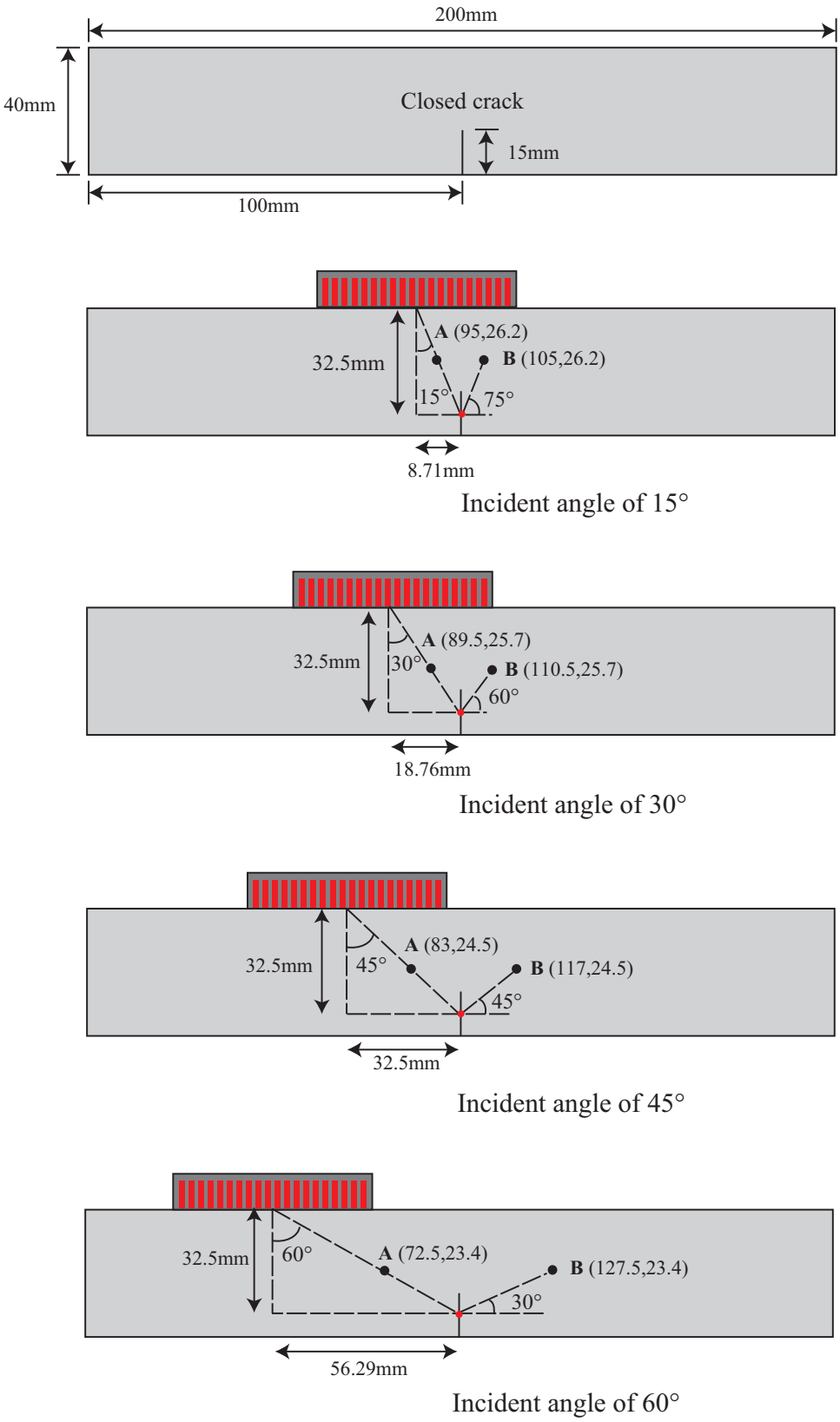

Fig. A.3 Model of the closed crack with a height of 15 mm.

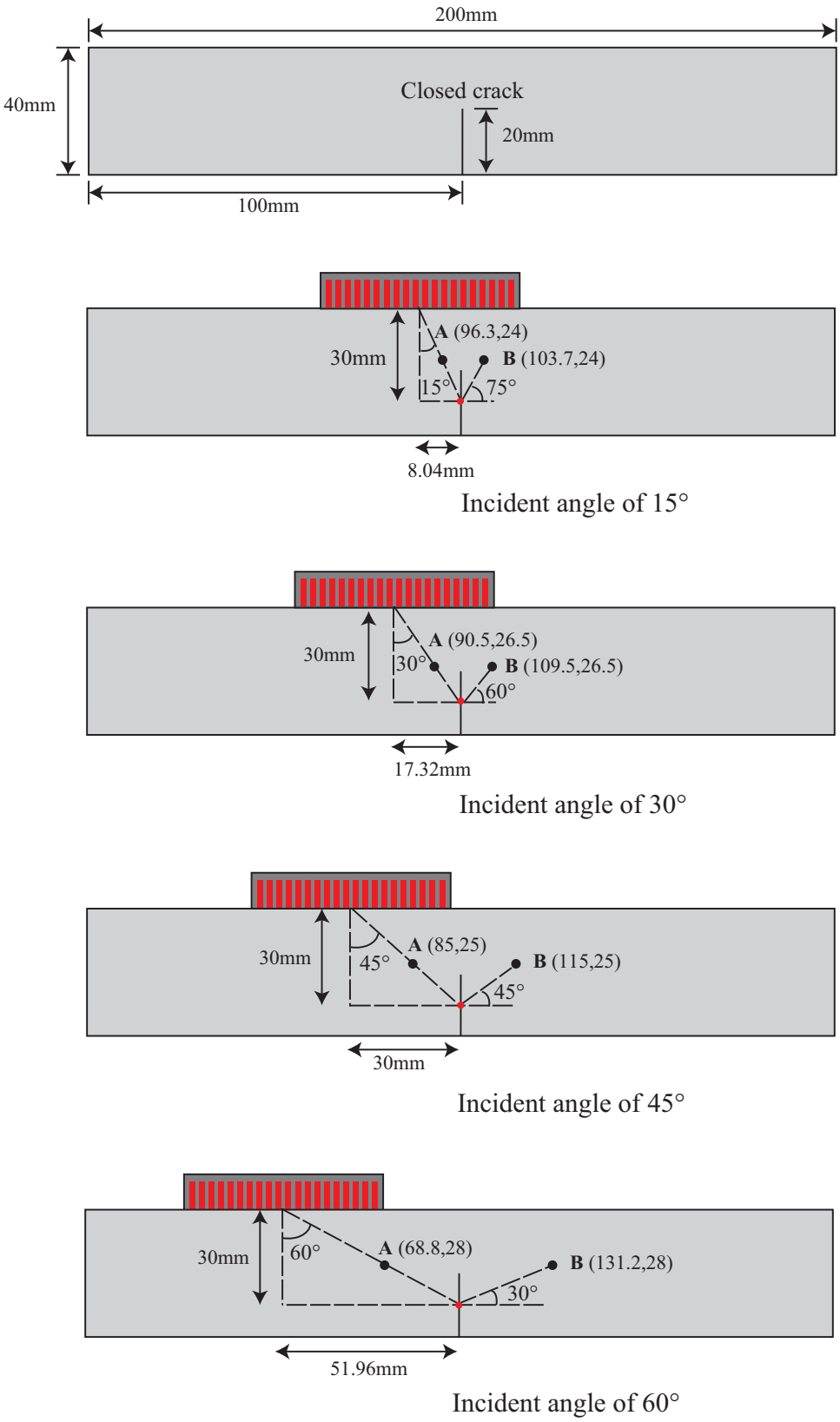

Fig. A.4 Model of the closed crack with a height of 20 mm.

Appendix B VISUALIZATION OF THE SCATTERED WAVE

(1) Visualization of the scattered wave propagation for the closed crack with a height of 5 mm.

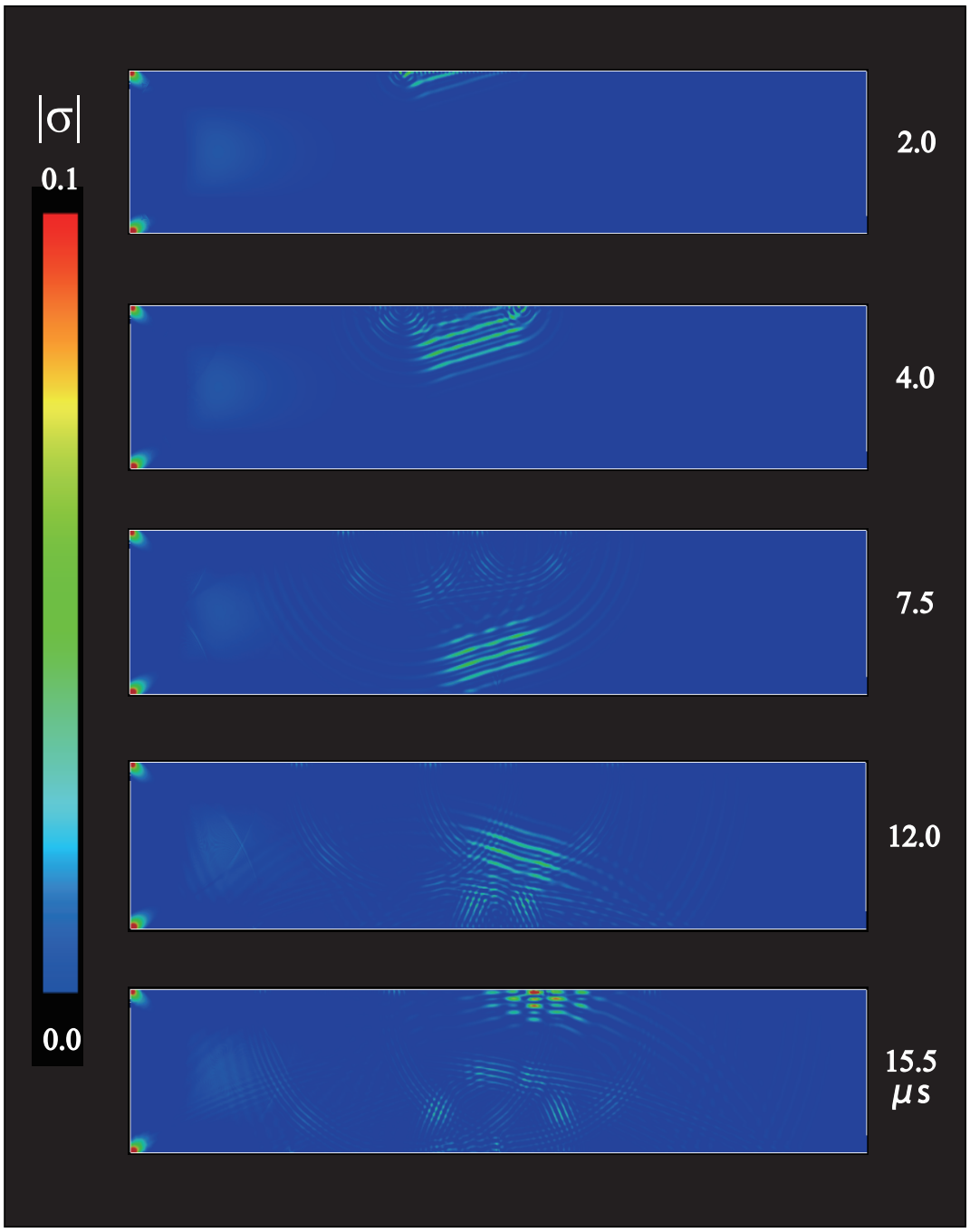

Fig. B.1 Visualization at the incident angle of 15° in the case of η = 1.6 for the closed crack with a height of 5 mm.

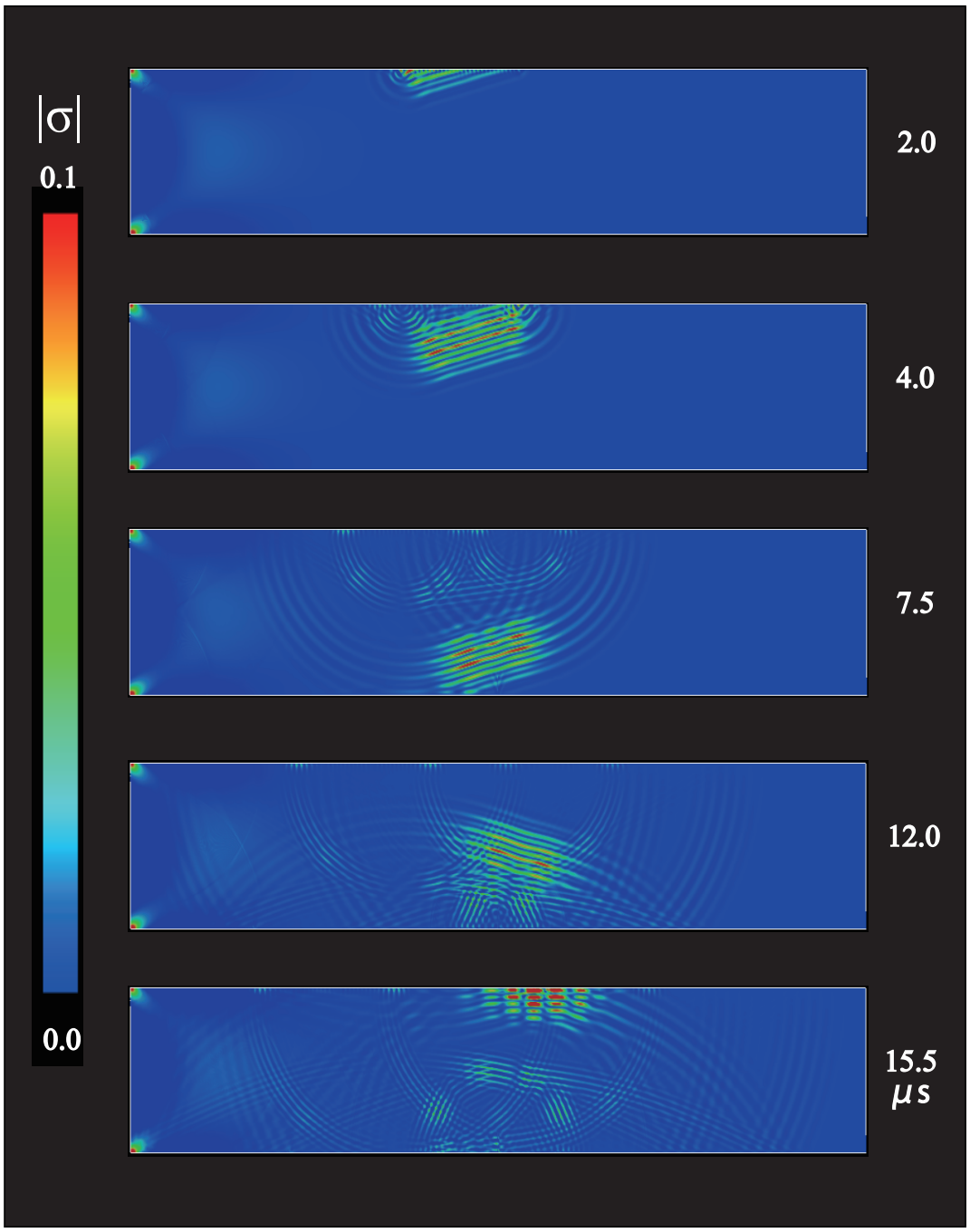

Fig. B.2 Visualization at the incident angle of 15° in the case of $\eta = 0.8$ for the closed crack with a height of 5 mm.

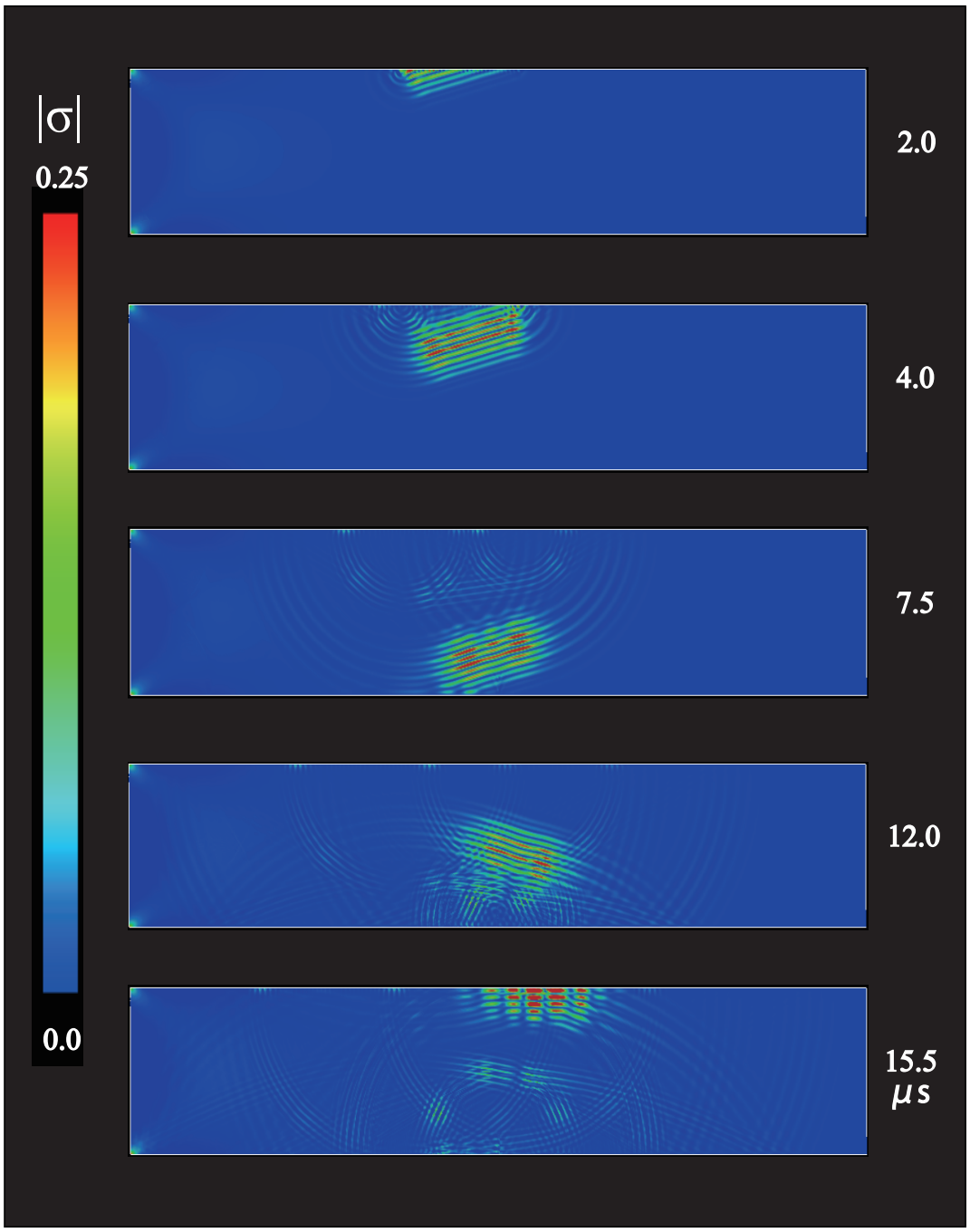

Fig. B.3 Visualization at the incident angle of 15° in the case of $\eta = 0.4$ for the closed crack with a height of 5 mm.

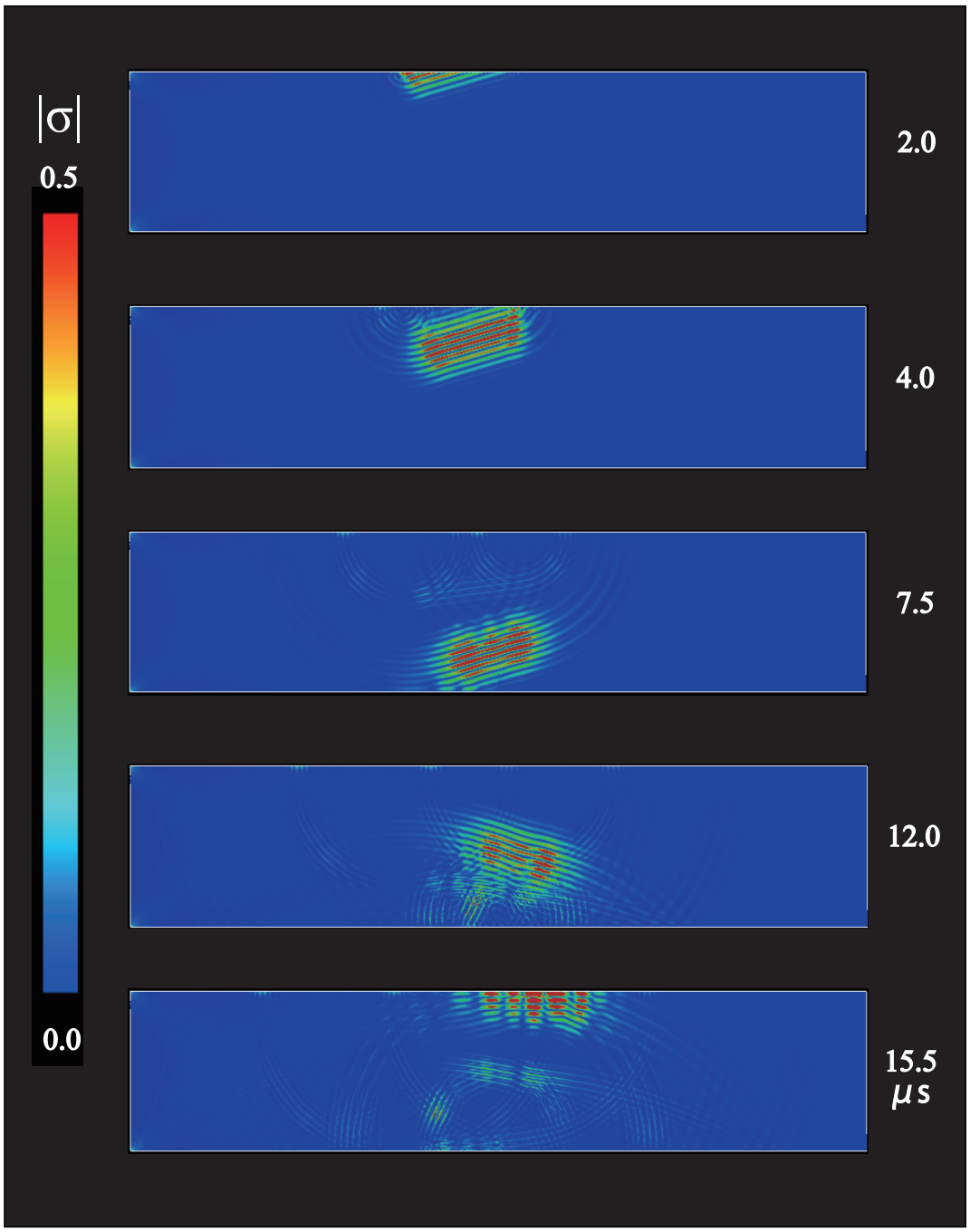

Fig. B.4 Visualization at the incident angle of 15° in the case of $\eta = 0.2$ for the closed crack with a height of 5 mm.

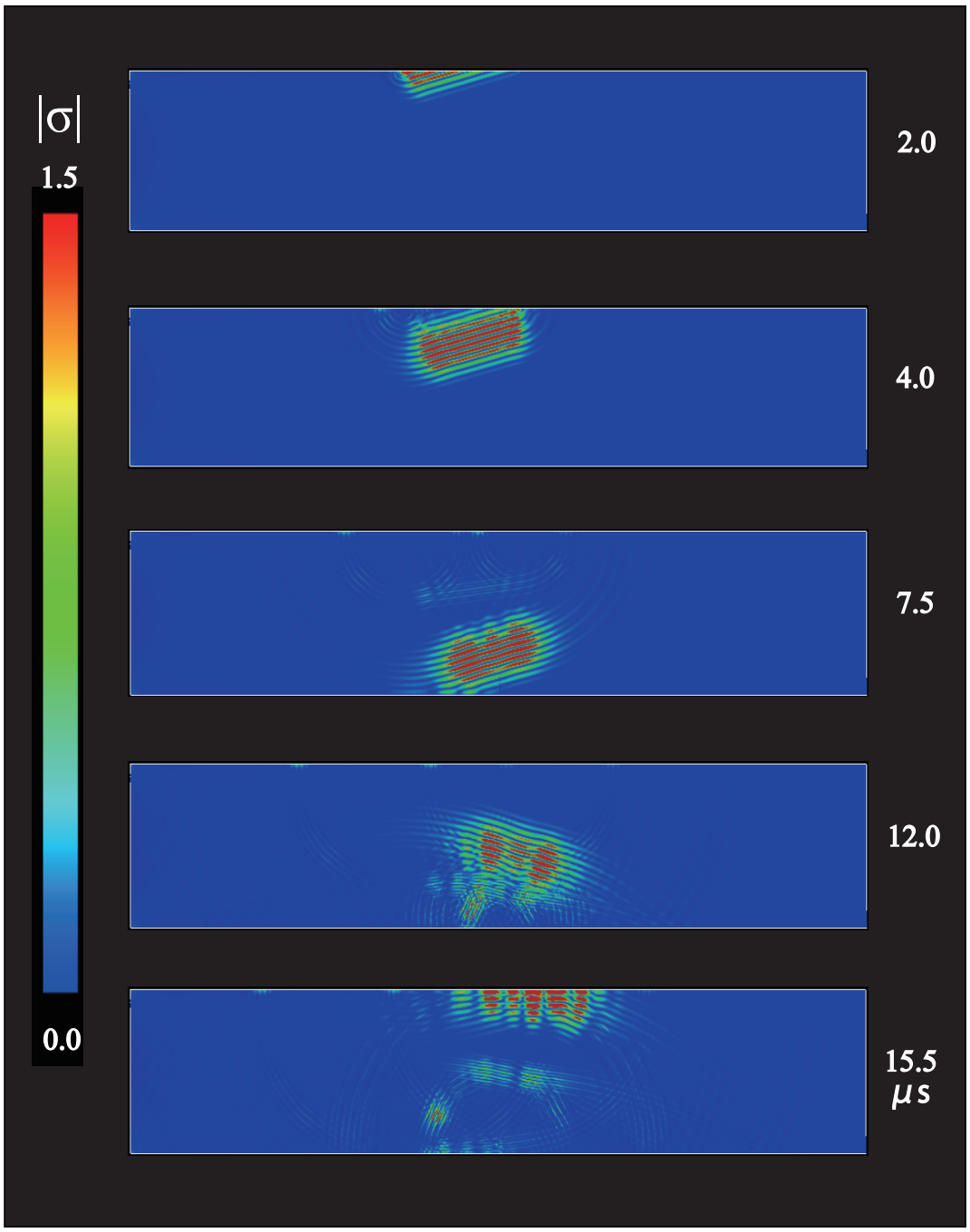

Fig. B.5 Visualization at the incident angle of 15° in the case of $\eta = 0.1$ for the closed crack with a height of 5 mm.

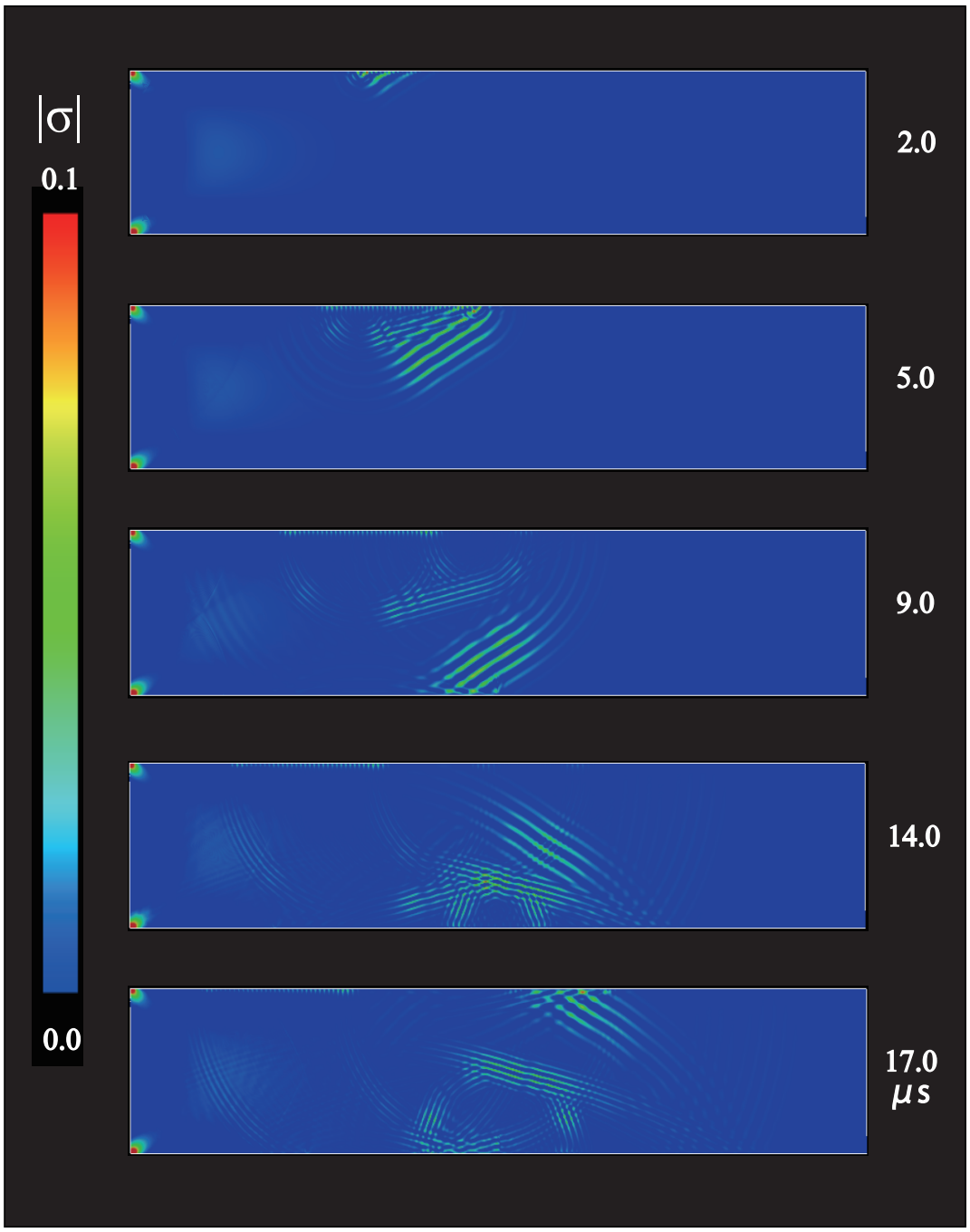

Fig. B.6 Visualization at the incident angle of 30° in the case of $\eta = 1.6$ for the closed crack with a height of 5 mm.

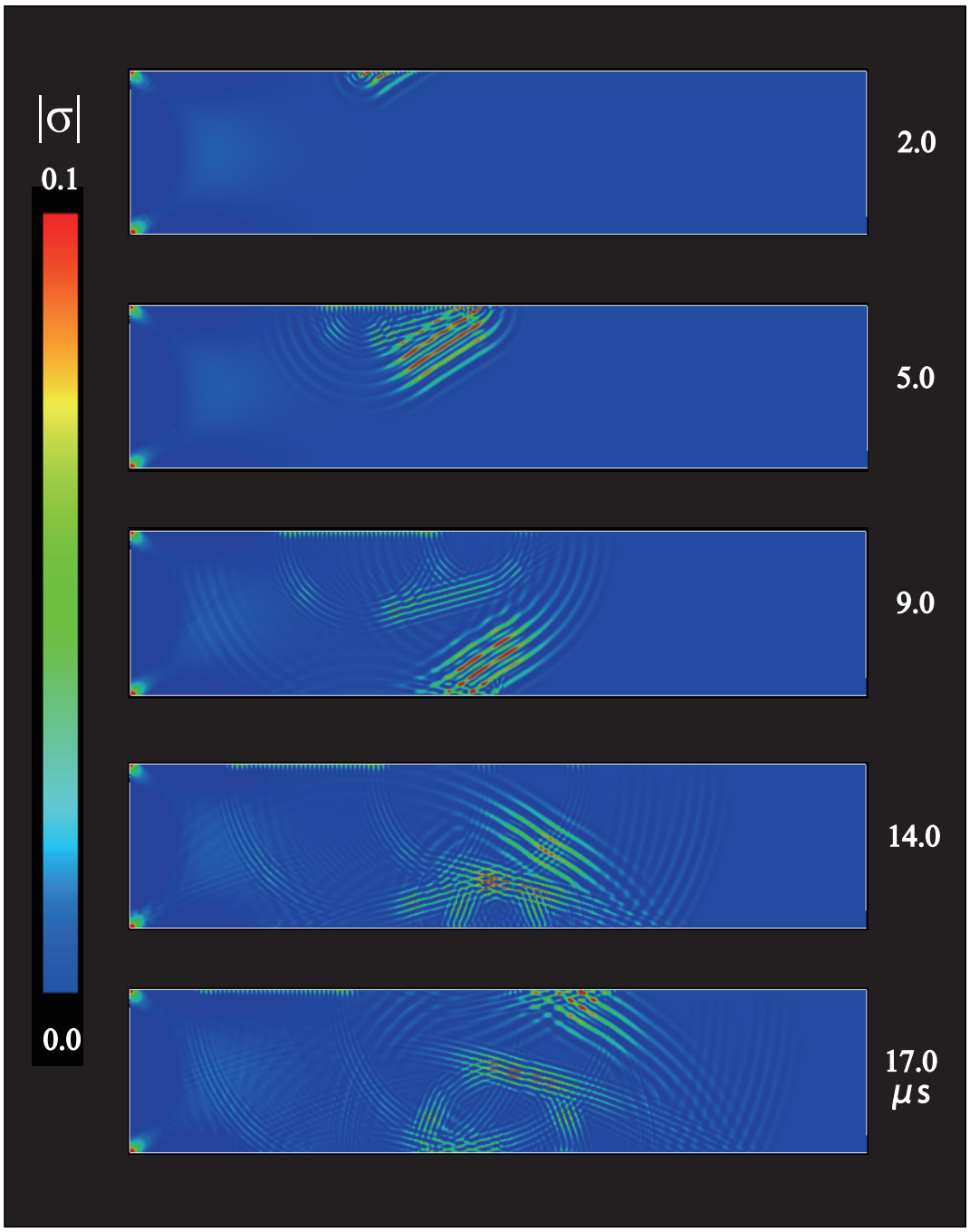

Fig. B.7 Visualization at the incident angle of 30° in the case of $\eta = 0.8$ for the closed crack with a height of 5 mm.

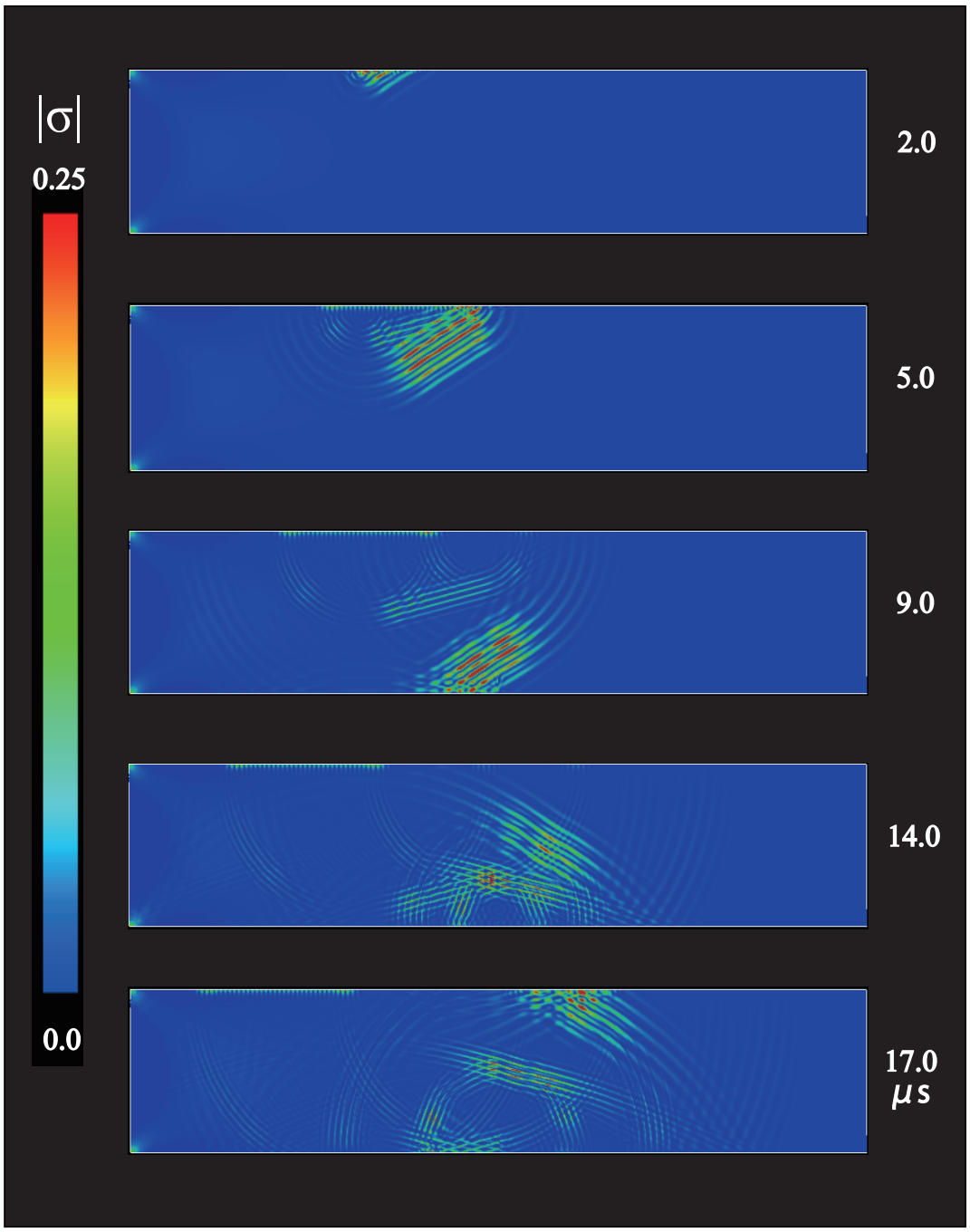

Fig. B.8 Visualization at the incident angle of 30° in the case of $\eta = 0.4$ for the closed crack with a height of 5 mm.

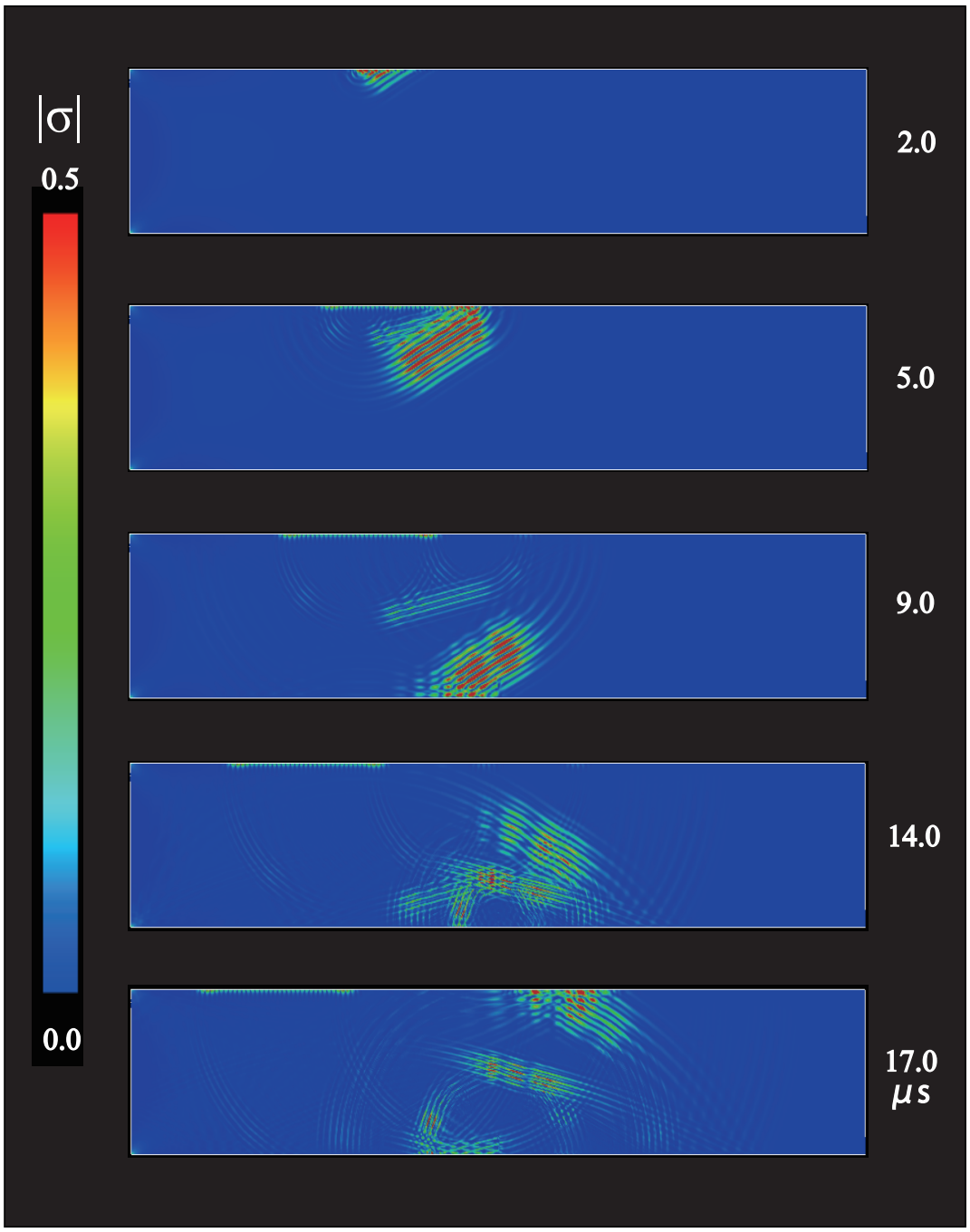

Fig. B.9 Visualization at the incident angle of 30° in the case of $\eta = 0.2$ for the closed crack with a height of 5 mm.

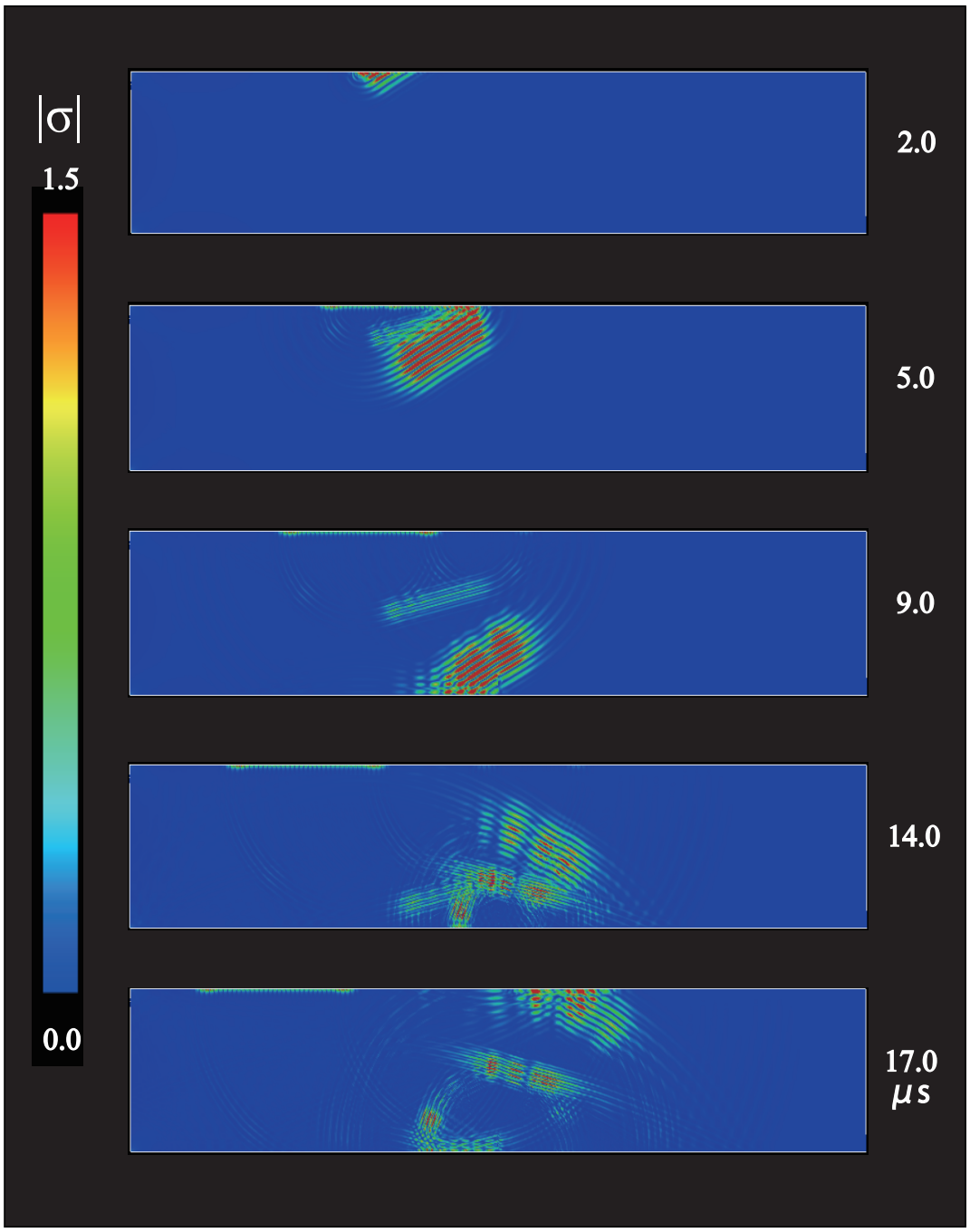

Fig. B.10 Visualization at the incident angle of 30° in the case of $\eta = 0.1$ for the closed crack with a height of 5 mm.

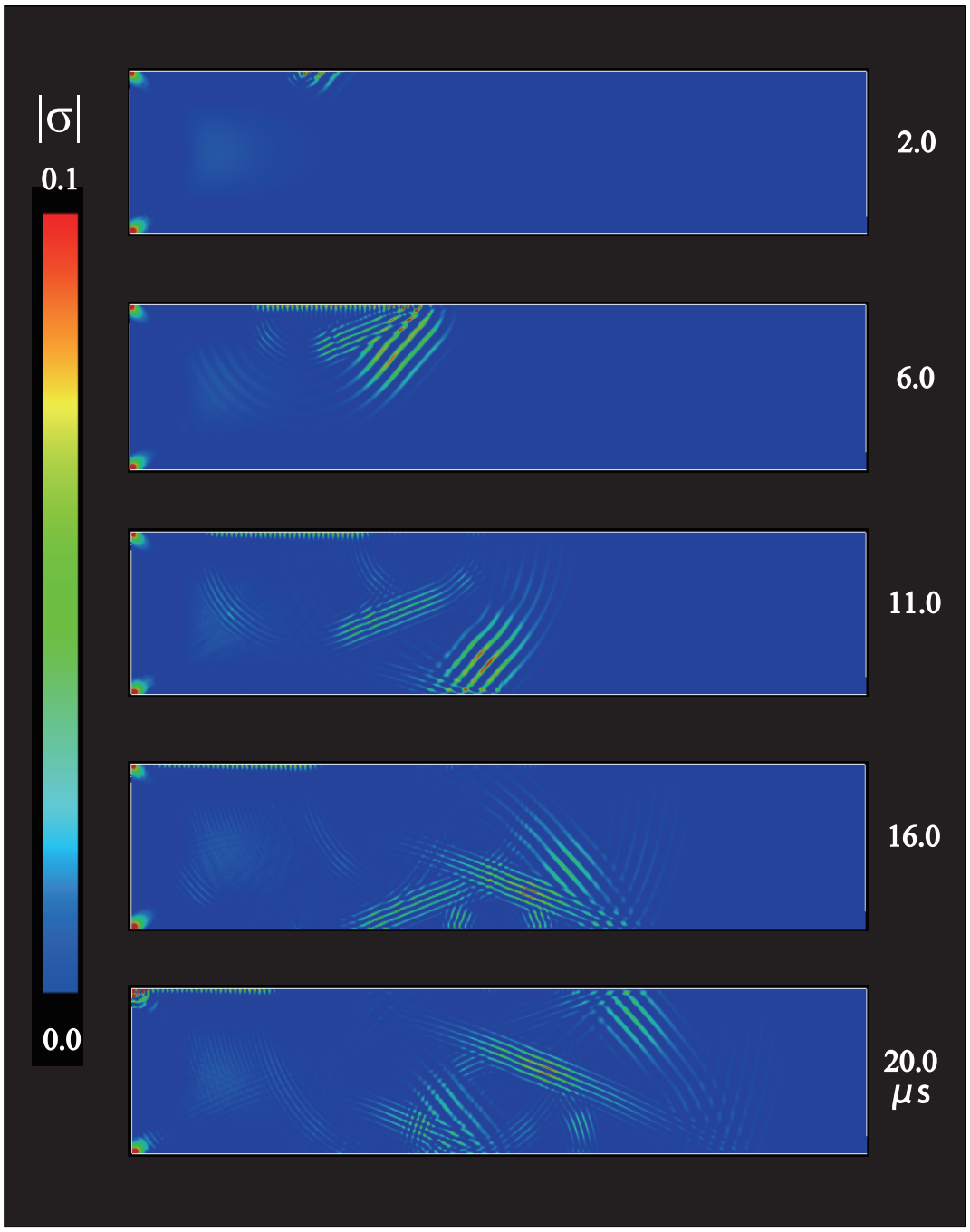

Fig. B.11 Visualization at the incident angle of 45° in the case of $\eta = 1.6$ for the closed crack with a height of 5 mm.

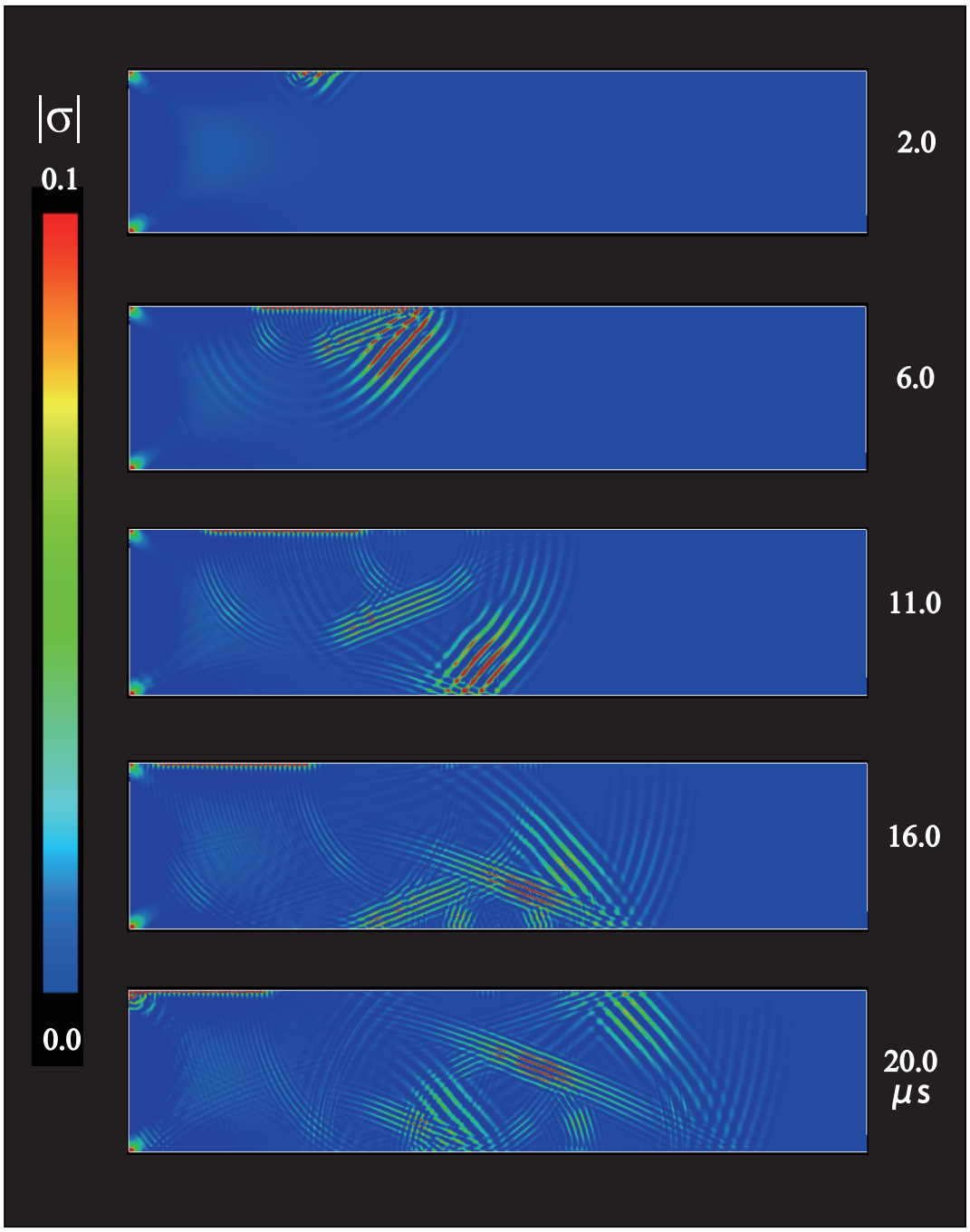

Fig. B.12 Visualization at the incident angle of 45° in the case of $\eta = 0.8$ for the closed crack with a height of 5 mm.

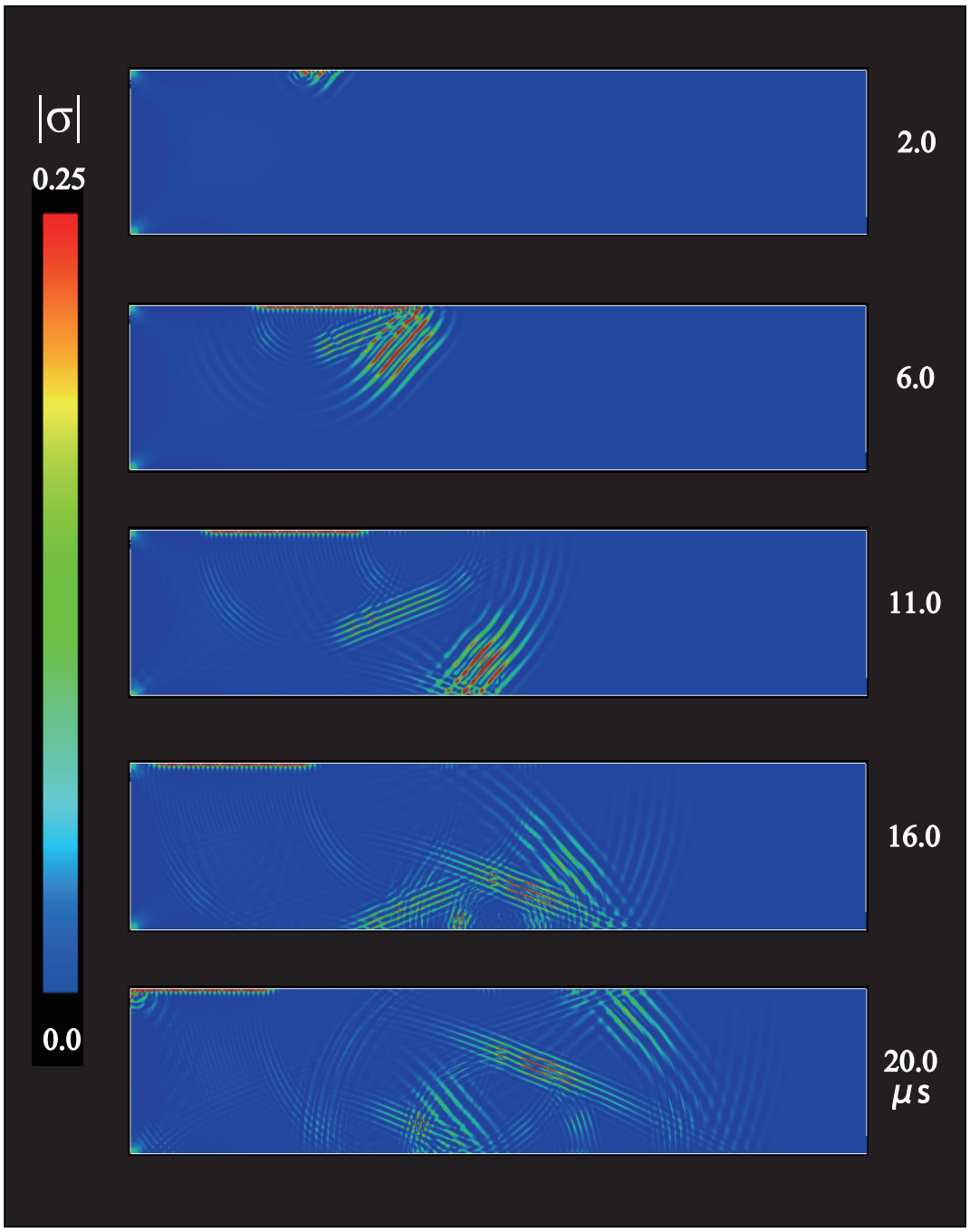

Fig. B.13 Visualization at the incident angle of 45° in the case of $\eta = 0.4$ for the closed crack with a height of 5 mm.

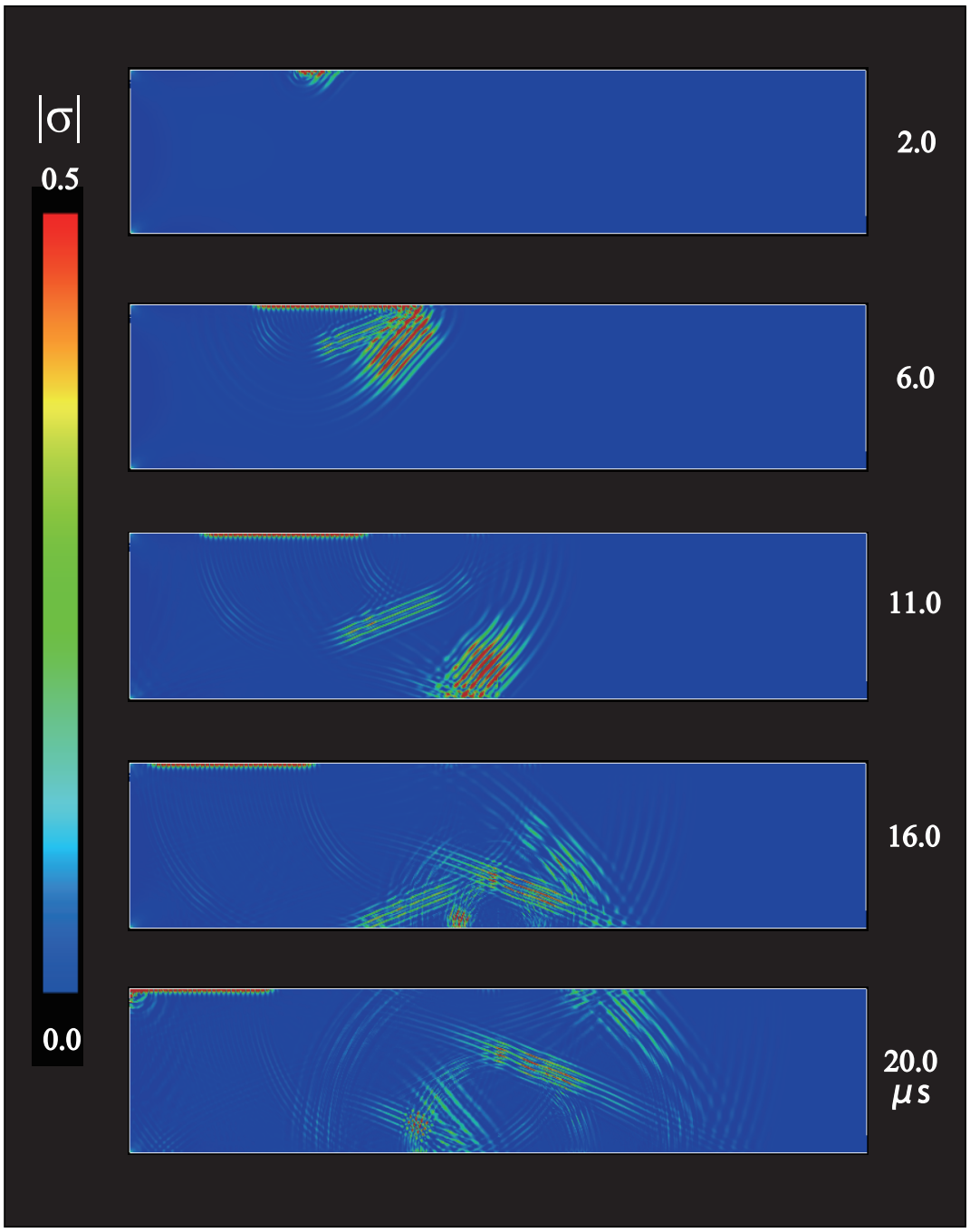

Fig. B.14 Visualization at the incident angle of 45° in the case of $\eta = 0.2$ for the closed crack with a height of 5 mm.

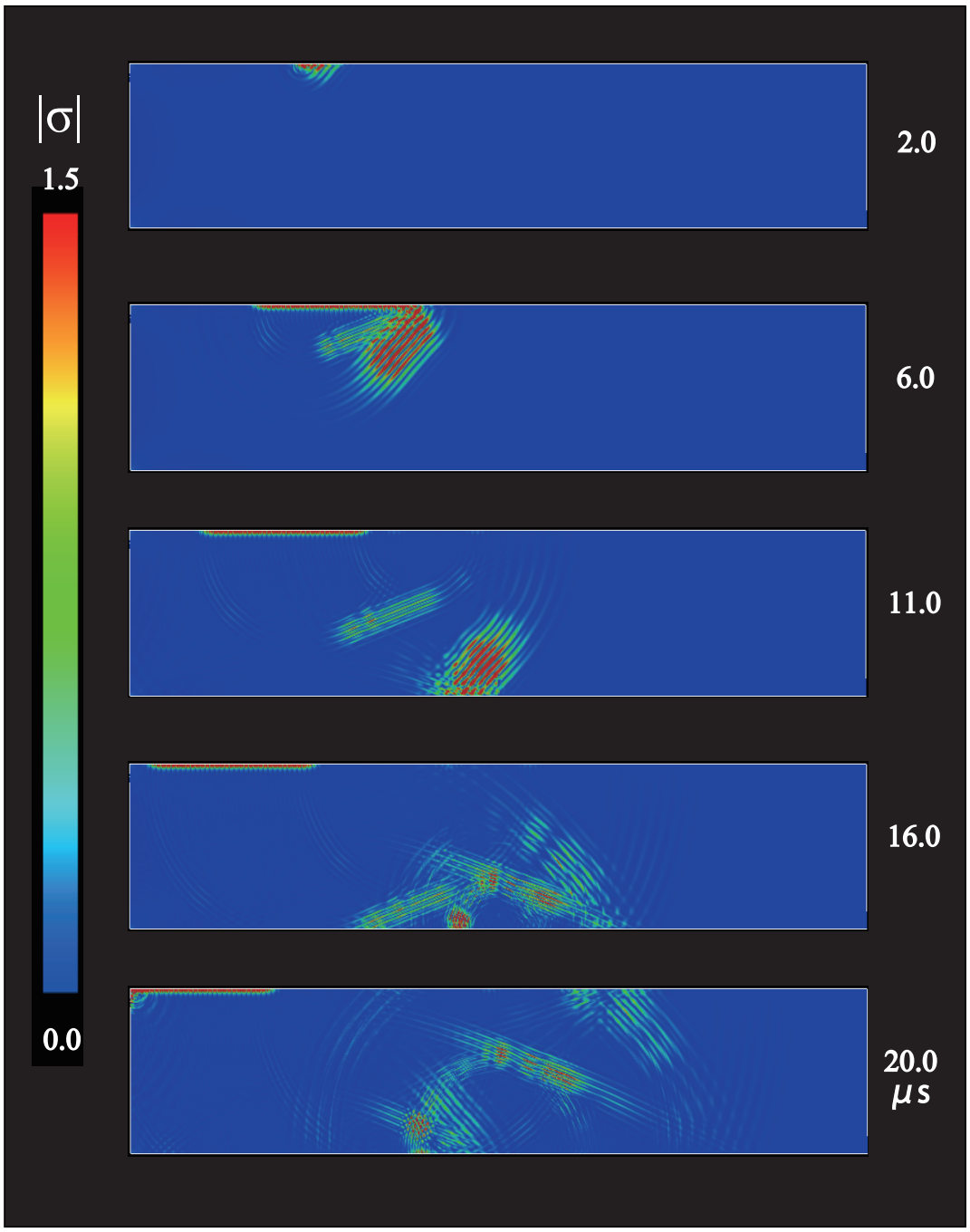

Fig. B.15 Visualization at the incident angle of 45° in the case of $\eta = 0.1$ for the closed crack with a height of 5 mm.

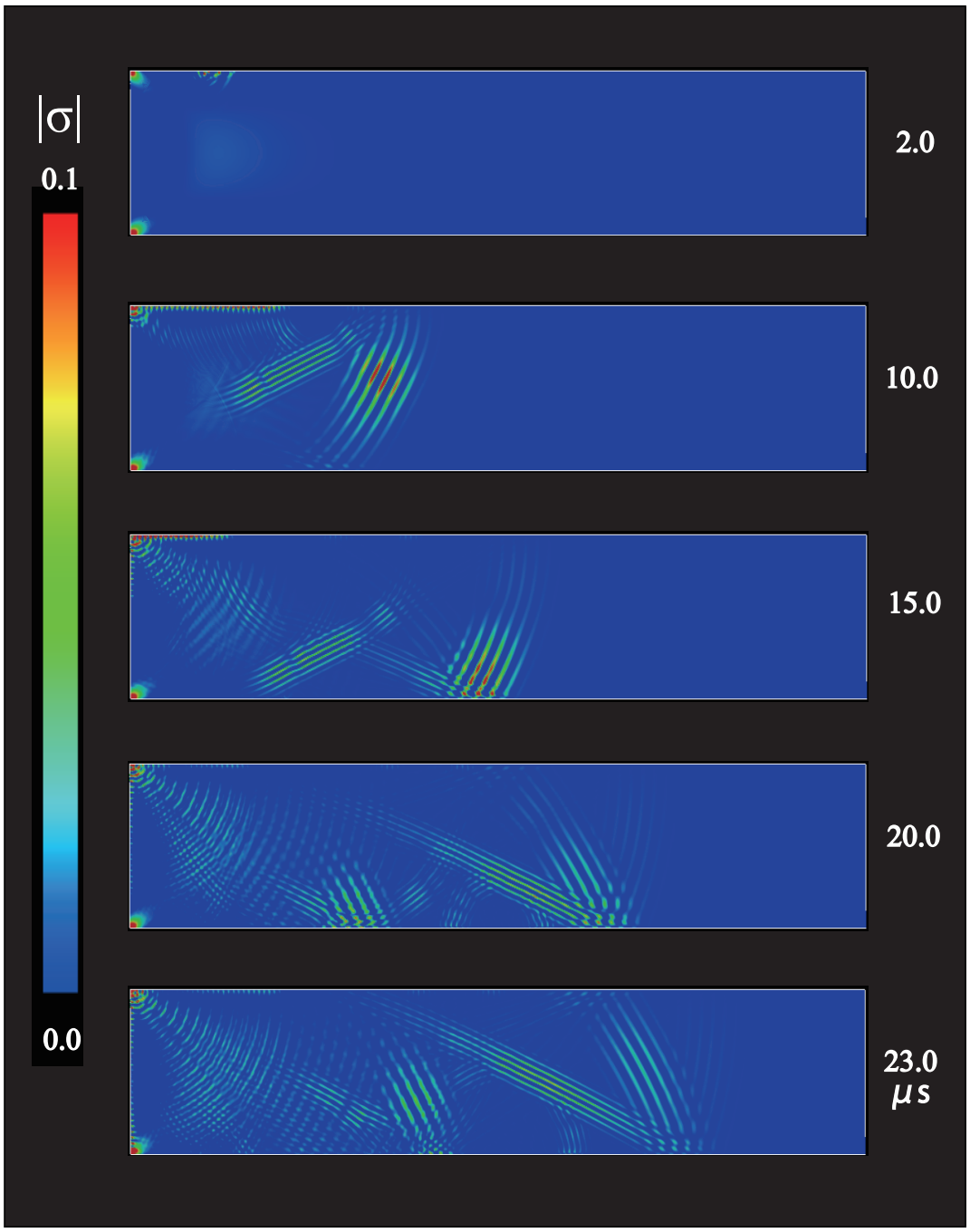

Fig. B.16 Visualization at the incident angle of 60° in the case of $\eta = 1.6$ for the closed crack with a height of 5 mm.

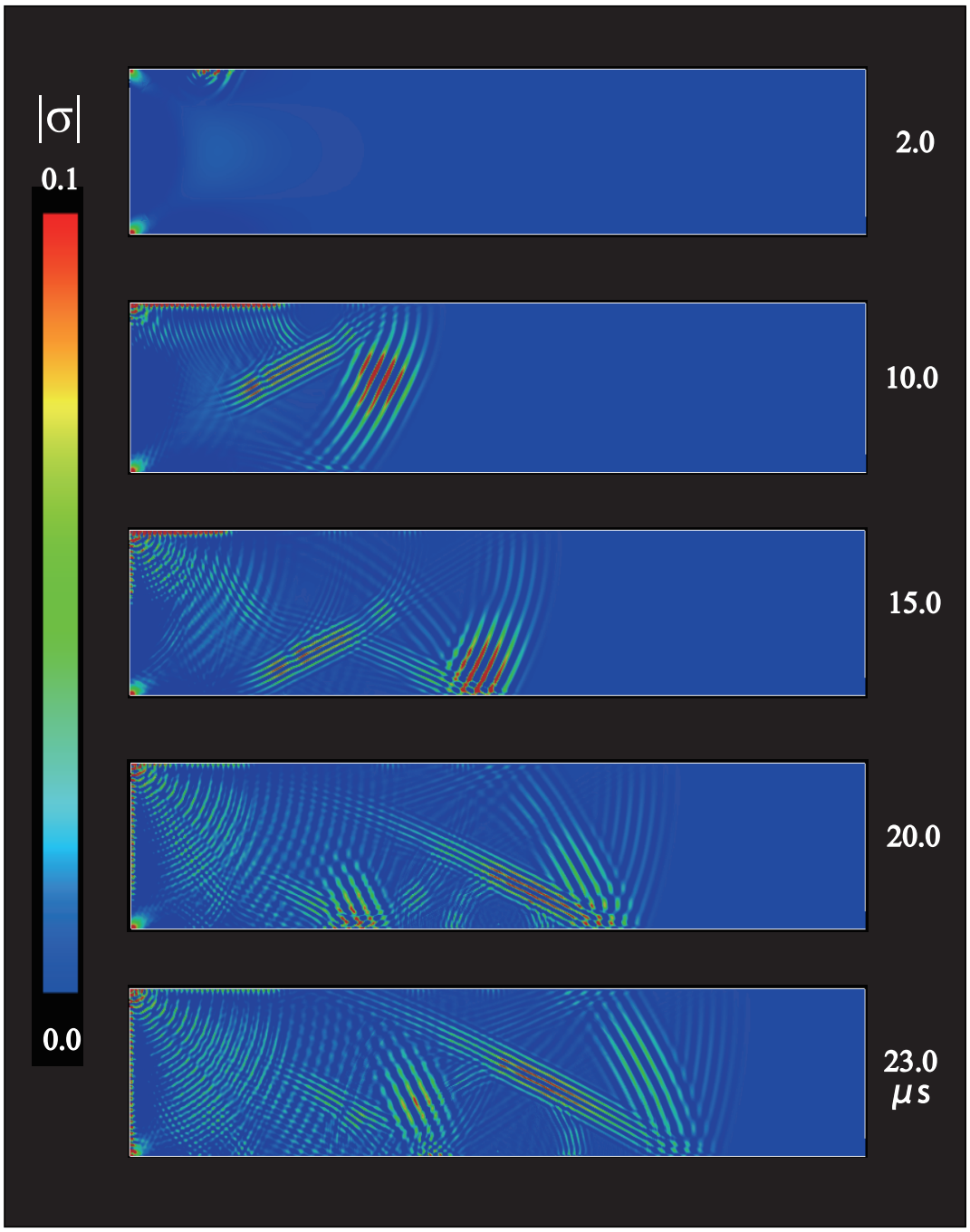

Fig. B.17 Visualization at the incident angle of 60° in the case of $\eta = 0.8$ for the closed crack with a height of 5 mm.

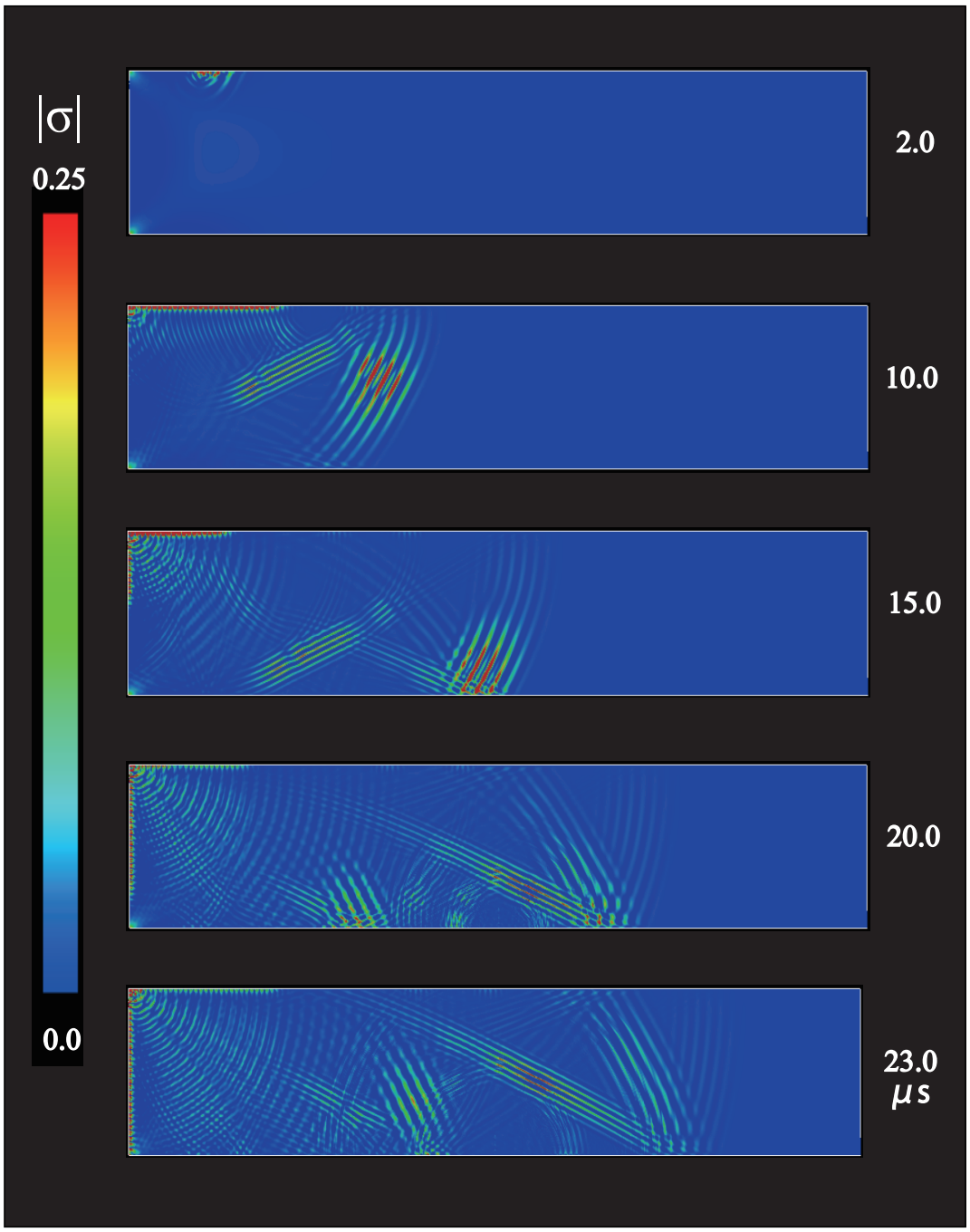

Fig. B.18 Visualization at the incident angle of 60° in the case of $\eta = 0.4$ for the closed crack with a height of 5 mm.

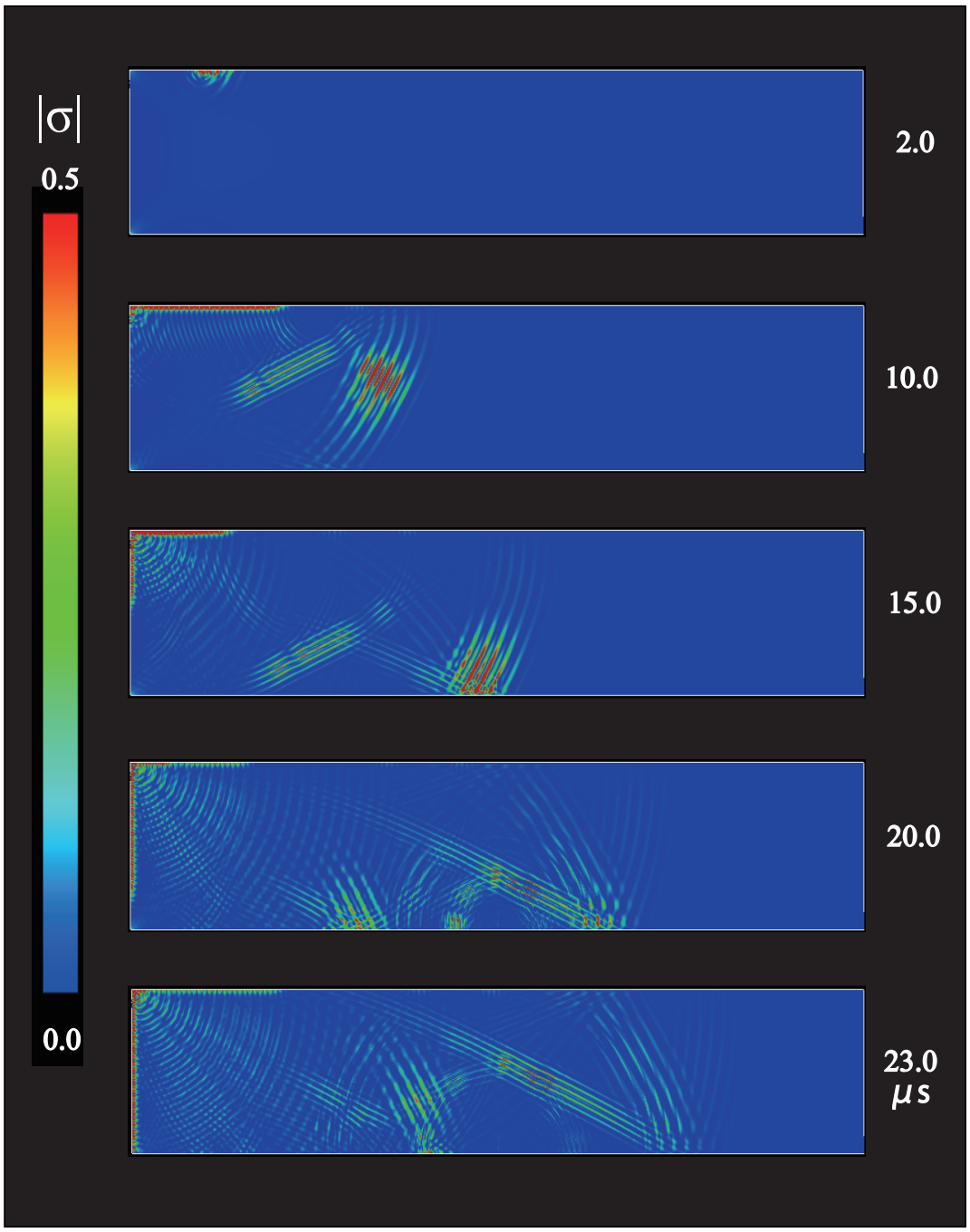

Fig. B.19 Visualization at the incident angle of 60° in the case of $\eta = 0.2$ for the closed crack with a height of 5 mm.

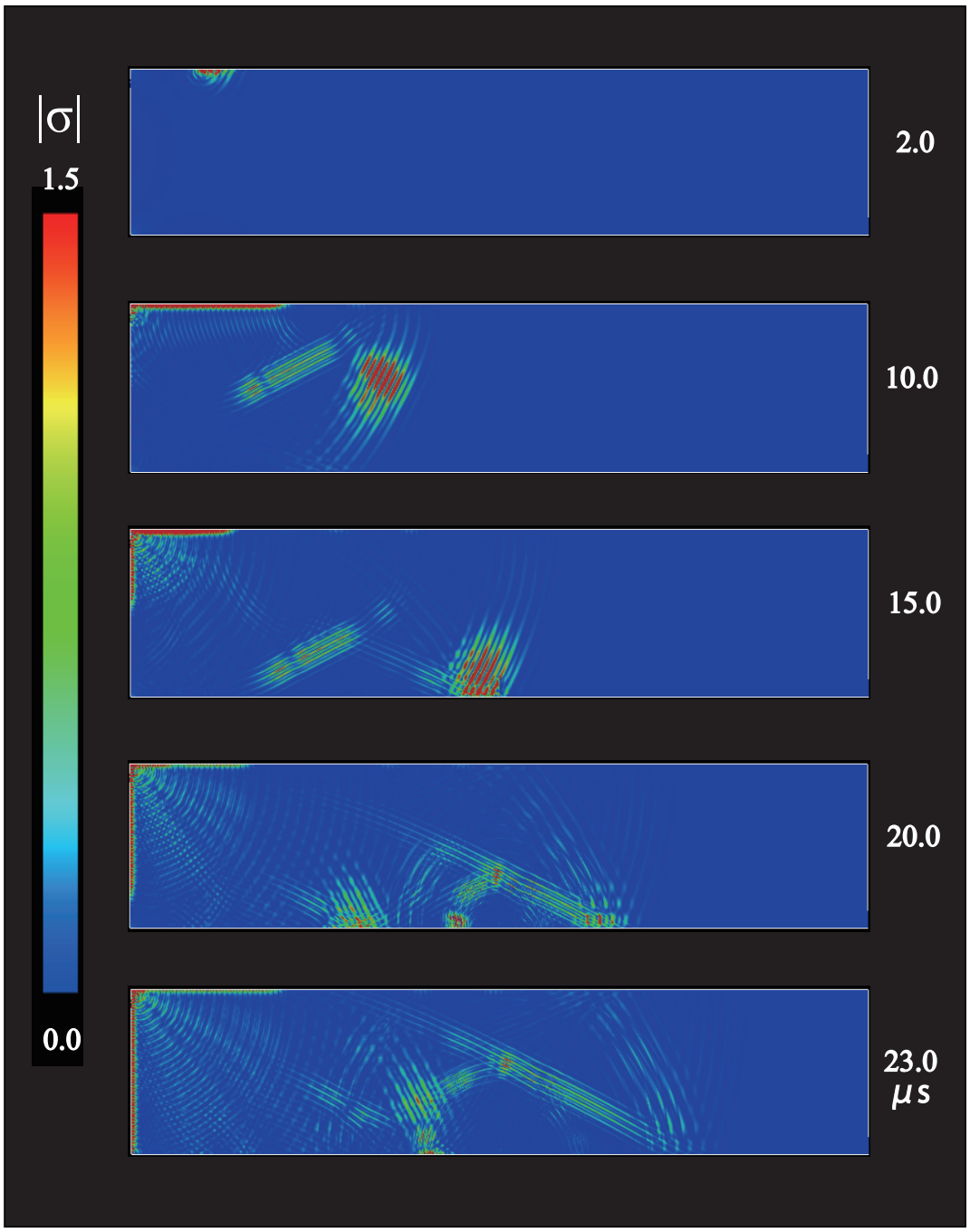

Fig. B.20 Visualization at the incident angle of 60° in the case of $\eta = 0.1$ for the closed crack with a height of 5 mm.

(2) Visualization of the scattered wave propagation for the closed crack with a height of 10 mm.

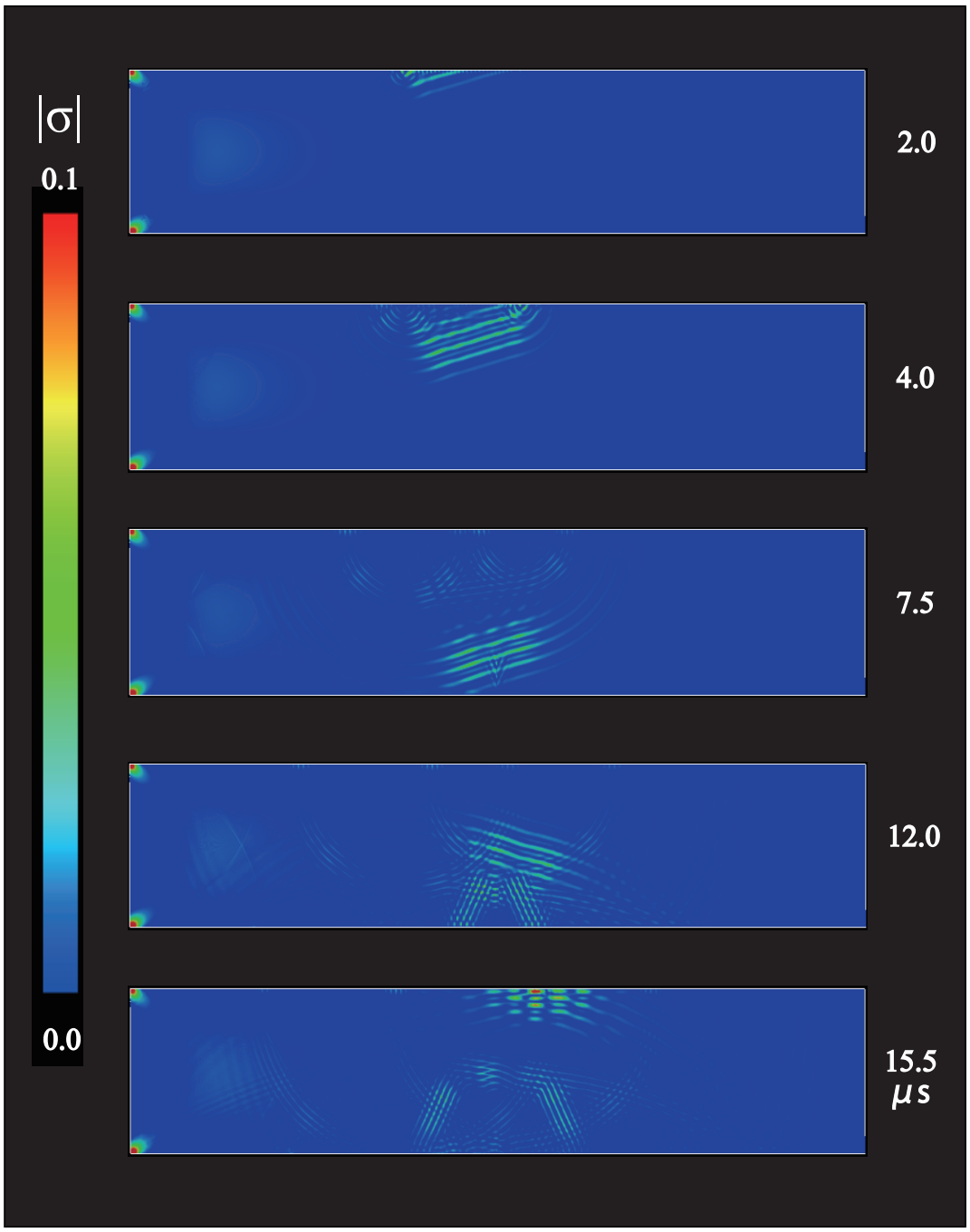

Fig. B.21 Visualization at the incident angle of 15° in the case of $\eta = 1.6$ for the closed crack with a height of 10 mm.

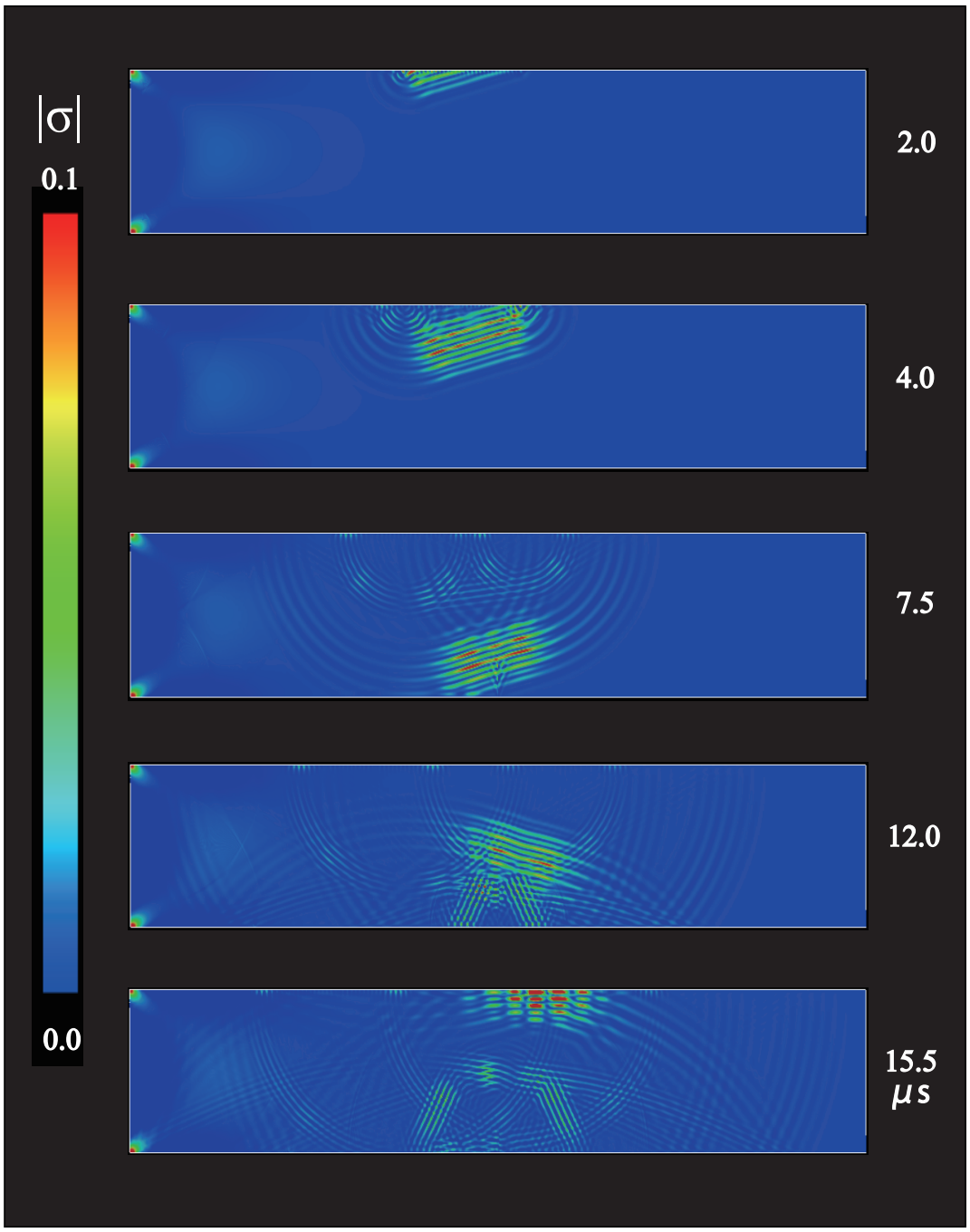

Fig. B.22 Visualization at the incident angle of 15° in the case of $\eta = 0.8$ for the closed crack with a height of 10 mm.

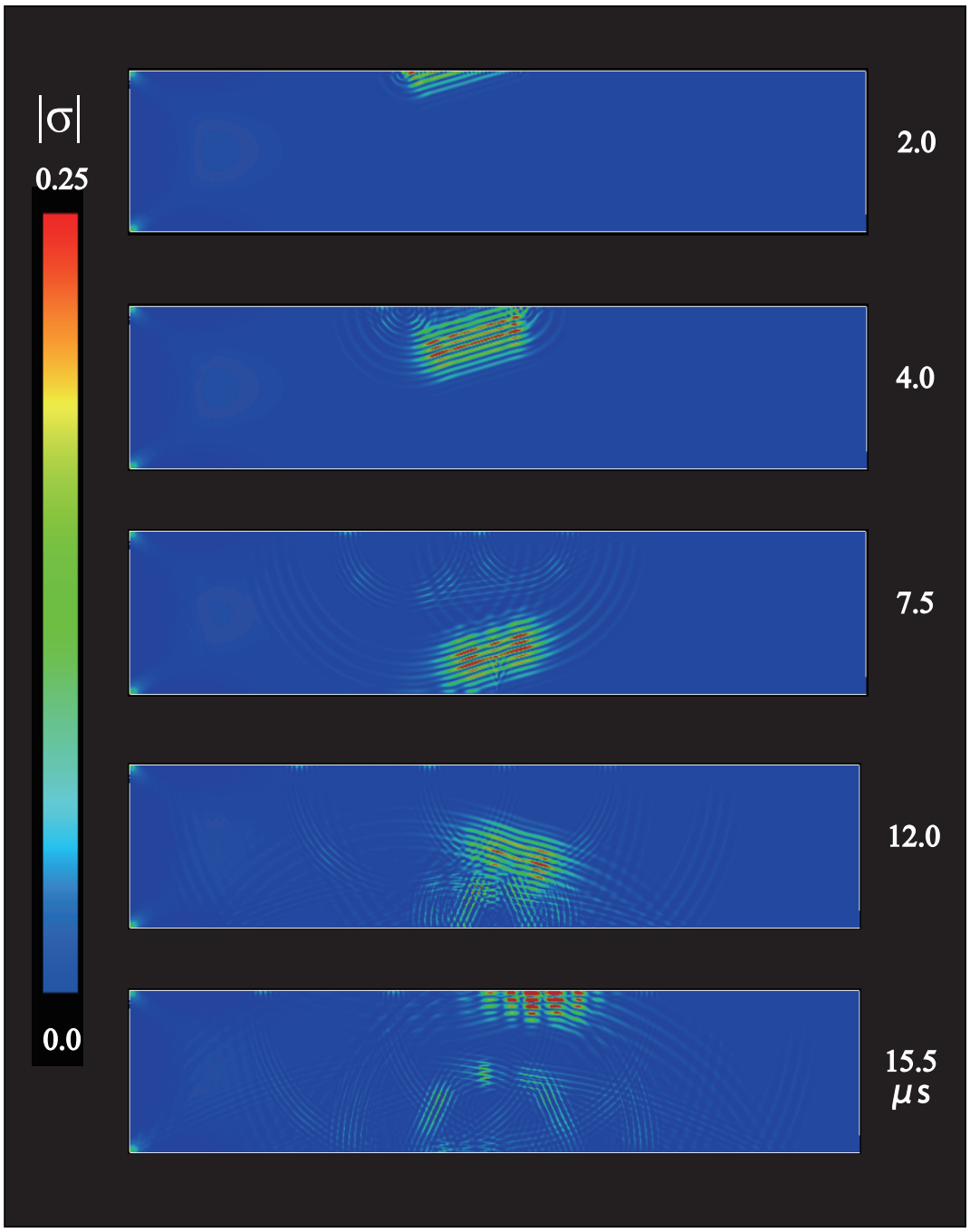

Fig. B.23 Visualization at the incident angle of 15° in the case of $\eta = 0.4$ for the closed crack with a height of 10 mm.

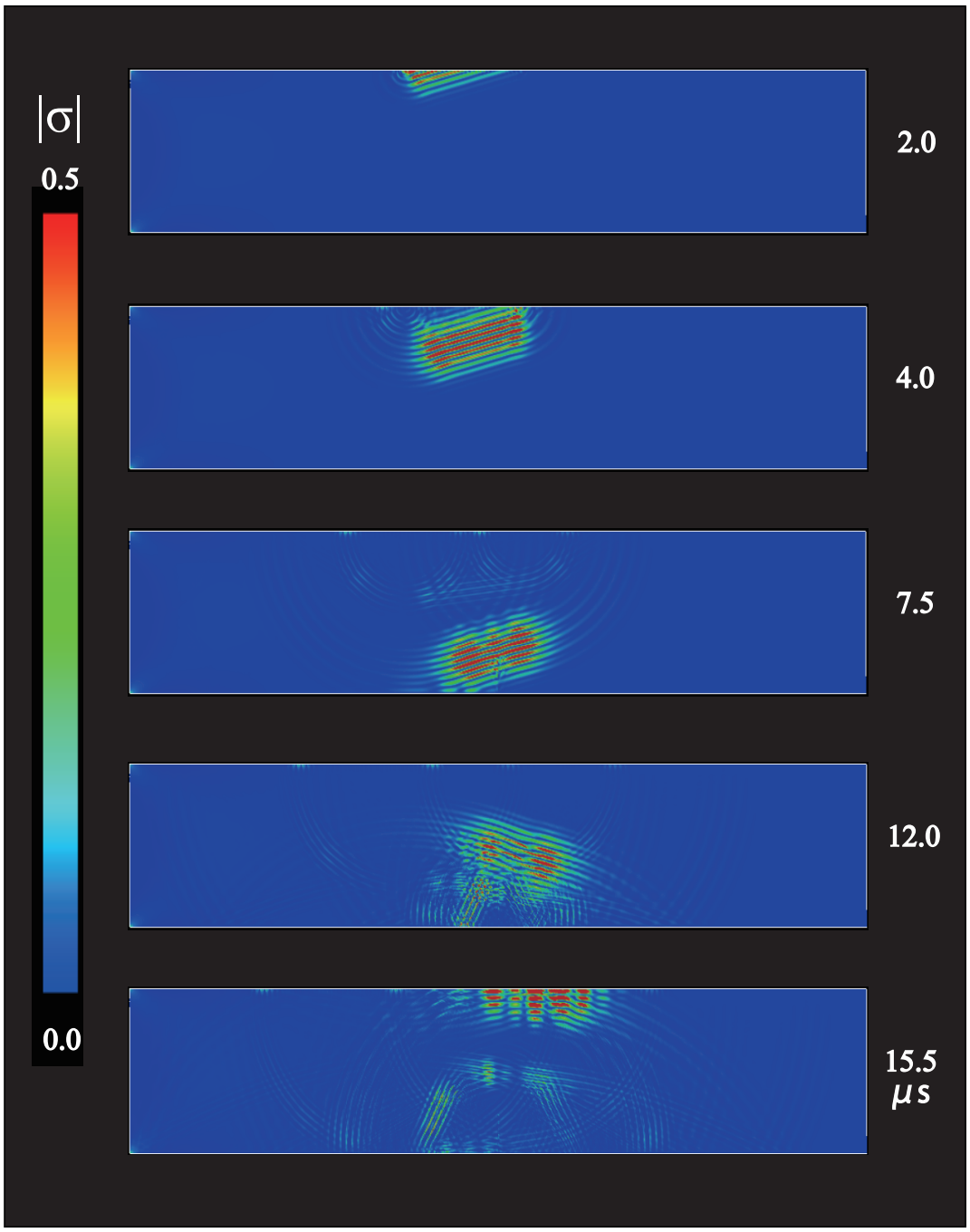

Fig. B.24 Visualization at the incident angle of 15° in the case of $\eta = 0.2$ for the closed crack with a height of 10 mm.

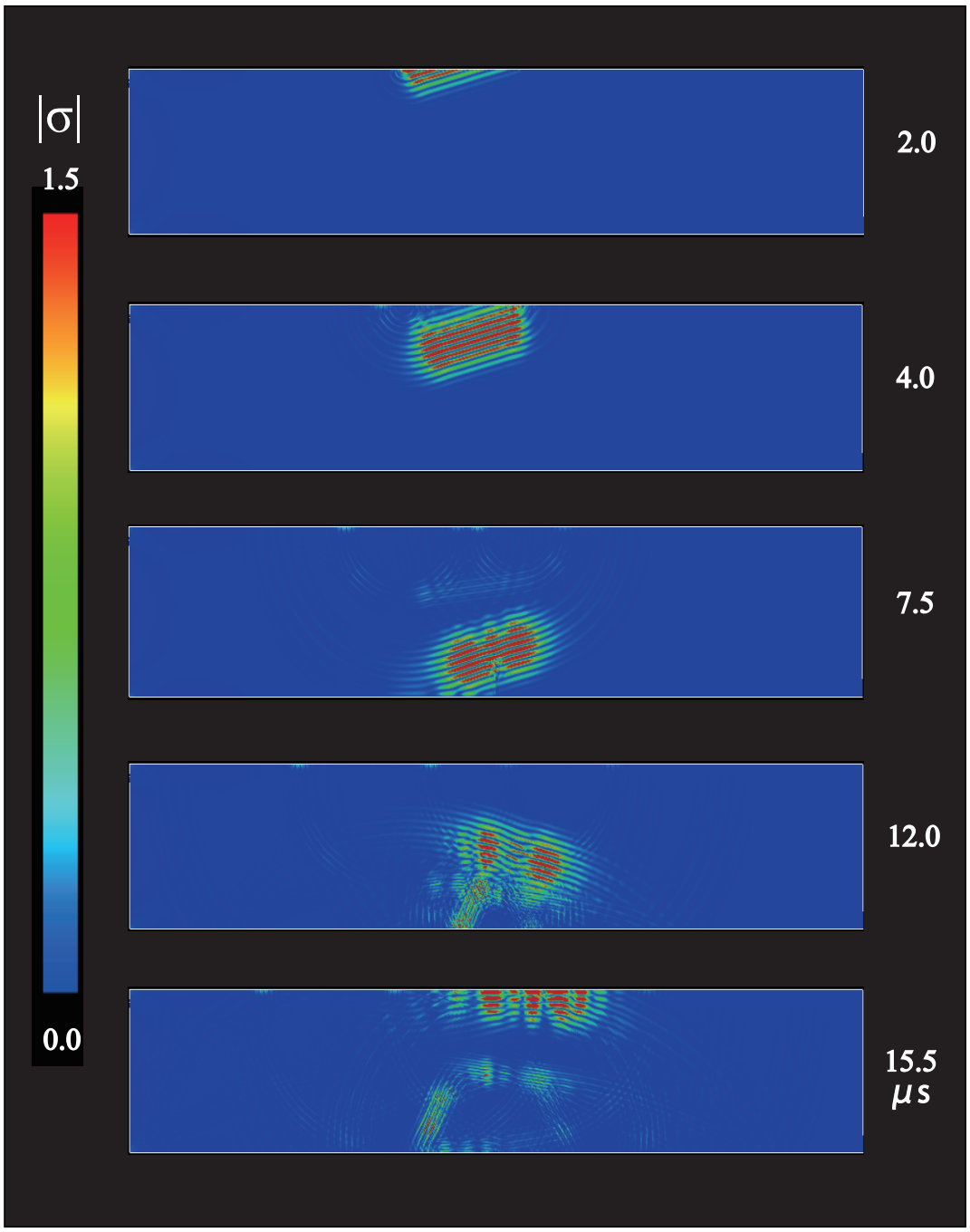

Fig. B.25 Visualization at the incident angle of 15° in the case of $\eta = 0.1$ for the closed crack with a height of 10 mm.

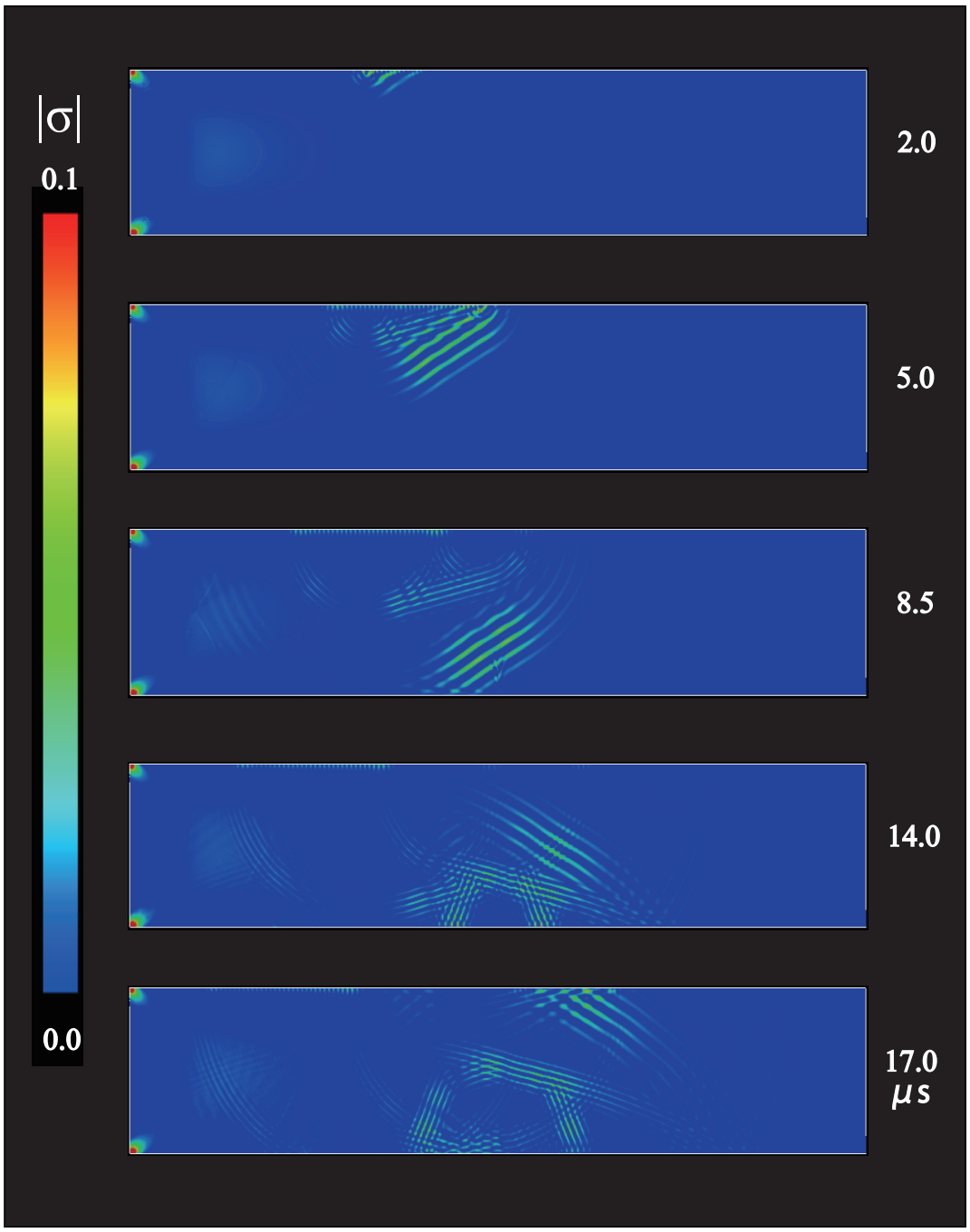

Fig. B.26 Visualization at the incident angle of 30° in the case of $\eta = 1.6$ for the closed crack with a height of 10 mm.

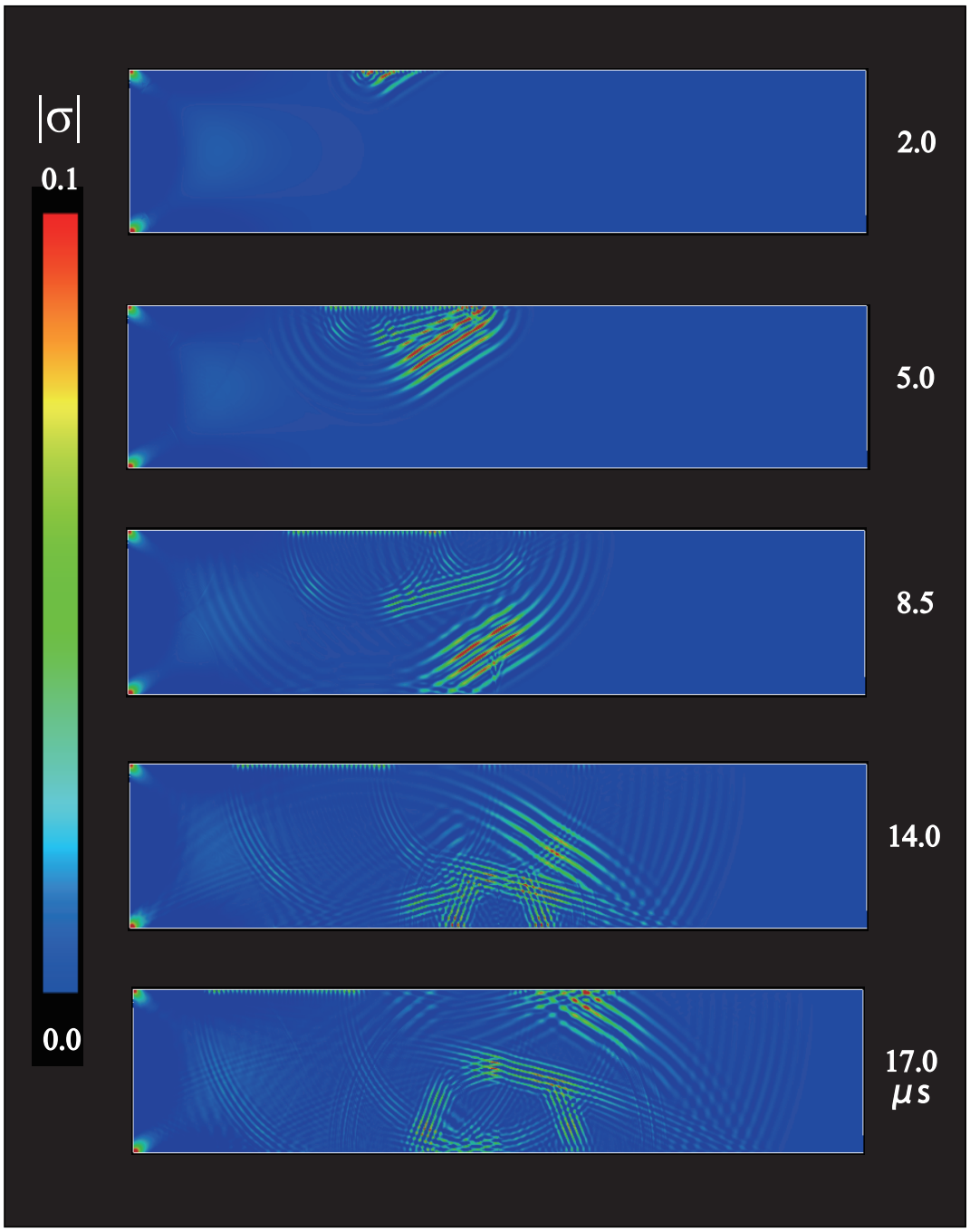

Fig. B.27 Visualization at the incident angle of 30° in the case of $\eta = 0.8$ for the closed crack with a height of 10 mm.

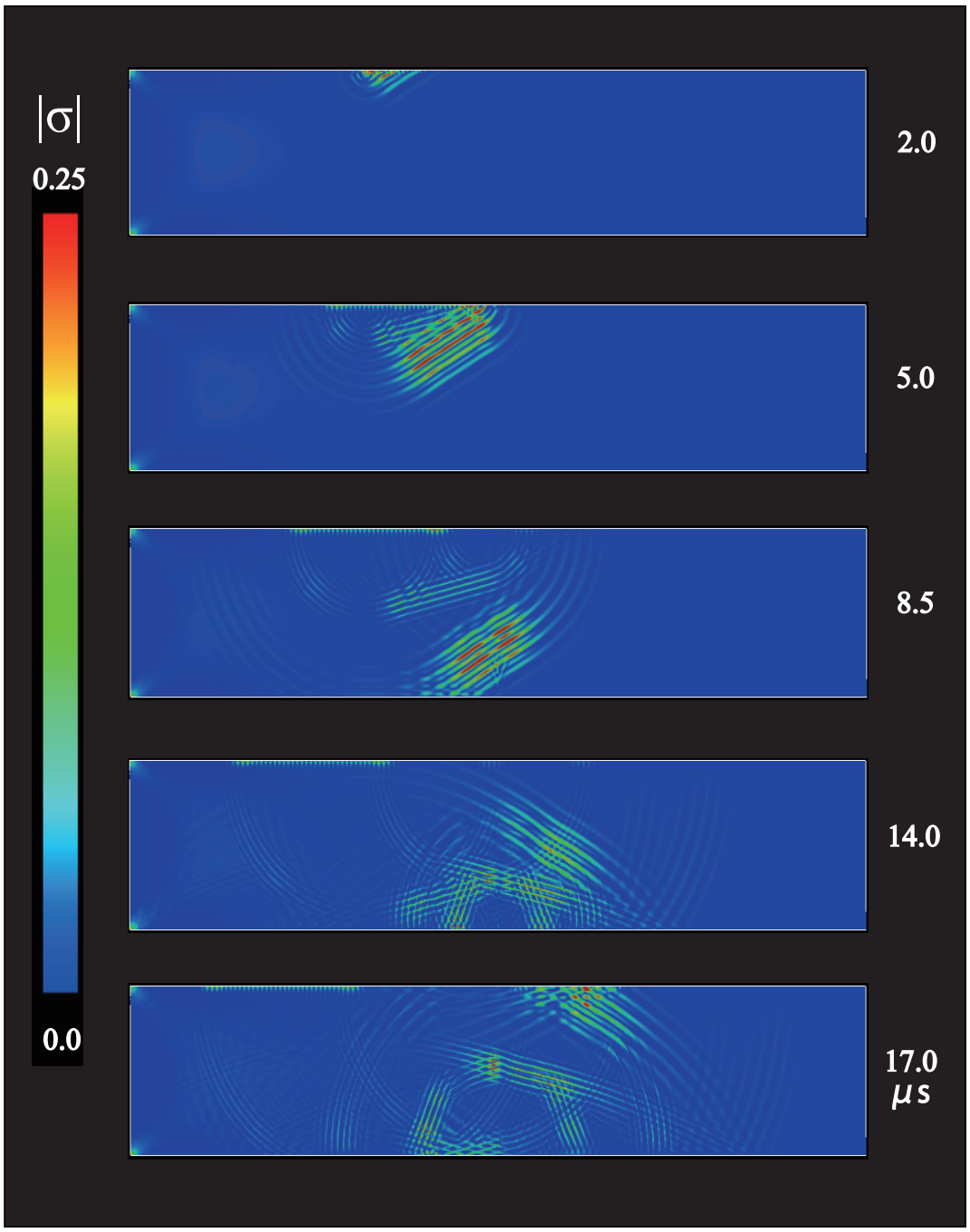

Fig. B.28 Visualization at the incident angle of 30° in the case of $\eta = 0.4$ for the closed crack with a height of 10 mm.

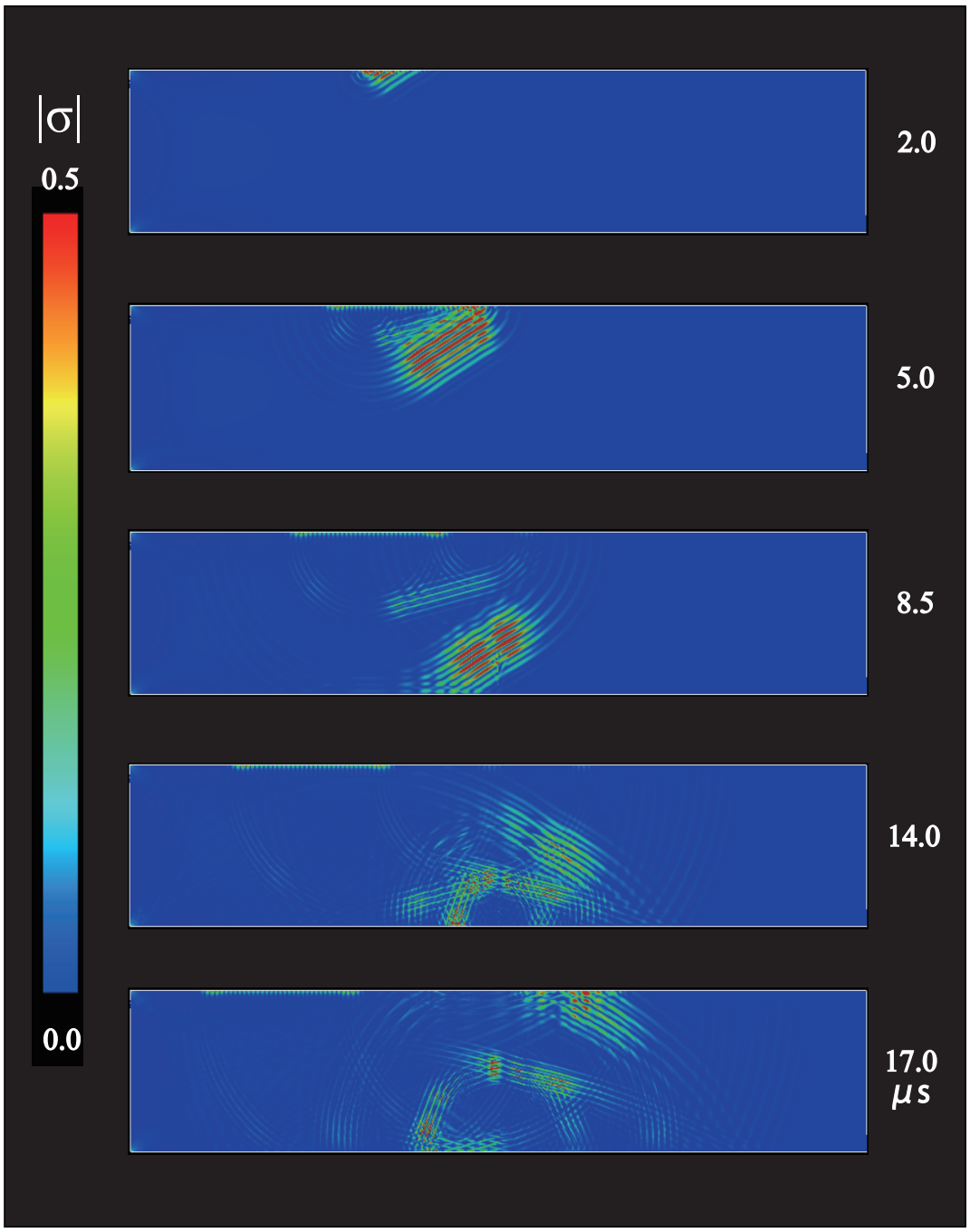

Fig. B.29 Visualization at the incident angle of 30° in the case of $\eta = 0.2$ for the closed crack with a height of 10 mm.

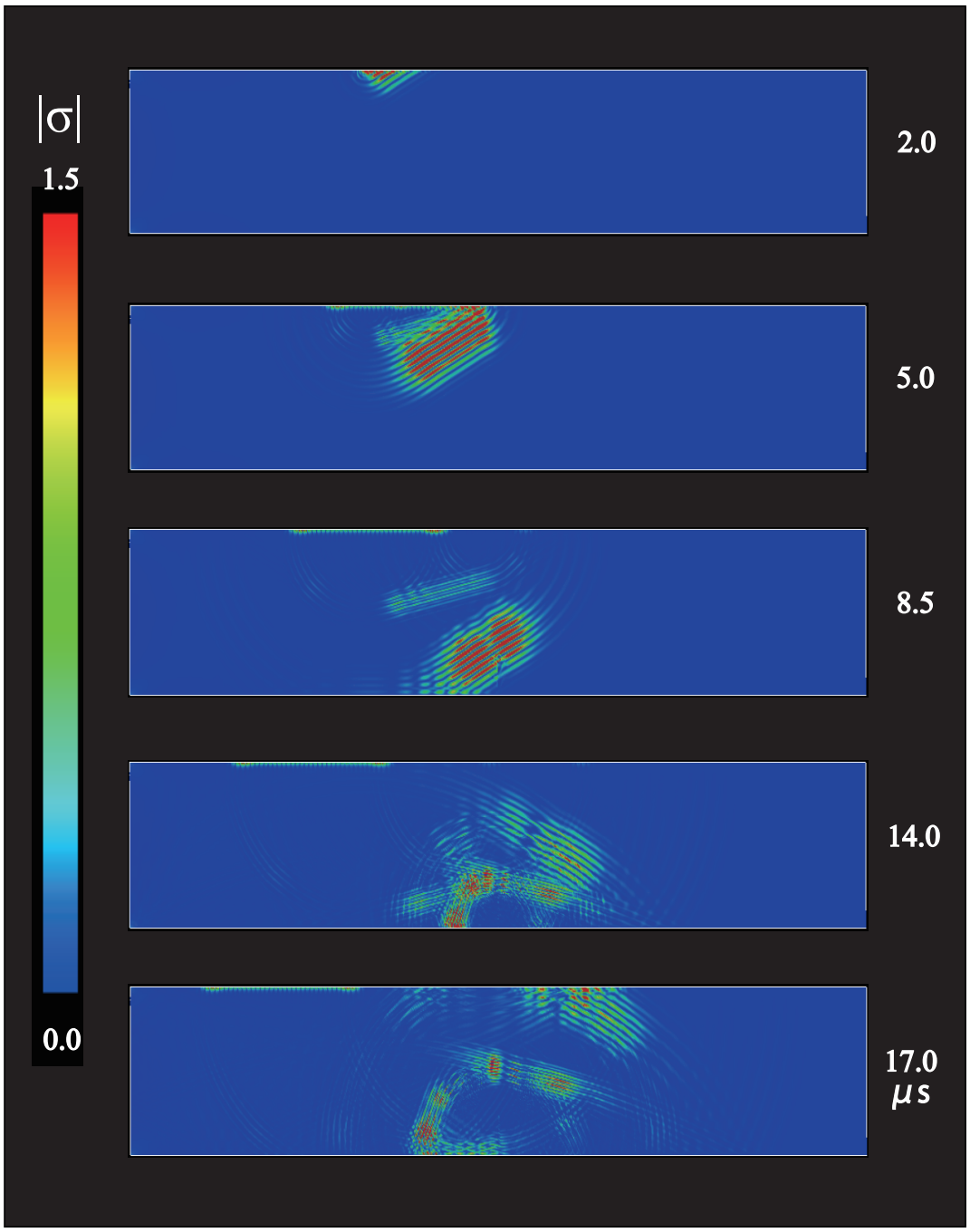

Fig. B.30 Visualization at the incident angle of 30° in the case of $\eta = 0.1$ for the closed crack with a height of 10 mm.

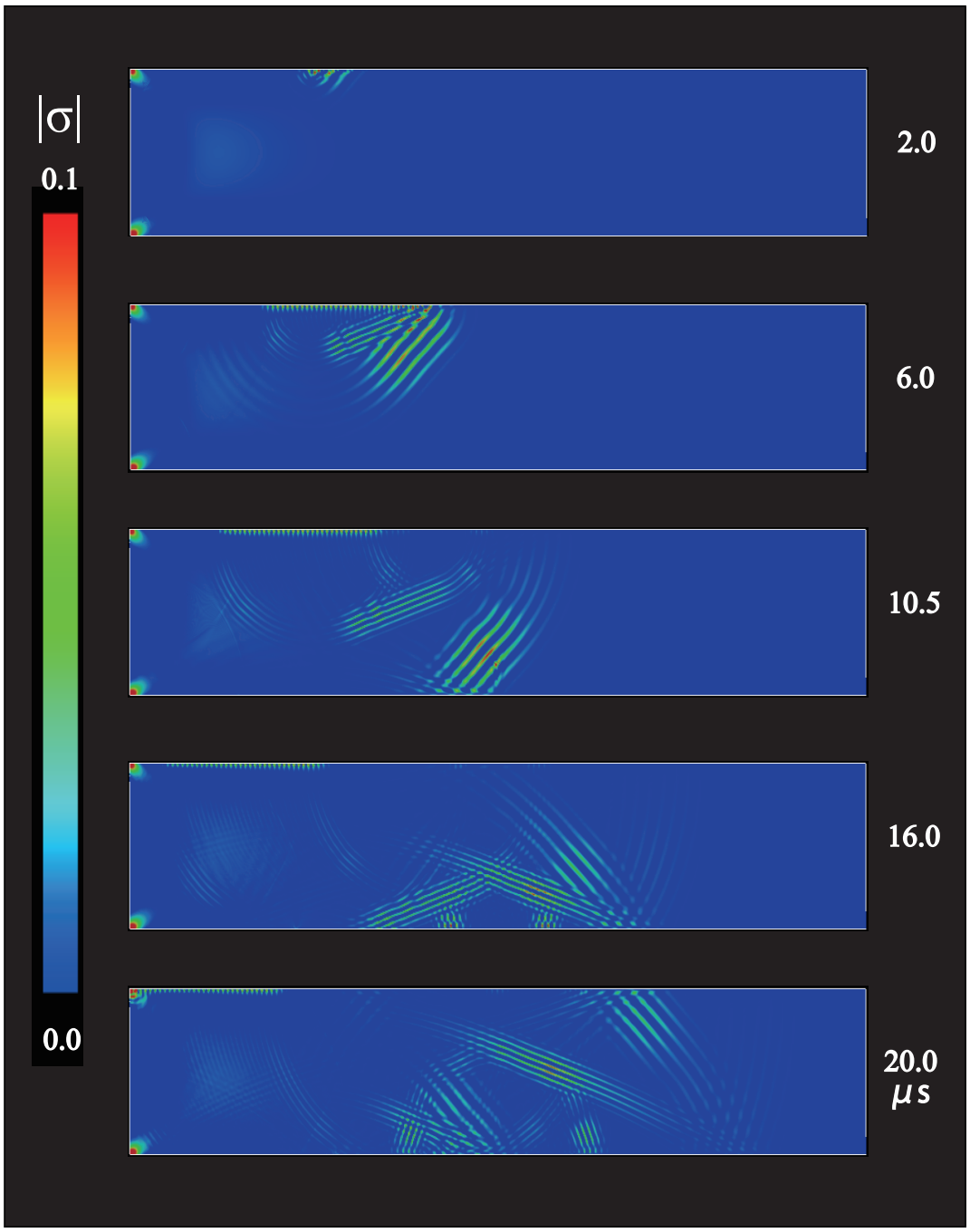

Fig. B.31 Visualization at the incident angle of 45° in the case of $\eta = 1.6$ for the closed crack with a height of 10 mm.

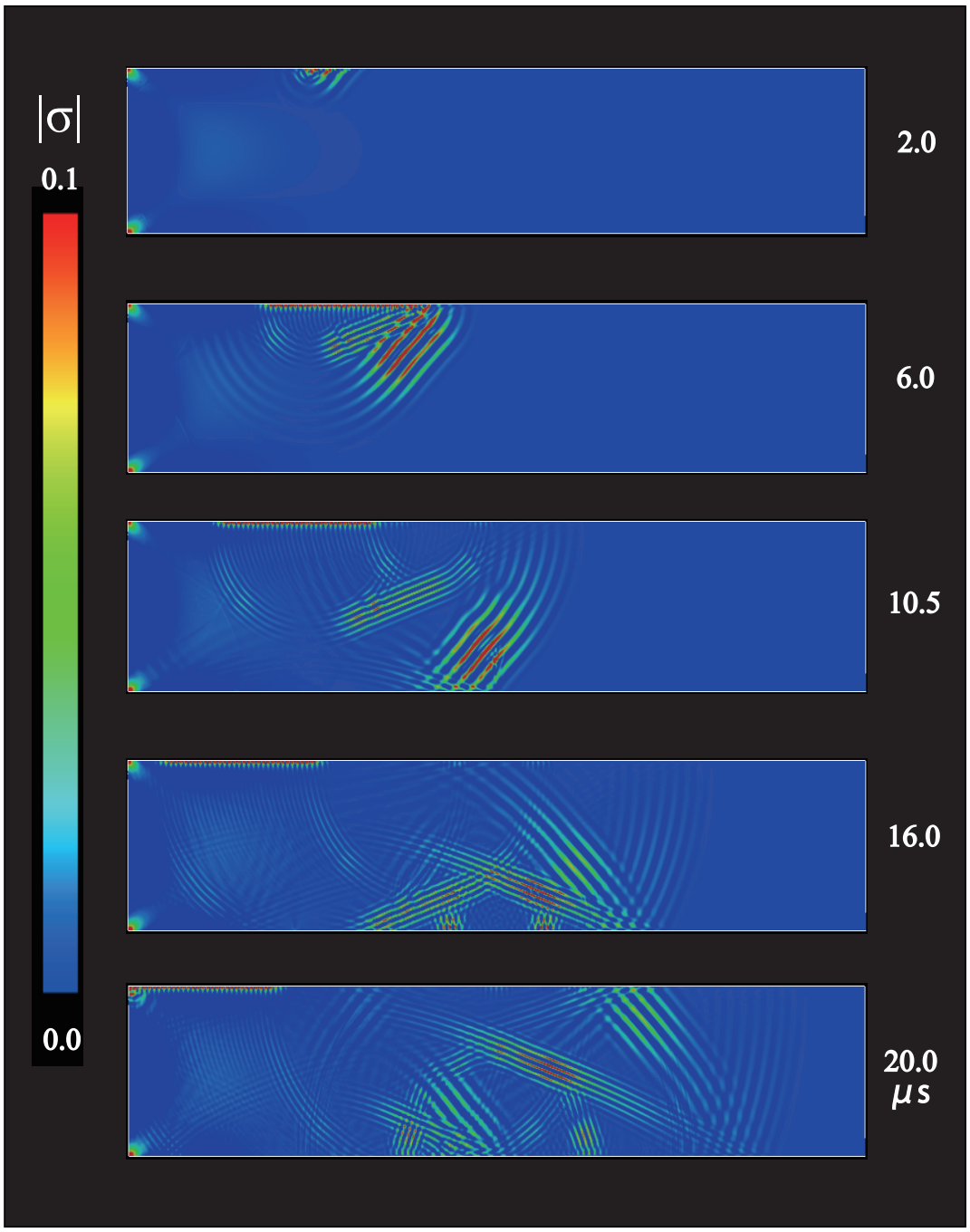

Fig. B.32 Visualization at the incident angle of 45° in the case of $\eta = 0.8$ for the closed crack with a height of 10 mm.

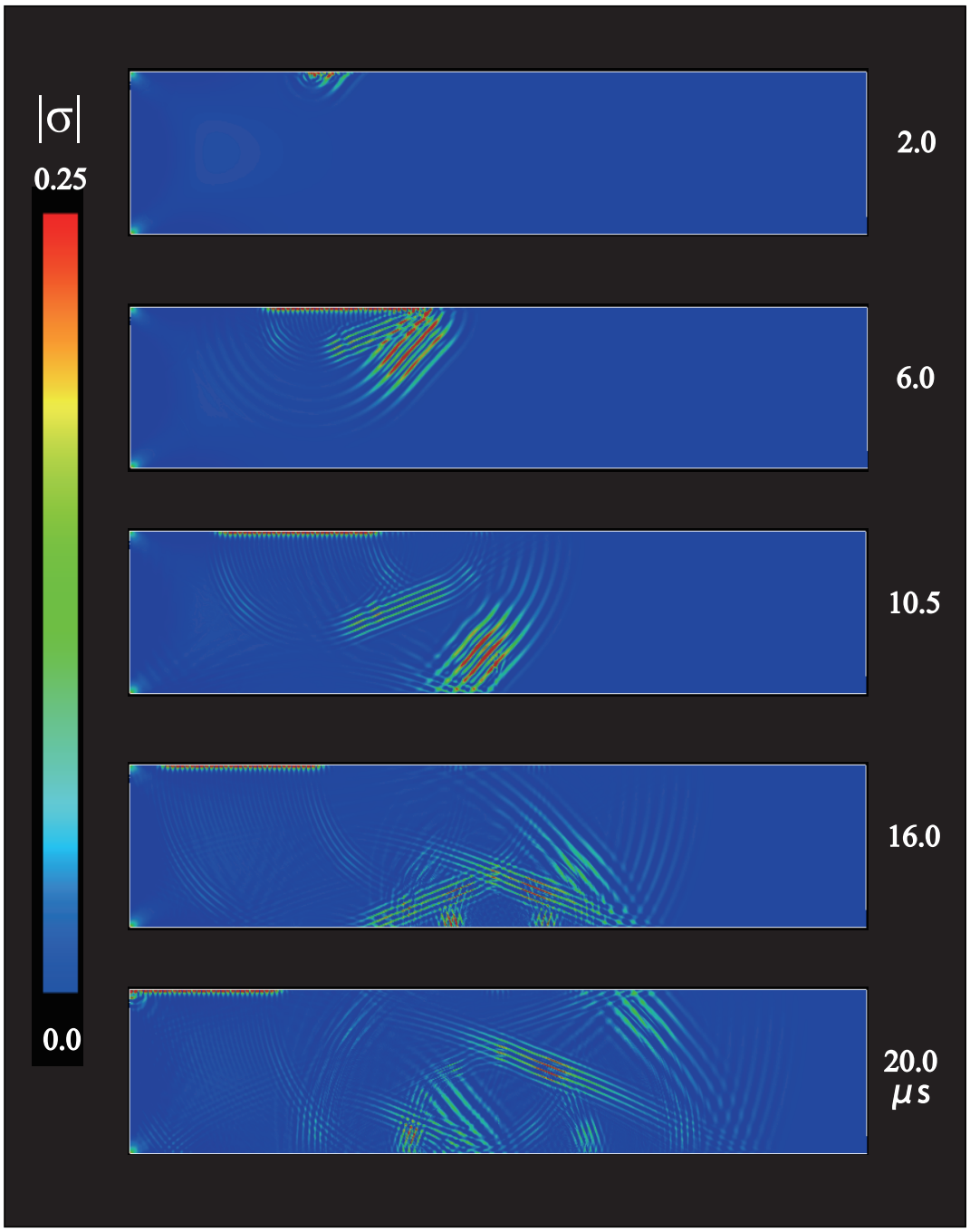

Fig. B.33 Visualization at the incident angle of 45° in the case of $\eta = 0.4$ for the closed crack with a height of 10 mm.

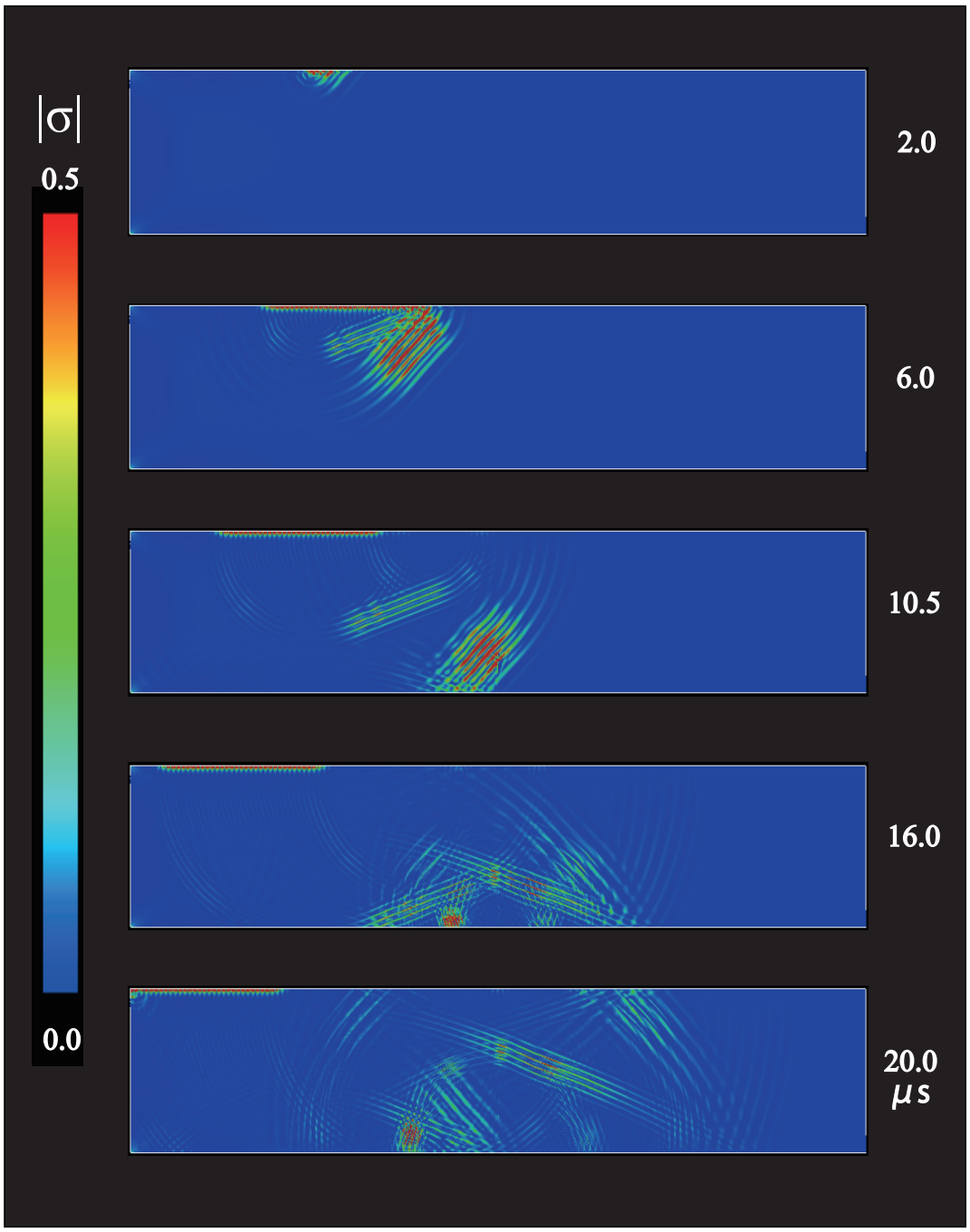

Fig. B.34 Visualization at the incident angle of 45° in the case of $\eta = 0.2$ for the closed crack with a height of 10 mm.

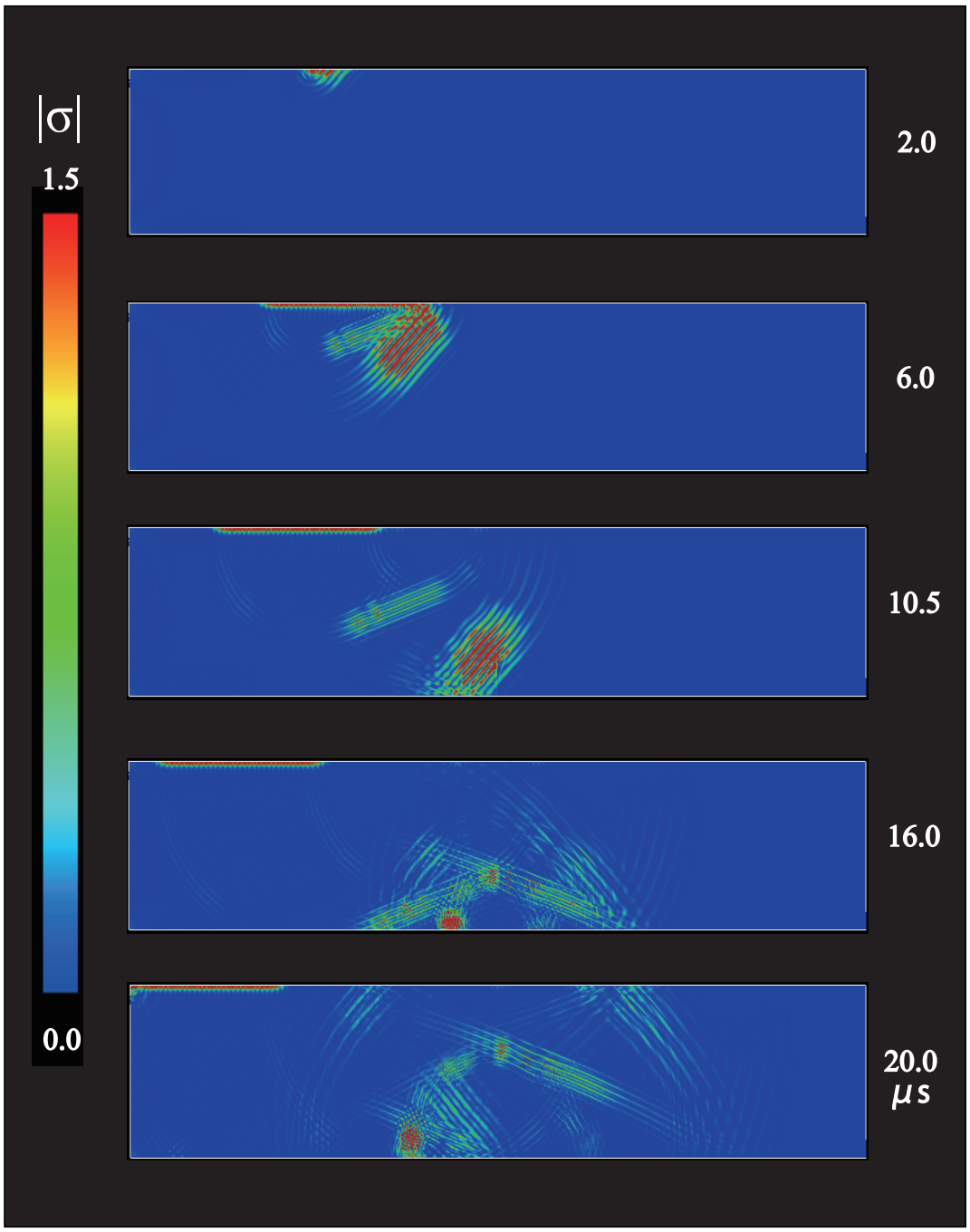

Fig. B.35 Visualization at the incident angle of 45° in the case of $\eta = 0.1$ for the closed crack with a height of 10 mm.

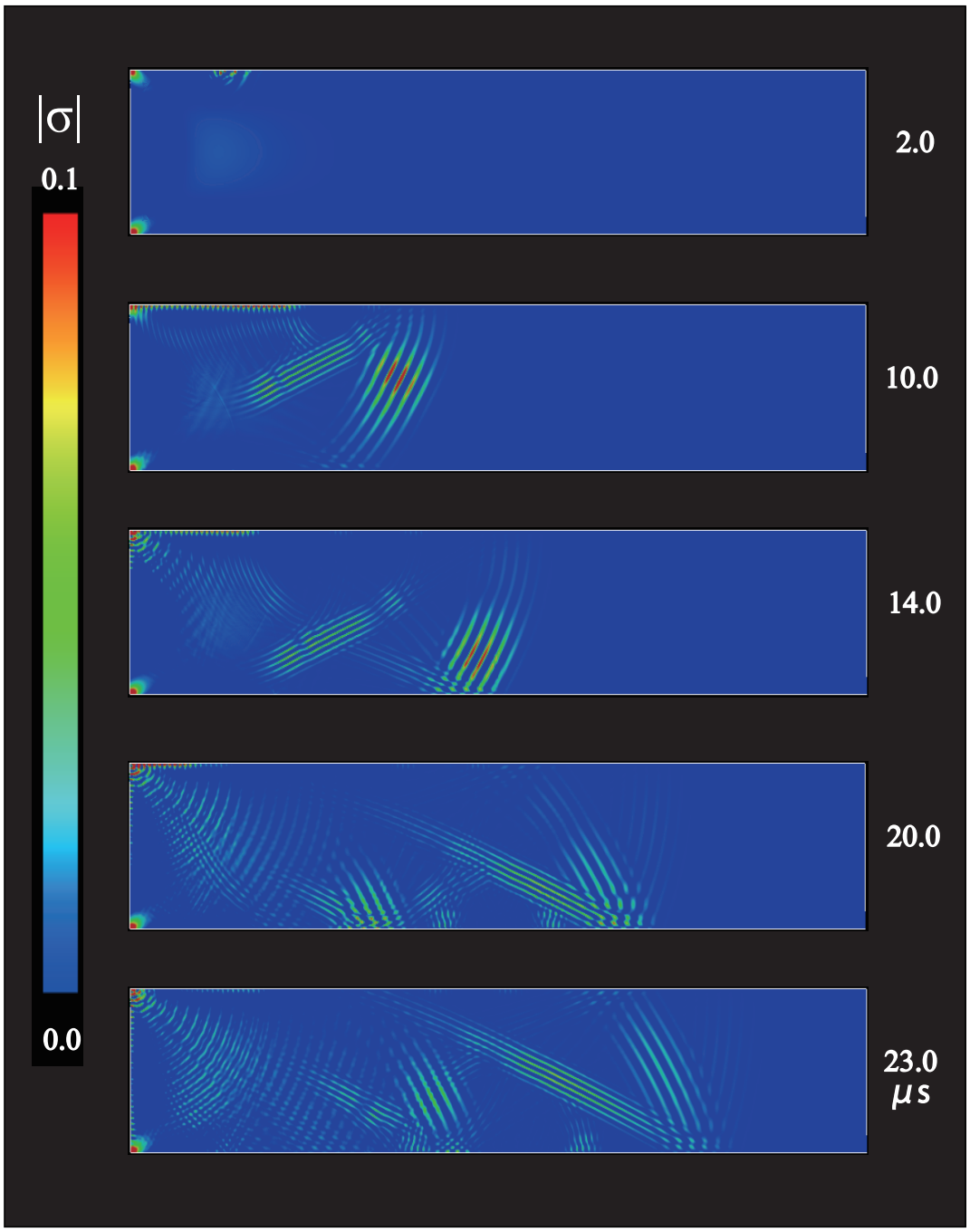

Fig. B.36 Visualization at the incident angle of 60° in the case of $\eta = 1.6$ for the closed crack with a height of 10 mm.

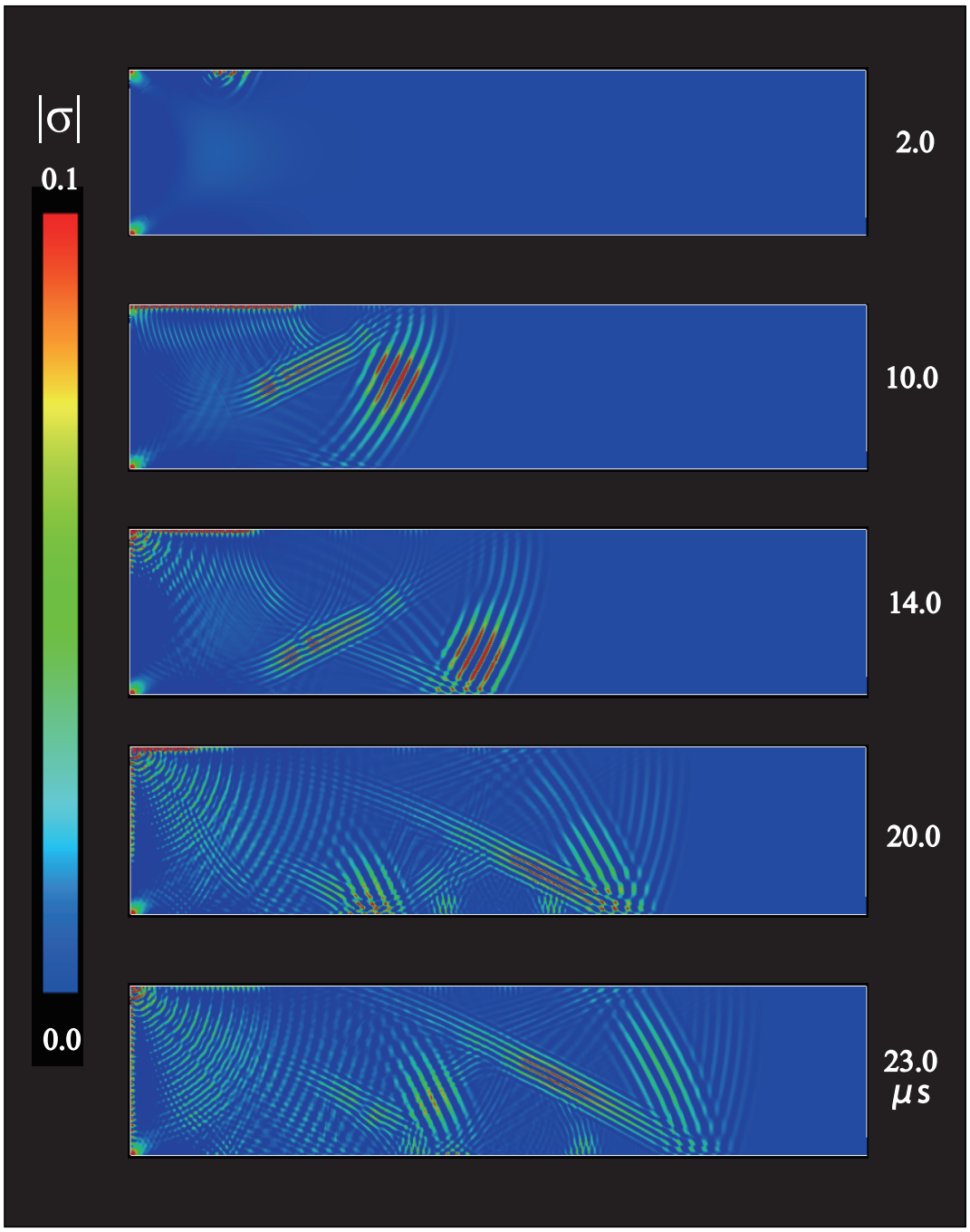

Fig. B.37 Visualization at the incident angle of 60° in the case of $\eta = 0.8$ for the closed crack with a height of 10 mm.

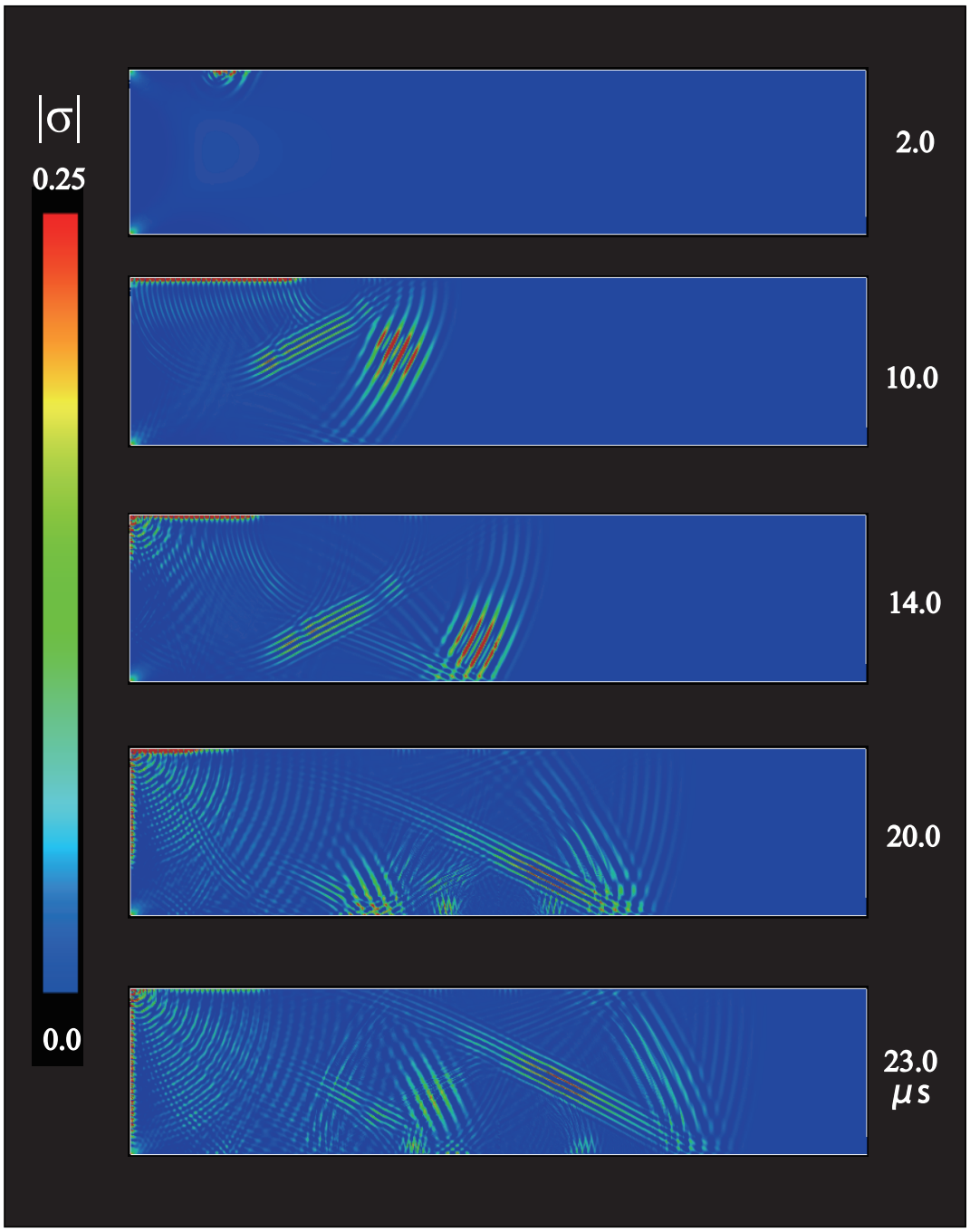

Fig. B.38 Visualization at the incident angle of 60° in the case of $\eta = 0.4$ for the closed crack with a height of 10 mm.

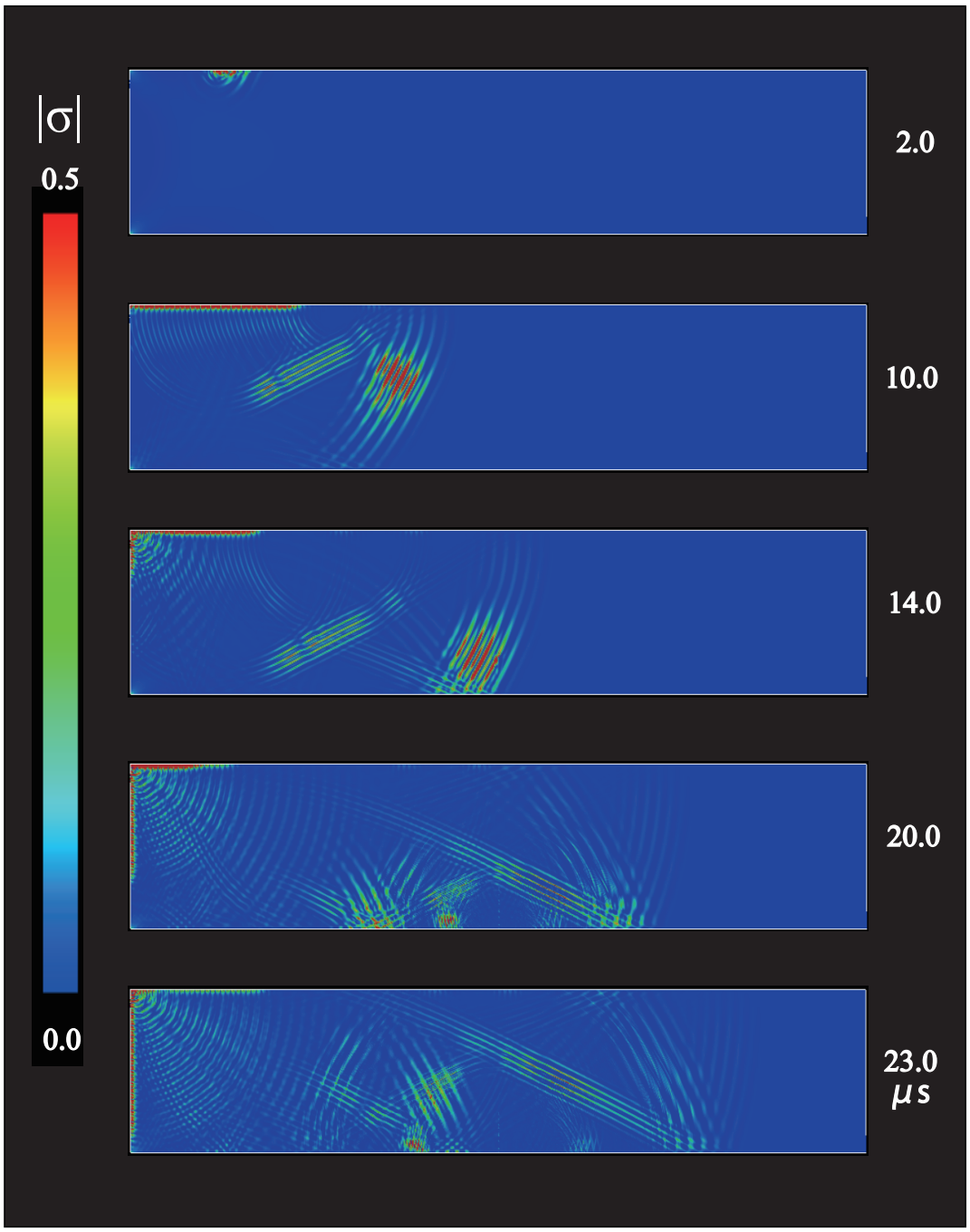

Fig. B.39 Visualization at the incident angle of 60° in the case of $\eta = 0.2$ for the closed crack with a height of 10 mm.

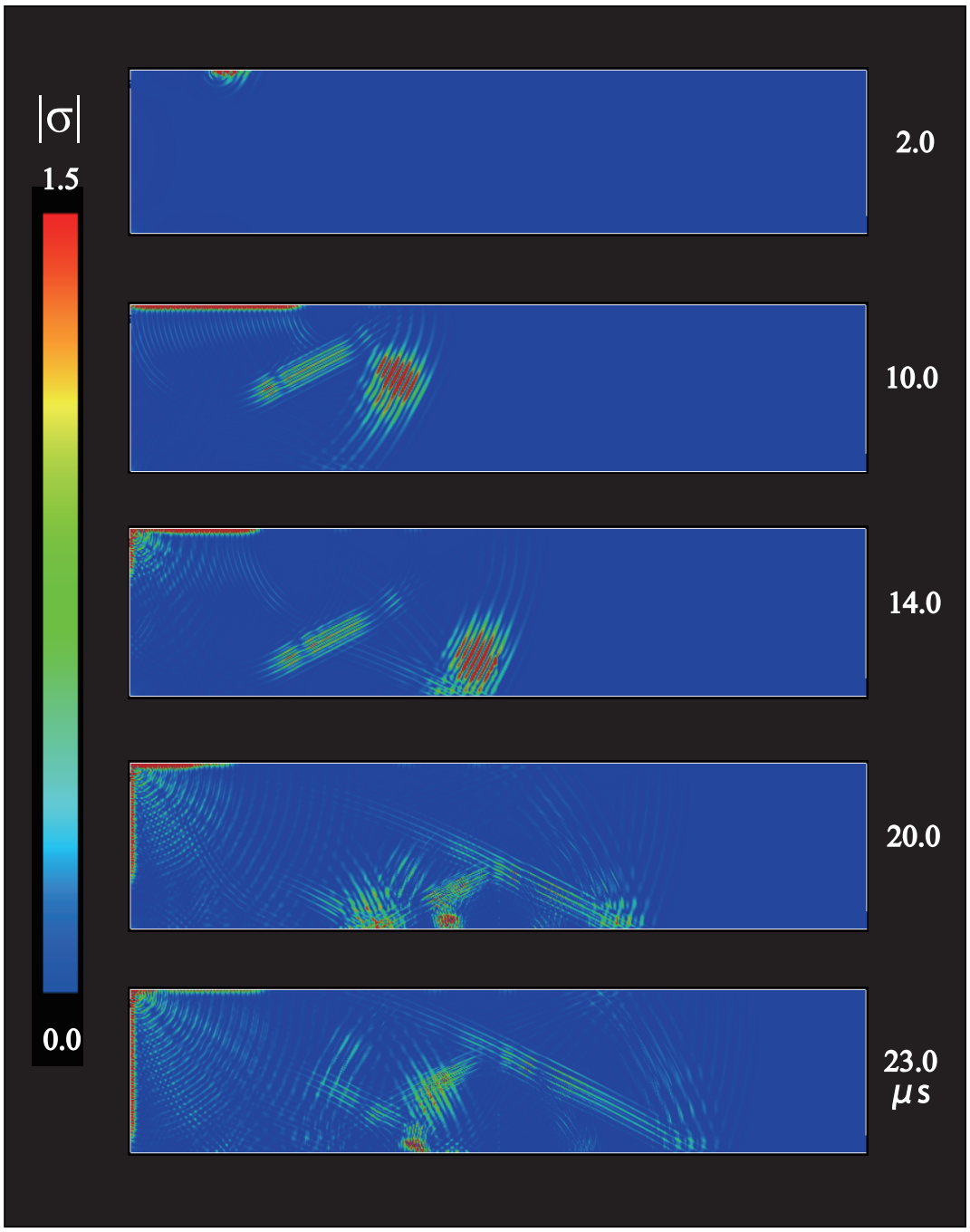

Fig. B.40 Visualization at the incident angle of 60° in the case of $\eta = 0.1$ for the closed crack with a height of 10 mm.

(3) Visualization of the scattered wave propagation for the closed crack with a height of 15 mm.

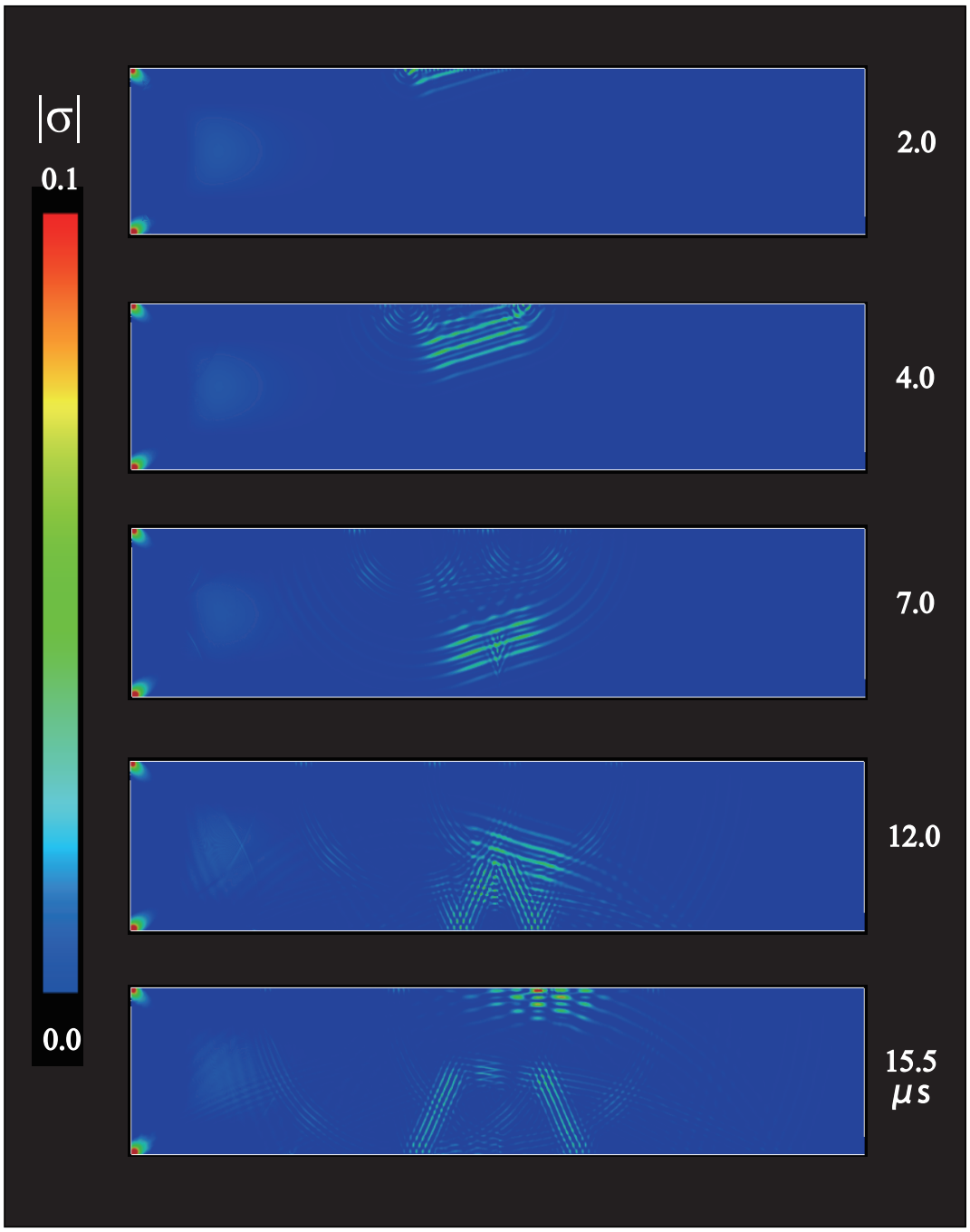

Fig. B.41 Visualization at the incident angle of 15° in the case of $\eta = 1.6$ for the closed crack with a height of 15 mm.

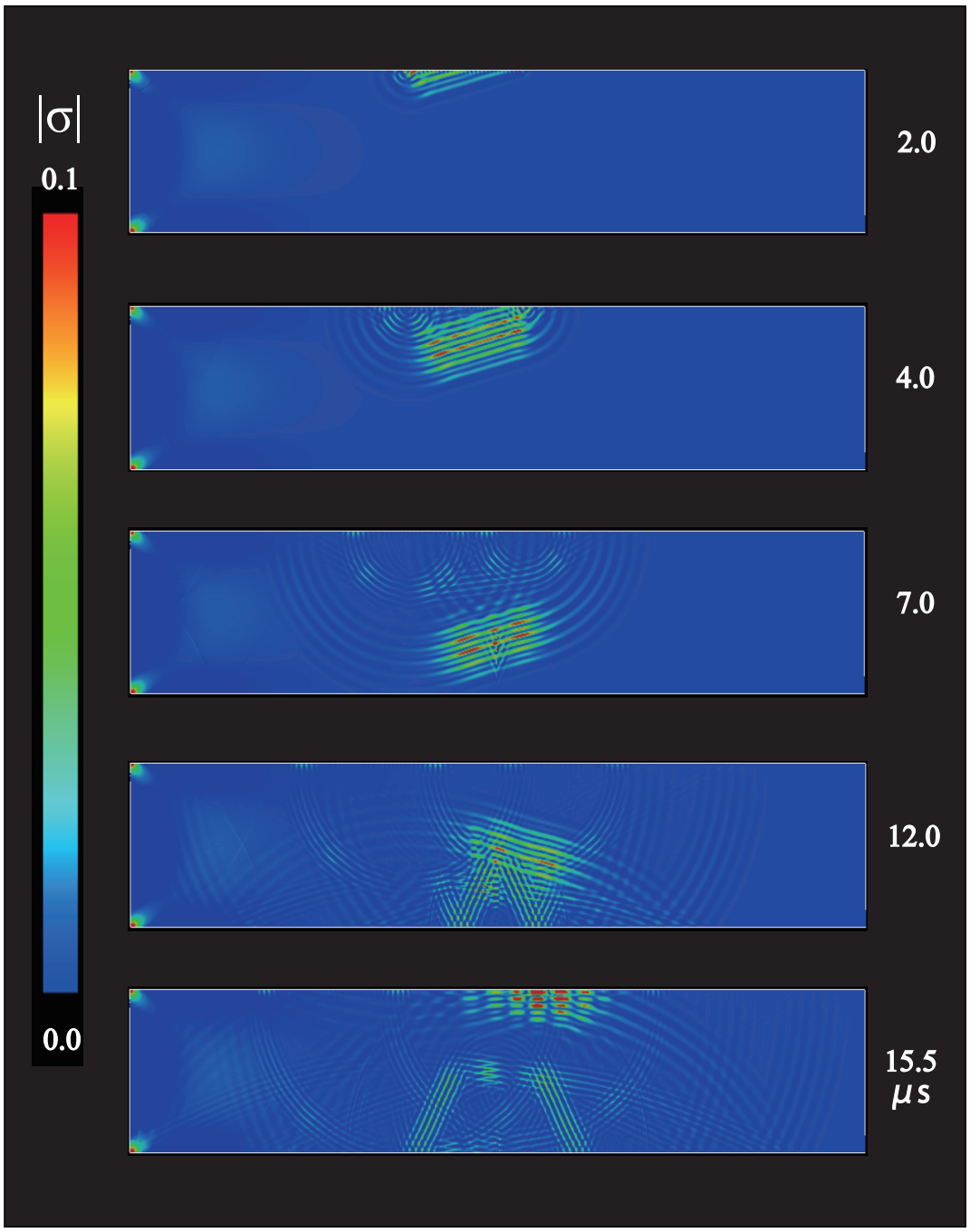

Fig. B.42 Visualization at the incident angle of 15° in the case of $\eta = 0.8$ for the closed crack with a height of 15 mm.

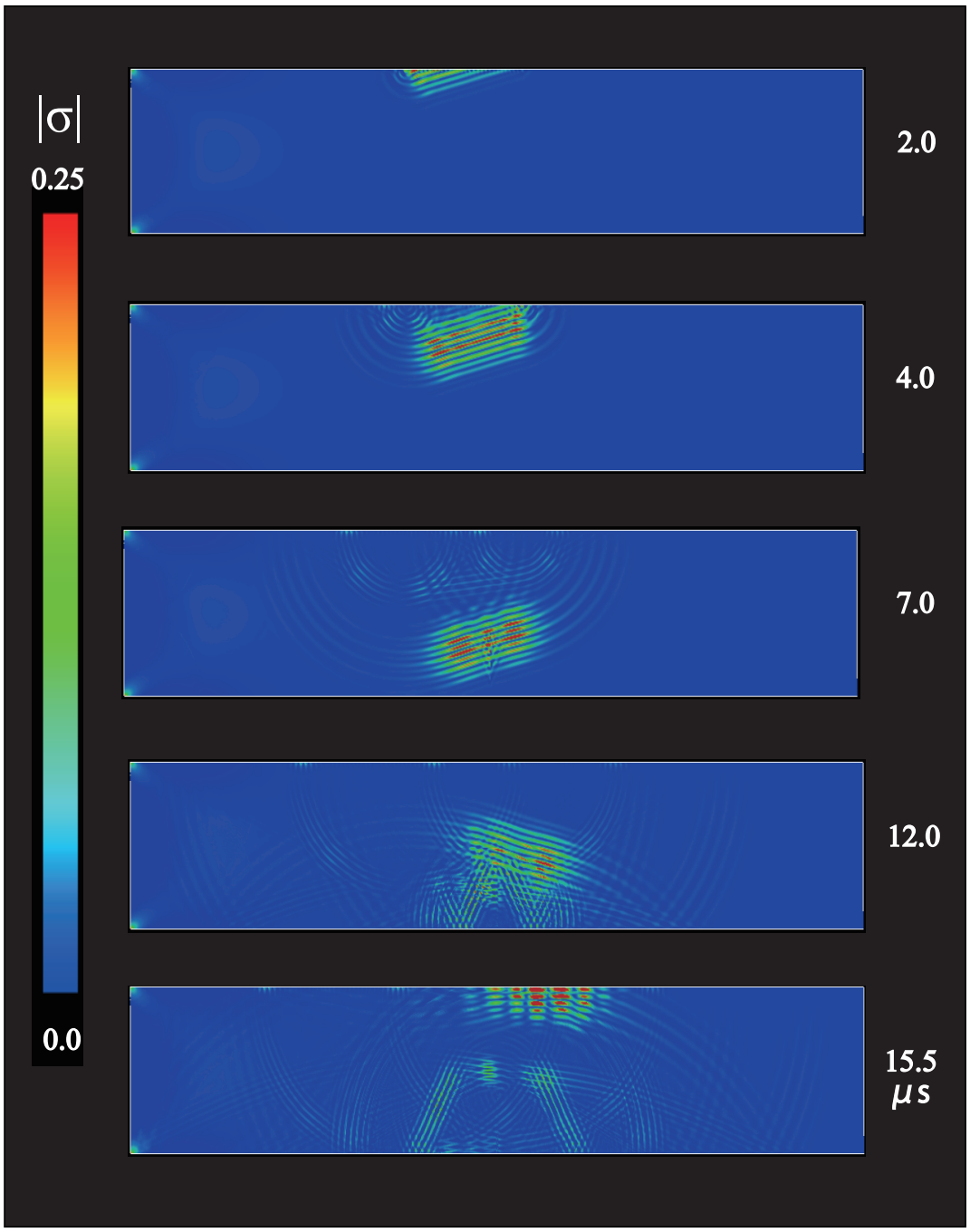

Fig. B.43 Visualization at the incident angle of 15° in the case of $\eta = 0.4$ for the closed crack with a height of 15 mm.

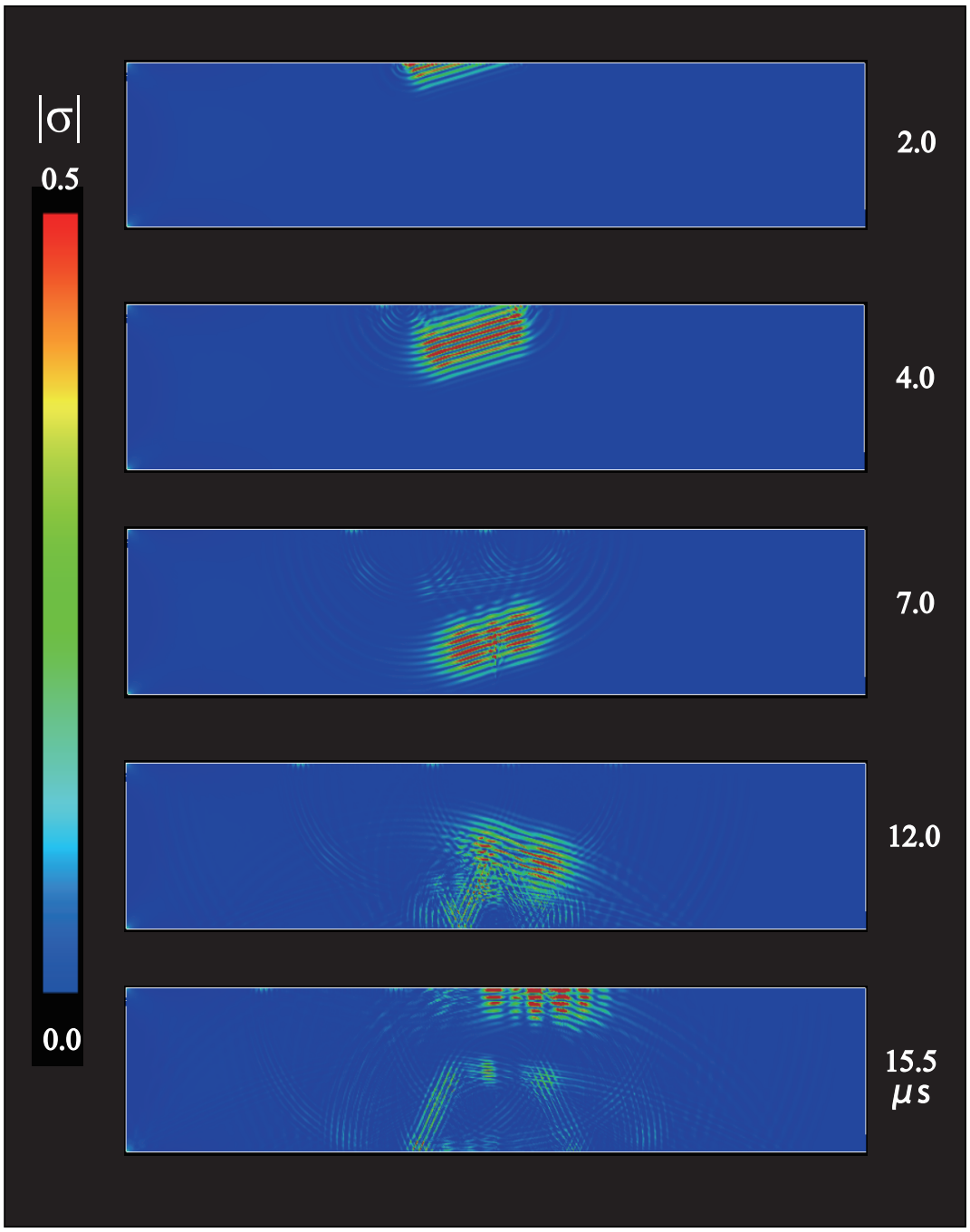

Fig. B.44 Visualization at the incident angle of 15° in the case of $\eta = 0.2$ for the closed crack with a height of 15 mm.

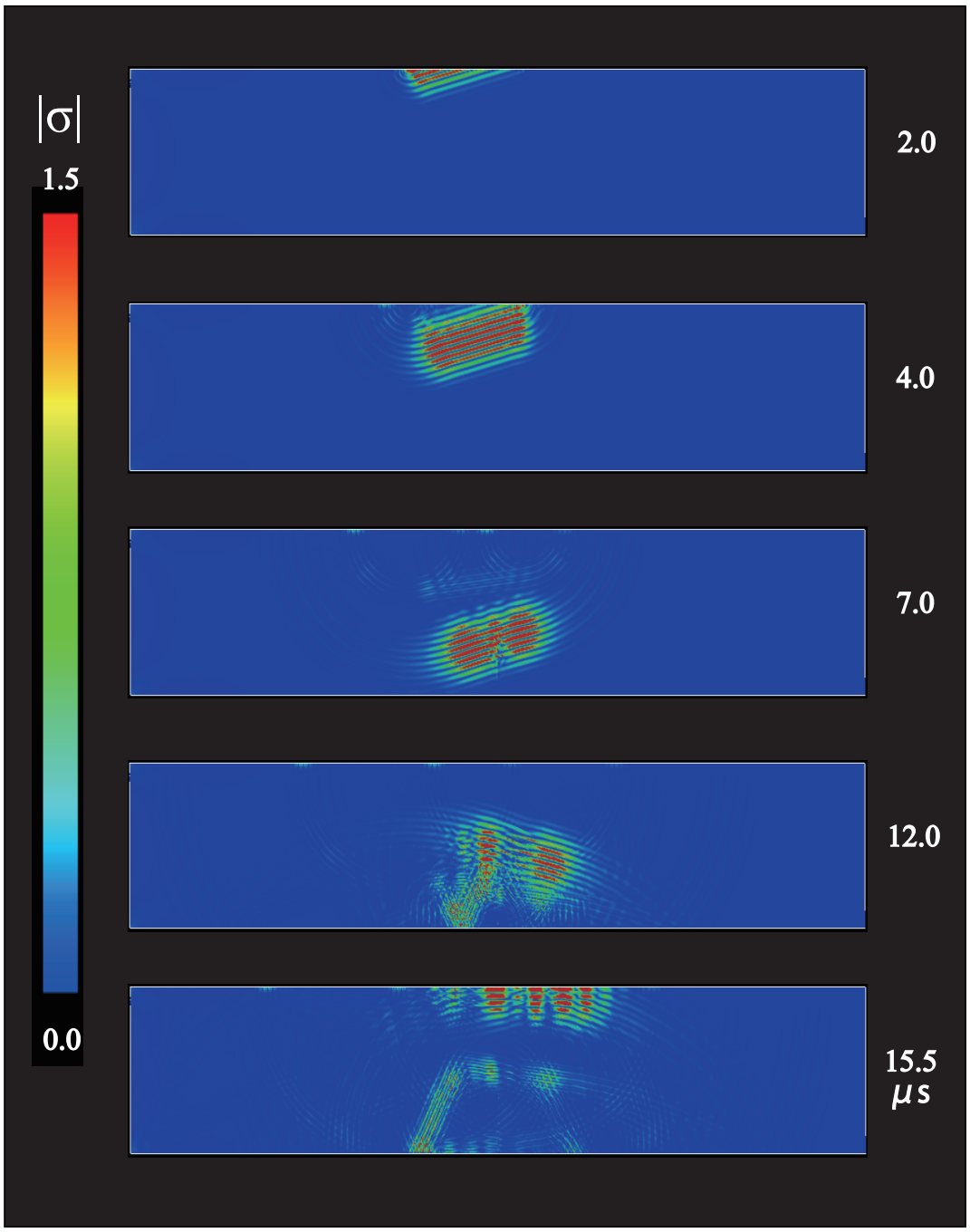

Fig. B.45 Visualization at the incident angle of 15° in the case of $\eta = 0.1$ for the closed crack with a height of 15 mm.

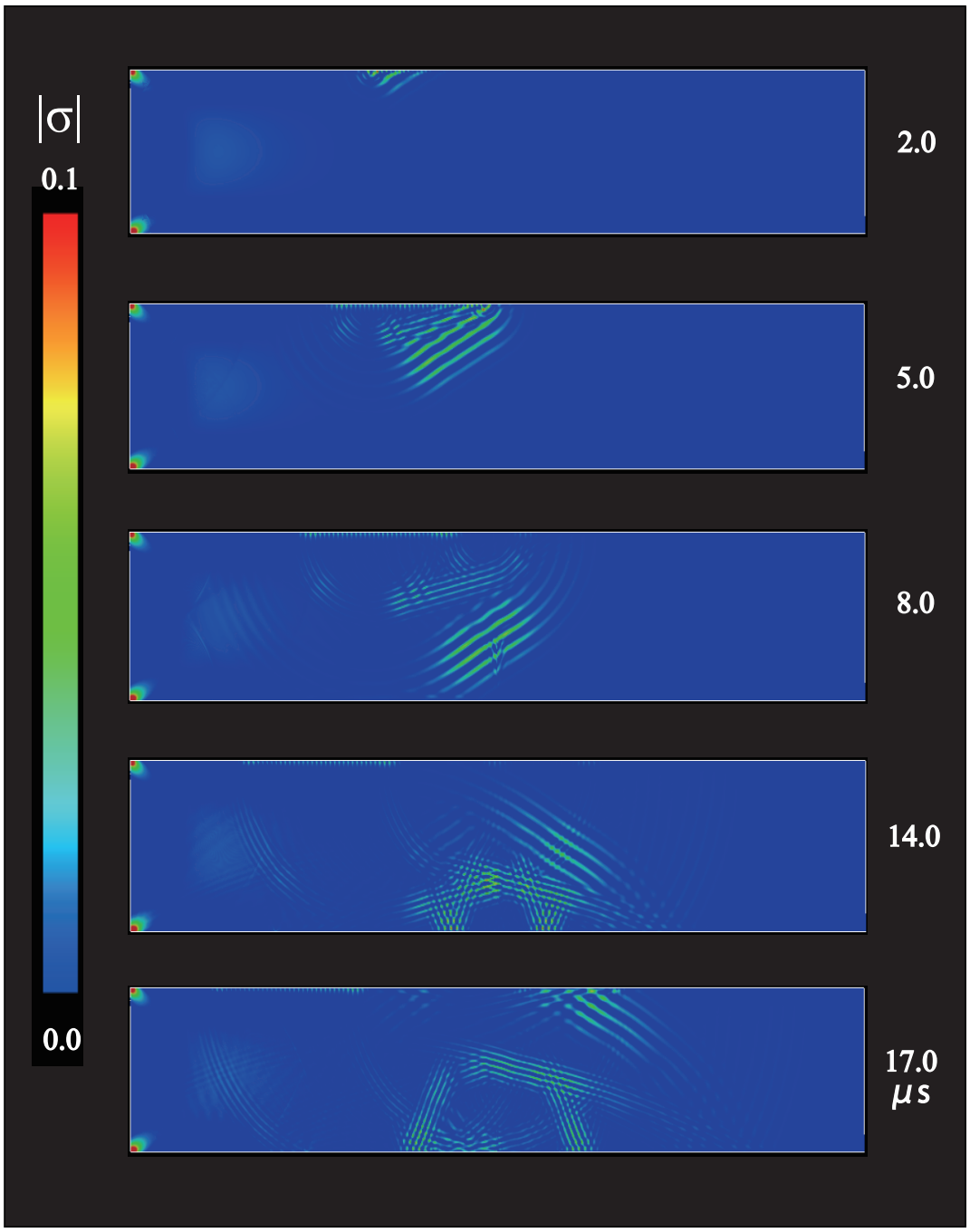

Fig. B.46 Visualization at the incident angle of 30° in the case of $\eta = 1.6$ for the closed crack with a height of 15 mm.

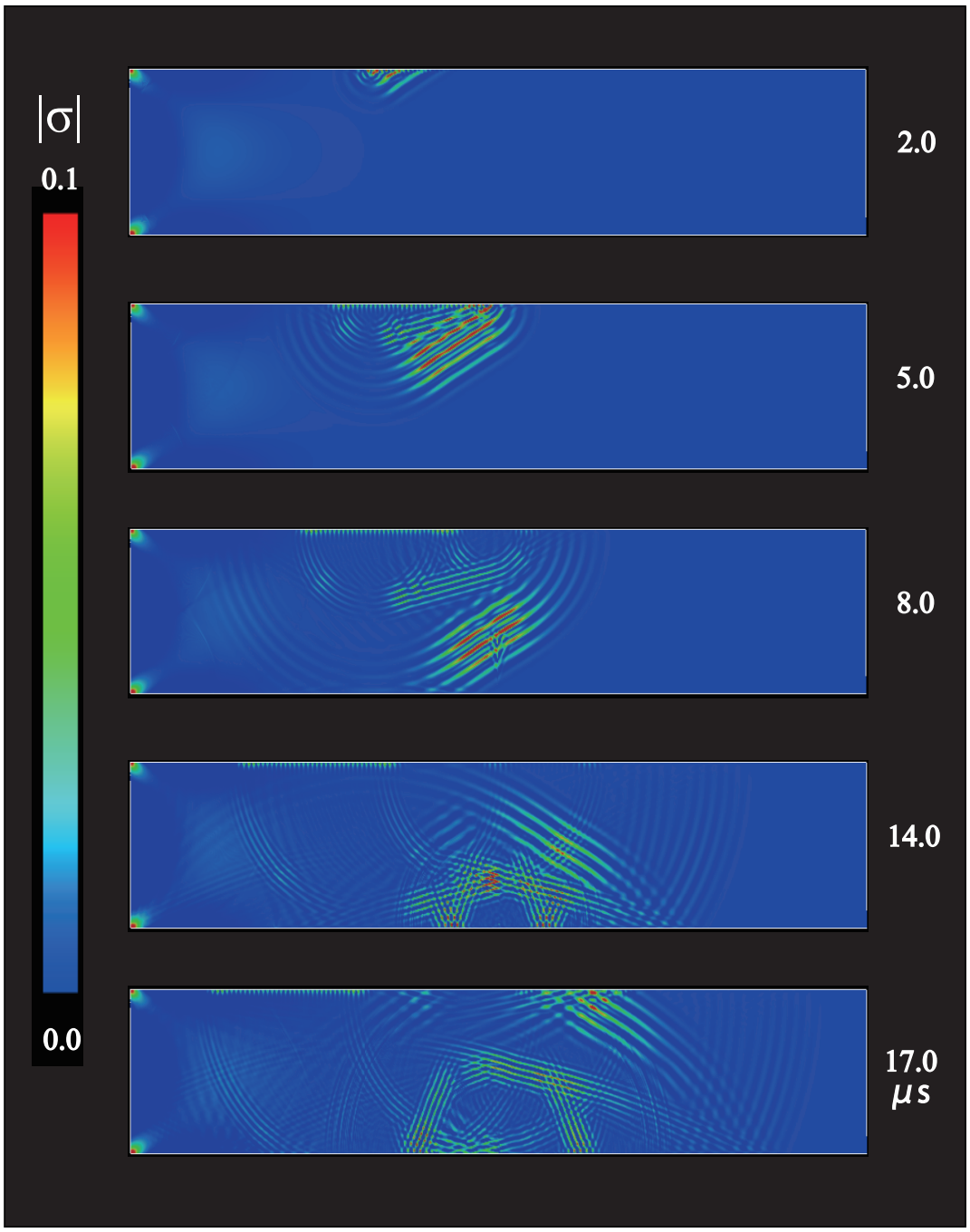

Fig. B.47 Visualization at the incident angle of 30° in the case of $\eta = 0.8$ for the closed crack with a height of 15 mm.

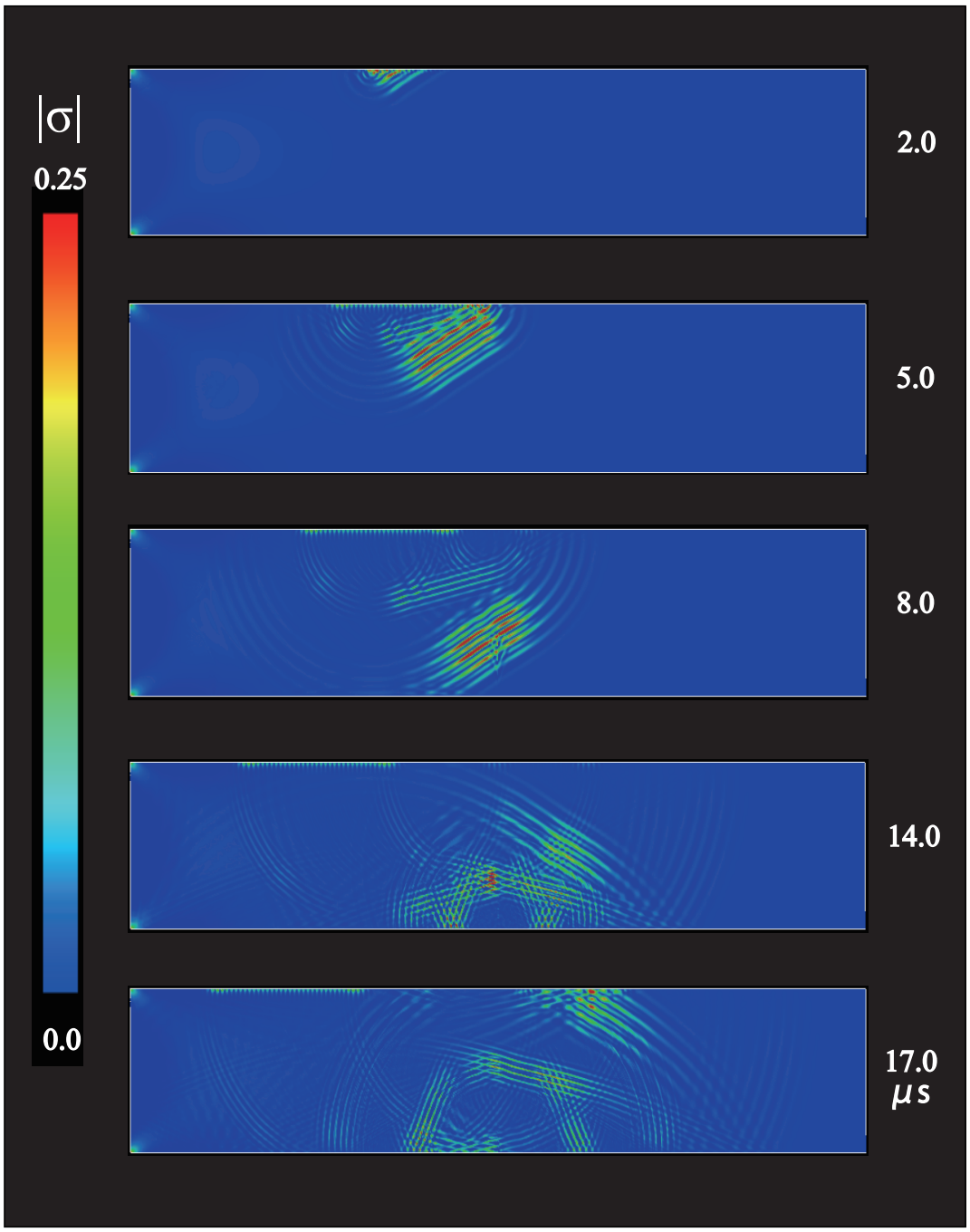

Fig. B.48 Visualization at the incident angle of 30° in the case of $\eta = 0.4$ for the closed crack with a height of 15 mm.

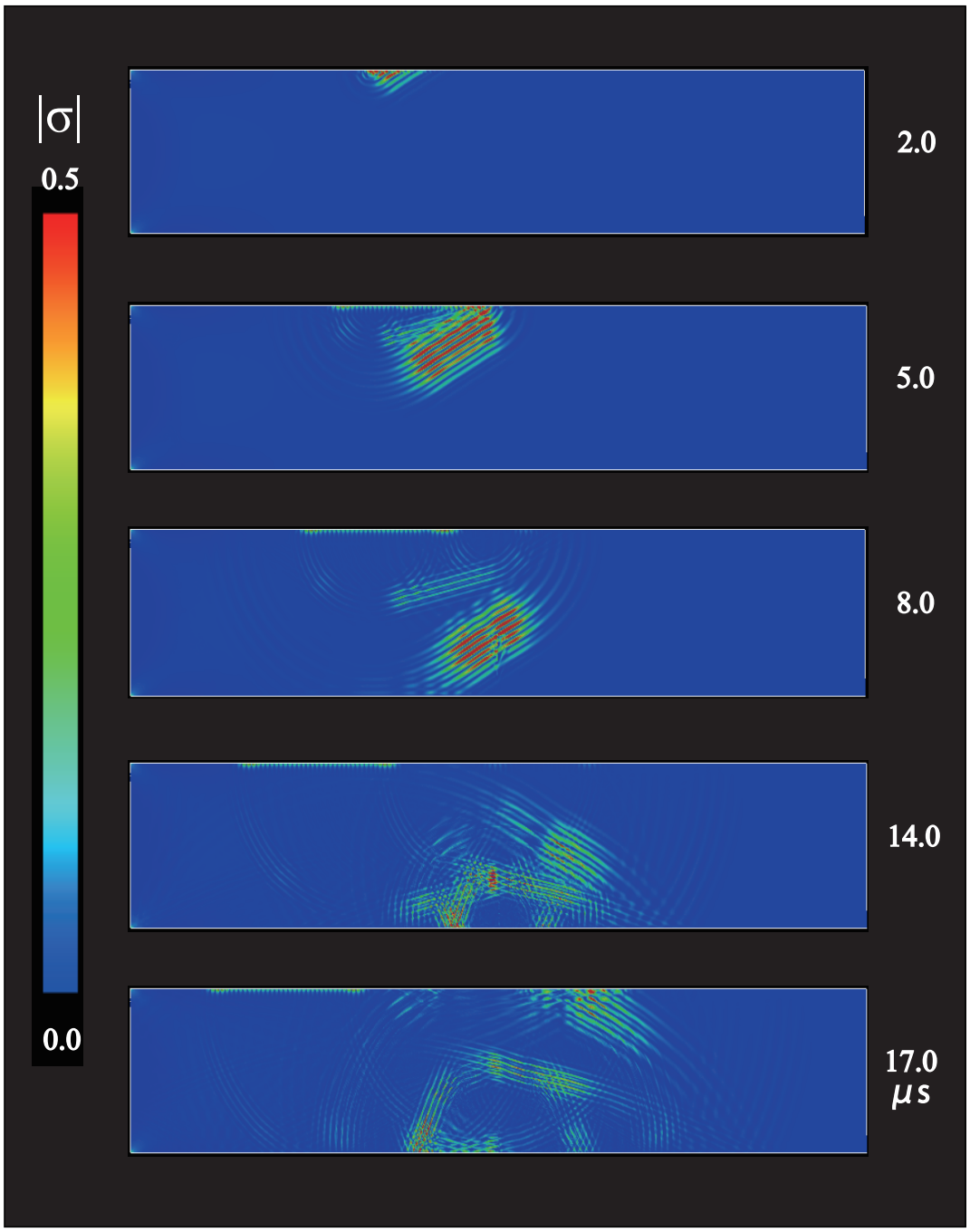

Fig. B.49 Visualization at the incident angle of 30° in the case of $\eta = 0.2$ for the closed crack with a height of 15 mm.

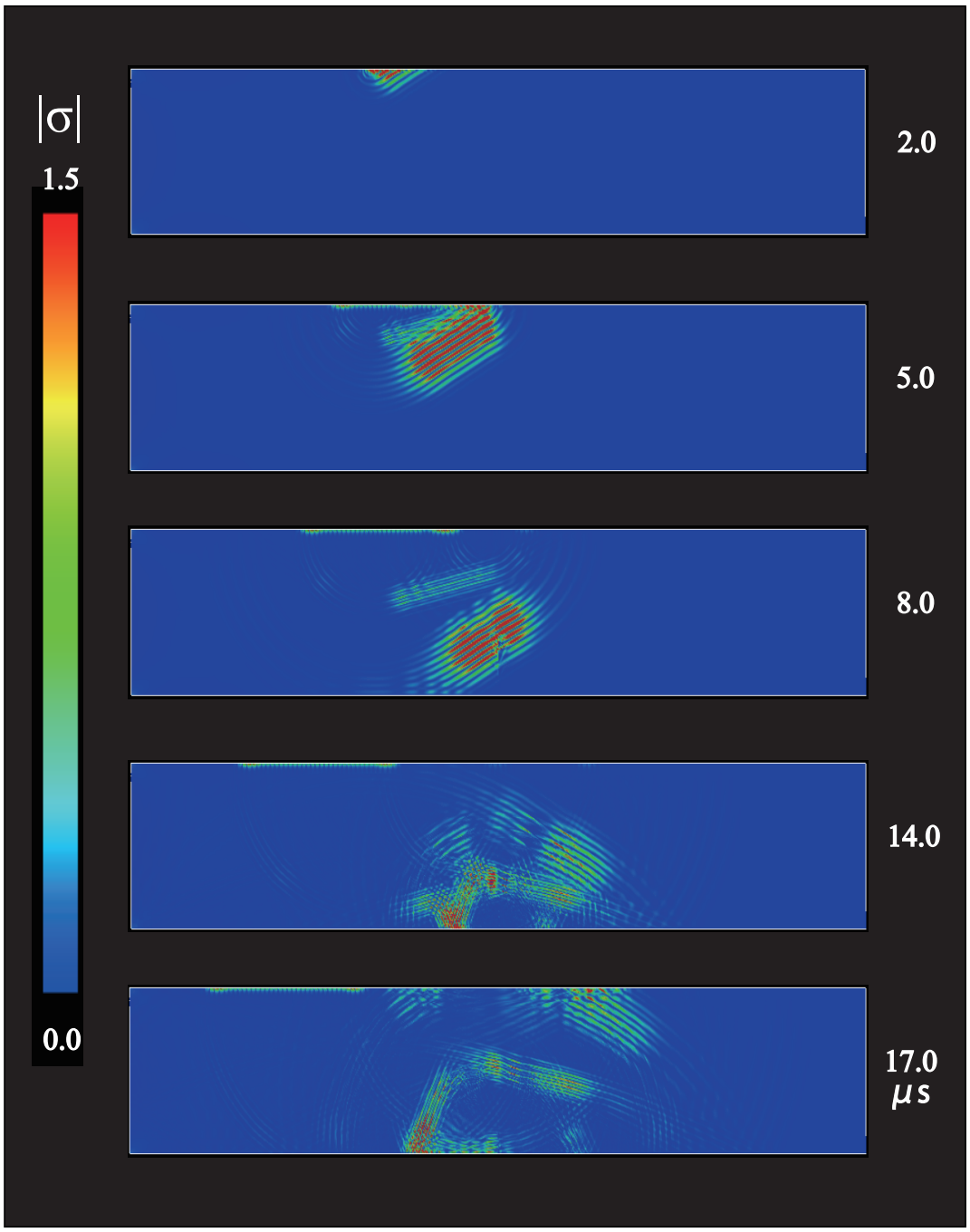

Fig. B.50 Visualization at the incident angle of 30° in the case of $\eta = 0.1$ for the closed crack with a height of 15 mm.

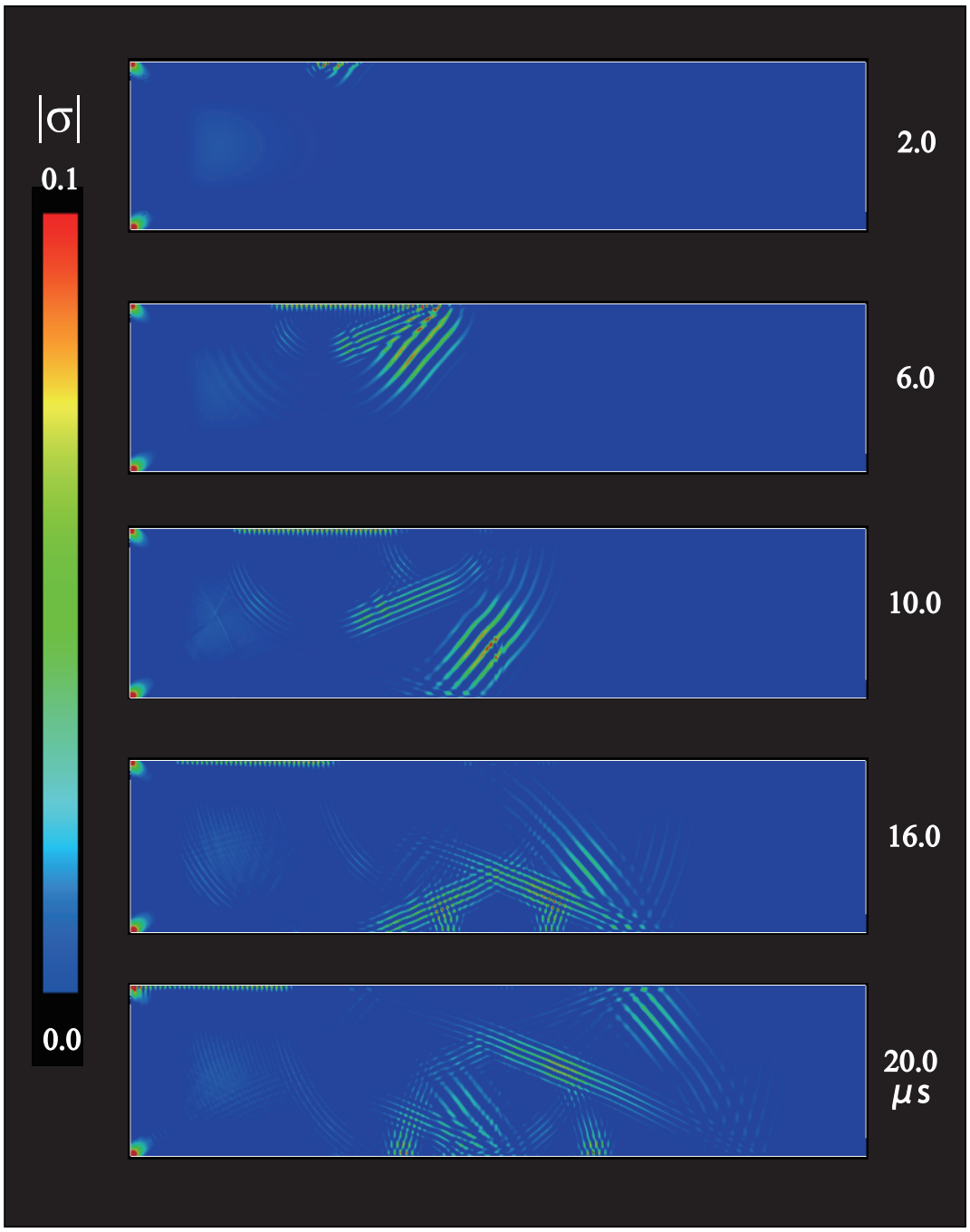

Fig. B.51 Visualization at the incident angle of 45° in the case of $\eta = 1.6$ for the closed crack with a height of 15 mm.

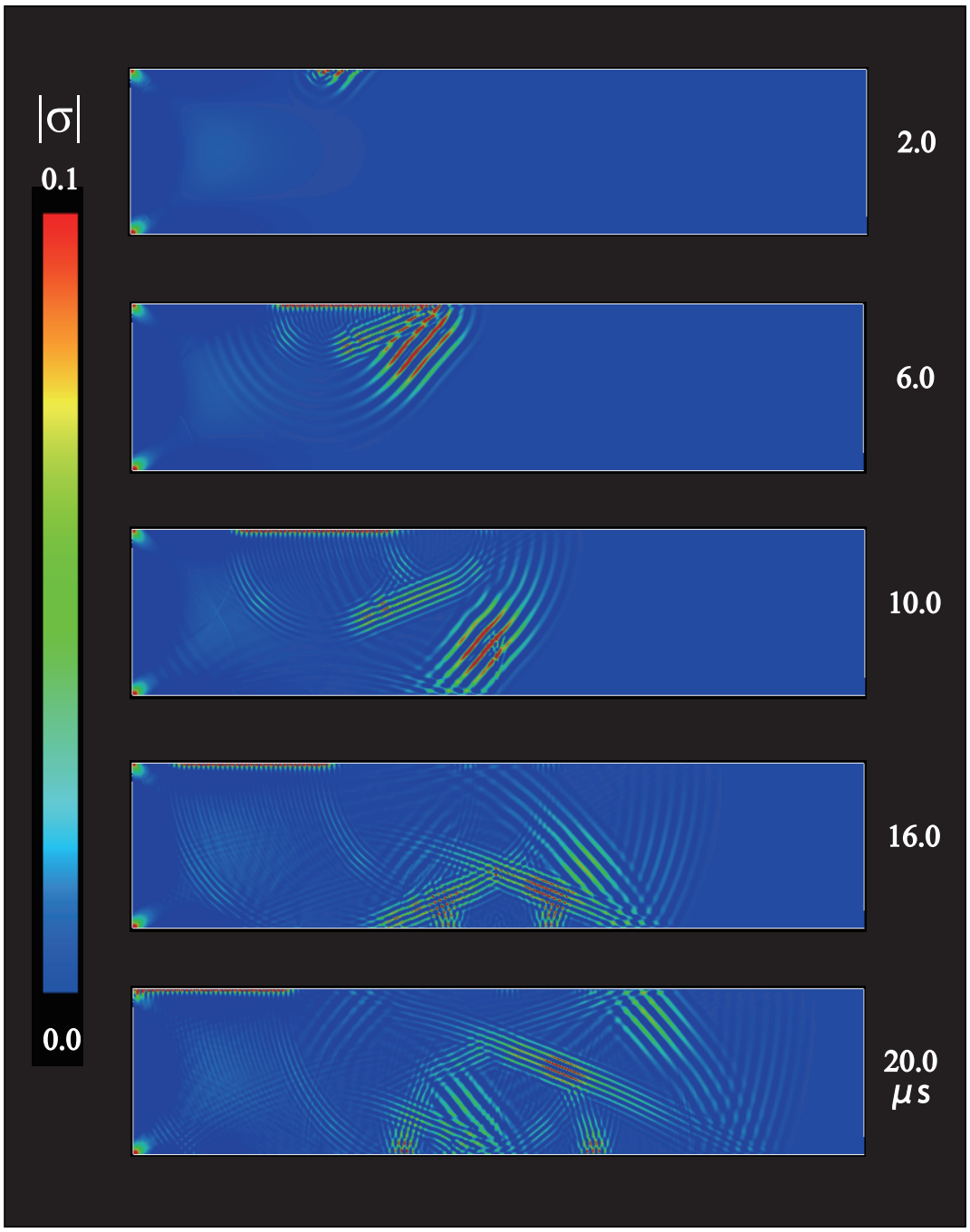

Fig. B.52 Visualization at the incident angle of 45° in the case of $\eta = 0.8$ for the closed crack with a height of 15 mm.

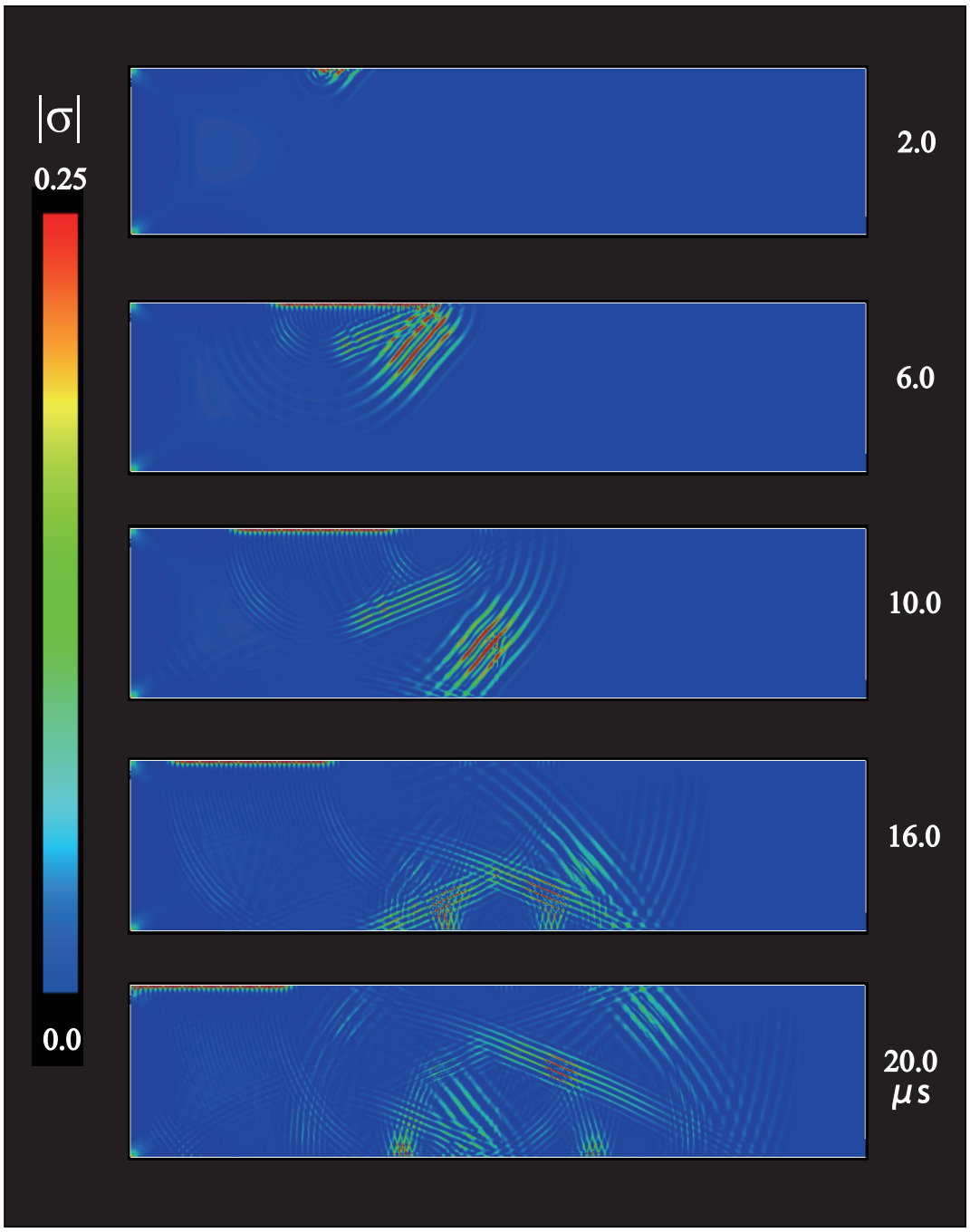

Fig. B.53 Visualization at the incident angle of 45° in the case of $\eta = 0.4$ for the closed crack with a height of 15 mm.

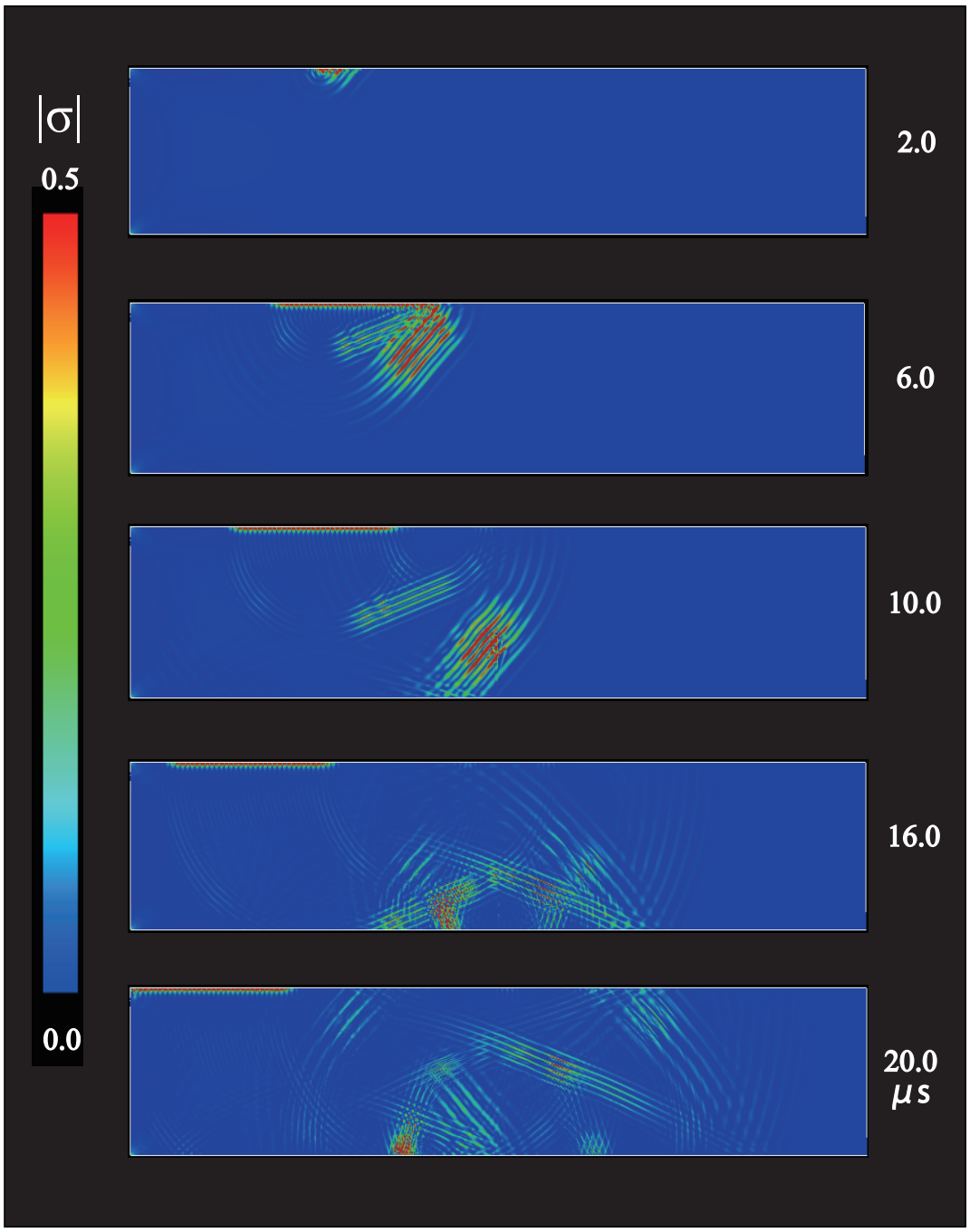

Fig. B.54 Visualization at the incident angle of 45° in the case of $\eta = 0.2$ for the closed crack with a height of 15 mm.

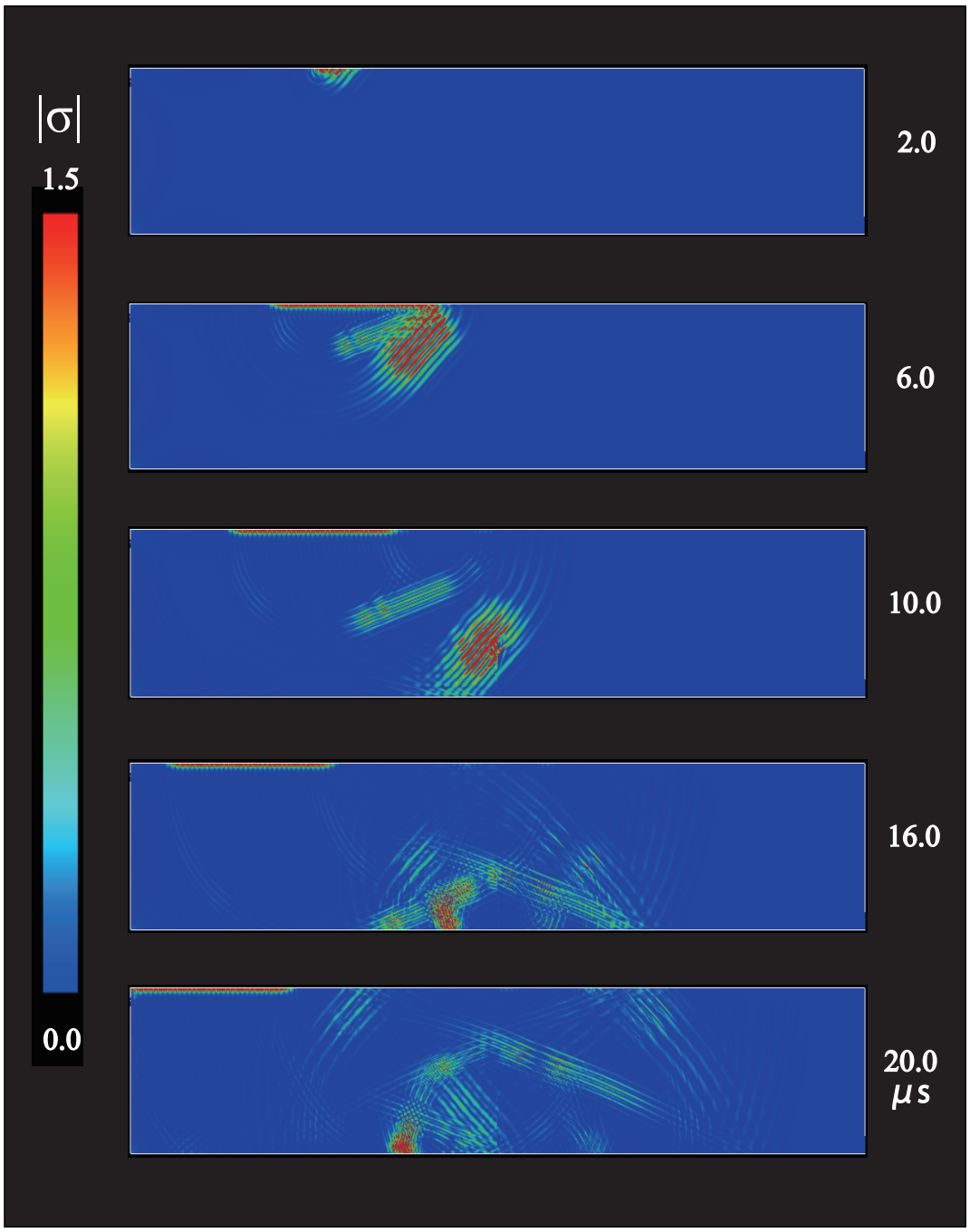

Fig. B.55 Visualization at the incident angle of 45° in the case of $\eta = 0.1$ for the closed crack with a height of 15 mm.

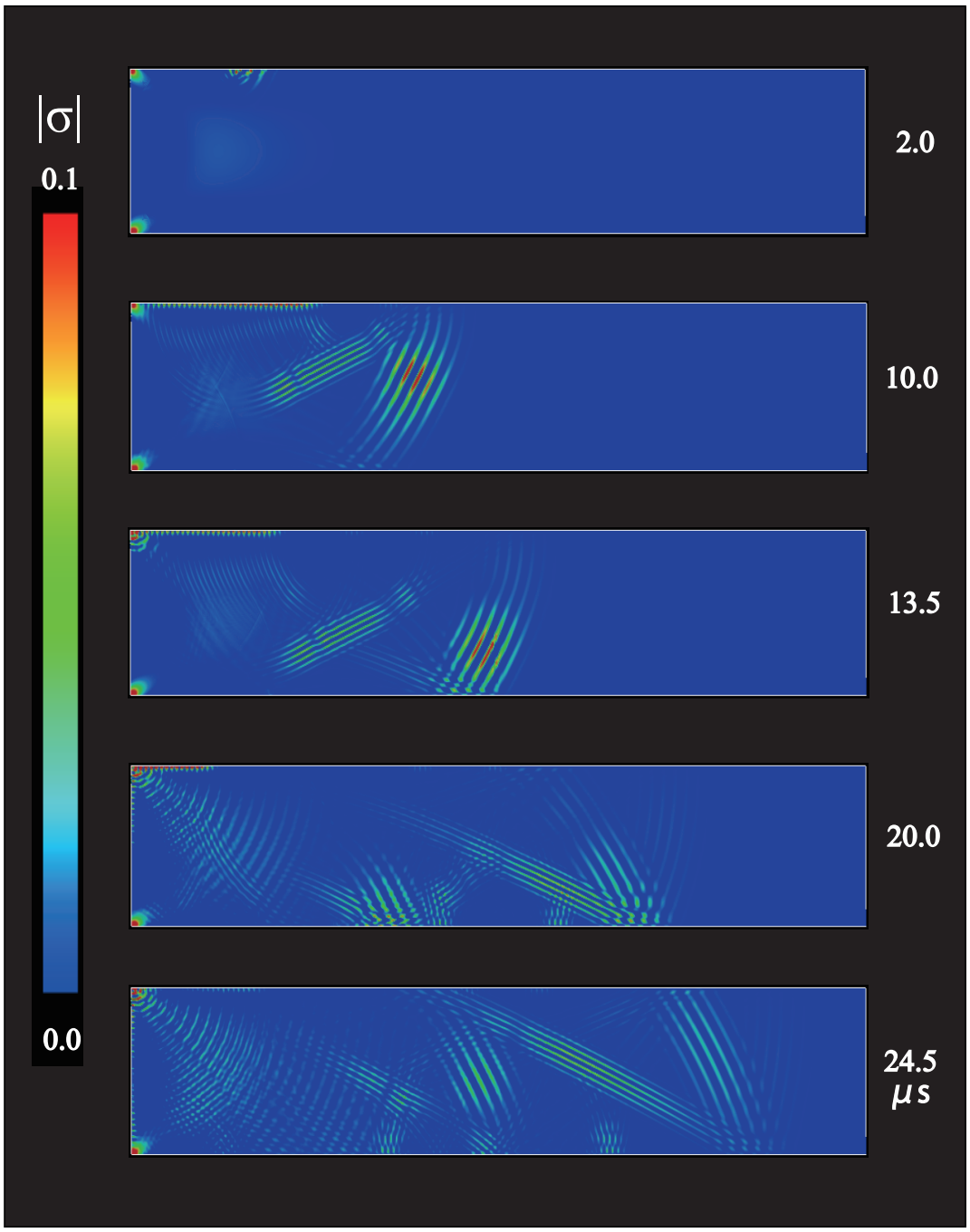

Fig. B.56 Visualization at the incident angle of 60° in the case of $\eta = 1.6$ for the closed crack with a height of 15 mm.

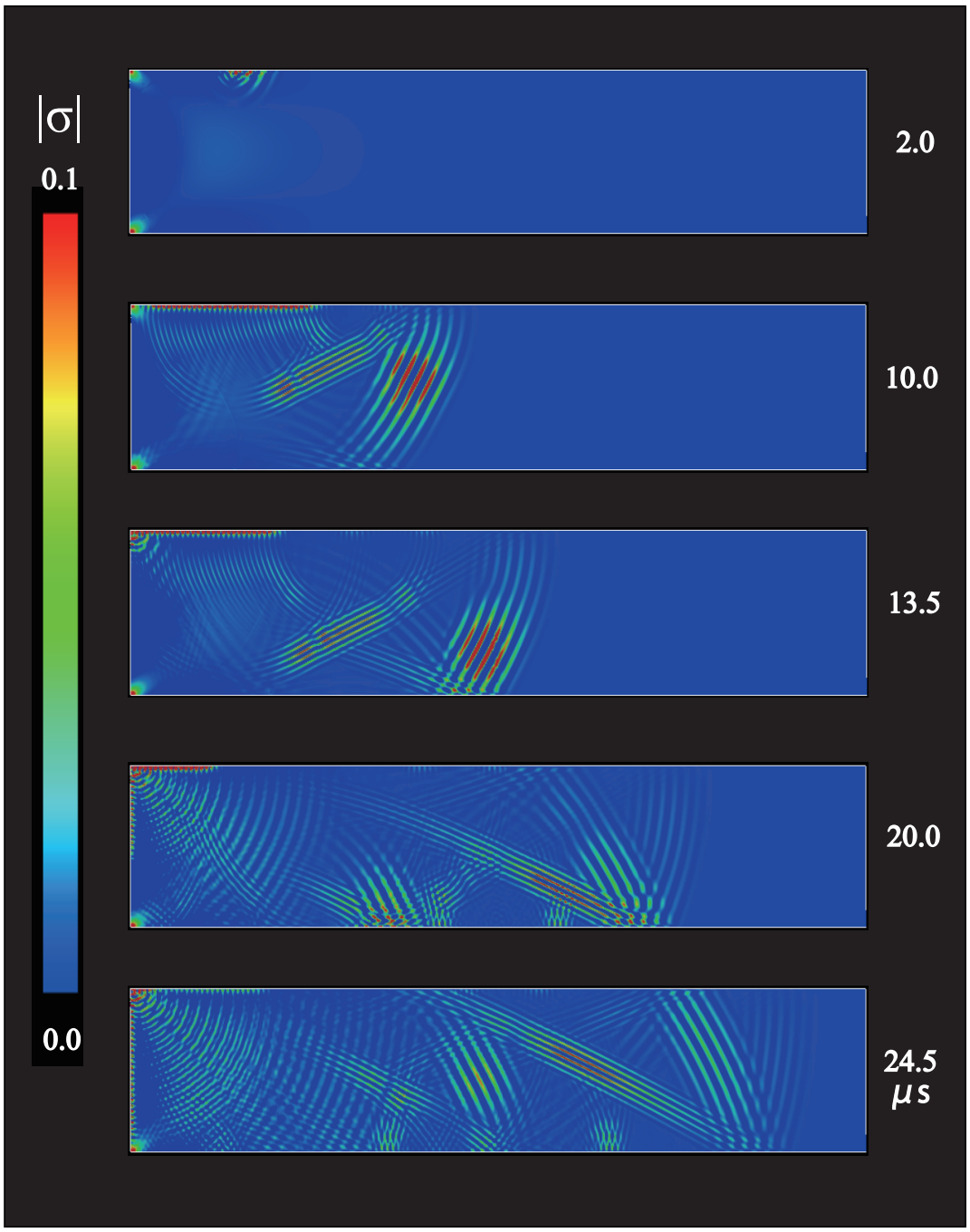

Fig. B.57 Visualization at the incident angle of 60° in the case of $\eta = 0.8$ for the closed crack with a height of 15 mm.

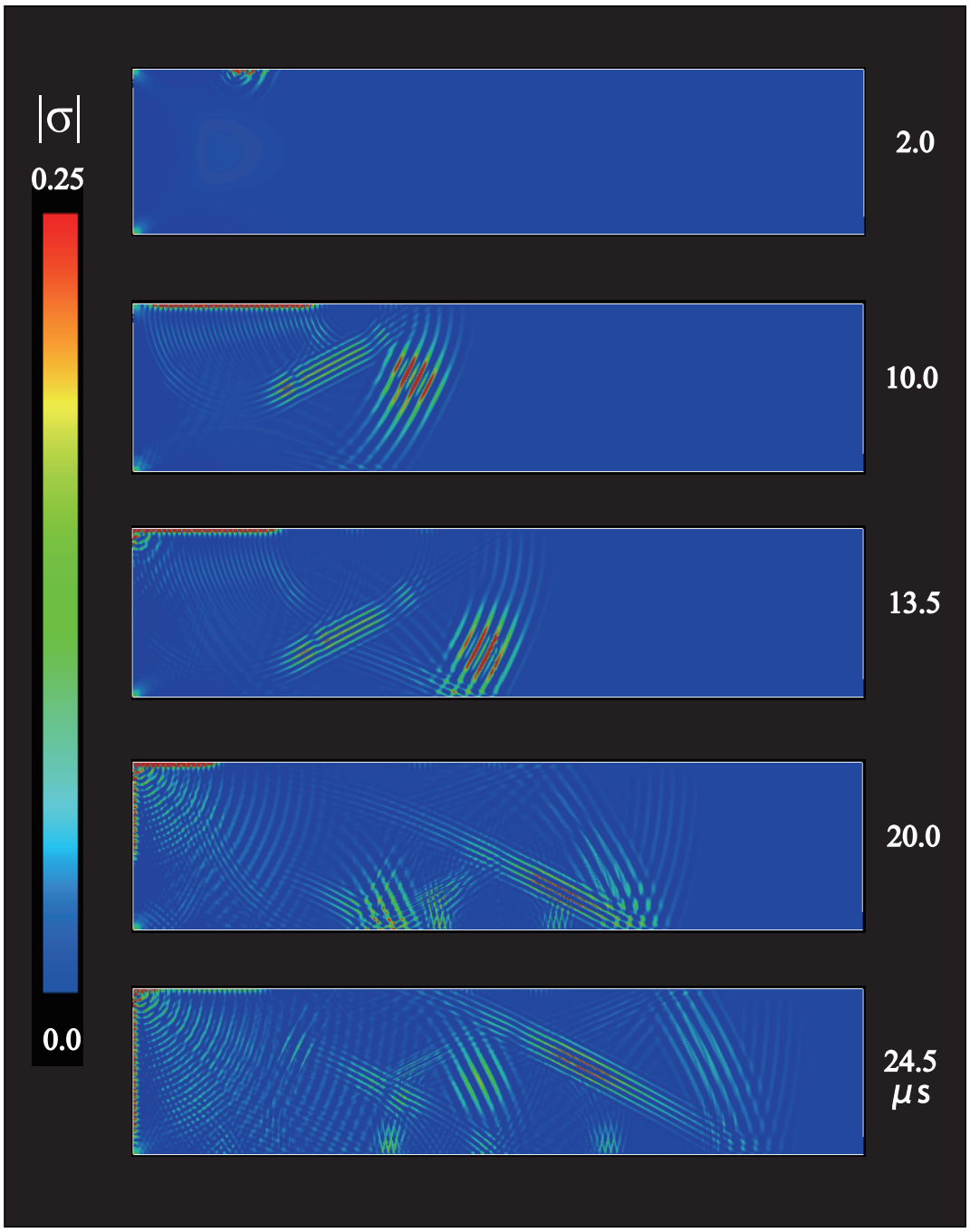

Fig. B.58 Visualization at the incident angle of 60° in the case of $\eta = 0.4$ for the closed crack with a height of 15 mm.

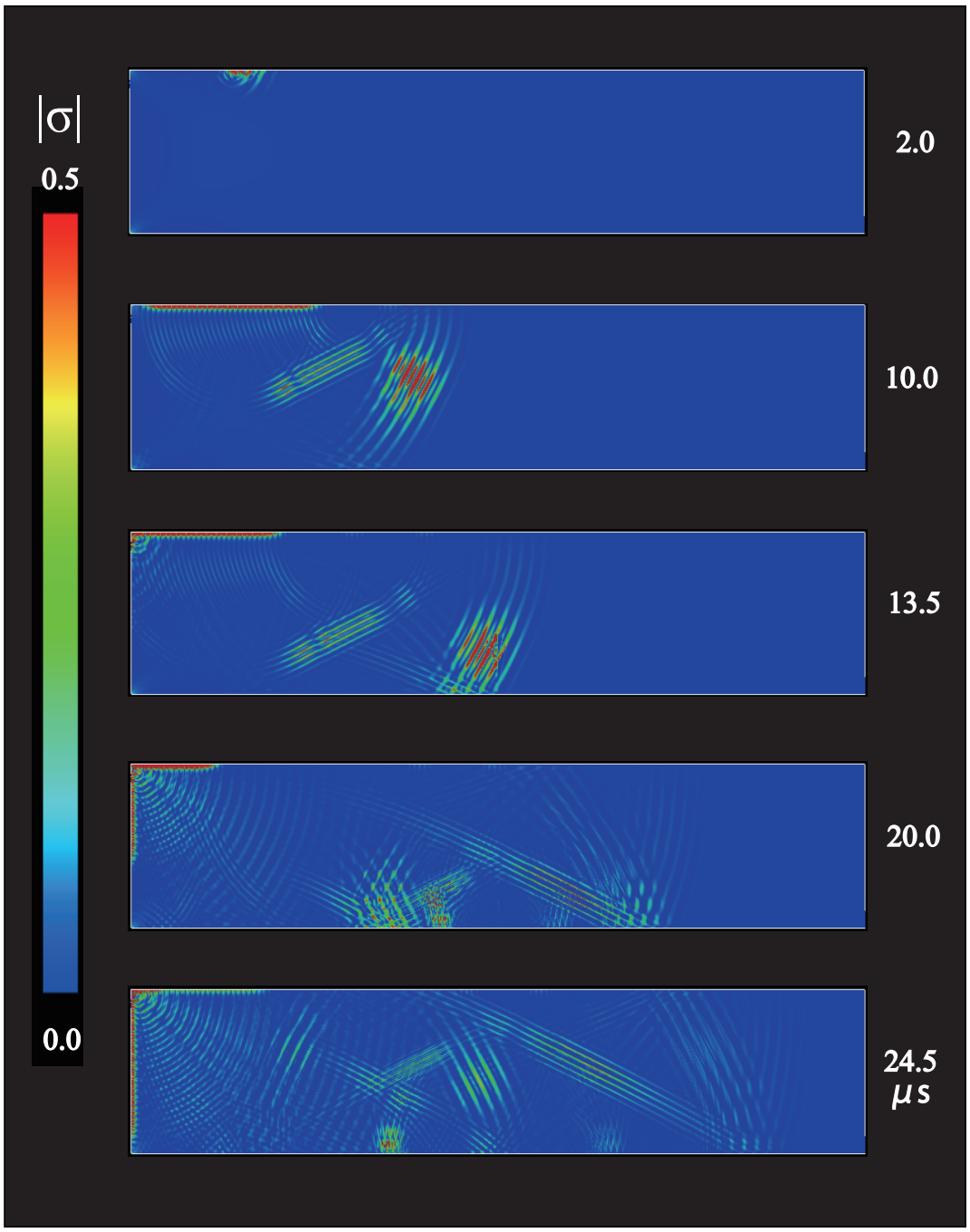

Fig. B.59 Visualization at the incident angle of 60° in the case of $\eta = 0.2$ for the closed crack with a height of 15 mm.

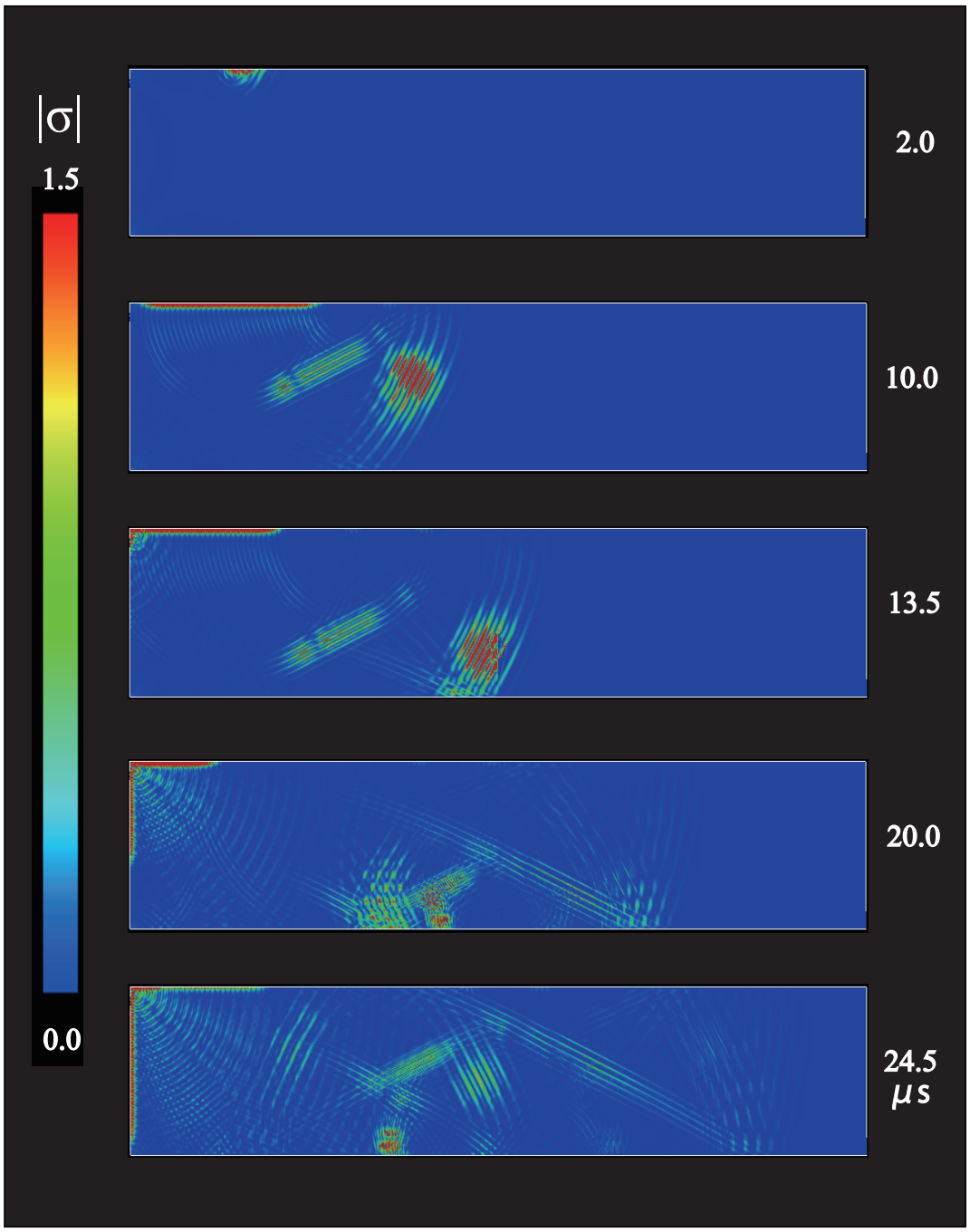

Fig. B.60 Visualization at the incident angle of 60° in the case of $\eta = 0.1$ for the closed crack with a height of 15 mm.

(4) Visualization of the scattered wave propagation for the closed crack with a height of 20 mm.

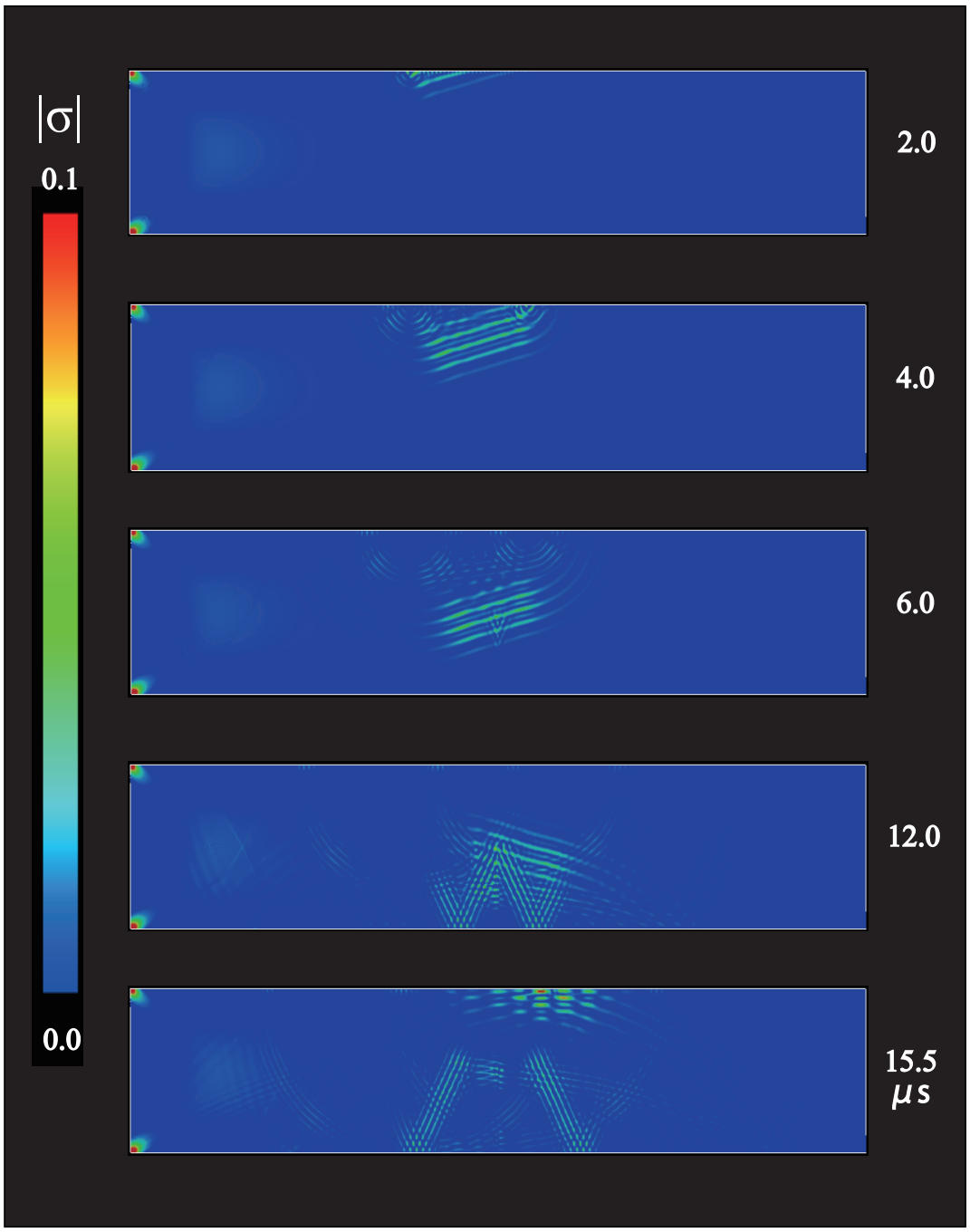

Fig. B.61 Visualization at the incident angle of 15° in the case of $\eta = 1.6$ for the closed crack with a height of 20 mm.

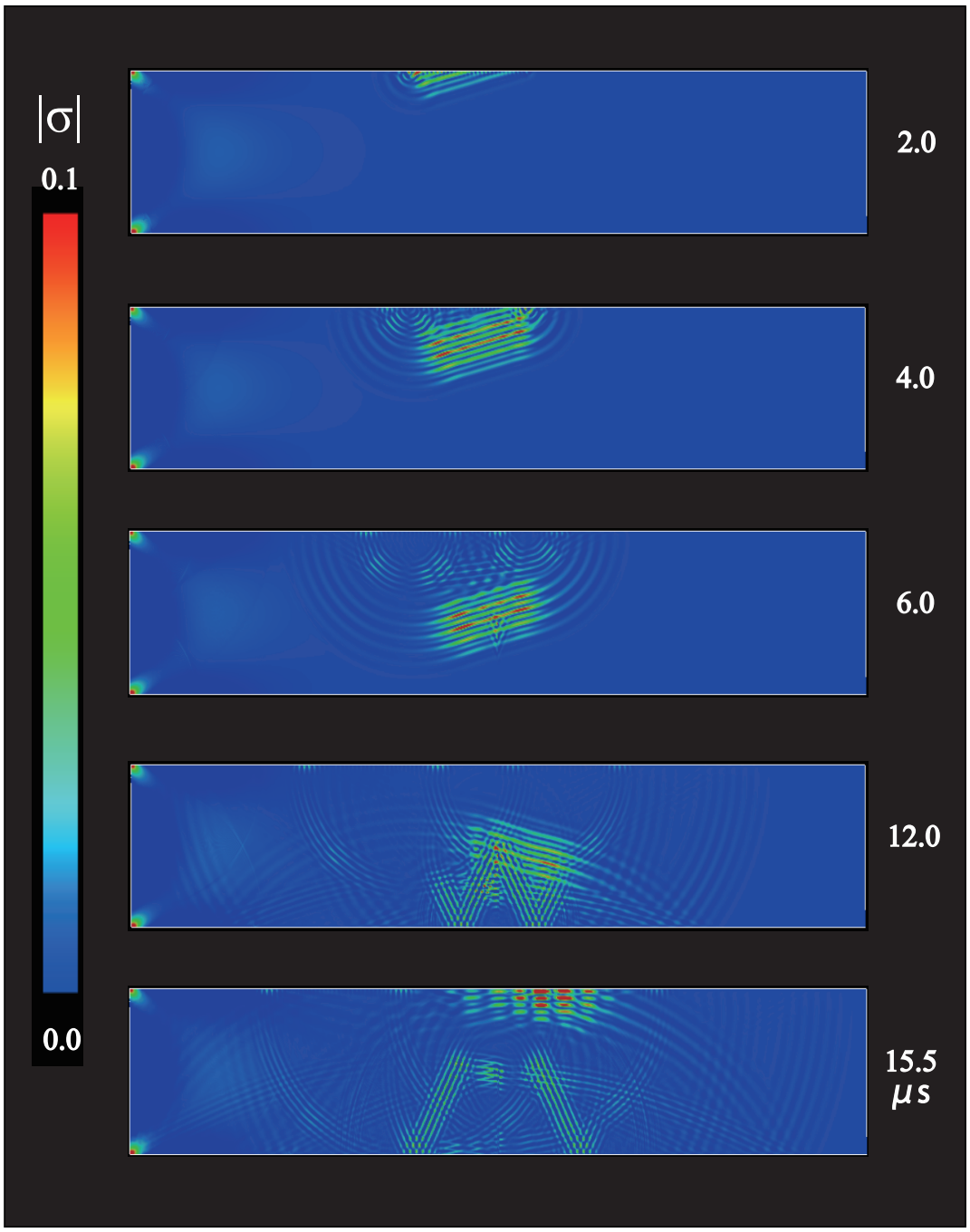

Fig. B.62 Visualization at the incident angle of 15° in the case of $\eta = 0.8$ for the closed crack with a height of 20 mm.

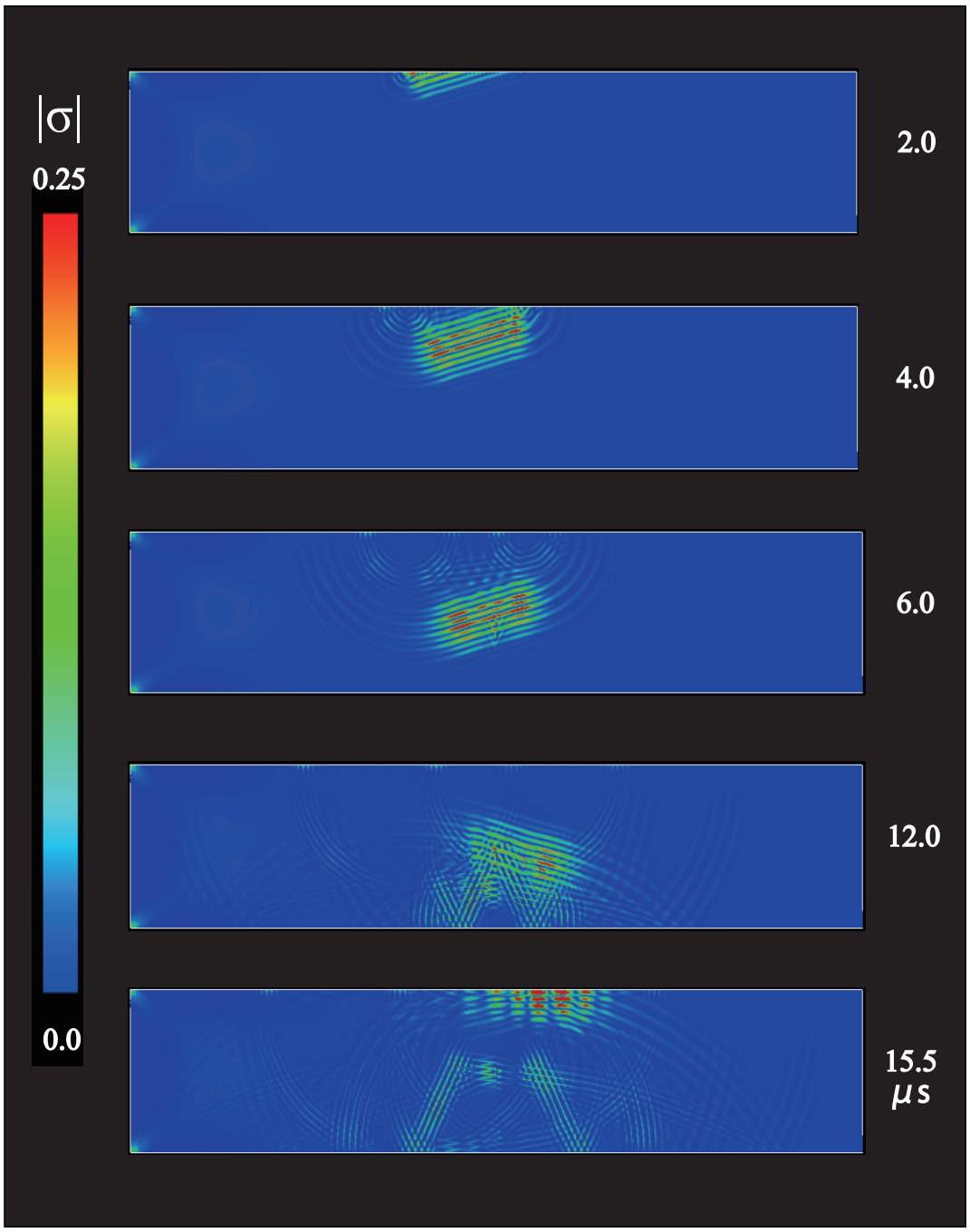

Fig. B.63 Visualization at the incident angle of 15° in the case of $\eta = 0.4$ for the closed crack with a height of 20 mm.

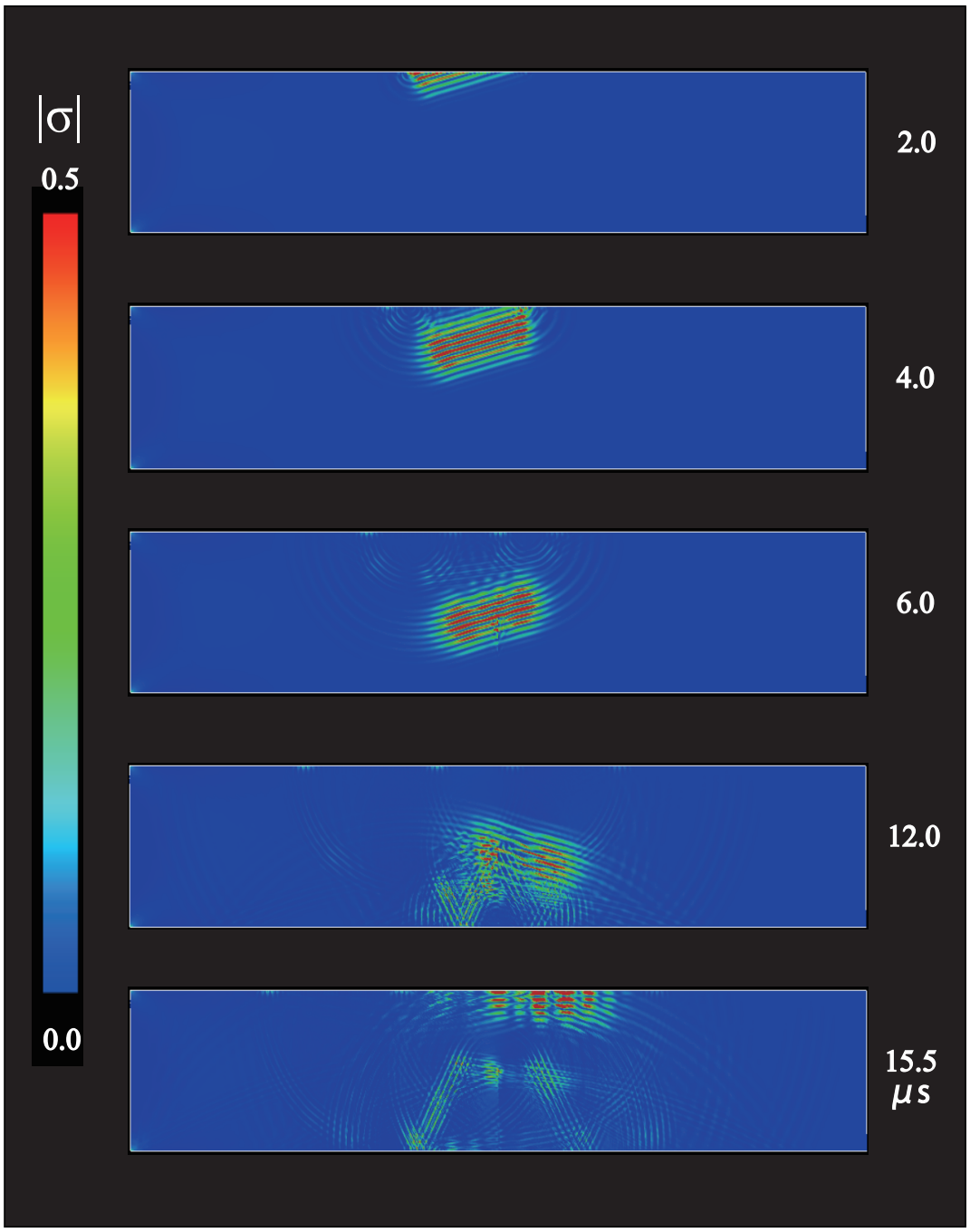

Fig. B.64 Visualization at the incident angle of 15° in the case of $\eta = 0.2$ for the closed crack with a height of 20 mm.

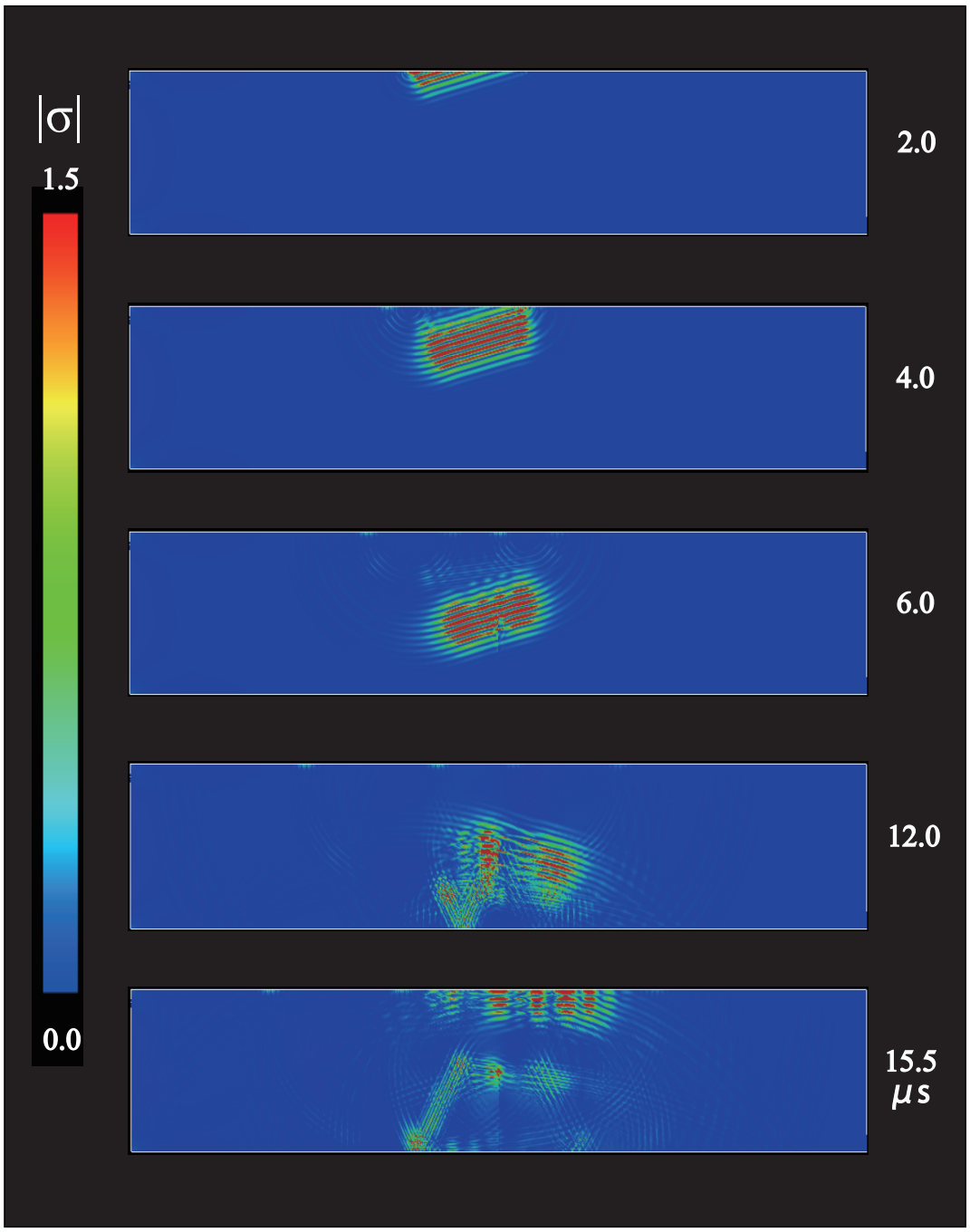

Fig. B.65 Visualization at the incident angle of 15° in the case of $\eta = 0.1$ for the closed crack with a height of 20 mm.

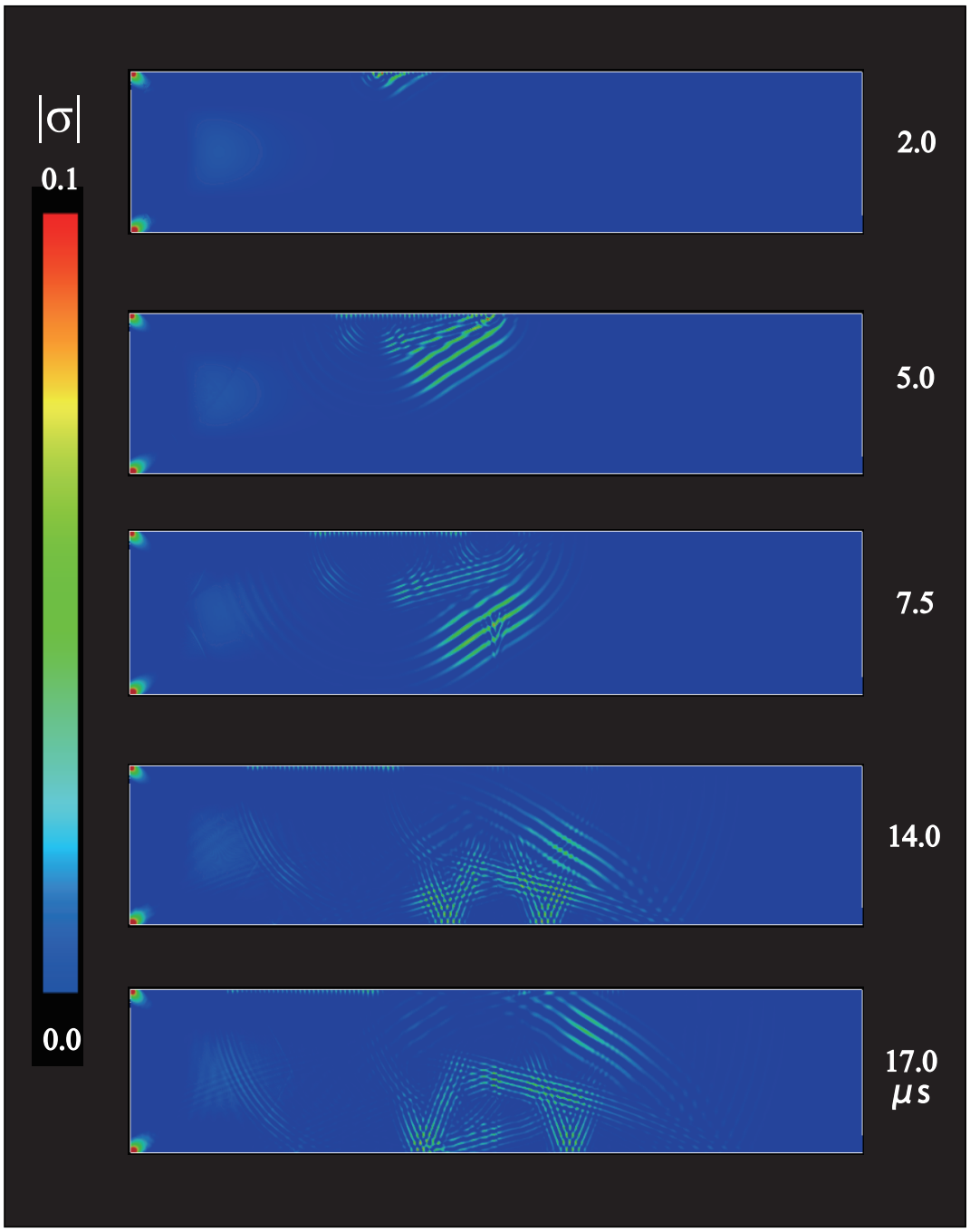

Fig. B.66 Visualization at the incident angle of 30° in the case of η = 1.6 for the closed crack with a height of 20 mm.

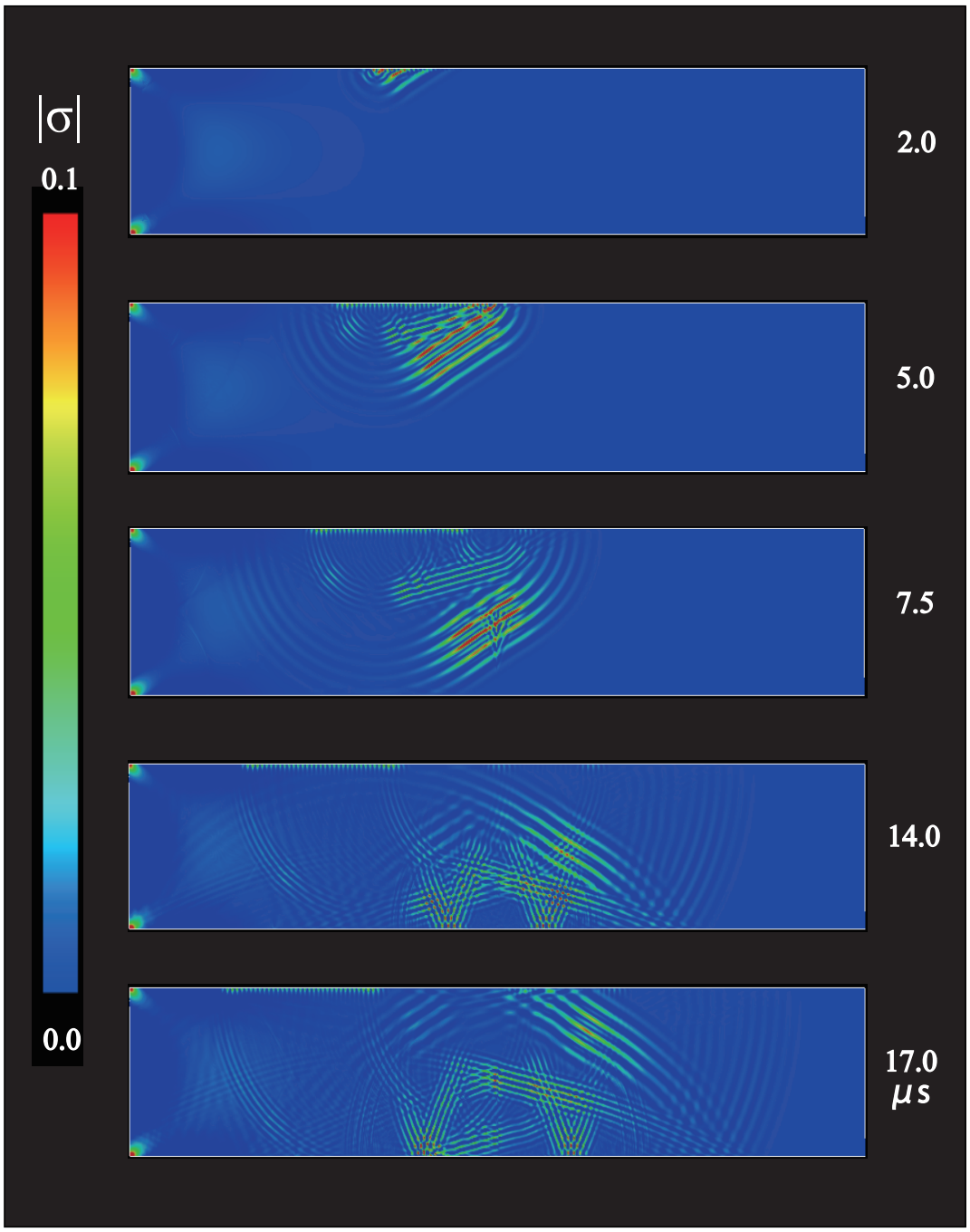

Fig. B.67 Visualization at the incident angle of 30° in the case of $\eta = 0.8$ for the closed crack with a height of 20 mm.

h]

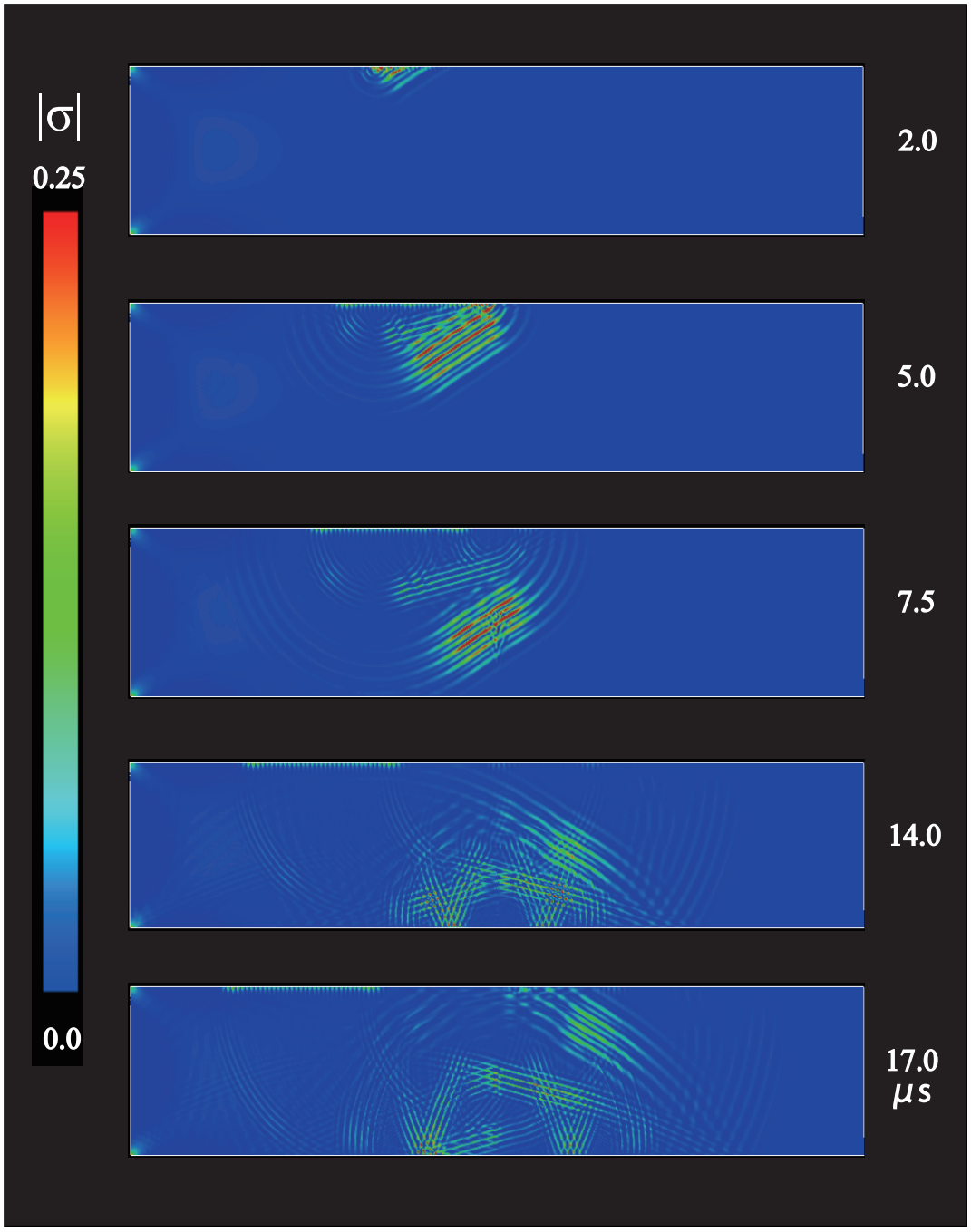

Fig. B.68 Visualization at the incident angle of 30° in the case of $\eta = 0.4$ for the closed crack with a height of 20 mm.

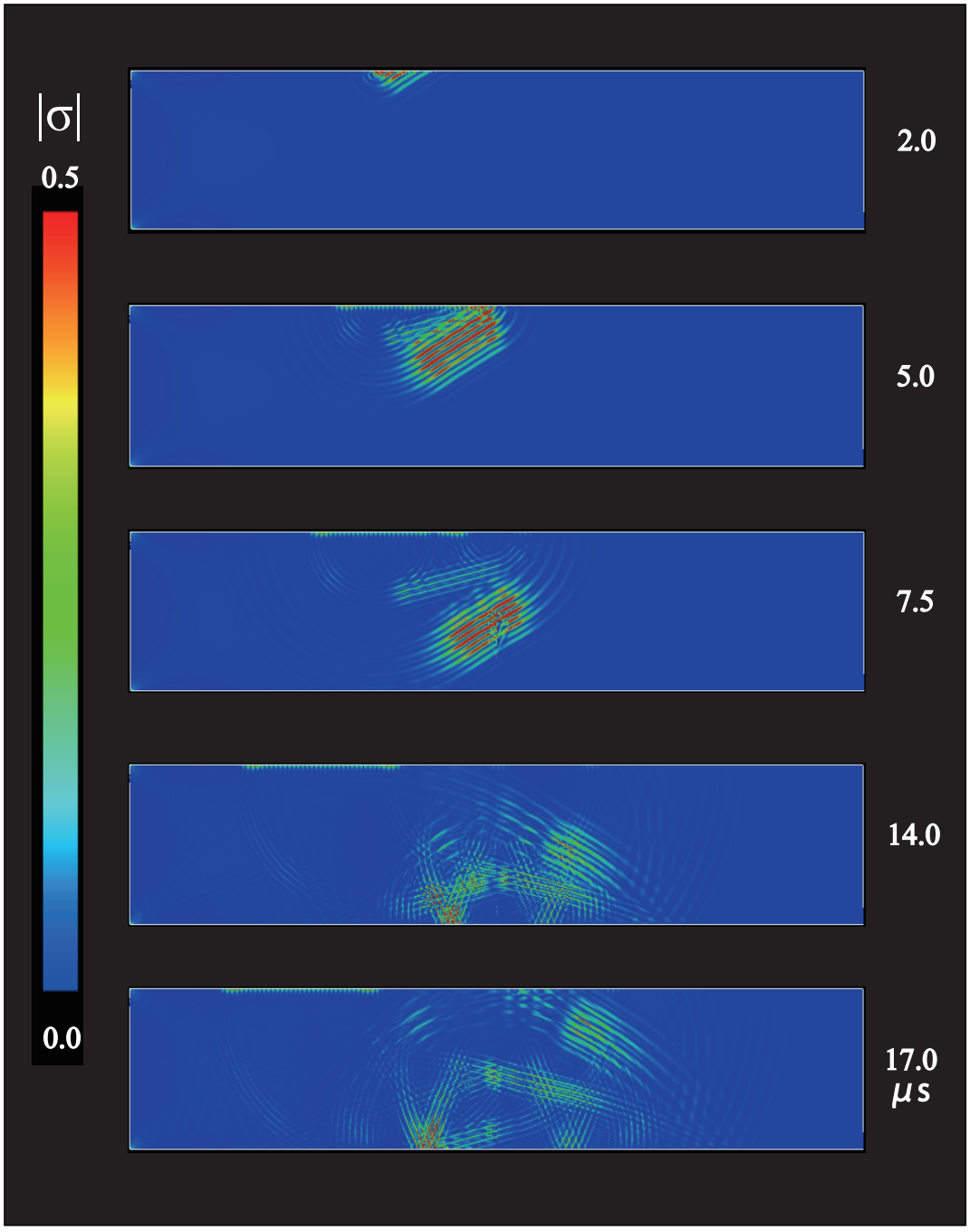

Fig. B.69 Visualization at the incident angle of 30° in the case of $\eta = 0.2$ for the closed crack with a height of 20 mm.

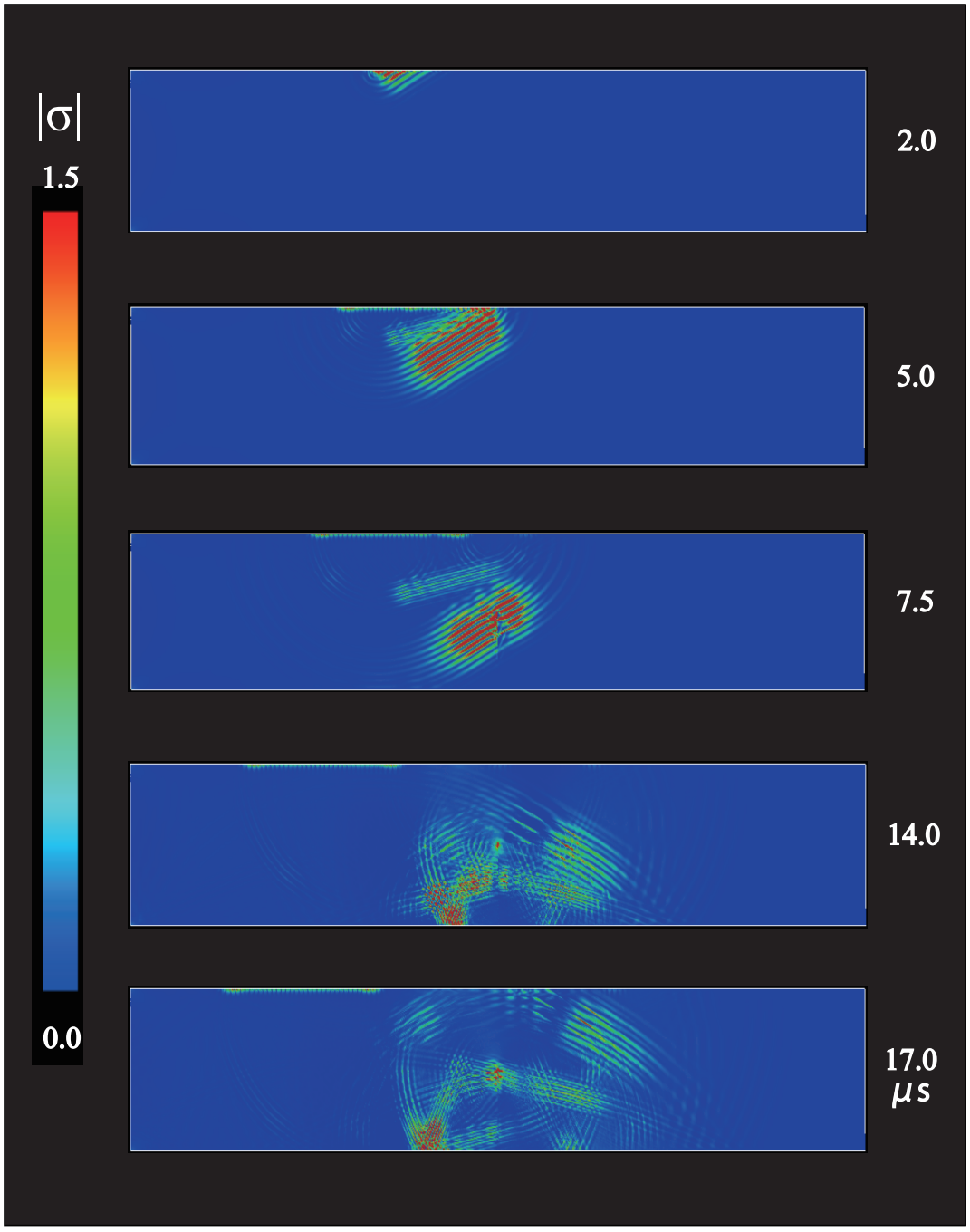

Fig. B.70 Visualization at the incident angle of 30° in the case of $\eta = 0.1$ for the closed crack with a height of 20 mm.

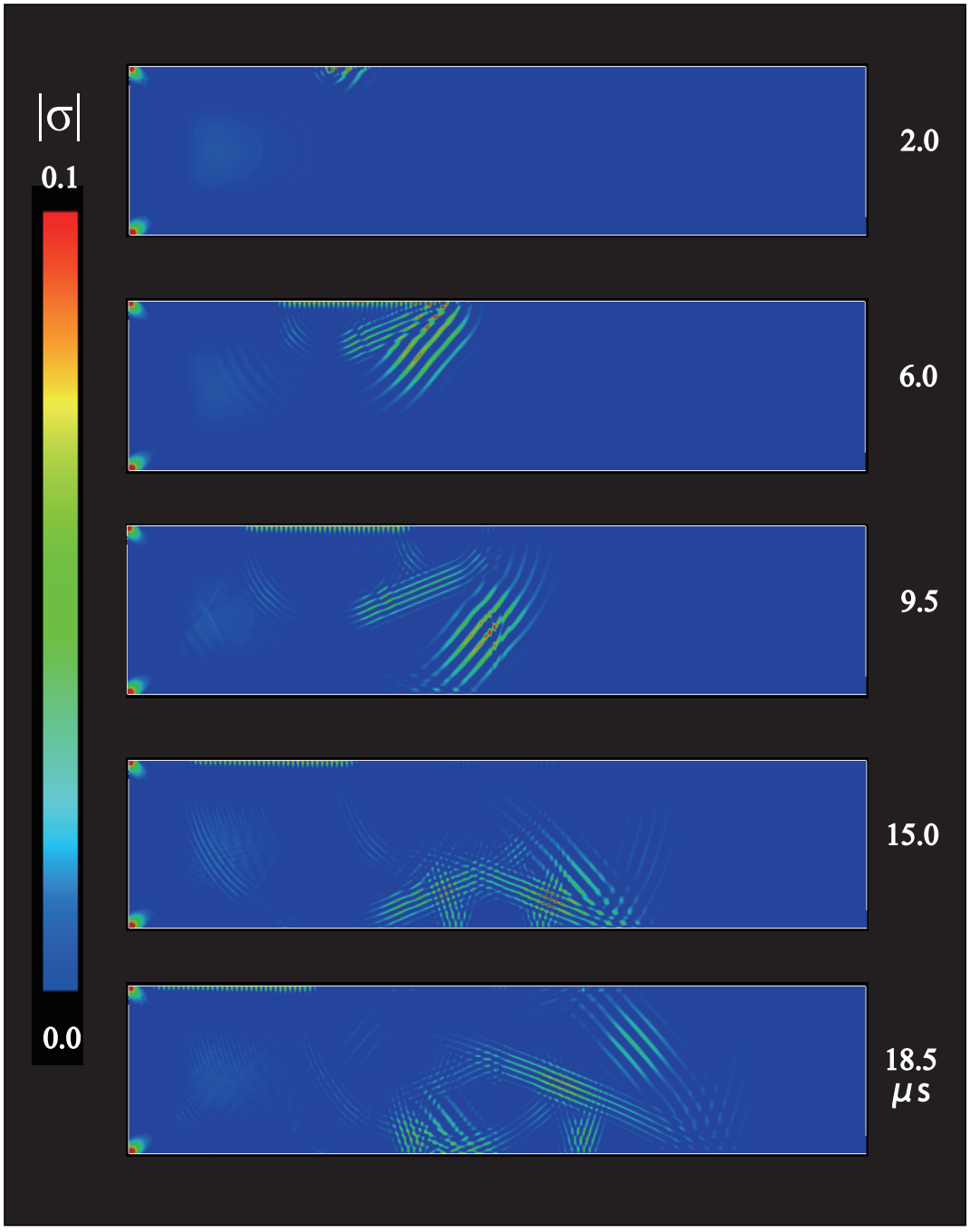

Fig. B.71 Visualization at the incident angle of 45° in the case of $\eta = 1.6$ for the closed crack with a height of 20 mm.

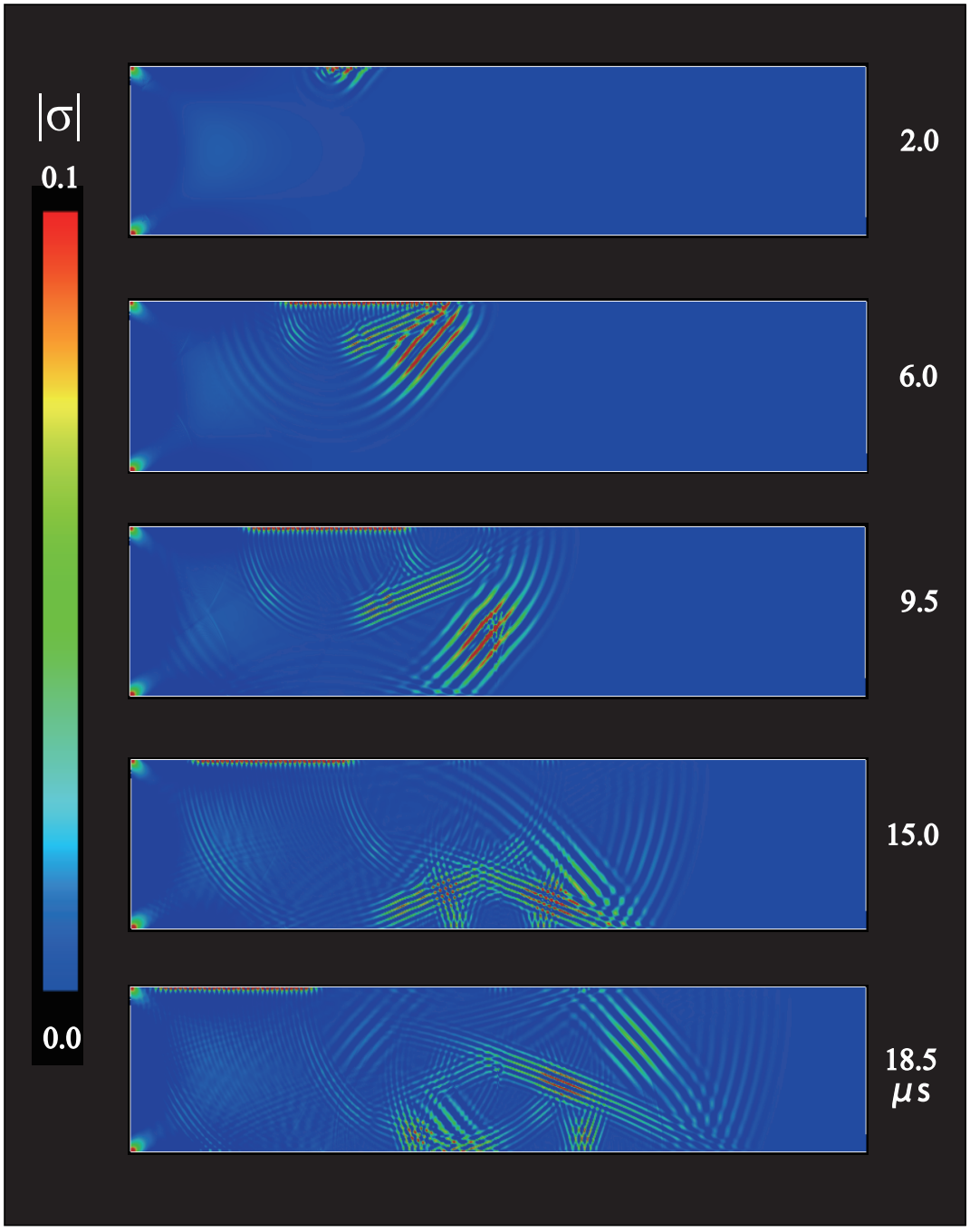

Fig. B.72 Visualization at the incident angle of 45° in the case of $\eta = 0.8$ for the closed crack with a height of 20 mm.

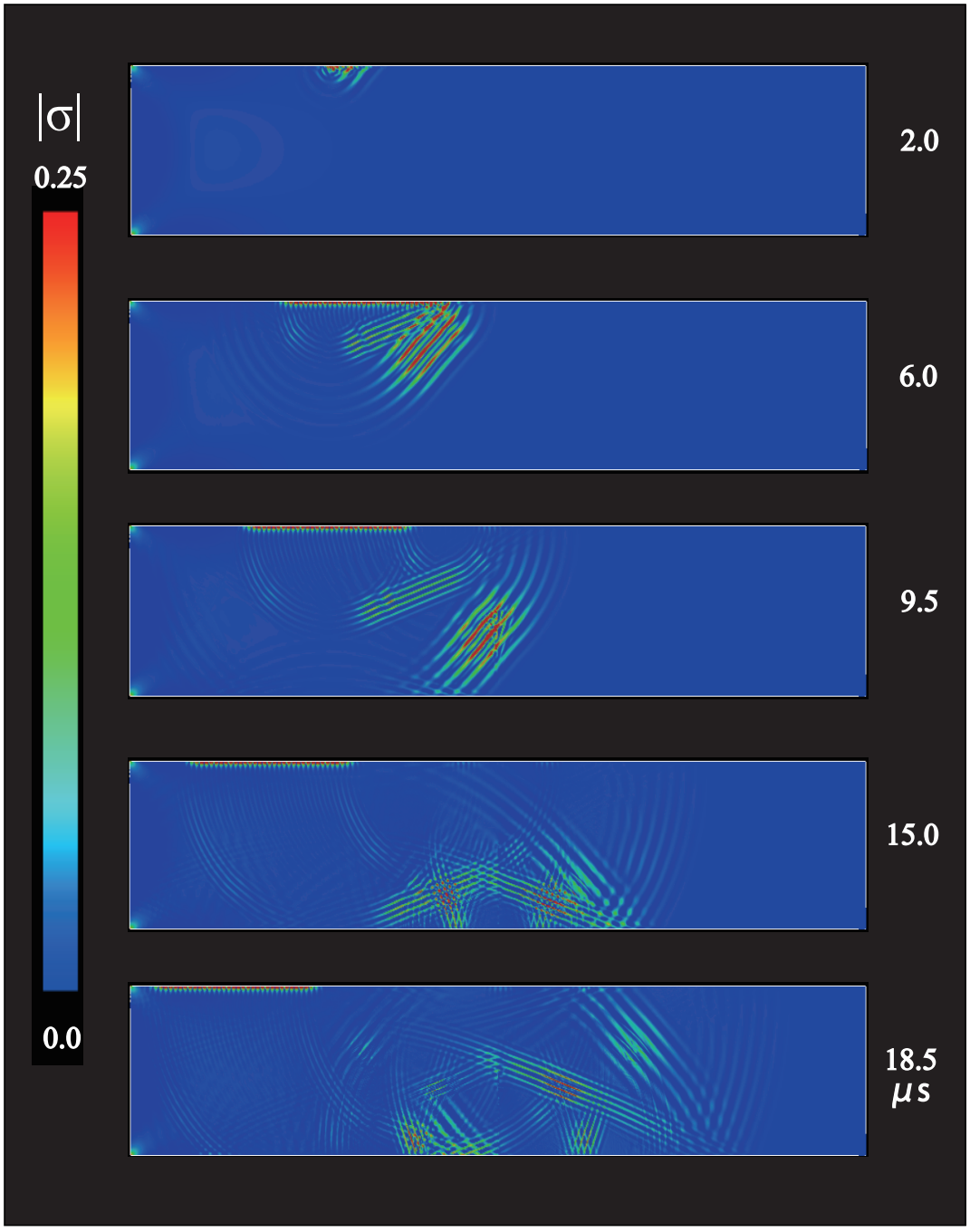

Fig. B.73 Visualization at the incident angle of 45° in the case of $\eta = 0.4$ for the closed crack with a height of 20 mm.

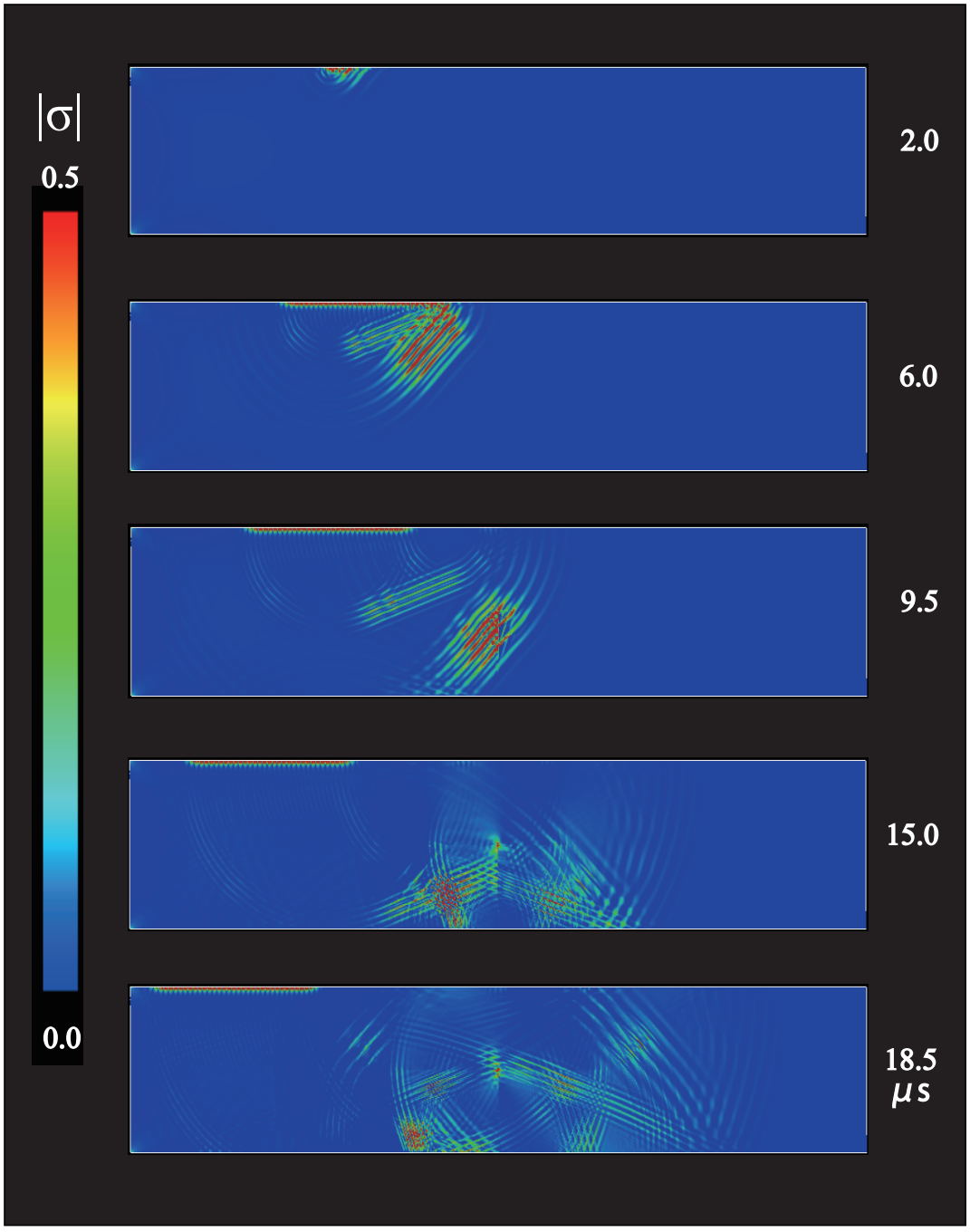

Fig. B.74 Visualization at the incident angle of 45° in the case of $\eta = 0.2$ for the closed crack with a height of 20 mm.

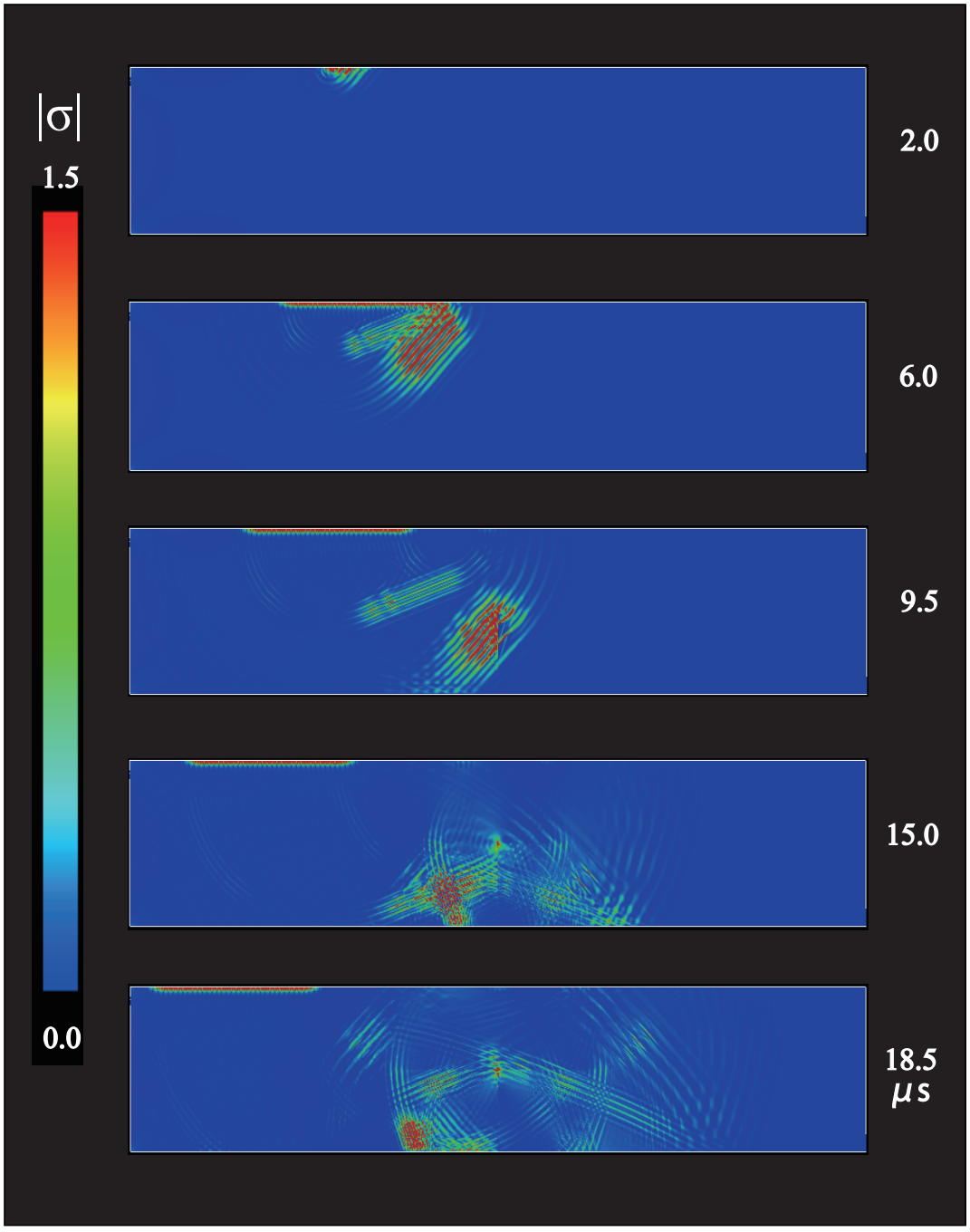

Fig. B.75 Visualization at the incident angle of 45° in the case of $\eta = 0.1$ for the closed crack with a height of 20 mm.

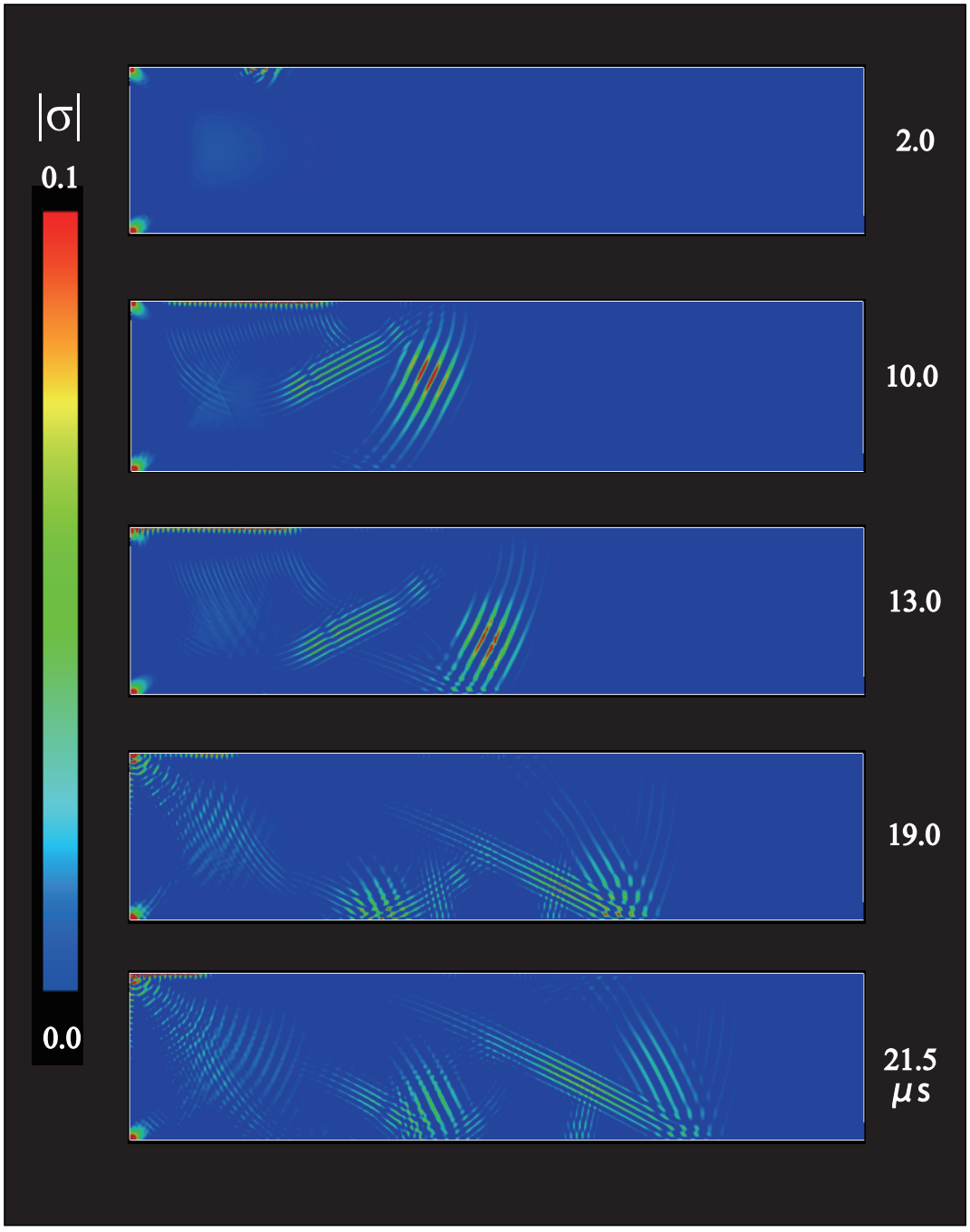

Fig. B.76 Visualization at the incident angle of 60° in the case of $\eta = 1.6$ for the closed crack with a height of 20 mm.

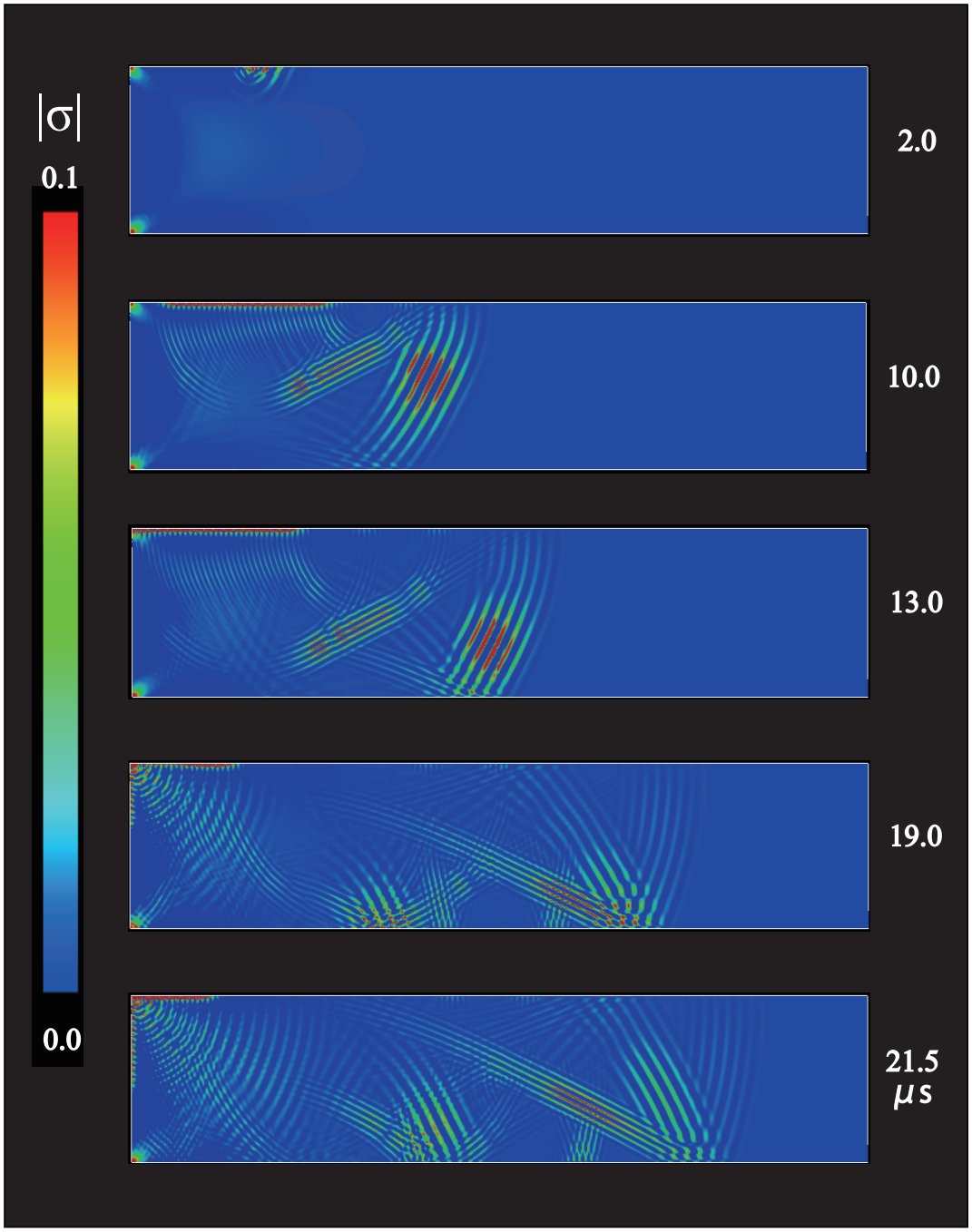

Fig. B.77 Visualization at the incident angle of 60° in the case of $\eta = 0.8$ for the closed crack with a height of 20 mm.

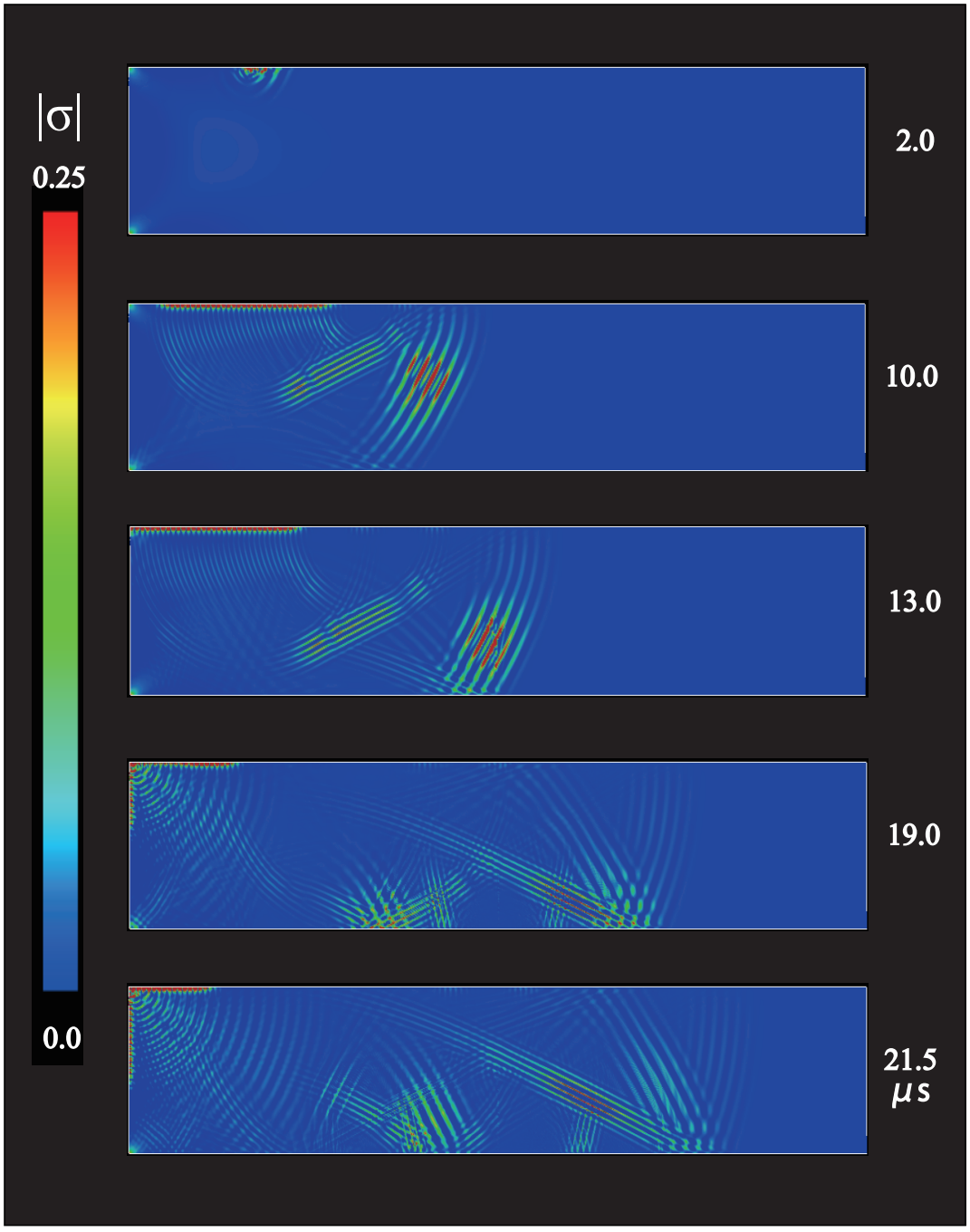

Fig. B.78 Visualization at the incident angle of 60° in the case of $\eta = 0.4$ for the closed crack with a height of 20 mm.

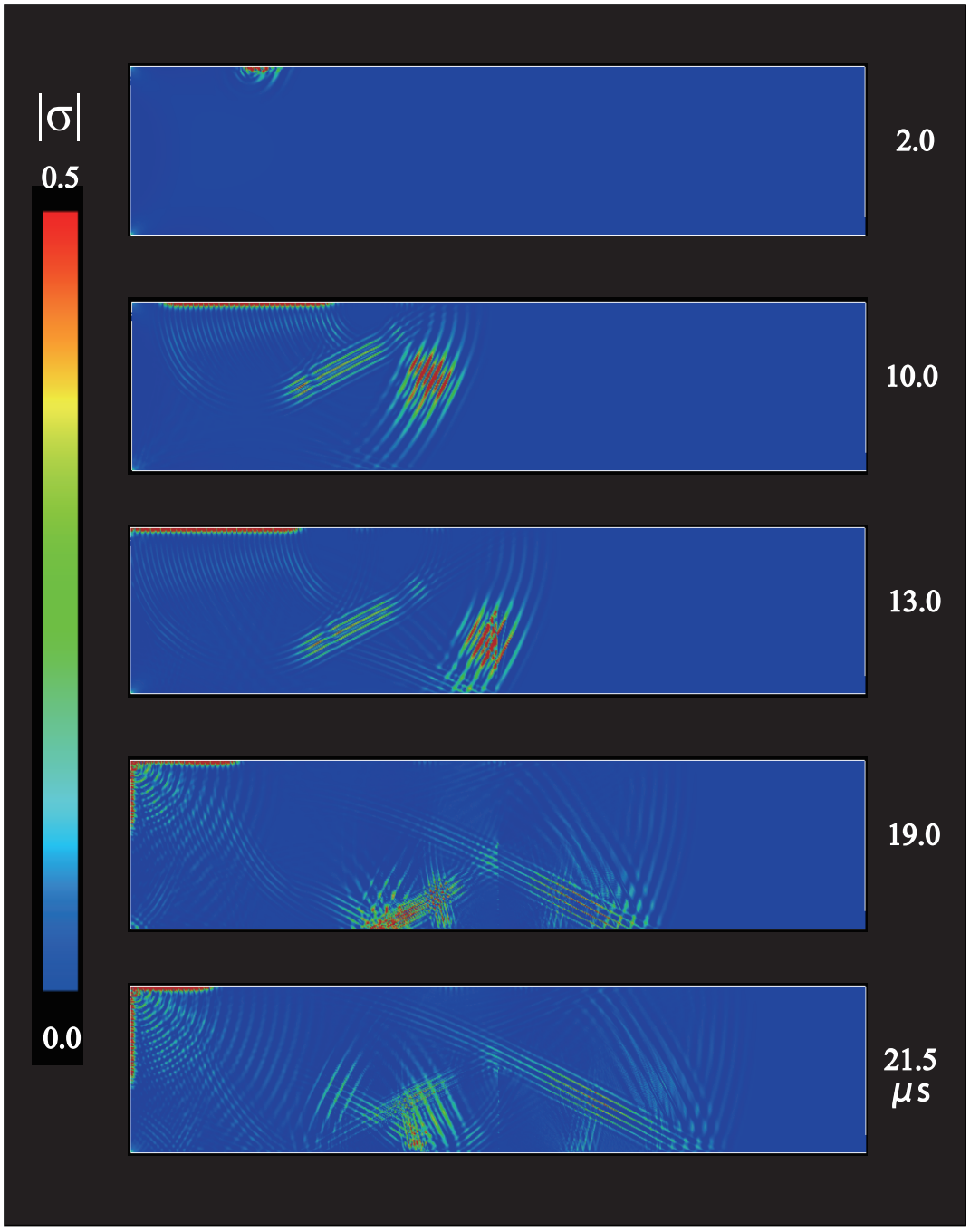

Fig. B.79 Visualization at the incident angle of 60° in the case of $\eta = 0.2$ for the closed crack with a height of 20 mm.

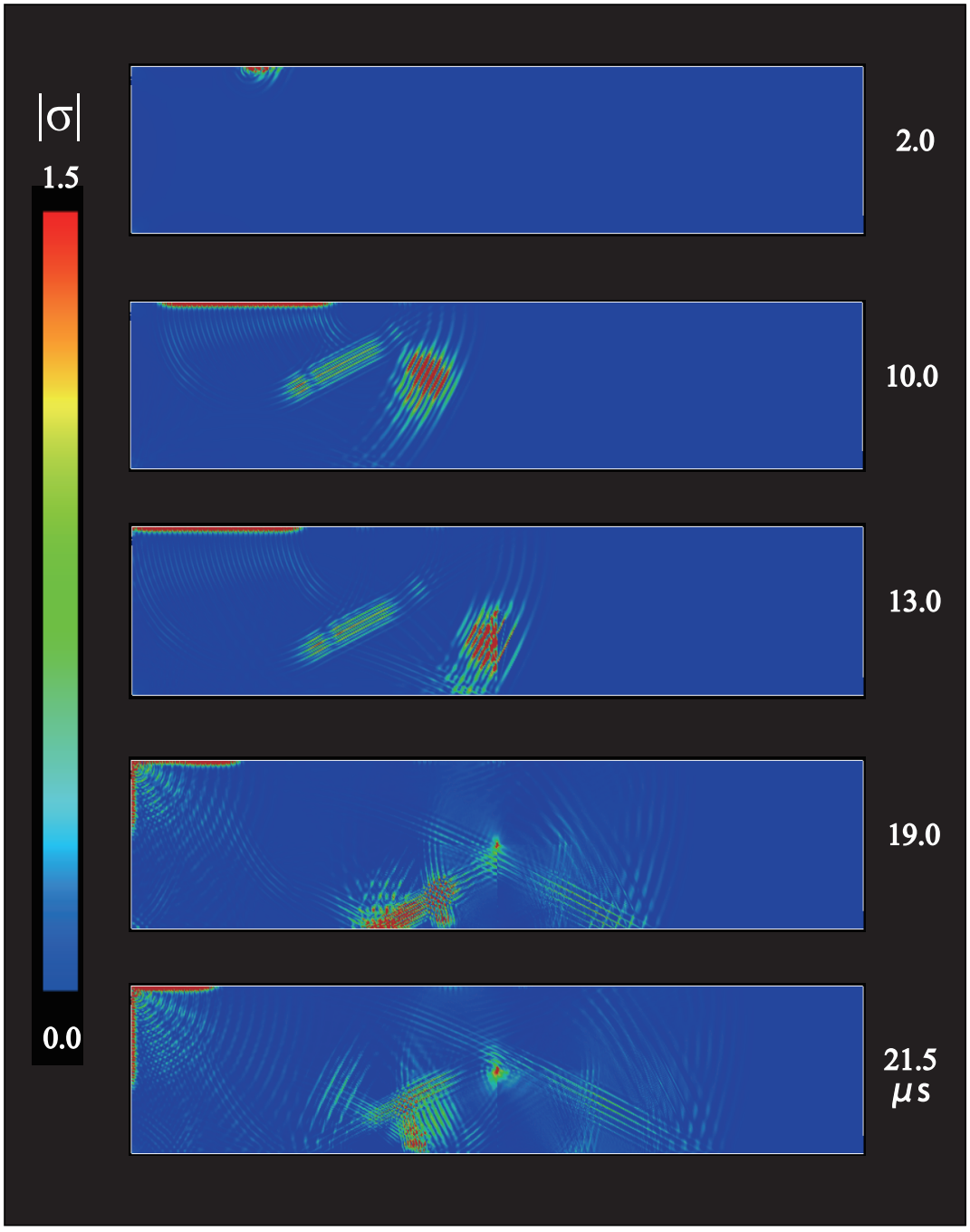

Fig. B.80 Visualization at the incident angle of 60° in the case of $\eta = 0.1$ for the closed crack with a height of 20 mm.